

**A high-resolution large-area detector
for quality assurance in cancer radiation therapy**

Inaugural dissertation
of the Faculty of Science,
University of Bern

presented by

Andreia Cristina Maia Oliveira

from Portugal

Supervisor of the doctoral thesis:
Prof. Dr. Saverio Braccini
Albert Einstein Center for Fundamental Physics
Laboratorium für Hochenergiephysik
Physikalisches Institut

Co-supervisor:
Dr. Marco Silari
CERN

**A high-resolution large-area detector
for quality assurance in cancer radiation therapy**

Inaugural dissertation
of the Faculty of Science,
University of Bern

presented by

Andreia Cristina Maia Oliveira

from Portugal

Supervisor of the doctoral thesis :
Prof. Dr. Saverio Braccini
Albert Einstein Center for Fundamental Physics
Laboratorium für Hochenergiephysik
Physikalisches Institut

Accepted by the Faculty of Science.

Bern, 12.04.2024

The Dean
Prof. Dr. Marco Herwegh

This work is licensed under CC BY 4.0. To view a copy of this license, visit <https://creativecommons.org/licenses/by/4.0/>

The art of simplicity is a puzzle of complexity.

Douglas Horton

To my parents.

Contents

Introduction	1
I Part I	9
1 The Physics of Radiotherapy	11
1.1 The Role of Radiotherapy	11
1.2 Radiation in Cancer Therapy	13
1.2.1 Interaction of Radiation with Matter	14
1.2.2 Dose Deposition in the Patient	17
1.3 Hadron Therapy	19
1.4 Clinical Practice Workflow in Radiation Oncology	22
1.4.1 Quality Assurance	24
1.4.2 Detectors for Quality Assurance (QA) in Particle Therapy	27
Bibliography	31
2 The LaGEMPix Detector Concept	39

2.1	GEMPix – the Point of Departure	40
2.2	Large Area GEMPix	41
2.2.1	Optical Readout Using Cameras	42
2.2.2	Optical Readout Using Light Sensitive Timepix3	43
2.2.3	Optical Readout Using Thin Film Transistor and Organic Photodiode	43
2.2.4	Charge Readout Using Thin Film Transistor	46
2.2.5	Charge Readout Using Timepix	46
2.3	Triple-Gas Electron Multiplier	47
2.3.1	Gaseous Detectors	47
2.3.2	Gas Electron Multiplier	48
2.3.3	Proton Irradiations at the Bern Cyclotron of the Large Area Triple-Gas Electron Multipliers	50
2.3.4	Light Production in Gas Electron Multipliers	53
2.4	Radiation-Induced Effects in Glass Windows for Optical Readout	60
2.4.1	Indium Tin Oxide-based glass materials	61
2.4.2	Proton Beam Irradiation	62
2.5	Readout of the Triple-GEM	65
2.5.1	Active Matrices	65
2.5.2	Circuits and Readout	71
	Bibliography	77
	3 Characterization with X-ray Beams	87

<i>CONTENTS</i>	vii
3.1 Precision in Radiotherapy	88
3.2 Optical Readout: GEM-OPD Array Detector	90
3.2.1 Edge Spread Function	91
3.2.2 Line Spread Function	92
3.2.3 Modulation Transfer Function	94
3.3 Comparison with Other Detectors and Simulation	95
3.3.1 GAFCHROMIC [®] Films	95
3.3.2 GEMPix	97
3.3.3 FLUKA Simulations	99
3.3.4 Discussion on the Spatial Resolution	105
3.4 Optical Readout: GEM-OPD Upgraded Version	107
3.4.1 Modulation Transfer Function	109
3.4.2 Line Spread Function	109
3.4.3 Discussion	110
3.5 Charge Readout: GEM-TFT Array Detector	111
3.6 Conclusions	113
Bibliography	115
4 Tests with Photon, Protons and Carbon Beams	121
4.1 Proton Radiation Hardness Testing	122
4.2 Proton Beam Irradiation	126
4.3 Photon Irradiation	127

4.4	Test with Protons and Carbon Ions at CNAO	129
4.5	Conclusions	135
	Bibliography	137
	Conclusions and Outlook	139
	List of Acronyms	143
	List of Figures	147
	List of Tables	155
	II Part II	157
	Reprinted Publications	159
	Contributors and Funding Sources	219

Introduction

*"Research is formalized curiosity. It is
poking and prying with a purpose."*

Zora Neale Hurston

Medical Physics is a branch of Applied Physics that uses physics principles, methods, and techniques in practice and research for the prevention, diagnosis, and treatment of human diseases with a specific goal of improving human health and well-being.

Physics and medicine have a history of a long-standing and successful symbiosis. Disciplines such as oncology and bio-mechanics, benefit from the improvement of medical practices due to the integration of physics knowledge. Additionally, new techniques emerged from this symbiosis and revolutionized some fields of medicine, such as radiotherapy. Its development was only possible with the discovery of radiation and radioactivity made by Röntgen, Becquerel, the Curies and many other scientists in the years 1895–1898.

Radiotherapy is one of the treatment modalities used to cure or control cancer. It is a field in continuous evolution aiming at prolonging substantially patient life expectancy, alleviating symptoms and improving the quality of life. The technological progress in the transformation of its practices and tools over the past decades is very remarkable. For instance, Cobalt-60 teletherapy machines dominated the X-ray teletherapy after their introduction in the early 1950s. Nowadays, more than 20,000 linacs are installed in hospitals worldwide and are the standard machines used for modern radiotherapy, making all ^{60}Co sources obsolete.

An advanced modality of cancer radiotherapy is hadron therapy. At the moment, it relies on cyclotrons and synchrotrons to accelerate predominantly protons and carbon ions.

This technique offers compelling improvements to conventional treatments due to the possibility of better dose conformity to the tumor. However, treatment with hadrons requires not only an extremely accurate dose calculation but also a precise verification of the dose delivered to the patient with high spatial resolution. Therefore, it is critical to test and validate that the planned dose is delivered exactly where needed in order to deposit energy to each point of the tumor volume while sparing the nearby healthy tissue. This is in turn guaranteed by appropriate Quality Assurance (QA) protocols and a proper set of detectors for measuring the beam parameters, in particular the beam position and the delivered dose distribution.

The present work aims at addressing the question: *“How can we improve the QA procedures by providing higher quality treatment for better patient outcomes and reducing health-care costs?”*. The answer to this question involves the development of advanced detector systems to improve current quality control protocols and dosimetry procedures. Improvements towards an all-in-one system offering precise and real-time measurements with sub-millimeter spatial resolution and uniform response to the beam energy are feasible today. The goal of this project is to facilitate the inclusion of all necessary information in the QA and treatment plan verification to enhance the quality of treatment for patients. A detector that combines a better performance than current commercial devices with significant time reduction at every step of the Machine and Patient QA chain leading to more efficient QA workflow is our ultimate goal. Hence, the purpose of the work presented in this thesis is to develop a novel large area Gas Electron Multiplier (GEM)-based detector, the LaGEMPix, providing the 2D dosimetric imaging of ion beams with sub-millimetre spatial resolution. A large sensitive area is required in order to cover the typical radiation field size and evaluate the dose distribution in the entire area.

The research for this thesis was conducted in the context of the PhD in Medical Applications of Particle Physics at the Laboratory for High Energy Physics (LHEP) and Albert Einstein Center for Fundamental Physics (AEC) of the University of Bern. During my PhD, I was based at CERN and worked in HSE-RP-SP (Occupational Health & Safety and Environmental Protection Unit - Radiation Protection group - Special Projects section). This dissertation was carried out following the establishment of a contract for a Portuguese Trainee Programme (entitled Medical Applications Detector Engineering) between the PhD's degree student, FCT (Portuguese national funding agency for science, research and technology) and CERN, which was carried out at the latter's facilities. Moreover, this project has received

funding from the ATTRACT project funded by the EC under Grant Agreement 777222, which allowed the development of the first LaGEMPix prototype in collaboration with TNO/Holst Center, Eindhoven, The Netherlands. Additionally, this project has been co-funded by the CERN Budget for Knowledge Transfer to Medical Applications.

Many of the experimental activities presented in Chapter 3 were performed at the Calibration Laboratory of CERN's Radiation Protection group. Measurements with accelerated protons were performed at the medical cyclotron laboratory located at the SWAN-Haus at the Bern University Hospital (Inselspital). In this laboratory, an 18 MeV proton cyclotron (an IBA Cyclone 18/18) is used for PET radioisotope production. The measurements were performed in a bunker served by a Beam Transport Line (BTL) that allows multi-disciplinary research also at beam intensities much lower than standard beam intensities for radioisotope production. The performance of the final system described in Chapter 4 was studied at the Centro Nazionale di Adroterapia Oncologica (CNAO) in Pavia, Italy, using clinical carbon ion beams and a water phantom. Additionally, the calibration measurements with GAFCHROMIC[®] films were performed at the Institute of Radiation Physics (IRA) in Lausanne, Switzerland. The studies of the optical transmission for several exit glass windows were realized at the Optical Quality Control Lab - Thin Film & Glass.

The present thesis is divided into two major parts: the manuscript and the scientific publications, which are the most significant with respect to the work presented in this thesis.

The first part is structured into five chapters.

Chapter 1 aims to clarify concepts and crucial approaches to this work. Firstly, it presents the role of radiotherapy as an important treatment of cancer. Then, essential concepts of ionizing radiation and radiobiology are described. Emphasis is laid on the physical processes inherent to the interaction of radiation with matter and the principles of radiotherapy. Notations and advantages of hadron therapy over conventional radiotherapy are introduced. In addition, the theoretical framework on Treatment Planning (TP) and QA is presented, giving an overview of the role and current limitations of the available dosimetry systems.

Chapter 2 covers the various readout options considered at the beginning of the project, ultimately leading to the introduction of the triple-GEM. The chapter also describes two novel readout systems and their respective operations. Detailed attention is given to the

design of the two LaGEMPix prototypes, which have an active area of $60 \times 80 \text{ mm}^2$. The first prototype combines a triple-GEM with an optical readout that utilizes a matrix of organic photodiodes on top of an oxide-based Thin Film Transistor (TFT) backplane. The second prototype eliminates the Organic Photodiode (OPD) frontplane, using only a TFT-only electronic readout. It also presents the results of the irradiation measurements conducted at Bern University Hospital (Inselspital), where we assessed different transparent anode substrates for an optical readout detector using low-energy protons. These findings are essential in ensuring the optimal functioning of the first prototype of the LaGEMPix detector with optical readout.

Chapter 3 describes the details of the X-Ray generator set-up and a collection of the measurements and results in terms of spatial resolution for various experimental configurations. A comparison of the results with Monte Carlo simulations and other detectors such as GAFCHROMIC[®] films is also given. Modifications that were implemented in order to improve the spatial resolution of the detector with optical readout are also reported. Finally, the limitations of the optical readout compared to the charge readout are discussed and summarized.

Chapter 4 encompasses the experimental results obtained with GEM-TFT detector using clinical beams, along with their respective analysis and discussion. The prototype was tested at a commercial Linac TrueBeam Varian, utilizing a 6 MV Flattening Filter (FF) photon beam, and was also tested at CNAO with clinical proton and carbon ion beams. The chapter highlights the performance of the detector with charge readout electronics in terms of dose rate dependence, dose linearity, and depth dose distribution. Additionally, a comparative study of spatial resolution in clinical proton beams using GAFCHROMIC[®] films is presented. Lastly, the chapter describes exploratory tests conducted at Bern University Hospital (Inselspital) in the field of radiation-hardness of the detector, using low energy protons.

Finally, the main conclusions drawn from the analysis I performed for this dissertation are presented. The GEM-TFT detector achieved the desired sub-millimetre resolution and was able to measure secondary electrons produced by triple-GEM structures under high-intensity beams of various high-energy radiation sources, including X-rays, protons, and carbon ion beams. Moreover, it demonstrated a linear response over a wide range of proton intensities, spanning typical doses used in hadron therapy. This chapter also summarizes some thoughts and challenges concerning promising future work that appears to be interesting for

the development of the LaGEMPix detector with an active area of 200 x 200 mm².

In the second part of this thesis, I reprinted the following selected scientific publications, which I co-authored and for which I am the corresponding author:

- **A. Maia Oliveira**, HB. Akkerman, S. Braccini, A. J. J. M. van Breemen, L. Manzano, N. Heracleous, I. Katsouras, J. Leidner, F. Murtas, B. Peeters, M. Silari, “Characterization with X-rays of a Large-Area GEMPix Detector with Optical Readout for QA in Hadron Therapy,” *Applied Sciences*, vol. 11, no. 14, Art. no. 14, Jan. 2021, doi: 10.3390/app11146459.
- **A. Maia Oliveira**, S. Braccini, P. Casolaro, N. Heracleous, J. Leidner, I. Mateu; F. Murtas, M. Silari, “Radiation-induced effects in glass windows for optical readout GEM-based detectors,” *J. Inst.*, vol. 16, no. 07, p. T07009, Jul. 2021, doi: 10.1088/1748-0221/16/07/T07009.
- HB. Akkerman, S. Braccini, A. J. J. M. van Breemen, L. Manzano, N. Heracleous, I. Katsouras, J. Leidner, **A. Maia Oliveira**, F. Murtas, B. Peeters, M. Silari, “A large area GEMPix detector with optical readout for hadron therapy (LaGEMPix),” ATTRACT Project. <https://phase1.attract-eu.com/selected-projects/lagempix-a-large-area-gempix-detector-with-optical-readout-for-hadron-therapy/> (accessed Feb. 25, 2021).
- **A. Maia Oliveira**, HB. Akkerman, S. Braccini, A. J. J. M. van Breemen, L. Manzano, N. Heracleous, I. Katsouras, J. Leidner, F. Murtas, B. Peeters, M. Silari, “A Large Area GEMPix detector for treatment plan verification in hadron therapy” *J. Phys.: Conf. Ser.* 2374 012177, DOI 10.1088/1742-6596/2374/1/012177.
- H.B. Akkerman, S. Braccini, L. Manzano, N. Heracleous, I. Katsouras, J. Leidner, **A.C. Maia Oliveira**, F. Murtas, B. Peeters, M. Silari, A.J.J.M. van Breemen, A large Area GEMPix detector for treatment plan verification in hadron therapy, *Physica Medica*, Volume 92, Supplement, 2021, Pages S124-S125, ISSN 1120-1797, doi:10.1016/S1120-1797(22)00265-4.

Furthermore, I will be the primary author of the following paper under revision:

- **A.C. Maia Oliveira**, H.B. Akkerman, S. Braccini, A.J.J.M. van Breemen, Gerwin H. Gelinck, N. Heracleous, J. Leidner, F. Murtas, B. Peeters, M. Silari, "A high-resolution large-area detector for quality assurance in radiotherapy" (submitted to Scientific Reports - Nature).

In addition, part of the results obtained during my PhD contributed to the "Section 7 - LaGEMPix" of the following publication:

- Leidner, Johannes; Murtas, Fabrizio; Silari, Marco. 2021. "Medical Applications of the GEMPix" Appl. Sci. 11, no. 1: 440, doi:10.3390/app11010440.

Moreover, I also wrote intermediate CERN technical notes:

- Maia Oliveira, A. et al. LaGEMPix: optimization of electric fields for operation with Ar:CF₄ gas mixture. CERN RP Tech Note-GEM_EDMS_2331474, EDMS no. 2331474 (2020).
- Maia Oliveira, A. et al. LaGEMPix: a new imaging sensor. CERN_RP_Tech_Note-Imager_EDMS_2426552, EDMS no. 2426552 (2020).
- Maia Oliveira, A. et al. OptiGEM – ITO Glass. Technical Note CERN_RP_Tech_Note-ITO_EDMS_2379041, EDMS no. 2379041 (2020).
- Maia Oliveira, A. et al. OptiGEM. Technical Note CERN_RP_Tech_Note-OPD_EDMS_2169268, EDMS no. 2169268 (2019).

The results of this thesis were presented at the following conferences, workshops, meetings, and seminars:

- AEC Graduate Student Seminar, Nov. 24 2021, Bern.
- HEP Group Seminar of Royal Holloway, University of London, Nov. 10 2021, online.
- Joint Conference of the ÖGMP, DGMP and SGSMP - Dreiländertagung der Medizinischen Physik, Sept. 19 - 22, 2021, online.
- 3rd European Congress of Medical Physics (ECMP 2021), Jun. 16-19 2021, online.

- 5th Technology and Instrumentation in Particle Physics Conference (TIPP 2021), May 24-28 2021, online.
- Early Career Researchers in Medical Applications online Seminar, Jun. 15 2020.
- Medical Application Projects Forum, Sept. 15 2021, Feb. 24 2021, Dec. 11 2019.
- 3rd International Conference on Dosimetry and its Applications (ICDA-3), May 27-31 2019, Lisbon, Portugal.

Part I

Part I

Chapter 1

The Physics of Radiotherapy

*"I am one of those who think, like
Nobel, that humanity will draw more
good than evil from new discoveries."*

Marie Curie

The purpose of this chapter is to introduce the basics of radiation therapy and the physics concepts crucial for this work. Firstly, it introduces the current role of radiotherapy as a crucial treatment for cancer. Then, it presents essential concepts about ionizing radiation and radiobiology. The physical processes inherent to the interaction of radiation with matter are explained. Next, terms and advantages of hadron therapy over conventional radiotherapy are introduced. The theoretical framework of Treatment Planning and Quality Assurance is presented, providing an overview of the capacity as well as the limitations of the dosimetry systems currently available.

1.1 The Role of Radiotherapy

Cancer is the medical term used to define a group of diseases characterized by abnormal and uncontrolled cell growth [1]. Cancer is the second cause of death worldwide [2] with 9.9 million deaths registered in 2020 as depicted in Figure 1.1. The International Agency for Research on

Cancer predicts that the incidence of cancer will increase in the coming years and mortality will reach 16.4 million people in 2040 [3].

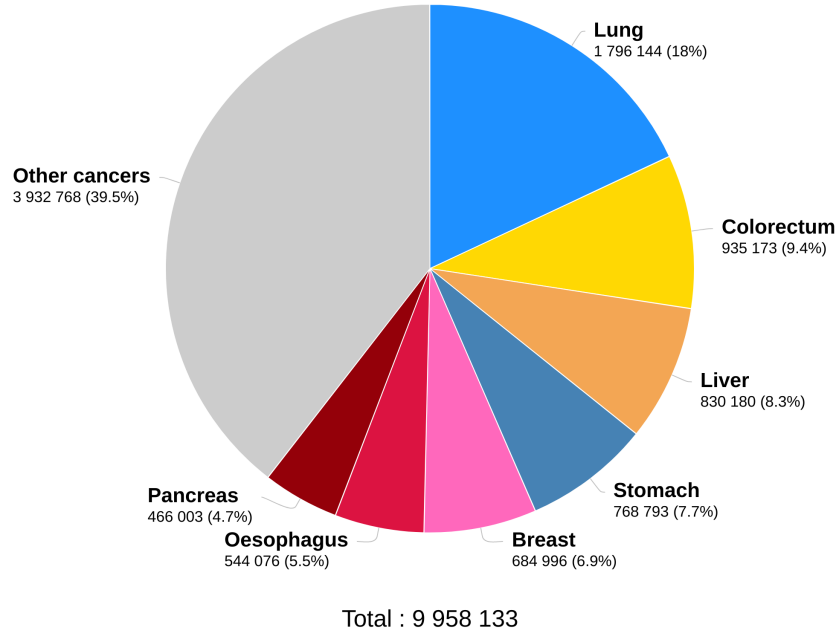


Figure 1.1: Estimated number of deaths in 2020, both sexes, all ages [4].

Apart from the pain, loss of life quality and the risk of death for the patient, cancer is also an economic burden for patients, healthcare systems, and countries, resulting in direct healthcare costs as well as lost productivity linked to illness and early mortality. The economic impact from cancer worldwide is unknown. The overall cost of cancer in Europe was 199 billion Euros in 2018 with Switzerland leading the list with the highest value of 578 Euros per capita [5]. Future advancements are motivated not only by scientific curiosity, but also by economic pressure to produce cost-effective therapies without compromising the treatment quality, aiming to save lives, contribute to longer lifespans, minimize side effects, and enhance the overall life quality of cancer survivors.

Nowadays, surgery, chemotherapy, immunotherapy, hormone therapy, and Radiotherapy (RT) are different types of treatments prescribed to cure or control cancer. The major goal is to treat numerous types of malignant and non-malignant anomalies by providing the best possible treatment and consequently, to decrease the number of deaths caused by cancer. Several parameters such as the type of cancer, the staging, and the age of the patient determine

the treatment or combination of treatments that each person will receive [6].

Each treatment modality plays a specific role in cancer therapy due to different advantages and weaknesses. RT aims to irradiate only the tumour volume. It targets a specific volume of the body and consequently has generally fewer side effects than chemotherapy. However, healthy tissue is also irradiated and radiation may still have a negative impact on healthy cells of the patient's body and cause side effects such as digestive issues and fatigue, for example. Moreover, a long-term worrying side effect is the increased risk of radiation-induced secondary malignancies in the years after receiving treatment [7]. RT has a decisive curative role in several types of cancer such as breast, lower gastrointestinal, and lung cancer [8]. Moreover, it is the only selected modality to treat many early carcinomas, such as the prostate, cervix, head and neck by teams at medical centers across the world [9]. Accordingly to Baskar et al. [9] RT contributes nearly 40% of cancer curative treatment. Hence, RT is a crucial component of cancer management. A concrete proof of that is the fact that Delaney et al. [10] estimate that the ideal fraction of novel patients that should have access to radiotherapy is 52.3%. Borrás [11] also corroborates the use of RT as one of the main strategies employed for the treatment of cancer. It is predicted that the number of patients in Europe who would have an indication for RT at least one time during the route of their treatment will reach 2,000,000 in 2025, representing an increase of 16% compared to 2012. Hadron therapy is an advanced radiation treatment modality, however, it is still not an easily accessible therapy option worldwide. It is estimated that hadron therapy, which currently uses protons and carbon ions, may be appropriate for 10–15% of the patients with indication for RT [12].

1.2 Radiation in Cancer Therapy

Radiotherapy can be used as the primary modality to treat cancer, or in combination with other therapies, for example, to kill any leftover cancer cells after surgery, or to reduce a tumor volume before surgery, and to relieve symptoms in palliative treatments. The formation of small breaks in the Deoxyribonucleic Acid (DNA) chains inside the cell's nucleus is the radiation mechanism behind this cancer treatment modality.

1.2.1 Interaction of Radiation with Matter

High-energy electromagnetic radiation (X-rays), energetic subatomic particles are used in radiotherapy as ionizing radiation (electrons, protons) or ions heavier than protons such as carbon ions.

In turn, ionizing radiation can be categorized as directly or indirectly ionizing radiation depending on the way the energy is transferred from particles to matter. On one hand, directly ionizing radiation (charged particles such as electrons, protons or alpha particles) transfer their energy to matter directly and deposit energy in the medium by means of direct Coulomb interactions. On the other hand, indirectly ionizing radiation (neutral particles such as photons or neutrons) transfers energy to the medium via a two-step process. First, they transfer their energy to charged particles of the medium and put the electrons, for example, in motion and then the subsequently released charged particle transfers its energy to the medium.

Depending on the characteristics of the incident particles and the target medium, ionizing radiation can interact with and deposit energy in traversed matter through a variety of mechanisms. The quantity of ionization energy deposited (J) per unit mass (kg) in the volume of interest is measured as absorbed dose (Gy). Furthermore, it is necessary to define the Relative Biological Effectiveness (RBE) to take into account the biological effects of different kinds of ionizing radiation on living systems. RBE is the ratio of a photon dose to any other particle dose required to achieve the same biological effect. The effectiveness of cell killing in radiation therapy depends on several factors, including the total radiation dose, the dose per fraction, the LET, as well as the specific cell or tissue type being treated. For example, heavy ions such as carbon ions are more effective than photons for a given absorbed dose (in Gy), have a higher RBE and consequently, inflict more harm to malignant cells [13]. Besides that, the prevailing interaction that gives the major contribution to the patient's dose may vary significantly depending on properties such as the charge, the energy, the particle type or the material characteristics such as the density and the atomic number Z of the absorbing medium. Each interaction has a probability associated and can be measured by the respective cross section σ . Hence, the observed effect of radiation on target materials must be viewed as a combination of all possible interactions.

Photons

The photoelectric effect, Compton scattering, and pair production are the three main processes by which photons interact. Photons can induce photonuclear interactions in addition to atomic processes, which will not be described here since they are only significant for photon energies typically above 8 MeV.

The relative importance of these three processes is determined by the absorbing medium's atomic number Z and the photon quantum energy, as explained in Figure 1.2.

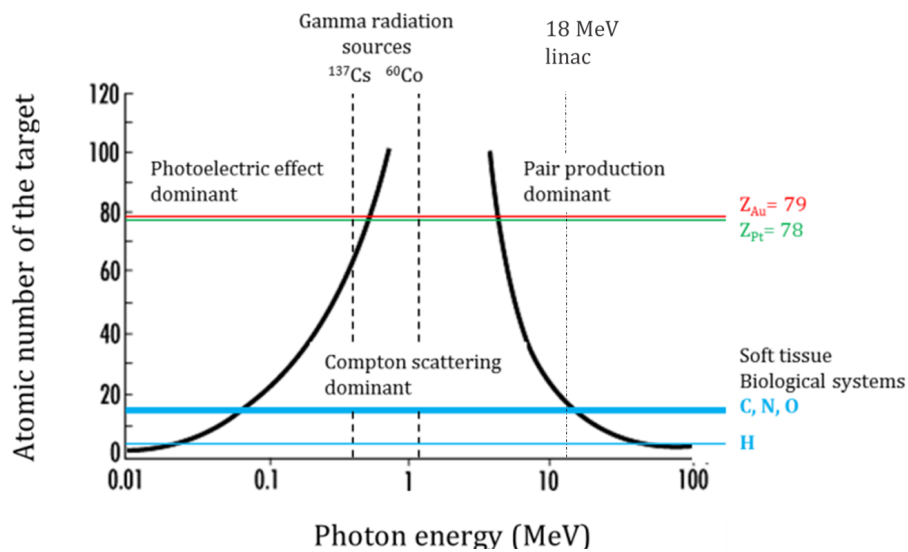


Figure 1.2: Dominant interaction as a function of the atomic number Z of the absorbing medium and the energy of the incident photon. The black curves show where two types of interactions have the same probability. The blue lines indicate carbon, hydrogen, oxygen, and nitrogen atoms, which are the main components of human tissue, fat and muscle. Adapted from [14].

Charged Particles

Charged particles lose energy in a way that is different from uncharged radiation such as X-rays. Charged particles traveling through matter are constantly interacting with the electrons and nuclei of the atoms around them [15, pp. 160-165].

Charged particles can interact with matter in several ways, including inelastic Coulomb interaction with atomic electrons, elastic Coulomb scattering with atomic nuclei, non-elastic nuclear interaction, Bremsstrahlung, and Cerenkov radiation.

Stopping Power

The stopping power, which is defined as the mean energy loss per unit path length traversing matter, can be described by the well-known Bethe-Bloch formula:

$$-\left(\frac{1}{\rho} \frac{dE}{dx}\right) = K z^2 \frac{Z}{A} \frac{1}{\beta^2} \left[\frac{1}{2} \ln \frac{2m_e c^2 \beta^2 \gamma^2 T_{max}}{I^2} - \beta^2 - \frac{\delta}{2} \right] \quad (1.1)$$

where

$$\frac{K}{A} = \frac{4\pi N_A r_e^2 m_e c^2}{A} \quad \text{with the classical electron radius}$$

$$r_e = \frac{e^2}{m_e c^2}$$

$$T_{max} = 2m_e c^2 \beta^2 \gamma^2 \quad \text{max. energy transfer in a single collision,}$$

for $M \gg m_e$

The Bethe-Bloch formula adequately predicts the stopping power of heavy charged particles, which are significantly heavier than the rest mass of an electron, in the range of $\beta\gamma$ of 0.1 to 100. This range matches with the interval of energies of protons and carbon ions used in hadrontherapy. The energy loss increases dramatically at low energies for hadrons. Hadrons have this distinctive feature of increasing energy deposition with penetration depth, with a maximum at the end of the range followed by a sharp decrease (Bragg curve). The equation does not adequately represent the energy loss of light charged particles like electrons since they can be significantly deflected by the target material as its mass is equal to the mass of the target.

1.2.2 Dose Deposition in the Patient

A few of the numerous particles found to date are suitable for RT: for example photons, protons, neutrons, electrons, and ions heavier than hydrogen like carbon. The relative dose deposited in tissue for photons, electrons and protons is depicted in Figure 1.3.

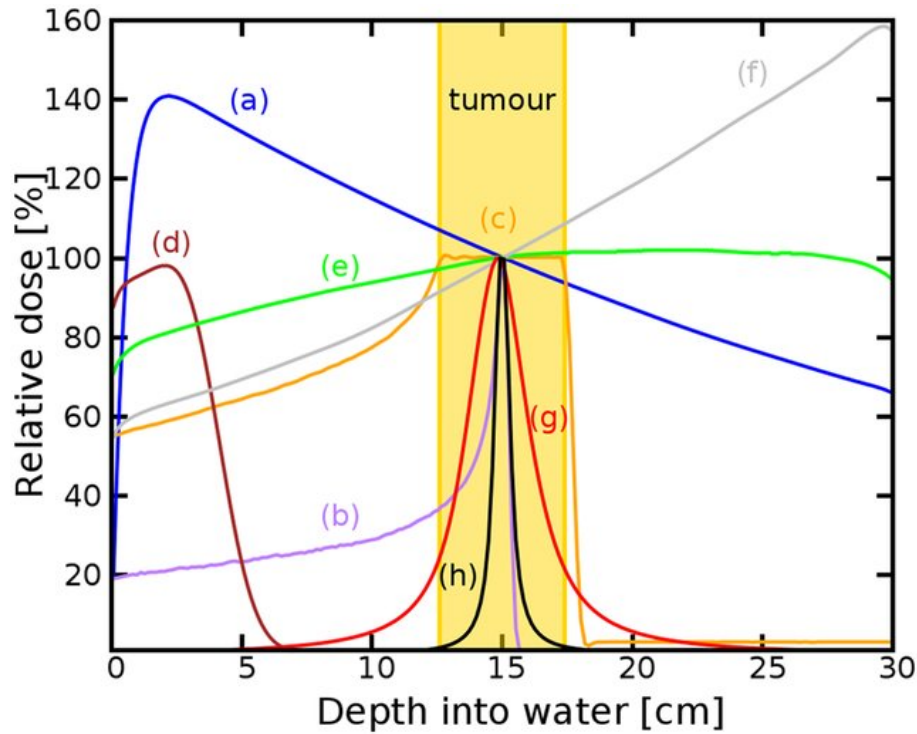


Figure 1.3: Juxtaposition of photon, proton, and electron relative dose distributions with increasing tissue depth. These include (a) 6 MV Photons, (b) Bragg peak 147 MeV protons, (c) spread-out Bragg peak, (d) 10 MeV electrons, (e) collimated 200 MeV electrons, (f) collimated 2 GeV electrons, (g) 200 MeV electrons focused at 15 cm, and (h) 2 GeV electrons focused at 15 cm. To facilitate comparison, each curve is normalized to the dose at the reference depth of 15 cm, with the exception of the 10 MeV electron beam, which is normalized to its peak dose. [16].

Conventional radiotherapy is the mainstay of RT and it uses 4–24 MV photon beams. The greatest dose is deposited within the first centimeters of tissue, followed by an exponential decrease of the dose deposition with the depth (blue curve). An X-ray photon in the therapeutic

target volume.

A more conformal dose distribution to the tumour can be achieved by using hadrons, mainly protons and carbon ions, which have this distinctive feature of increasing energy deposition with penetration depth, with a maximum at the end of the range (Bragg curve, curve (a) in Figure 1.3.). The energy deposited rapidly decreases following the Bragg peak. The orange curve (c) in Figure 1.3 shows a Spread-Out Bragg Peak (SOBP) from numerous modulated proton beams, demonstrating that the whole tumor volume can be covered. The entrance dose increases when several beams with varying energies are superimposed, yet the entrance dose remains lower than for conventional therapy. In comparison with conventional X-ray radiotherapy, there is a significant reduction of the dose in the entrance and a huge difference beyond the tumor. These features allow the minimization of the detrimental side effects due to the reduction of the radiation received by healthy tissue.

The depth dose curve in the patient for Electron Beam Therapy (EBT) is radically different as shown by the curve (d) in Figure 1.3. The short range of clinical electrons makes electron radiotherapy appropriate for the treatment of skin cancer, e.g. squamous cell carcinoma, melanoma, mycosis fungoides. Electron beams are commonly used for intraoperative radiotherapy and in treatment of the head and neck tumours [19, 20, 21]. Electrons lose energy mostly through collisions and produce ionization processes very frequently in the patient's body due to their low mass. In addition, electrons are constantly slowing down due to Coulomb interactions. Consequently, the energy is deposited in the patient in the first few centimeters and the maximum range is determined by the initial electron energy. Bremsstrahlung photons produce a low dose tail with a longer range with a minor contribution to the total delivered dose. Alternative modality techniques to reach deep-seated tumors using Very High Energy Electrons (VHEE) beams (curves (h) and (g) in in Figure 1.3) have been studied [22].

1.3 Hadron Therapy

Hadron therapy is a type of radiotherapy for the treatment of tumors that uses beams of particles consisting of quarks: neutrons, protons, helium ions, lithium ions, boron ions, carbon ions, oxygen ions, pions, antiprotons, etc [23].

The history of applications of hadrons in medicine began when Ernest Lawrence built the first cyclotron capable of producing a proton beam at the end of 1932 [24, pp. 4]. Lawrence and his brother John decided to employ fast neutrons and radioisotopes produced at this new accelerator for cancer treatment purposes [25, pp. 13-19] [26]. In 1946, Robert Wilson, who was Lawrence's student and afterwards became the Fermilab founder, suggested the irradiation of cancer patients predominantly with protons, taking advantage of the Bragg peak [27]. This particular characteristic provides a more conformal dose distribution to some tumors, reducing the negative side-effects due to radiation delivered to healthy tissue, as explained in Figure 1.3. The first patient was treated with protons in 1954 at the Lawrence Berkeley Laboratory using a 340 MeV cyclotron. This remarkable event was followed by a clinical trial with metastatic breast cancer. Further research in other facilities broadened this modality's application to the use of ions, launching a broad field now known as hadron therapy. The first hospital-based proton treatment facility was built in the US in 1990 [28]. The main advantage of this advanced modality is the better sparing of healthy tissue relative to the photon beams. At the moment, hadron therapy is especially indicated in the treatment of pediatric malignancies, where potential long-term collateral effects are of particular concern, as well as tumors in difficult surgical access areas or adjacent to vulnerable organs or even in re-irradiation scenarios [12]. Tumors in the skull base, spinal cord, brain, eyes, lungs, and esophagus are examples of typical cases indicated to hadron therapy. Treatment with heavy ions is also recommended for the cure of radio-resistant tumors due to the high RBE.

Currently, there are vendors in the market that sell cyclotrons and synchrotrons, which provide reliable particle beams. Cyclotrons, in particular, have gained attention for being less expensive compared to synchrotrons, making them an attractive choice for medical institutions seeking this advanced technology. As a result, more and more hospitals and clinics are investing in hadron therapy centers with cyclotron technology to offer this cutting-edge treatment option to their patients. As of May 2023, there are over 120 particle therapy centers worldwide, with more being planned or under construction. Of these, 109 centers utilize proton therapy in external beam radiation, while 13 centers use carbon ion therapy. Notably, 6 of these centers are dual ion facilities that offer both proton and carbon ion treatments. Nowadays, treatment with hadrons is gaining popularity globally and more than 60 centers are planned for the near future. By the end of 2020, more than 290'000 patients had been treated globally using particle therapy, including almost 250'000 with protons, nearly 40'000 with carbon ions,

and around 3'500 with He, pions, and other ions [29]. This modality is currently based on two different types of accelerators. Proton therapy requires 4-5 m diameter cyclotrons and 6-8 m diameter synchrotrons, while 20-25 m diameter synchrotrons are used to accelerate carbon ions.

The beam delivery system coupled to the accelerators might be either "passive" or "active". Initially, hadrons were viewed as photons and the beam was spread over the target volume using "passive" shaping components adopted from conventional RT, such as range shifters, scatterers, collimators, and compensators. The alignment of all these components is very critical and the exposure of material in beam leads to the production of neutrons. Moreover, a workshop is required to manufacture patient specific devices. "Passive" beam delivery system do not profit from one of the most essential features of hadrons, its electric charge. Due to their electric charge, hadrons can be directed by means of magnetic fields. Active scanning techniques (spot or raster scanning) permit to magnetically control a narrow pencil beam and paint a layer across the tumor target at a given depth. The selected layer to paint can be changed by varying the energy of the beam and in this way, it is possible to guarantee a full coverage of the tumor volume. On one side, the ability to generate any geometries of homogeneous high-dose zones with a single beam is a benefit of "active" over a "passive" beam delivery. Other advantages are the possibility of Intensity Modulated Proton Therapy (IMPT) and the fact that no patient specific hardware is needed. The downside is that the "active" approach is more sensitive to organ motion during scanning and the dose distribution and homogeneity can be compromised [30]. Monitoring the intensity and position of the beam in real-time is crucial.

Despite the rapidly growing interest, hadron therapy is still not a widely available treatment option. The necessary hardware/equipment is costly, it requires regular maintenance and spacious facilities that can occupy a large territory of up to a few hectares, and involves a steady operating environment and highly educated/trained personnel. A particle treatment center's expense and space are substantially bigger than those necessary for conventional radiotherapy. As a consequence, this has delayed or inhibited access to this radiation modality in low- and middle-income countries. Design of new options for next generation accelerators, beam lines, detectors and other hardware should improve accessibility for this type of therapy in general by being more compact, cost-effective and less intricate.

1.4 Clinical Practice Workflow in Radiation Oncology

Cancer therapy is a fairly complex chain of processes that includes several phases as depicted in Figure 1.5 and ends, ideally, with the confirmation that the treatment was effective.

In the beginning, the oncologist evaluates the patient's overall clinical condition in order to indicate the best therapeutic method possible. After being referred to radiation treatment, the patient is normally submitted to structural imaging using contrast CT or MRI. This first imaging step is crucial to help the oncologist to delimit the extension of the tumor and to define the prescribed dose as well as the fractionation (dose per fraction, dose per day, and total dose). Moreover, a combination with molecular imaging using Photon Emission Tomography (PET) or Single Photon Emission Tomography (SPECT) allows a more functional evaluation of the cancer leading to more accurate contouring of the volume to irradiate.

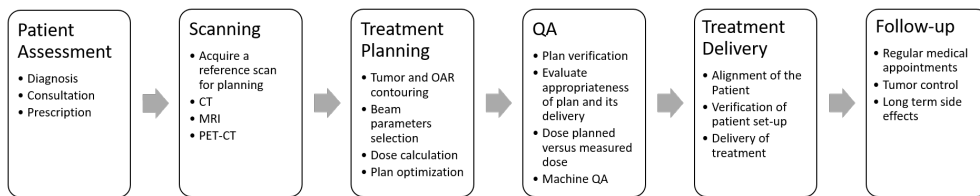


Figure 1.5: Summary of the typical stages in radiotherapy workflow.

Ideally, a huge amount of dose should be delivered to the target volume while zero dose should be delivered to the surrounding healthy tissues, especially the Organ At Risk (OAR). Unfortunately, the real scenario of all the modalities of RT is disparate. Margins for several uncertainties have to be taken into account by the radiation oncologist in order to assure that the entire tumor volume is irradiated. Several volumes are defined after the analysis of these images by the radiation oncologist, such as the Planning Target Volume (PTV) and OAR. The PTV includes the margins for: uncertainties in patient positioning; alignment of the beam; variations in the size, shape of the tumor, and position of the Clinical Target Volume (CTV), that can happen during the course of the treatment; subclinical malignant disease [31].

The Treatment Planning (TP) is usually done by a dosimetrist and/or medical physicist using a treatment planning system. The Treatment Planning System (TPS) simulates the spatial distribution of the radiation dose by employing computer algorithms to the patient's

images to modulate the interactions between the radiation beam and the patient's anatomy. A specific plan is developed and the characteristics of the beams, such as the optimum beam angles and collimation, are selected. The plan is created taking into consideration the instructions given by the physician and keeping the OAR's tolerance limits as strict restrictions. Once the treatment plan is completed, it has to be approved by the physician.

Following this step, it is important to establish a comprehensive QA program. QA is “*all those planned or systematic actions necessary to provide adequate confidence that a product or service will satisfy given requirements for quality*” as defined by the International Standard Organization (ISO) [32]. To deliver safe radiation treatment, it is critical to test it and confirm that the delivered dose matches the prescribed dose. The treatment plan verification is done by the medical physicist to ensure that the dose distribution generated by the TPS is correct for the specific patient. Each treatment facility must establish a well-defined QA process. A typical one normally involves measuring the dose deposition predicted by each individual treatment plan at some points in a homogeneous water phantom or water equivalent phantom representing the patient and comparing the measured values of dose to the equivalent values computed by the TPS under similar circumstances.

The therapeutic phase is handled by radiotherapy technologists who interact directly with the patients and are responsible for accurately positioning the patient. However, anatomical patient alterations due to weight reduction or tumor shrinking, for example, may exist within a few weeks of fractionated treatments. Adaptive radiation therapy (ART) is a therapeutic method that employs imaging on a regular or near-daily basis to correct for anatomical variations during the course of the entire treatment.

The radiation oncologist sees the patient on a regular basis. The follow-up continues even after the completion of the treatment and the physician conducts inquiries in which the technical data is archived into the clinical process of the patient. The registration of the treatment outcome and the side effects from irradiation that may occur during therapy provide essential information to physicians for making educated decisions regarding expected benefits versus anticipated adverse effects.

1.4.1 Quality Assurance

The aim of radiation therapy is to kill the cancer cells, while minimizing the risk of side effects to the adjacent healthy tissue. Tumor control and normal tissue complication probabilities are functions of the dose as shown in Figure 1.6 [33, 34].

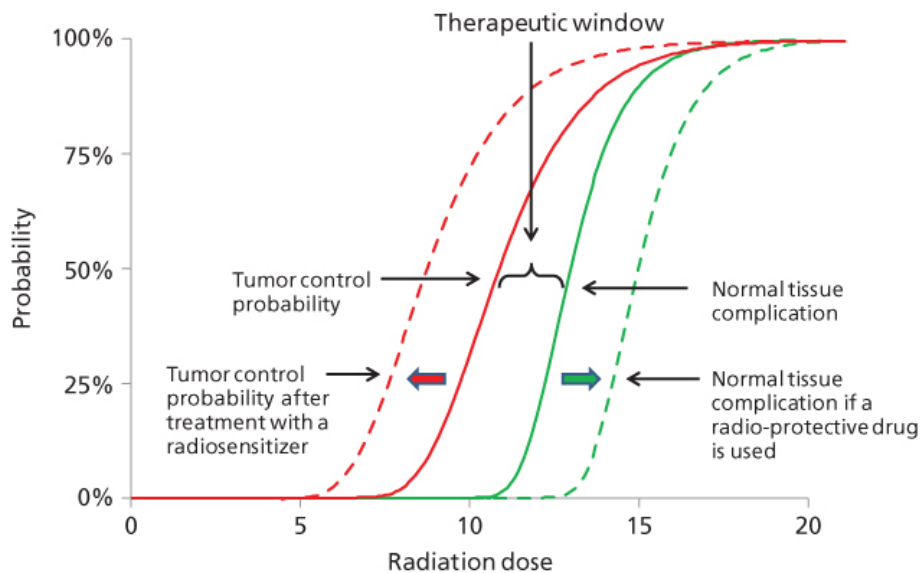


Figure 1.6: The principle of therapeutic ratio. Dose–response red curves represent the tumor control probability (TCP) and the green curves the normal tissue complications probability (NTCP). Chemotherapy for example, can increase the separation between the two curves in order to achieve an optimal therapeutic window [34].

As the dose increases, the likelihood of tumor control is also higher. Unfortunately, the effect of small variations in the absorbed dose in this high dose region can have major clinical impacts on healthy tissue, since the therapeutic window shrinks. There are other complementary therapies to change the response curves of tumor cells and the healthy tissue toxicity to radiation [35]. In spite of the efforts to increase this separation gap, the therapeutic window between the dose–response curves can be narrow depending on the clinical situation. Consequently, the evaluation of the dose and the dose distribution administered to the patient is a fundamental quality control process during the radiation treatment. The International Commission on Radiation Units and Measurements (ICRU) states that at the level of one standard deviation, relative accuracy of 3% is desirable, although 5% is often accepted, while

relative precision (reproducibility) of 2% is required [36]. Therefore, it is critical to validate that the required dose is delivered exactly where needed and no healthy tissue is unnecessarily irradiated.

The advantage of the hadrons stopping at certain depth in the patient is also a huge challenge for QA. Measuring the range with precision is important for an accurate dose deposition. Figure 1.7 compares a 5 mm range error using photons and carbon ion beams.

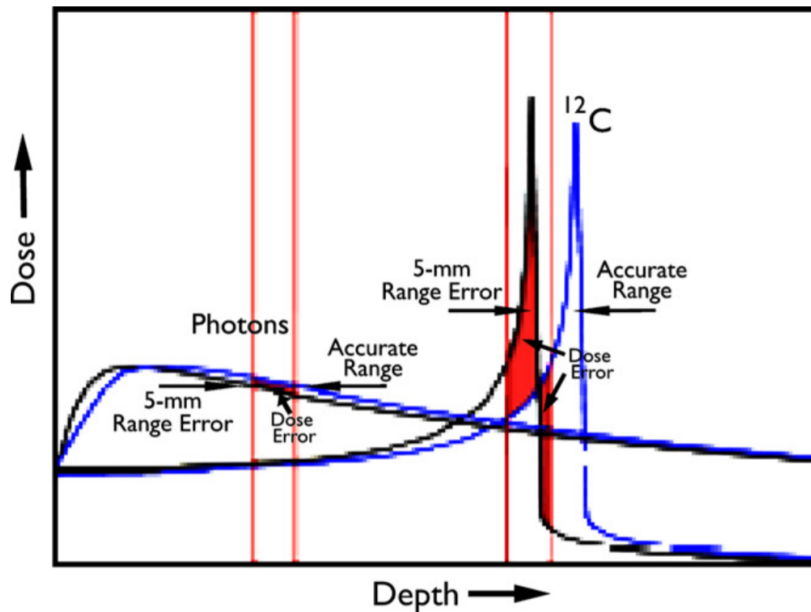


Figure 1.7: A slight inaccuracy in photon target depth (red vertical lines on the left) results in a tiny dose error (shaded region). A comparable slight target-depth inaccuracy with carbon-ions, on the other hand, leads in significantly more critical mistakes (shaded areas illustrate substantial areas of under- and over-dose) [37].

The same slight target-depth error with carbon-ions may drastically alter the dose to both the tumor and healthy normal tissue, as seen in Figure 1.7. In contrast, it is also shown that the same error has a substantially lower influence on X-ray treatments. Since hadrons are more sensitive to density changes, uncertainty in the translation of the patient's CT scan to stopping power data or the breathing motion during the treatment administration may alter the depth of the Bragg peak, which can drastically affect the dose to both, the tumor and the crucial healthy tissue. Taking into account this uncertainty, the precise lateral penumbra of a proton beam is commonly utilized to spare sensitive normal structures like OAR during the

treatment of clinical sites where the target volume either comes into close proximity with or encompasses these structures.

During a proton or heavy ion therapy course of more than one month, the patient's anatomy might differ from the initial defined PTV due to factors such as patient weight loss, tumor shrinking, or gas in the intestine. As a result, a significant deviation of the planned deposited dose may occur when using hadrons, as seen in Figure 1.7. These facts reinforce the crucial role of an efficient and high precision QA protocol.

The effectiveness and the success of hadron therapy are determined by the accuracy with which the required dose is delivered to the target volume while sparing healthy tissues. In order to maximize tumor control and minimize detrimental effects QA is the key to the success of hadron therapy. To reduce treatment uncertainties and avoid mistakes, aspects from the beginning of the RT workflow such as the patient's diagnostic images to the final positioning of the patient on the treatment day, passing through the technical aspects of the beam delivery system must be checked. Additionally, QA also improves the likelihood that problems will be identified and corrected sooner if they occur, lowering the repercussions for patient treatment. Furthermore, it allows a reliable exchange and intercomparison of clinical data clinical between several facilities.

During the past years several international and national regulations and recommendations, such as the "*IEC 62667:2017 Medical electrical equipment - Medical light ion beam equipment - Performance characteristics*" or "*PTCOG Safety Group Report on Aspects of Safety in Particle Therapy, 2016*", defined a few detailed and hard requirements. Then, each facility has to define and document a specific and detailed QA procedure that takes into consideration the particular equipment available and existing personnel. The medical physicist is deeply involved in the verification of the appropriate physical and clinical factors, such as the dosimetric tests on dose distributions. An integrated team from all groups must ensure that a comprehensive QA program is applied. Two examples of the detailed list of test tolerances and test methods can be found in [38, 39].

1.4.2 Detectors for Quality Assurance (QA) in Particle Therapy

To accomplish an efficient QA protocol, it is critical to monitor the beam parameters as well as the delivered dose using a proper set of dosimeters [40]. A radiation dosimeter is a device, instrument, or system that directly or indirectly detects and assesses exposure, absorbed dose or dose equivalent, kerma, or any physical quantity related to ionizing radiation. Kerma, or Kinetic Energy Released per unit Mass, is a measure of the energy transferred from ionizing radiation to a material per unit mass, providing insights into the radiation dose deposited in the material. A dosimetry system is composed of a dosimeter, a reader, and a measurement/calibration procedure [41].

Various types of dosimeters are used to measure 2D dose distribution during normal QA controls [42]. 2D/3D systems are particularly efficient in measuring the dose deposition of a dynamic beam (scanning). In hadron therapy, typical sensitive areas of $200 \times 200 \text{ mm}^2$ are required to cover the maximum typical clinical field size [38]. However, larger fields can be reached with the available solutions and, for example, the maximum field size of the Varian Probeam is $300 \times 400 \text{ mm}^2$ at isocenter [43].

Due to their proven performance, accuracy, and stability (small variation in response with energy, dose and dose rate), international dosimetry guidelines propose the use of an array of ionization chambers for QA testing [36]. Nevertheless, the spatial resolution of ionization chamber-based devices is limited by the size of the currently available detectors. The OCTAVIUS[®] Detector 1600 SRS, for example, is composed of a matrix of 1521 vented plane-parallel ion chambers spaced between 2.5 mm and 5 mm in the central area [44].

Films such as radiochromic EBT3 are widely used as relative dosimeters e.g. for constancy checks because of their superior spatial resolution of up to $25 \mu\text{m}$. Several groups also established films based dosimetry protocols to obtain absolute dose values [45, 46, 47]. However, they give an offline response that is strongly reliant on particle energy and time-consuming [48, 49].

Optical readout-based detectors, such as scintillating screens coupled to CCD cameras with high spatial resolution have been developed for 2D dosimetry and can be used for online monitoring of the beam [50]. Other examples include the Lynx[®] commercial detector, which

is made of gadolinium-based plastic and is only appropriate for relative 2D dosimetry studies due to its high energy dependency [51].

IBA launched recently the myQA[®] Phoenix, an high-resolution digital detector array with a sensitive area of 400 x 400 mm². It is an amorphous silicon panel with 0.2 mm pixel pitch, which works in direct conversion mode. A calibration curve of the detector signal has to be determined for each energy [52]. Moreover, The Sphinx Compact is a solution from IBA for daily QA workflow in radiotherapy, tailored specifically for Pencil Beam Scanning (PBS) machines. It is comprised of three main components: a carbon fiber frame, a high-resolution photo-diode type flat-panel imager and a diverse array of block modules crafted from high-density plastic material with various shapes. Based on the findings in reference [53], it can be inferred that the device under investigation effectively meets the requirements outlined in the American Association of Physicists in Medicine Task Group 224 Report for daily QA tests. Despite the observed quenching effect at the Bragg peak region, the device still provides accurate and reliable results, which is essential for maintaining patient safety and ensuring high-quality radiotherapy treatment. Therefore, the results of this study demonstrate the device's suitability for routine use in clinical settings, providing confidence in its ability to deliver precise dose measurements during daily QA checks. The Sphinx Compact represents a comprehensive all-in-one solution for daily PBS machine QA, providing radiotherapy clinics with a rapid, efficient, and comprehensive tool to uphold the highest standards of quality and safety in their treatments. With its compact design, it offers streamlined setup and rapid testing, allowing for completion of all daily QA tests in under 10 minutes, according to IBA. This translates to the potential to treat an additional patient each day, optimizing patient throughput. Hence, it is a very promising device for an efficient QA of proton beams [53].

QA programs based on different kinds of detectors can be very complex and time consuming. The ESTRO-EPTN survey results presented in 2020 show that there is a discontent with complex, inefficient and time-consuming measurements protocols due to the restricted capabilities of the commercially available devices [54, 55]. Nowadays, there is still room for improvement towards an all-in-one solution providing accurate and real-time measurements with submillimeter spatial resolution, and a linear response to the beam current. Moreover, an ideal dosimeter should have a response independent of LET, be radiation hard and supply a fast analysis of the data. A complete solution that includes all the information will minimize the equipment costs, the setup time and therefore the resources required in the treatment

facility, improving the overall performance of the QA programs. This single solution project would provide patients with higher quality treatment for better patient outcomes and reduced healthcare costs, contributing to the goal of providing “access to the best treatment for all”.

Treatment with hadrons (currently protons and ^{12}C ions) is a radiotherapy technique that for several types of tumours offers considerable advantages over conventional photon and electron treatments. Since its initial application in 1954, it is gaining popularity as a cancer treatment modality, with a growing number of patients benefiting from its unique properties. By the end of 2022, more than 360,000 patients have undergone particle therapy globally [56]. However, it is worth noting that despite its potential, the utilization of this cutting-edge approach remains relatively limited when compared to the conventional use of photons and electrons in radiotherapy, which annually treats around 7 million patients [57].

The initial envisaged application for the detector centered on its deployment in the realm of hadron therapy, owing to the promising potential it holds within this domain. Nevertheless, it is noteworthy that the prevailing global trend in cancer treatment predominantly favors photon-based therapies over hadron therapy. This observation underscores the imperative for continued advancements in both of these treatment modalities.

The objective of this thesis is to contribute to the creation of tools, which will ensure an optimal dose delivery to patients undergoing cancer radiation therapy by providing 2D dosimetric information with high spatial resolution. The work I performed for this thesis, resulted in the development of two detector prototypes: one with an optical readout based on a matrix of OPDs fabricated on top of a TFT backplane and another one based on an TFT-only charge readout with an active area of $60 \times 80 \text{ mm}^2$.

Bibliography

- [1] “Cancer,” library Catalog: [www.who.int](http://www.who.int/westernpacific/health-topics/cancer). [Online]. Available: <https://www.who.int/westernpacific/health-topics/cancer>
- [2] M. Roser and H. Ritchie, “Cancer,” *Our World in Data*, 2020, <https://ourworldindata.org/cancer>.
- [3] “Cancer tomorrow,” library Catalog: gco.iarc.fr. [Online]. Available: <http://gco.iarc.fr/tomorrow/home>
- [4] “Cancer today,” (accessed on 2021-01-19). [Online]. Available: <http://gco.iarc.fr/today/home>
- [5] T. Hofmarcher, P. Lindgren, N. Wilking, and B. Jönsson, “The cost of cancer in Europe 2018,” *European Journal of Cancer*, vol. 129, pp. 41–49, Apr. 2020. [Online]. Available: <https://linkinghub.elsevier.com/retrieve/pii/S0959804920300265>
- [6] “Treatment for cancer | Cancer in general | Cancer Research UK,” (accessed on 2020-04-26). [Online]. Available: <https://www.cancerresearchuk.org/about-cancer/cancer-in-general/treatment>
- [7] C. B. Dracham, A. Shankar, and R. Madan, “Radiation induced secondary malignancies: a review article,” *Radiation Oncology Journal*, vol. 36, no. 2, pp. 85–94, Jun. 2018. [Online]. Available: <https://www.ncbi.nlm.nih.gov/pmc/articles/PMC6074073/>
- [8] M. K. Thompson, P. Poortmans, A. J. Chalmers, C. Faivre-Finn, E. Hall, R. A. Huddart, Y. Lievens, D. Sebag-Montefiore, and C. E. Coles, “Practice-changing radiation therapy trials for the treatment of cancer: where are we 150 years after

- the birth of Marie Curie?" *British Journal of Cancer*, vol. 119, no. 4, pp. 389–407, Aug. 2018, number: 4 Publisher: Nature Publishing Group. [Online]. Available: <https://www.nature.com/articles/s41416-018-0201-z>
- [9] R. Baskar, K. A. Lee, R. Yeo, and K.-W. Yeoh, "Cancer and Radiation Therapy: Current Advances and Future Directions," *International Journal of Medical Sciences*, vol. 9, no. 3, pp. 193–199, Feb. 2012. [Online]. Available: <https://www.ncbi.nlm.nih.gov/pmc/articles/PMC3298009/>
- [10] G. Delaney, S. Jacob, C. Featherstone, and M. Barton, "The role of radiotherapy in cancer treatment: Estimating optimal utilization from a review of evidence-based clinical guidelines," *Cancer*, vol. 104, no. 6, pp. 1129–1137, Sep. 2005. [Online]. Available: <http://doi.wiley.com/10.1002/cncr.21324>
- [11] J. M. Borrás, "How many new cancer patients in Europe will require radiotherapy by 2025? An ESTRO-HERO analysis," *Radiotherapy and Oncology*, p. 7, 2025.
- [12] S. I. P. Álvarez, F. J. L. Ruiz, F. M. Magos, and A. M. García, *Proton Therapy in Lower-Middle-Income Countries: From Facts and Reality to Desire, Challenges and Limitations*. IntechOpen, Aug. 2021, publication Title: Proton Therapy - Current Status and Future Directions. [Online]. Available: <https://www.intechopen.com/chapters/75221>
- [13] *Relative Biological Effectiveness in Ion Beam Therapy*, ser. Technical Reports Series. Vienna: INTERNATIONAL ATOMIC ENERGY AGENCY, 2008, no. 461. [Online]. Available: <https://www.iaea.org/publications/7682/relative-biological-effectiveness-in-ion-beam-therapy>
- [14] D. Salado, "Development of platinum based nanoparticles to enhance cancer cell killing by gamma rays and carbon ion radiation," Ph.D. dissertation, Nov. 2016.
- [15] F. H. Attix, *Introduction to Radiological Physics and Radiation Dosimetry*, 1st ed. Wiley, Nov. 1986. [Online]. Available: <https://onlinelibrary.wiley.com/doi/book/10.1002/9783527617135>
- [16] K. Kokurewicz, E. Brunetti, G. H. Welsh, S. M. Wiggins, M. Boyd, A. Sorensen, A. J. Chalmers, G. Schettino, A. Subiel, C. DesRosiers, and D. A. Jaroszynski, "Focused very high-energy electron beams as a novel radiotherapy modality for producing high-dose

- volumetric elements,” vol. 9, no. 1, p. 10837, number: 1 Publisher: Nature Publishing Group. [Online]. Available: <https://www.nature.com/articles/s41598-019-46630-w>
- [17] S. R. Cherry, J. A. Sorenson, and M. E. Phelps, *Physics in Nuclear Medicine E-Book*. Elsevier Health Sciences, Feb. 2012, google-Books-ID: UnDrbqfM2HUC.
- [18] H. P. Lars, “Medical Applications of Particle Accelerators (NPAP MOOC),” Lund University, 2019.
- [19] A. I. Zablow, T. R. Eanelli, and L. J. Sanfilippo, “Electron beam therapy for skin cancer of the head and neck,” *Head & Neck*, vol. 14, no. 3, pp. 188–195, Jun. 1992.
- [20] R. J. Kudchadker, J. A. Antolak, W. H. Morrison, P. F. Wong, and K. R. Hogstrom, “Utilization of custom electron bolus in head and neck radiotherapy,” *Journal of Applied Clinical Medical Physics*, vol. 4, no. 4, pp. 321–333, Sep. 2003. [Online]. Available: <https://www.ncbi.nlm.nih.gov/pmc/articles/PMC5724465/>
- [21] S. Dieterich, E. Ford, D. Pavord, and J. Zeng, “Chapter 23 - Intraoperative Radiotherapy (IORT),” in *Practical Radiation Oncology Physics*, S. Dieterich, E. Ford, D. Pavord, and J. Zeng, Eds. Philadelphia: Elsevier, Jan. 2016, pp. 305–312. [Online]. Available: <https://www.sciencedirect.com/science/article/pii/B9780323262095000237>
- [22] T. T. Böhlen, J.-F. Germond, E. Traneus, J. Bourhis, M.-C. Vozenin, C. Bailat, F. Bochud, and R. Moeckli, “Characteristics of very high-energy electron beams for the irradiation of deep-seated targets,” *Medical Physics*, vol. 48, no. 7, pp. 3958–3967, Jul. 2021.
- [23] U. Amaldi, “History of hadrontherapy,” *Modern Physics Letters A*, vol. 30, no. 17, p. 1540018, Jun. 2015, publisher: World Scientific Publishing Co. [Online]. Available: <https://www.worldscientific.com/doi/10.1142/S0217732315400180>
- [24] A. Chao, H. O. Moser, and Z. Zhao, *Accelerator Physics, Technology, and Applications: Selected Lectures of OCPA International Accelerator School 2002, Singapore*. World Scientific, 2004, google-Books-ID: ldBgDQAAQBAJ.
- [25] I. Atomenergie-Organisation, *Cyclotron produced radionuclides: principles and practice*, ser. Technical reports series / International Atomic Energy Agency, Vienna, 2008, no. 465.

- [26] J. H. Lawrence, "Nuclear Physics and Therapy: Preliminary Report on a New Method for the Treatment of Leukemia and Polycythemia," *Radiology*, vol. 35, no. 1, pp. 51–60, Jul. 1940, publisher: Radiological Society of North America. [Online]. Available: <https://pubs.rsna.org/doi/10.1148/35.1.51>
- [27] R. R. Wilson, "Radiological Use of Fast Protons," *Radiology*, vol. 47, no. 5, pp. 487–491, Nov. 1946, publisher: Radiological Society of North America. [Online]. Available: <https://pubs.rsna.org/doi/10.1148/47.5.487>
- [28] J. D. Slater, "Development and operation of the loma linda university medical center proton facility," vol. 6, no. 4, pp. 67–72.
- [29] "PTCOG - Patient Statistics," (accessed on 2021-01-03). [Online]. Available: <https://www.ptcog.ch/index.php/patient-statistics>
- [30] W. T. Chu, B. A. Ludewigt, and T. R. Renner, "Instrumentation for treatment of cancer using proton and light-ion beams," *Review of Scientific Instruments*, vol. 64, no. 8, pp. 2055–2122, Aug. 1993, publisher: American Institute of Physics. [Online]. Available: <https://aip.scitation.org/doi/10.1063/1.1143946>
- [31] A. K. Berthelsen, J. Dobbs, E. Kjellén, T. Landberg, T. R. Möller, P. Nilsson, L. Specht, and A. Wambersie, "What's new in target volume definition for radiologists in ICRU Report 71? How can the ICRU volume definitions be integrated in clinical practice?" *Cancer Imaging*, vol. 7, no. 1, pp. 104–116, Jun. 2007. [Online]. Available: <https://www.ncbi.nlm.nih.gov/pmc/articles/PMC1906985/>
- [32] 14:00-17:00, "ISO 8402:1994," (accessed on 2021-01-15). [Online]. Available: <https://www.iso.org/cms/render/live/en/sites/isoorg/contents/data/standard/02/01/20115.html>
- [33] E. H. Balagamwala, S. T. Chao, and J. H. Suh, "Principles of radiobiology of stereotactic radiosurgery and clinical applications in the central nervous system," *Technology in Cancer Research & Treatment*, vol. 11, no. 1, pp. 3–13, Feb. 2012.
- [34] U. F. O. Themes, "Principles of radiation oncology," Apr. 2017, (accessed on 2021-12-15). [Online]. Available: <https://oncohemakey.com/principles-of-radiation-oncology-2/>
- [35] R. Nuraini and R. Widita, "Tumor Control Probability (TCP) and Normal Tissue Complication Probability (NTCP) with Consideration of Cell Biological Effect," *Journal*

- of Physics: Conference Series*, vol. 1245, no. 1, p. 012092, Aug. 2019, publisher: IOP Publishing. [Online]. Available: <https://doi.org/10.1088/1742-6596/1245/1/012092>
- [36] “ICRU REPORT No. 78 PRESCRIBING, RECORDING, AND REPORTING PROTON-BEAM THERAPY,” *Journal of the International Commission on Radiation Units and Measurements*, vol. 7, no. 2, pp. 49–81, 12 2007. [Online]. Available: <https://doi.org/10.1093/jicru/ndm027>
- [37] R. P. Levy, “Evolving role of hadron irradiation: Potential and risks of hadrons heavier than protons,” *Nuclear Instruments and Methods in Physics Research Section B: Beam Interactions with Materials and Atoms*, vol. 261, no. 1, pp. 763–767, Aug. 2007. [Online]. Available: <https://www.sciencedirect.com/science/article/pii/S0168583X07007586>
- [38] A. Mirandola, S. Molinelli, G. Vilches Freixas, A. Mairani, E. Gallio, D. Panizza, S. Russo, M. Ciocca, M. Donetti, G. Magro, S. Giordanengo, and R. Orecchia, “Dosimetric commissioning and quality assurance of scanned ion beams at the Italian National Center for Oncological Hadrontherapy,” *Medical Physics*, vol. 42, no. 9, pp. 5287–5300, 2015, _eprint: <https://onlinelibrary.wiley.com/doi/pdf/10.1118/1.4928397>. [Online]. Available: <https://onlinelibrary.wiley.com/doi/abs/10.1118/1.4928397>
- [39] L. Grevillot, J. Osorio Moreno, V. Letellier, R. Dreindl, A. Elia, H. Fuchs, A. Carlino, G. Kragl, H. Palmans, S. Vatnitsky, and M. Stock, “Clinical implementation and commissioning of the MedAustron Particle Therapy Accelerator for non-isocentric scanned proton beam treatments,” *Medical Physics*, vol. 47, no. 2, pp. 380–392, 2020, _eprint: <https://onlinelibrary.wiley.com/doi/pdf/10.1002/mp.13928>. [Online]. Available: <https://onlinelibrary.wiley.com/doi/abs/10.1002/mp.13928>
- [40] S. Rana, J. Bennouna, E. J. J. Samuel, and A. N. Gutierrez, “Development and long-term stability of a comprehensive daily QA program for a modern pencil beam scanning (PBS) proton therapy delivery system,” *Journal of Applied Clinical Medical Physics*, vol. 20, no. 4, pp. 29–44, Apr. 2019.
- [41] *Radiation oncology physics : a handbook for teachers and students*, Eb podgorsak ed., ser. Non-serial Publications. Vienna: INTERNATIONAL ATOMIC ENERGY AGENCY, 2005. [Online]. Available: <https://www.iaea.org/publications/7086/radiation-oncology-physics>

- [42] L. Grevillot, M. Stock, H. Palmans, J. Osorio Moreno, V. Letellier, R. Dreindl, A. Elia, H. Fuchs, A. Carlino, and S. Vatnitsky, "Implementation of dosimetry equipment and phantoms at the MedAustron light ion beam therapy facility," *Medical Physics*, vol. 45, no. 1, pp. 352–369, Jan. 2018.
- [43] U. W. Langner, J. G. Eley, L. Dong, and K. Langen, "Comparison of multi-institutional Varian ProBeam pencil beam scanning proton beam commissioning data," *Journal of Applied Clinical Medical Physics*, vol. 18, no. 3, pp. 96–107, 2017, _eprint: <https://onlinelibrary.wiley.com/doi/pdf/10.1002/acm2.12078>. [Online]. Available: <https://onlinelibrary.wiley.com/doi/abs/10.1002/acm2.12078>
- [44] "OCTAVIUS Detector 1600 SRS - PTW Freiburg GmbH," (accessed on 2021-01-04). [Online]. Available: <https://www.ptwdosimetry.com/en/products/octavius-detector-1600-srs/>
- [45] J.-F. Calvo-Ortega, M. Pozo, S. Moragues, and J. Casals, "Fast protocol for radiochromic film dosimetry using a cloud computing web application," *Physica Medica*, vol. 39, pp. 1–8, Jul. 2017. [Online]. Available: <https://linkinghub.elsevier.com/retrieve/pii/S1120179717301886>
- [46] N. Wen, S. Lu, J. Kim, Y. Qin, Y. Huang, B. Zhao, C. Liu, and I. J. Chetty, "Precise film dosimetry for stereotactic radiosurgery and stereotactic body radiotherapy quality assurance using Gafchromic™ EBT3 films," *Radiation Oncology*, vol. 11, no. 1, p. 132, Oct. 2016. [Online]. Available: <https://doi.org/10.1186/s13014-016-0709-4>
- [47] D. Lewis, A. Micke, X. Yu, and M. F. Chan, "An efficient protocol for radiochromic film dosimetry combining calibration and measurement in a single scan," *Medical Physics*, vol. 39, no. 10, pp. 6339–6350, 2012, _eprint: <https://onlinelibrary.wiley.com/doi/pdf/10.1118/1.4754797>. [Online]. Available: <https://onlinelibrary.wiley.com/doi/abs/10.1118/1.4754797>
- [48] B. Spielberger, M. Scholz, M. Krämer, and G. Kraft, "Experimental investigations of the response of films to heavy-ion irradiation," *Physics in Medicine and Biology*, vol. 46, no. 11, pp. 2889–2897, Nov. 2001.
- [49] "Garchromic EBT Films - GAFchromic™," (accessed on 2021-01-04). [Online]. Available: <http://www.gafchromic.com/gafchromic-film/radiotherapy-films/EBT/index.asp>

- [50] S. Safai, S. Lin, and E. Pedroni, "Development of an inorganic scintillating mixture for proton beam verification dosimetry," *Physics in Medicine and Biology*, vol. 49, no. 19, pp. 4637–4655, Oct. 2004.
- [51] S. Russo, A. Mirandola, S. Molinelli, E. Mastella, A. Vai, G. Magro, A. Mairani, D. Boi, M. Donetti, and M. Ciocca, "Characterization of a commercial scintillation detector for 2-D dosimetry in scanned proton and carbon ion beams," *Physica medica: PM: an international journal devoted to the applications of physics to medicine and biology: official journal of the Italian Association of Biomedical Physics (AIFB)*, vol. 34, pp. 48–54, Feb. 2017.
- [52] I. D. GmbH, "High-resolution digital detector array | Unrivaled accuracy, efficiency, and reliability for independent Proton Therapy system commissioning and acceptance," Nov. 2021, (accessed on 2021-01-04). [Online]. Available: <https://www.iba-dosimetry.com/product/myqa-phoenix/>
- [53] Z. Su, W. Hsi, J. Forthomme, and S. Rossomme, "Evaluations of a flat-panel based compact daily quality assurance device for proton pencil beam scanning (PBS) system," *Physica medica: PM: an international journal devoted to the applications of physics to medicine and biology: official journal of the Italian Association of Biomedical Physics (AIFB)*, vol. 80, pp. 243–250, Dec. 2020.
- [54] M. Togno, "59th ANNUAL CONFERENCE OF THE PARTICLE THERAPY CO-OPERATIVE GROUP|myQA Phoenix - User experience on a new pixelated detector for PBS proton beams characterization," (accessed on 2021-01-17). [Online]. Available: <https://www.iba-dosimetry.com/product/myqa-phoenix/>
- [55] "Proceedings to the 2020 Online Conference of the Particle Therapy Cooperative Group (PTCOG2020Online)," *International Journal of Particle Therapy*, vol. 7, no. 4, pp. 74–199, Mar. 2021. [Online]. Available: <https://www.ncbi.nlm.nih.gov/pmc/articles/PMC8019577/>
- [56] "PTCOG - Facilities under Construction." [Online]. Available: <https://www.ptcog.ch/index.php/facilities-under-construction>
- [57] H. Majeed and V. Gupta, "Adverse Effects of Radiation Therapy," in *StatPearls*.

Treasure Island (FL): StatPearls Publishing, 2023. [Online]. Available: <http://www.ncbi.nlm.nih.gov/books/NBK563259/>

Chapter 2

The LaGEMPix Detector Concept

“There is no applied science if there is no science to apply.”

Bernardo Houssay

This chapter is dedicated to the description of the *LaGEMPix* project. I initially briefly describe the foundation and several options explored during this project. It then introduces the triple-GEM detector technology, which serves as the foundation of the LaGEMPix. Next, the composition and development of the optical readout of the detector are presented. Finally, the chapter reports on the development of the first LaGEMPix prototype with a TFT-based charge readout, which represents a significant milestone in the project’s progress. The chapter also covers the results of irradiation measurements conducted at the medical cyclotron located at the Bern University Hospital (Inselspital). These measurements were aimed at evaluating various transparent anode substrates for an optical readout detector using low-energy protons. The insights from these measurements were crucial to ensure the optimal functionality of the initial detector prototype and the subsequent construction of the LaGEMPix prototype with GEM-OPD array readout. Overall, this chapter offers a comprehensive overview of the *LaGEMPix* project, highlighting its innovative design and potential impact on the field of particle detection. A user manual of the LaGEMPix can be found in [1].

2.1 GEMPix – the Point of Departure

The GEMPix detector, a promising tool for quality assurance in hadron therapy, is the starting point of the LaGEMPix project. This apparatus was developed by the Special Projects section of the Radiation Protection group at CERN. The GEMPix is an original detector that combines a triple-GEM, a type of gaseous ionization detector, and a quad Timepix Application-Specific Integrated Circuit (ASIC) used as a highly pixelated readout [2]. A more detailed explanation of the triple-GEM can be found in Section 2.3. The Timepix [3] is a pixelated silicon detector developed by the Medipix Collaboration, a family of photon-counting pixel detectors [4]. In this application, a 2 x 2 array of chips without a silicon sensor is used as a readout for a triple-GEM. This readout is based on a read-out chip consisting of a 256 x 256 pixels CMOS ASIC to which different pixelated semiconductor sensors are normally bump-bonded. Each pixel measures 55 x 55 μm^2 . Hence, in total, we have an active area of 28 x 28 mm^2 with more than two hundred and sixty thousand (262,144) pixels .

In combination, the resultant technology is a hybrid device able to measure and visualize the energy deposits in the gas of several types of radiation with a high spatial resolution. It may be used also for X-ray monitoring in burning plasma physics or clear radioactive waste, for example. Due to the wide gain range of the chamber, this device can also be used to measure particle beams (i.e. protons and carbon ions) in hadron therapy with good spatial resolution. It has been demonstrated that the GEMPix is capable of providing 2D images of the beam, the Bragg curve and the 3D energy deposition of a carbon ion beam in a water phantom [2, 5]. These results demonstrate the capability of the GEMPix in terms of proof-of-principle.

However, there are mismatches between the Bragg curve measured with the GEMPix and the results of the PTW Peakfinder, the standard detector. The Peakfinder, part of PTW's beam scanning systems, is designed for precise Bragg peak depth measurement. The device includes two parallel-plate ionization chambers (PTW Bragg Peak Ionization Chambers) and facilitates synchronization with accelerator spills for measurements of Bragg curves. A large sensitive area was simulated and shows that the size of the area has a significant effect, especially in the tail of the Bragg curve. This happens due to the fact that the beam is spread out with increasing depth in water. Hence, we cannot collect all the energy deposition even for a single pencil beam especially in the tail because the beam diverges. Moreover, we also need

to develop a detector with a large area detector for QA in order to cover the typical radiation field size, since an evaluation of the dose in one measurement of the entire area is desired.

2.2 Large Area GEMPix

Although promising, a larger sensitive area GEMPix is required to cover the typical radiation field size and to avoid losses due to beam spread out. We aim at developing an imaging detector with a wider area (of the order of $20 \times 20 \text{ cm}^2$) compared to the current GEMPix detector ($2.8 \times 2.8 \text{ cm}^2$). Large area GEMs already exist and are produced at CERN. Hence, my research was focused on checking new readout possibilities. I verified and tested several valid readout options, which could be used to increase the area of the LaGEMPix detector, as shown in Figure 2.1.

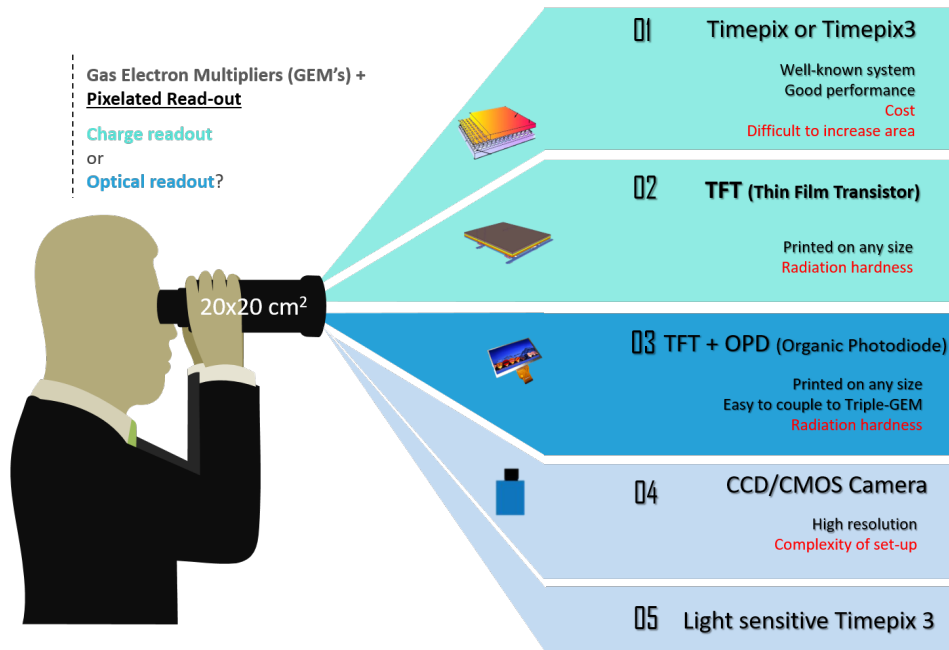


Figure 2.1: Readout options for the LaGEMPix.

We propose a novel detector for quality assurance in hadron therapy, for which an accurate dose calculation and verification with high spatial resolution is required. An original detector named LaGEMPix that consists of a triple-GEM coupled to a highly pixelated readout was proposed. I explored several routes of investigation concerning the readout in order to

reach the desired target submillimetre spatial resolution for QA in hadron therapy.

Two distinct types of readout can be distinguished as depicted in Figure 2.1. An electronic readout based on the Timepix or the TFT panel, relies on collecting charges or detecting induced charges from moving electrons, while an optical readout based OPD or on cameras relies on recording photons emitted during the electron avalanche multiplication processes.

While the GEMPix currently uses an electronic readout, we also used an optical readout with the OPDs, which can be achieved when specific gas mixtures are used. Other GEM based detectors with optical readout have been used in the past in particle therapy. In particular, the feasibility of optical readout GEM-based detectors filled with $Ar : CF_4$ was previously investigated with CCD CMOS cameras [6, 7, 8].

2.2.1 Optical Readout Using Cameras

The feasibility of using a camera as a readout option was validated at CERN with a simple test set-up. The triple-GEM filled with $Ar : CF_4$ gas was coupled with a CMOS camera Basler acA1920 - 40gm [9]. A Fe-55 source with characteristic 5.9 keV X-rays was placed in front of the Mylar window of the triple-GEM. First, images were acquired with the external light (room light) using the Fe-55 source. Then, all external lights were turned off, the detector and the camera were covered with black tissue and new images using the Fe-55 source were recorded as shown in Figure 2.2. A ROI indicated by a blue rectangle was defined around the GEMs.

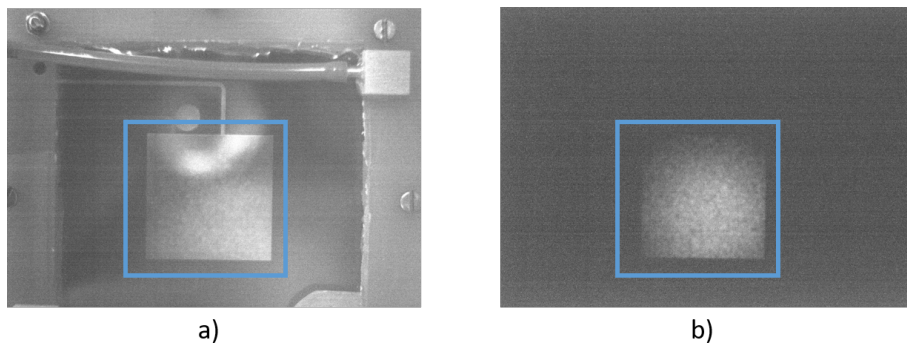


Figure 2.2: a) Image with external light. b) Image without external light.

The optical photons produced in triple-GEM are visible in images taken with a CMOS camera after all external light sources have been eliminated. Based on the results obtained, this option could be used to collect the optical signal from the triple-GEMs and, consequently, to increase the area of the detector. However, the degradation of the camera due to radiation damage requires placing it outside the beam path, requiring a more complex system with e.g. mirrors or lenses.

2.2.2 Optical Readout Using Light Sensitive Timepix3

The possibility of coupling other sensors other than cameras to the GEMs has been studied. For example, the light signal due to the scintillation in the Thick Gas Electron Multiplier (THGEM) holes was detected by TPX3Cam, which is a light sensitive silicon sensor bump bonded onto a Timepix3 chip [10]. I also prepared a simple set-up to test the light sensitive Timepix3. Resorting to the use of lasers, it was possible to verify that this chip is sensitive to UV and red light. However, the merging with the triple-GEM will also require a more complex device with a special shielded box and collimators.

Due to the need for a complex set-up, none of these last two options with optical readout was pursued. In contrast to CCD/CMOS-based detectors or the TPX3Cam, the highly pixelated matrix coated on an oxide TFT backplane readout can be adjacent to the GEM anode. This allows for a more compact, further scalable and low material budget set-up.

2.2.3 Optical Readout Using Thin Film Transistor and Organic Photodiode

Firstly, a small triple GEM detector with an active volume of $3 \times 3 \times 1.2 \text{ cm}^3$ was coupled to a single OPD with an active area of 4.91 m^2 for readout. The OPD was manufactured by ISORG (company in Grenoble, France) ¹. The single OPD (without any specially designed electronics such as a preamplifier) is mounted on a PCB and this prototype is called OptiGEM. The OPD is directly readout using a Sourcemeter Keithley Model 2450 [11]. The technical note "Maia Oliveira, A. (2019). OptiGEM." [12] provides a detailed description of the initial

¹ISORG, Grenoble FRANCE, <http://www.isorg.fr/>, Tel: +33 (0)4 38 88 18 36

steps performed to test the feasibility of the OptiGEM. The OptiGEM was able to detect the optical signal by measuring the current driven by the OPD with a sourcemeter of type Keithley Model 2450 [11], when illuminating the OPD with a mobile phone flashlight or ambient light. We measured a negative current in the OPD when exposing it directly to light. In a later test, we coupled the OPD directly to a triple-GEM setup to detect the scintillation photons produced in the last GEM. However, we observed an increase in the electric current towards positive values when placing radioactive sources in front of the Mylar entrance window of the triple-GEM setup. We did not expect the current to be positive, thus this fact led us to the hypothesis that electrons rather than photons were inducing a current in the photodiode. Indeed, when the induction field – responsible for drifting electrons from the last GEM to the readout - was set to zero, the signal disappeared. Therefore, we concluded that this current was due to the drifting electrons. In order to evaluate the feasibility of an optical readout, it is essential to place a transparent anode after the last GEM. The anode collects the drifting electrons while allowing the scintillation photons to pass through.

The subsequent technical note "Maia Oliveira, A. (2020). OptiGEM – ITO Glass" [13] presents studies performed to test the feasibility of the OptiGEM with an ITO glass. This was achieved by mounting the ITO glass with an 8 mm gap below the GEM structure, allowing the collection of electrons while enabling the passage of optical photons. These experiments took place at the CERN Calibration Laboratory [14]. The expected decrease of the electric current towards zero with the GEMs gain in the OPD was observed when using a 3 TBq Cs-137 source in front of the OptiGEM. In addition, when the induction electric field was set to zero, we continued to measure the signal in the OPD induced by the radioactive source. Therefore, we concluded that we detected the secondary scintillation photons emitted by the Ar:CF₄ gas molecules during the electron multiplication in the GEM holes using a single OPD.

The different electric fields of triple GEM detector with an active area of 100 x 100 mm² were optimized to achieve a high current in the anode. The results of the electric fields optimization based on the anode current measurements are presented in the Technical Note "Maia Oliveira, A. (2020). LaGEMPix: optimization of electric fields for operation with Ar:CF₄ gas mixture. [15]. Results show that the current measured on the anode increases linearly with the current in the last GEM. The Triple-GEM functioned as anticipated, marking a successful phase for the subsequent testing of coupling this detector with TNO's optical readout. The optimization study detailed in this report holds substantial significance, especially if

the readout's detection limit operates within the range spanning from the initial non-optimized configuration to the final optimized approach.

We developed an original detector that consists of a triple-GEM coupled to a highly pixelated readout based on a matrix of Organic Photodiode (OPD) coated on an oxide TFT backplane. We combined the two technologies to achieve a wider area ($60 \times 80 \text{ mm}^2$) imaging detector and to fully exploit its optical readout capabilities. Please refer to Section 2.5 for the explanation of the technical details of the readout. On the left side of the baseplate, the triple-OPD stack is connected to the optical readout array and secured by two blue 3D printed holders, as illustrated in Figure 2.3. This setup enables straightforward merging both components.

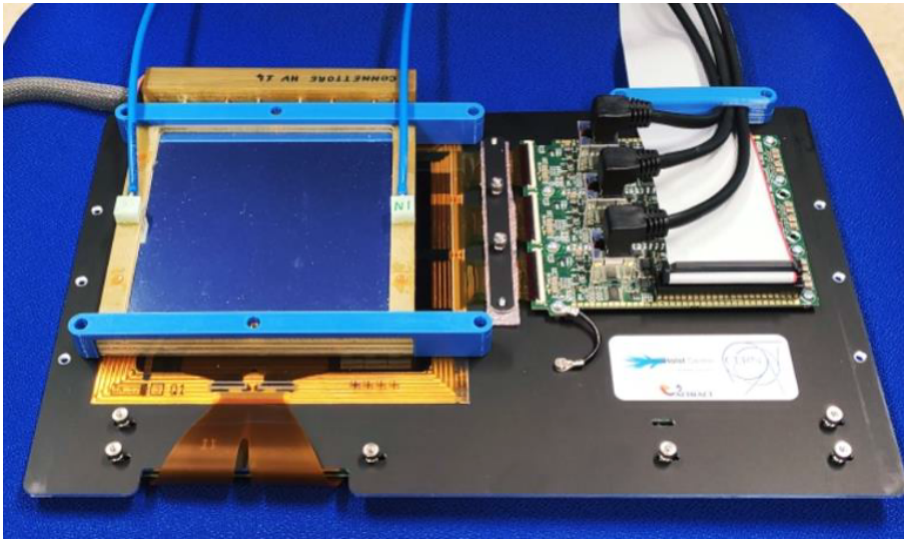


Figure 2.3: The LaGEMPix detector. The triple-GEM $10 \times 10 \text{ cm}^2$ stack coupled to the optical readout matrix is on the left side; on top, there is the thin Mylar window. The readout board and the cables to connect the detector to the FPGA module are on the right side.

After conducting the characterization of the first LaGEMPix prototype, it was concluded that the spatial resolution achieved was only a few millimeters due to the isotropic emission of photons (see Chapter 3). This resolution was deemed insufficient for QA in hadron therapy. As a first step towards improving the spatial resolution, we reduced the gap between the last GEM and the readout to minimize the impact of this effect. Although the results with the reduced gap demonstrated significant improvement, it was found that achieving sub-

millimeter spatial resolution in a compact system with optical readout is challenging without the introduction of collimators or lenses in the set-up. Therefore, further improvements in spatial resolution will require additional modifications to the system design.

2.2.4 Charge Readout Using Thin Film Transistor

In the second stage of this project, an original detector that utilizes a charge readout based on a matrix of thin-film transistors was designed. To build this new version of the LaGEMPix detector, the OPD frontplane present in the first version of the LaGEMPix was eliminated, leaving a TFT-only electronic readout. Please refer to Section 2.5 for the explanation of the technical details of the readout. With this charge readout approach, secondary electrons produced in the electron avalanche are directly collected by the readout, yielding an even more compact and efficient device with a higher signal-to-noise ratio. Additionally, the results demonstrate that the required sub-millimeter spatial resolution is achievable using low energy X-rays and protons.

2.2.5 Charge Readout Using Timepix

Regarding the charge readout options, the other option consisted to tile 15 x 15 Timepix chips. First, as wire bonds are only on one side of the current Timepix chip, the quad configuration (2 x 2 chips) utilized in the GEMPix cannot be expanded to a theoretical $n \times n$ chip layout ($n > 2$). To achieve a large sensitive area we could recur to the new Timepix4 version, which is nearly four times larger than the Timepix. The big advantage of the Timepix4 is the vertical interconnect access, which is only possible due to the connection for data transfer from underneath the chip by Through-silicon Via [16]. Although, merely the cost of the Timepix4 ASICs would make such a solution too costly. Furthermore, the 55-pixel size would depend on expensive and complex electronics to manage the vast number of signals, and each acquisition would produce a massive amount of data.

2.3 Triple-Gas Electron Multiplier

Both LaGEMPix prototypes combine the triple-Gas Electron Multiplier, a type of gaseous ionization detector and a high pixelated read-out.

2.3.1 Gaseous Detectors

There are a plentitude of radiation detectors and their applications are equally vast, from the fields of geology and space to medicine. A large majority of these detectors were first invented for particle physics experiments and then used or adapted to a specific field of application. Gaseous, scintillation, and solid state detectors are different types of instruments that have been used by the radiation detection community to, for example, measure the energy, the momentum, the position, the number of particles or even to identify a particle. Gaseous detectors offer radiation detection with a low material budget by adopting gases or gas mixtures as the active detection volume. Furthermore, another advantage of this type of detector is the possibility to be scaled up to cover large areas [17].

The premise of a gaseous detector is the detection of ionisation due to radiation interaction with the gas. Primary electron-ion pairs are created by the ionizing radiation passing through the sensitive volume of the detector.

It is possible to distinguish between two types of ionisation, primary and secondary. When incoming radiation interacts directly with the active gas volume, primary electrons are produced. Then, some of these primary electrons with sufficient energy to ionize the gas, such as δ -rays, can induce a second ionization process, which has an impact on the overall amount of ionization electrons as well as on the spatial resolution.

Another option to increase the number of released electrons is the Penning ionization, where an electrically excited gas atom (frequently the noble gas) interacts with other molecule or atom (quencher gas) with a lower ionization potential than the noble gas's metastable excited state. The molecule is ionized as a result of the collision, generating a cation, an electron, and a neutral gas molecule in the ground state. A Penning mixture, which is a combination of an inert gas and a smaller amount with another gas (commonly a molecular gas), has to be

selected as the filling gas.

Then, an external electric field is applied between two electrodes to collect the positive and negative charges. The electrons drift and diffuse through the gas in the direction of the readout and the positive charges, the gas ions, go in the opposing way through the cathode. These electrons can be captured by positive ions and a recombination between these two species might occur during their transport. To avoid these occurrences, a drift field must be applied and an electron cloud is generated due to the production of additional electrons and ions, called the secondary ionization.

Usually the number of primary electrons is not enough to produce a considerably strong signal for detection. As a result, initial electrons must be multiplied. John Sealy Townsend discovered this avalanche multiplication mechanism and defined the formula to calculate the rise dN in the number of electrons caused by successive ionisations across a drift distance dx :

$$dN = \alpha N_0 dx \quad (2.1)$$

The equation 2.1 may be integrated to get the total number of electrons after multiplication N , presuming that the Townsend coefficient, α , is constant throughout the path. The Gain, G , is defined by the ratio N/N_0 :

$$G = N/N_0 = \exp(\alpha x) \quad (2.2)$$

2.3.2 Gas Electron Multiplier

GEM detectors are a relatively modern detector technology developed at CERN by F. Sauli in the mid-90s [18]. The elementary component is a GEM foil, which consists of a 50 μm thick insulating Kapton layer electroplated with a conductive metal on both sides. Small holes are then etched in this foil and a voltage difference is applied across them. These holes have diameters of about 70 μm at the surface, 50 μm at the center and pitch (hole to hole distance) of 140 μm . This configuration produces electric fields as high as 100 kV cm^{-1} inside the

holes. When an electron traverses the hole, avalanche multiplication takes place producing secondary electrons. For each primary electron, the number of secondary electrons or gain is determined by the gas density, gas mixture and applied electric field. Other experiments have demonstrated that a multi-GEM structure can yield significantly higher gains than a single GEM [19, 20]. It is possible to achieve a given gain at considerably lower operating voltages. Therefore, the spark probability of this configuration decreases, permitting a safer operation. For example, the triple-GEM structure used in the GEMPix has gains in the range of $10^3 - 10^5$ [21] as shown in Figure 2.4.

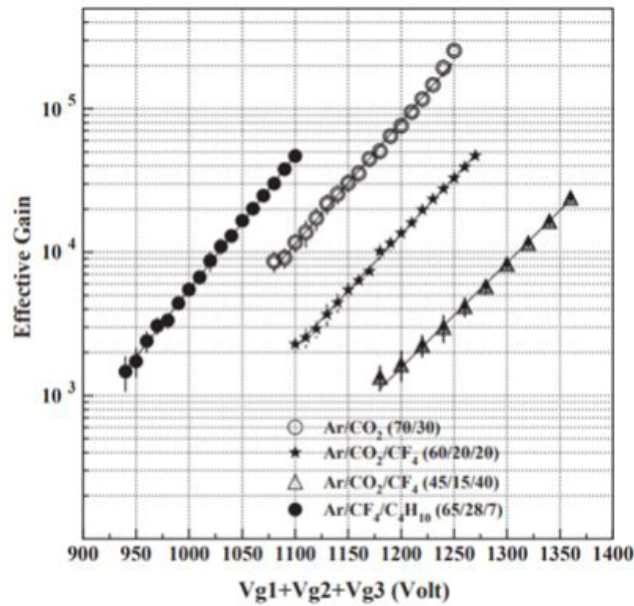


Figure 2.4: Gas gain for the different gas mixtures [21].

The triple-GEM built for the two versions of the LaGEMPix consists of a 15 μm thick Mylar window used as the cathode, located at a distance of 3.5 mm from the first GEM. The drift gap is large enough to minimise inefficiencies in charged particle detection [19] but not large enough to affect the time performance. The distance between the GEM1 and GEM2 is 1 mm, while the GEM2 and GEM3 are separated by 2 mm. This asymmetrical configuration does not compromise the temporal performance of the detector thanks to a first transfer gap of 1 mm, while reduces the probability of discharge by increasing the second transfer gap by 1 mm [19]. The last gas region between GEM3 and the anode, known as the induction gap, varies from 1 mm to 3 mm depending on the prototype. A schematic diagram of the assembly

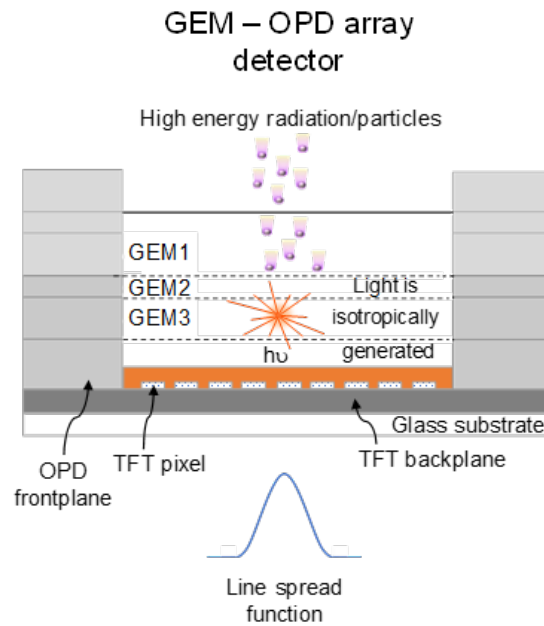
is shown in Figure 2.5 for the GEM-OPD and GEM-TFT configurations.

The drift field is applied between the cathode and the first GEM foil, hence the primary ionization electrons produced in the drift gap are attracted by GEM1. It is essential to apply an appropriate electric field in the drift region to avoid recombination of primary electrons with positive ions. After electron amplification in the GEM1, electrons need to be transferred from one GEM to the next one. Therefore, it is important to select the value of the transfer fields such that it allows efficient extraction of electrons from the holes as well as an efficient collection of charge carriers by the next GEM. After the electrons move across the last GEM foil, they drift towards the anode in the so-called induction gap due to the induction field. A detailed explanation of light production in GEMS can be found in the next Section 2.3.4.

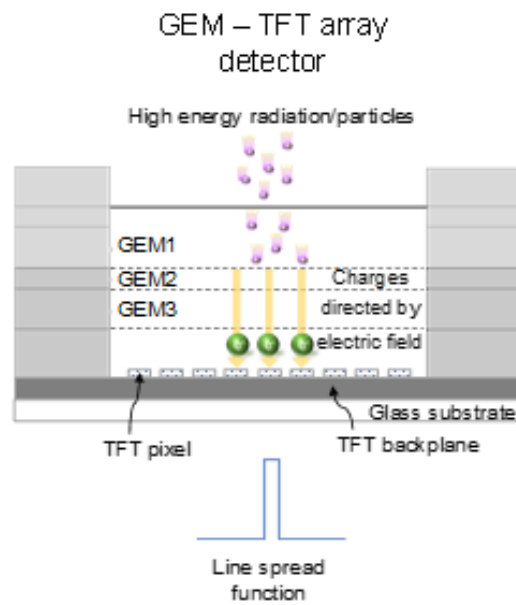
Depending on the type of readout (charge or optical) that is placed below, the triple-GEM chamber undergoes a significant modification. To assess the feasibility of an optical readout, it is crucial to position a transparent anode after the final GEM, as depicted in Figure 2.5a. On the bottom of the third GEM, the Indium Tin Oxide (ITO) coated glass anode with a thickness of 1.1 mm was placed in order to collect the electrons produced in the amplification process [22, 23]. Scintillation photons of certain wavelengths pass through the ITO glass and are detected by the image sensor. On the other side, for the charge readout option, I had to remove the ITO transparent anode in the triple-GEM design, since the electrons produced in the electron avalanche are read out directly by the TFT matrix placed below the triple-GEM. As in this case, the ITO glass is not present to guarantee that the triple-GEM chamber is gas-tight, it was necessary to add a 300 μm thin rubber when coupling the chamber to the readout.

2.3.3 Proton Irradiations at the Bern Cyclotron of the Large Area Triple-Gas Electron Multipliers

We conducted the first test with protons with the LaGEMPix detector at the 18-MeV cyclotron facility in Bern. We aimed at testing the behavior of a recently built triple GEM detector $10 \times 10 \text{ cm}^2$ with the TFT readout on a low-energy proton beam. This was the first time we tested the functionality of the LaGEMPix in a high-flux proton beam.



(a) Schematic of the GEM–OPD array detector, consisting of a TFT backplane array and OPD and triple-GEM frontplane.



(b) Schematic of the GEM–TFT array detector, consisting of a TFT backplane array and a triple-GEM frontplane.

Figure 2.5: Two configurations of GEM-based radiation detectors.

Our goal was to perform these measurements in the clinical range. Hence, we aimed to achieve values of beam intensities around 1 nA, which is not common in an isotope production cyclotron like the IBA Cyclone 18 MeV in operation at the Bern University Hospital (Inselspital). A Faraday cup connected to a high-precision electrometer, positioned after the UniBEaM detector at the BTL end, was used to measure beam profiles at various currents up to a few nA. Auger et al. [24] provides additional setup details, demonstrating the UniBEaM detector's high accuracy in beam current measurement in the pA range. After obtaining UniBEaM counts as a function of beam current in the interested low range of beam currents, the Faraday cup was removed from the end of the BTL, and the triple-GEM detector was installed.

We did a gain scan and we observed the same behavior measured with the GEMPix, exponential behavior. We performed the beam intensity scan and measured a linear behavior between 2 pA and 1.5 nA with the sum of the GEM voltages equal to 500 V as shown in Figure 2.6.

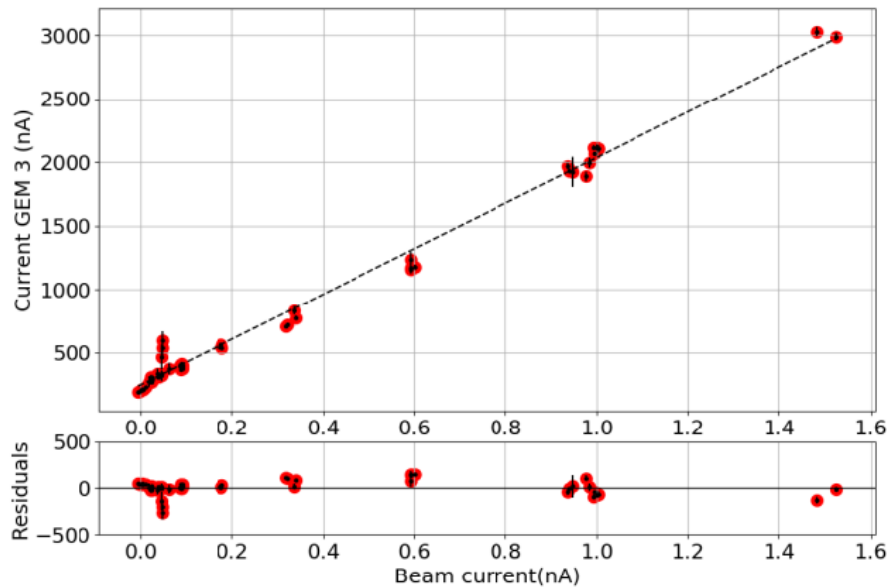


Figure 2.6: Current at the last GEM vs the proton beam current of the 18 MeV cyclotron. The black dashed line represents a linear fit to the data. The bottom plot shows the residuals.

Following the successful validation of the GEMs with a proton beam, the next critical step was to identify the ITO glass that best aligned with our requirements for constructing a

detector prototype with optical readout.

2.3.4 Light Production in Gas Electron Multipliers

While the GEMPix currently uses an electronic readout and relies on detecting the charge induced by moving electrons inside the detector, we explored the use of an optical readout with the OPDs, which relies on detecting photons emitted during the electron avalanche multiplication processes. This can only be achieved when specific gas mixtures are used and therefore we filled the triple-GEM with $Ar : CF_4$ gas mixture.

When an electron collides with gas particles like for example Ar, the latter absorbs its energy and re-emits it in the form of light during de-excitation. This secondary scintillation is the dominant process of light production in gaseous detectors like GEMs [25].

Scintillators are widely used in radiation detection applications [26, 27]. Certain materials emit a flash of light that is created by the path of radiation in material, i.e. scintillation. The molecules or atoms of these materials absorb the energy of the radiation and as a result get excited or ionized. Therefore, both processes can contribute to the transition to a higher energy state [28, pp. 115]. Then, when they return to their fundamental state, they re-emit the absorbed energy in the form of photons [28, pp. 157]. Luminescence is an inherent property of scintillators. There are two types of luminescence that a scintillator can exhibit: phosphorescence and fluorescence. Fluorescence consists in instantaneous reemission of the photons, after the absorption of energy of an incoming particle [29, pp. 158]. Occasionally, the excited state is metastable and the relaxation time from the excited state to a lower state can last between a few microseconds to hours and consequently, the reemission is delayed. In this case, this process is defined as phosphorescence [30].

Certain types of gases, such as noble gases like argon, helium or xenon exhibit scintillation. Their atoms are excited by ionizing radiation and then, decay to their ground state after a very short time with the emission of light mainly in the Ultra-Violet (UV) [29, pp. 166]. The addition of small quantities of a molecular gas such as CF_4 can not only have an impact on the diffusion and drift velocity of the electrons in the gas, but can also provide a wide light emission spectrum with an intense emission band in Visible (VIS) range. Scintillation light emission in the VIS range eases the detection of photons since it is compatible with most

available image sensors and photodetectors [30]. The detector LaGEMPix uses $Ar : CF_4$ as a gas mixture with 10% of CF_4 .

In gaseous detectors based on electron avalanche multiplication such as the GEMs, it is possible to differentiate primary and secondary scintillation. Primary scintillation is the emission of light as a result of the de-excitation of the gas atoms and molecules caused by an incident primary particle. The primary photons are emitted in the drift region, between the Mylar Window and the first GEM foil. Secondary scintillation, on the other hand, is produced by the secondary electrons generated during the multiplication process in high electric field regions [31]. If a gain is applied to the GEMs, the number of secondary electrons generated is higher than the number of primary electrons. Thus, the secondary scintillation can be brighter than the primary scintillation light. Even for the lowest gains, the impact of the primary scintillation is almost negligible, because the optical transmission of the GEM foil (thickness of 50 μm of copper and Kapton) is lower than 0.12 [32]. Hence, secondary scintillation is the basis of radiation detection with the GEMs through optical readout [32, 33]. Due to the strong electric field, the collected electrons inside the GEM holes experience a very localized multiplication. Hence, the holes are the place where the gas atoms and molecules are excited emitting photons along a short track [25]. The gain inside the holes can be adjusted in order to have a higher electron multiplication factor and consequently, a high number of emitted photons. In a triple-GEM detector, the greatest number of secondary electrons is produced in the holes of the last GEM, GEM3. Therefore, it is expected to also be the place of highest photon emission. Furthermore, the other GEM foils are opaque and absorb the majority of the light emitted from the first and the second GEMs [6]. Concerning the directionality of emission of the light, there is no precise study in the literature. Nevertheless, there is a consensus in the community that photons are emitted isotropically [29].

The light yield is one of the most important characteristics of scintillation detectors like the LaGEMPix [34]. In GEM detectors, the light yield is defined as the ratio of the number of emitted scintillation photons and the number of secondary electrons generated during electron avalanche multiplication [35]. Figure 2.7 shows the scintillation light yield as a function of the effective gain in a single GEM detector for different gas mixtures.

As can be seen in Figure 2.7, the light yield differs for each gas mixture and mixing ratios. For example, the total number of photons emitted per secondary electron for $Ar : CF_4$

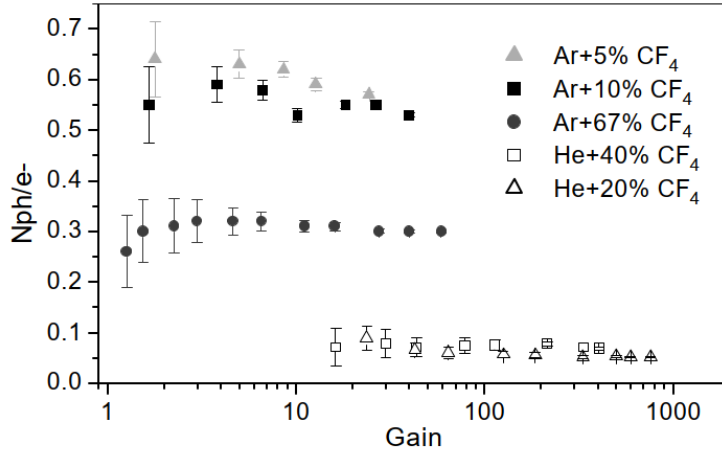


Figure 2.7: Number of photons produced in the gas above 400 nm per secondary electron for different CF_4 gas mixtures, as a function of the gain [35].

(90:10) is larger than 0.5, while for $Ar : CF_4$ (33:67) it is lower than 0.35. CF_4 fractions of 5% or 10% present the highest yields. The light yield has a variation of less than 20% for recorded gain values from 10 up to 100.

Scintillation Light in $Ar : CF_4$

The $Ar : CF_4$ (90:10) gas mixture was selected because it has the highest light yield among other typically used gas mixtures as described by other authors ($He : CF_4$, $Ne : CF_4$, $Ar : CO_2$, Ar-TEA (trimethylamine), Xe-TEA). The reported light yield varies between 0.1 to 0.5 photons per secondary electron [7, 35, 36]. The influence of the mixing ratio is shown in Figure 2.8.

The addition of CF_4 acting as a quencher allows for stable detector operation as well as other attractive properties like high electron drift velocities, low electron diffusion and fast scintillation (of the order of few ns) [31]. Additionally, $Ar : CF_4$ has a strong VIS emission band around 630 nm as shown in its secondary scintillation spectra in Figure 2.8, which is well-suited for standard optical readouts.

Scintillation photons in $Ar : CF_4$ gas mixtures are produced by processes that are a subsequence of ionization or excitation of the gas atoms and molecules. Figure 2.9 shows

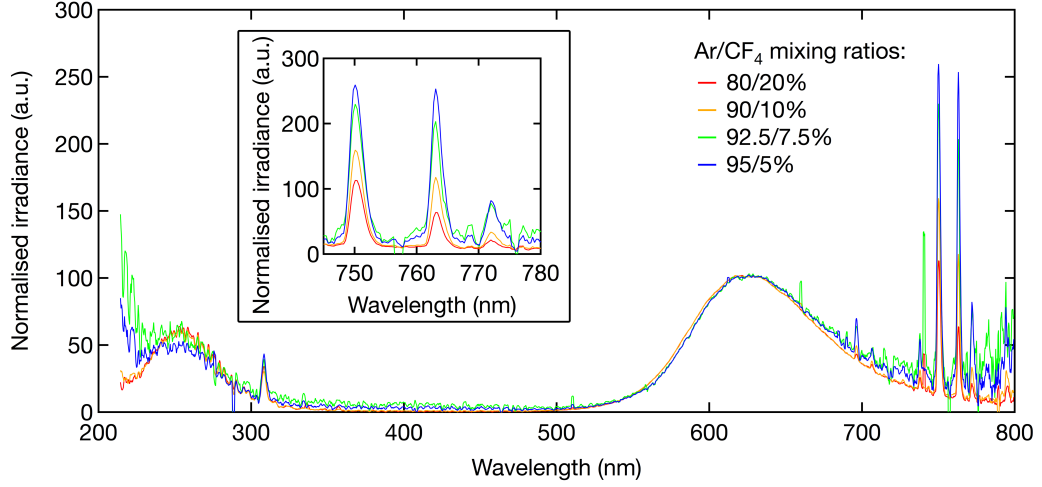


Figure 2.8: Secondary scintillation spectra of different $Ar : CF_4$ gas mixture. The broad emission bands in the UV (250 nm) and VIS (630 nm) wavelength ranges are characteristics of CF_4 scintillation. Sharp emission lines above 695 nm are due to the presence of Ar. Intensity normalized to amplitude of peak at 630 nm [7].

the different mechanisms of light production in $Ar : CF_4$. The black solid vertical arrows in Figure 2.9 denote both ionization processes, while the grey solid arrows indicate the excitation processes. The different emission bands in the scintillation light spectrum (Figure 2.8) are the results of the different scintillation emission processes. If the secondary electrons transfer enough energy to a neutral atom or molecule, Ar and $Ar : CF_4$ may be ionized to Ar^+ (15.7 eV) and $Ar : CF_4^+$ (15.9 eV) ions, correspondingly. Contrarily, it can occur that the energy is not enough to overcome the ionization energy threshold. In these conditions, excitation is another process that can take place [29, 30, 37]. Light can also be produced by direct excitation of Ar atoms and $Ar : CF_4$ molecules. A direct de-excitation transition accompanied by photon emission or additional reactions, like the formation of excited molecules and their consequent de-excitation by photon emission, can occur subsequently to excitation as seen in Figure 2.9.

UV band The UV scintillation band centered at 250 nm results from the fast dissociation of ionized CF_4 to CF^{3+} ions and atomic F [38]. This dissociation is represented by a double grey line in Figure 2.9. On the other hand, some studies support that CF_4^{+*} state (22.1 eV) could also contribute to the UV band [39, 40, 41]. Since the excitation due to the electron impact is

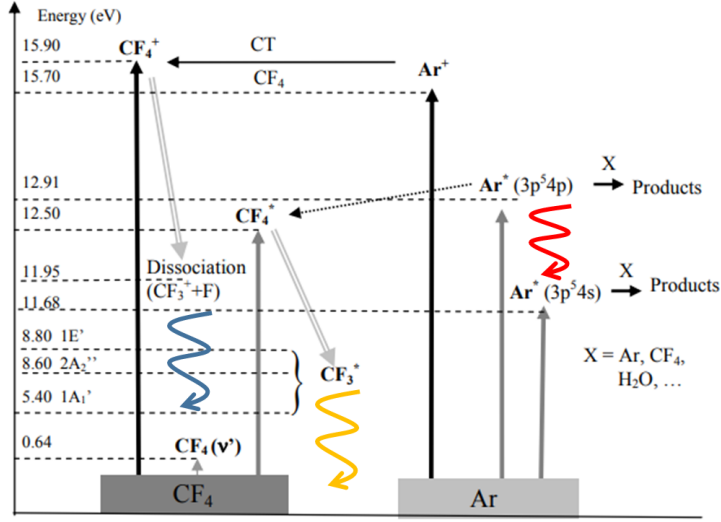
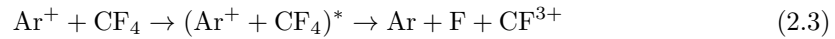


Figure 2.9: Scheme of the scintillation mechanisms leading to light emission in $Ar : CF_4$ in the wavelength range 400-820 nm. Emission of photons in the UV band (blue), in the VIS band (yellow) and in the Near-Infrared (NIR) range (red) is represented by undulating arrows. Image adapted from [6].

not state-selective, ionized or even already excited states can also be excited [42]. Ionized Ar atoms may also increase the number of CF_4^+ ions: a Charge Transfer Process (CT) between the Ar^+ and the CF_4 molecules leads to the production of CF_3^+ and the subsequent photon emission [43]. This process is identified by the thin solid black horizontal arrow pointing to the left in Figure 2.9. Since the ionization potential of CF_4 (15.9 eV) is higher than that of Ar (15.7 eV), a direct CT process between neutral CF_4 to Ar^+ is not allowed. However, there is another reaction that leads to the production of CF_3^+ with higher probability. This reaction, an electron ion recombination process, is described in Equation 2.3 [35].



The emission peak at 309 nm in Figure 2.8, results from OH^- emission due to the dissociative excitation of water vapor impurities present in the gas mixture [44].

In addition, Ar has also multiple emission lines in the UV wavelength range below 200 nm [45]. Nevertheless, this UV wavelength range is not of interest for this project, as

described in the following section.

VIS band As mentioned before, if ionization electrons do not have enough energy to ionize the gas atoms and molecules, they can excite the Ar atoms and CF_4 molecules instead. The solid grey lines in Figure 2.9 indicate excitation processes. The dissociation of excited CF_4 to CF_3^* and its subsequent de-excitation contributes to the broad band in the VIS region centered at 630 nm. Authors in [44] reported that the intensity of the VIS wavelength band is almost the same for different fractions of CF_4 in an Ar : CF_4 gas mixture (5%, 20% or even 67%). Therefore, the direct excitation of CF_4 molecules is not the only channel leading to light emission through CF_3^* de-excitation, but charge transfer mechanisms between excited Ar^* atoms and CF_4 molecules may also contribute [35, 43, 44]. This CT process is represented by the thin dashed black arrow pointing to the left in Figure 2.9.

NIR range As shown in Figure 2.8, the relative intensity of most of the NIR emission lines increases with higher fractions of Ar in an Ar : CF_4 gas mixture. Due to the monatomic nature of Ar, the energy gap between excited states is well-defined and leads to sharp emission lines at 695 nm, 705 nm, 726 nm, 737 nm, 749 nm, 762 nm, 771 nm and 794 nm. These so-called Ar I atomic lines correspond to transitions between the argon excited states of the ($3p^5 4p$) and the ($3p^5 4s$) electronic configurations [35]. To summarize, the processes with the highest probability of occurrence in the typical GEM electric fields are the ionization and excitation of Ar atoms and the excitation of CF_4 [6]. By applying a higher electric field to the GEM hole, the probabilities of both processes rise [6, 35].

ITO-coated Glass

In order to evaluate the feasibility of an optical readout, it is essential to place a transparent electromagnetic shielding below the last GEM as shown in Figure 3.14. The glass anode has to collect the drifting electrons while allowing the scintillating photons to pass through so they can be detected. The anode was glued onto a glass fibre FR-4 frame. To ground the anode, we made a direct contact between its conductive surface and the ground of the GEM detector using a wire. Indium Tin Oxide (ITO) can be used to produce optically transparent anodes due to the combination of electrical conductivity and high VIS light transmission. This type

of material has been used by other groups in optically readout GEM-based detectors [46]. ITO layers can be deposited by evaporation or sputtering. The thickness of the deposited layer determines the sheet resistivity [22, 47]. The first detector prototype was based on an ITOGLASS 100P consisting of a polished soda-lime glass with a thickness of 1.1 mm. The irradiation measurements performed at the IBA Cyclone 18 MeV cyclotron at the Bern University Hospital (Inselspital) to select a transparent anode substrate that best meets the requirements of an optical readout for the LaGEMPix are described in [48] and shortly summarized in the following Section 2.4.

The glass was coated with a first layer of Silicon Oxide (SiO_2) of 25 nm thick and a second layer of 80 nm of ITO, with a resistivity of $100 \Omega/\text{sq}$ [23]. Figure 2.10 shows the optical transparency of two ITO films with different thicknesses on a 1.1 mm thick glass substrate.

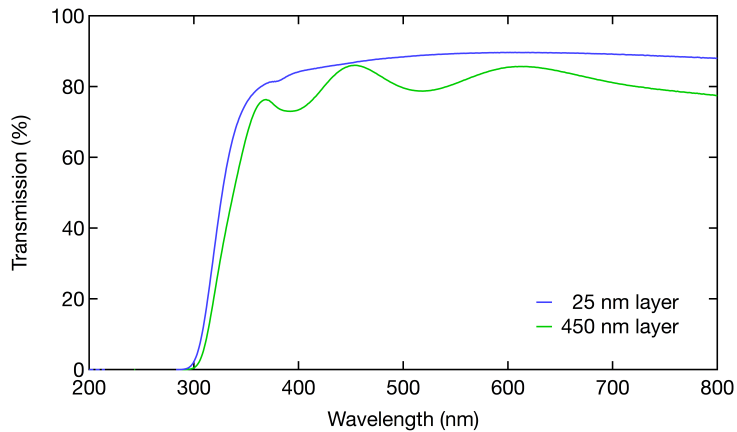


Figure 2.10: Optical transmission of ITO glass used in the first version of the LaGEMPix detector (blue line) measured for wavelengths ranging from 200 nm to 800 nm [7].

The ITO glass shows a transparency of around 80 % in the VIS range, compatible with the broad emission band of $Ar : CF_4$ in the VIS (see Figure 2.8). On the other hand, the absorption edge of the soda-lime glass is around 320 nm, thus the UV photons with wavelengths below 300 nm are absorbed. This absorption is due to the glass substrate. The transmission curve of an uncoated glass is very similar to the blue curve in Figure 2.10 and can be found in [49].

2.4 Radiation-Induced Effects in Glass Windows for Optical Readout

It is necessary to insert a transparent electromagnetic shielding below the final GEM and above the readout matrix [22], such as the ITO coated glass anode illustrated in Figure 2.11, in order to test the possibility of an optical readout. This transparent anode captures the drifting electrons while allowing scintillation photons to pass through, ensuring that photons, not electrons, are inducing a current in the image sensor's photodiodes. Several factors influence the probability of a photon reaching the image sensor, including the quantity of photons transmitted by the glass exit window. The higher the window transmission, the higher the induced signal in the readout system.

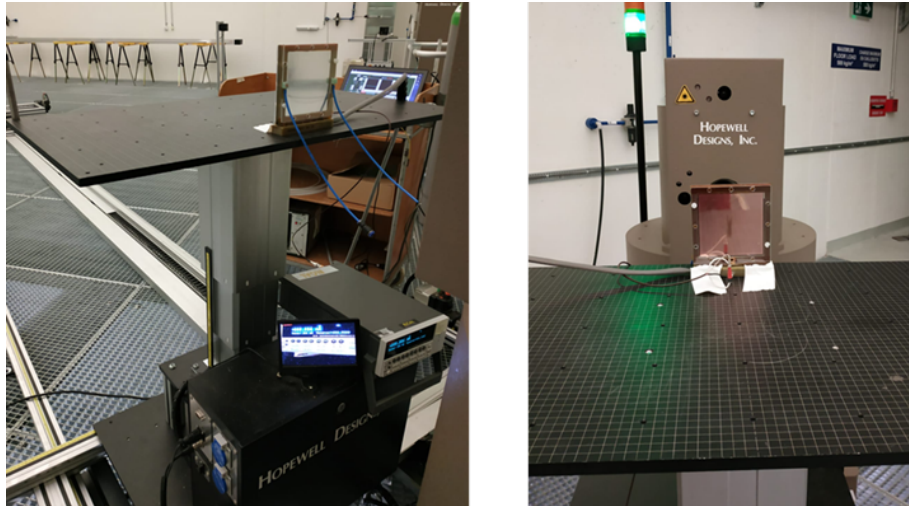


Figure 2.11: The 10 x 10 cm² Triple-GEM detector set-up in the CERN Calibration Laboratory.

Radiation effects can diminish window transmission efficiency and cause non-uniform responses in certain irradiated locations. As a result, the transparent anode material must be carefully chosen for this application because it impacts the detector's response uniformity and signal stability.

Several groups have investigated GEM-based detectors connected to CCD/CMOS cameras for particle therapy [22, 50, 6, 51, 52]. The setups incorporated transparent exit windows that were coated with ITO in some circumstances [22, 52, 46]. Because of its com-

bination of electrical conductivity and excellent visible light transmission, ITO is utilized to make optically transparent anodes. Apart from Seravalli et al., who utilized Duran 50 glass, no reduction in exit window transmission has been documented. Seravalli et al. and Klyachko et al. mentioned scintillation in the exit window as a possible source of light generation adding to noise, although it was either deemed insignificant [53] or easy to subtract [6].

Our focus was on examining the ability of photons to pass through different materials at visible wavelengths since Ar:CF₄ has a strong visible emission band around 630 nm, which is also suitable for standard optical measurements. Ar:CF₄ also has a broad emission band in the ultraviolet range (250 nm) and sharp emission lines above 695 nm. The aim was to identify the most effective ITO-coated transparent anode material that could be used with the triple-GEM detector. It is essential to maximize the transmission of Ar:CF₄ scintillation photons in order to maximize their detection and, therefore, increase the signal in the readout system.

2.4.1 Indium Tin Oxide-based glass materials

Three anodes were fabricated using ITO and had a rounded square shape with dimensions of 11 cm by 11 cm and rounded corners. The anodes had a thickness of 1.1 mm and one surface was coated with ITO, which had a resistivity of 100 Ω/sq . The materials used for these samples are detailed in Table 2.1.

Table 2.1: List of ITO-bases glass materials.

Material	Provider
Soda-lime glass	VisionTek Systems Ltd ⁽¹⁾
Heraeus ⁽²⁾ TSC-3 Quartz	Newcastle Optical Engineering Ltd ⁽³⁾
Heraeus Spectrosil [®] 2000	Newcastle Optical Engineering Ltd

The purity of the glass is an important factor in its ability to transmit light and resist damage from radiation. Defects in the glass, such as impurities or inclusions, can cause absorption bands that lower its transmission efficiency. The quality of the glass depends on the manufacturing process and the number of defects it contains. Soda-lime glass is less pure than fused silica, which is the most pure but also the most expensive option. Duran 50 glass

has previously been used as an exit window in optically readout GEM-based detectors, but it was found to have decreased transmission in the 400-600 nm range after being exposed to 3600 Gy of proton irradiation. As a result, it was not included in this study. A comprehensive description of the different materials can be found in [48].

2.4.2 Proton Beam Irradiation

The glasses were exposed to 18 MeV protons at intensities of up to 11 nA using the research Beam Transport Line (BTL) of the IBA Cyclone 18 MeV cyclotron in operation at the Bern University Hospital. The dose rate on the surface of the glasses was 53.8 Gy/s. A UniBEaM detector [24] was used to monitor the proton beam during the experiment as shown in Figure 2.12, and the protons were directed through a window towards the glasses. An aluminum disk was positioned behind the glass sample to measure the beam current connected to a Keysight B2985A electrometer. The glasses were oriented with the coated side facing the proton beam exit window, as they would be in a triple-GEM detector.

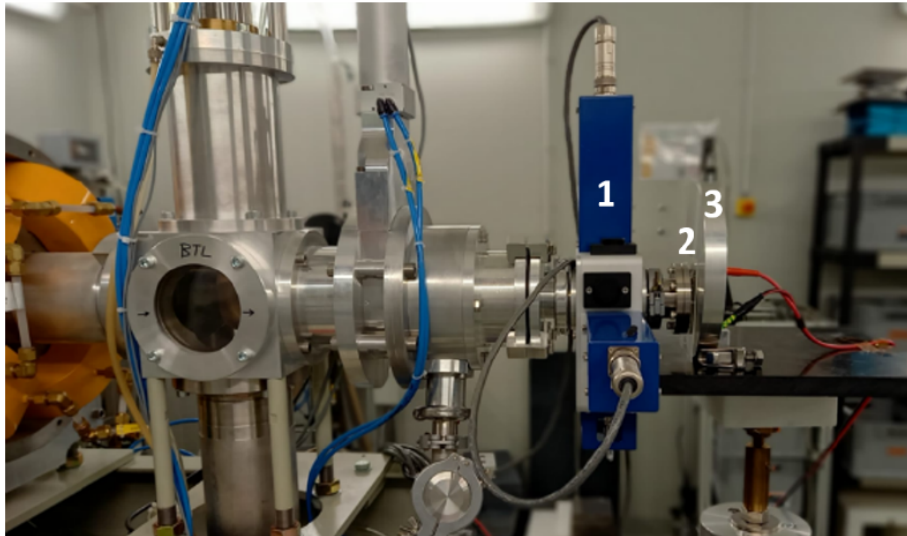


Figure 2.12: The UniBEaM (1) detector and the glass sample (2) installed at the end of the BTL of the IBA Cyclone 18MeV cyclotron at the Bern University Hospital (Inselspital). An aluminium disk (3) is placed behind the glass sample to measure the beam current.

An EBT3 Gafchromic TM film [54] was placed in front of the aluminium disk to assess the diameter and shape of the beam before irradiating the samples. The aim was to

2.4. RADIATION-INDUCED EFFECTS IN GLASS WINDOWS FOR OPTICAL READOUT63

have a proton flux similar to a hadron therapy beam. The proton flow at the CNAO in Italy is on the order of 10^8 protons/s/mm² [55]. To achieve the same flux from a uniform beam of 3 cm diameter coming from the Bern cyclotron (see Figure 2.13), a beam current of 11 nA must be set.

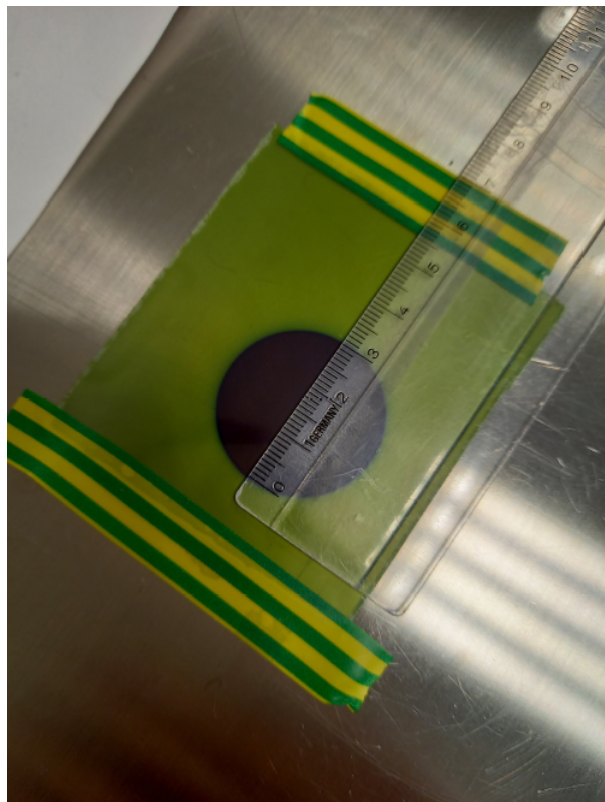


Figure 2.13: Irradiated EBT3 Gafchromic™ film showing a beam spot of 3 cm in diameter.

Figure 2.14 displays the horizontal and vertical beam profiles that the UniBEaM measured right before the extraction window. The average proton flux in the region of interest was estimated to be 1.5×10^8 protons/s/mm² based on the measured beam profile.

All samples were exposed to radiation twice: first for a brief period of time—about 20 seconds—to assess the scintillation light with a Bosh VTC-206 Mini Bullet Camera, and once for a period of 15 minutes to examine the optical effects. In order to use the camera to capture the light during the brief irradiation, we removed the aluminum disk from Figure 2.12 that is depicted. In order to capture photos and identify the scintillation light emitted by each sample, we positioned a camera with its lens directed toward the transparent anode. Following

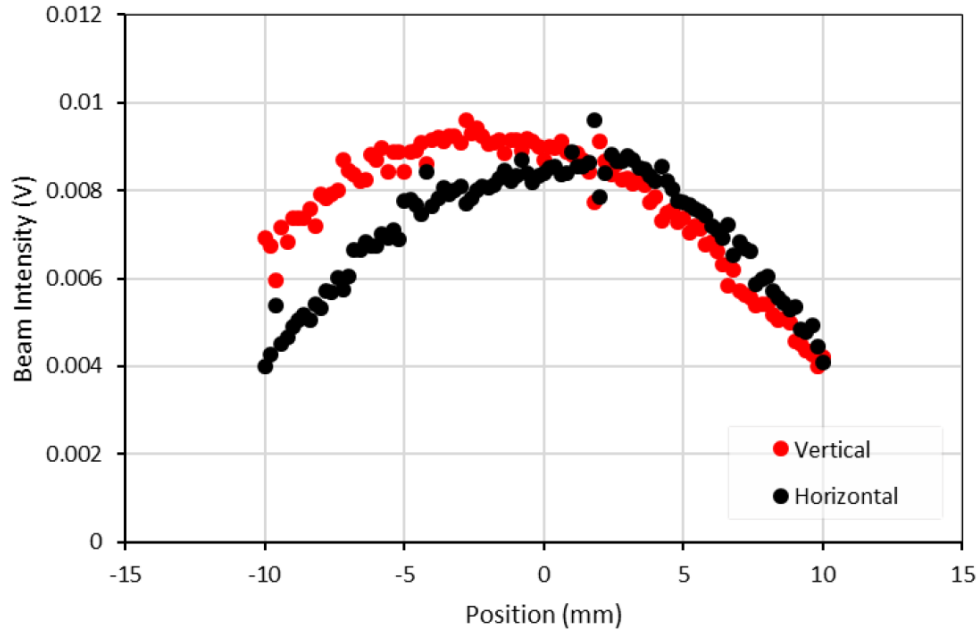


Figure 2.14: Proton beam profiles measured with the UniBEam.

each irradiation, each sample was examined visually to determine whether color centers were present.

By evaluating the transmission of each sample prior to and one week after irradiation, the effects of radiation were assessed. With a PerkinElmer Lambda 650UV/VIS Spectrometer (Standard detector Module), measurements were made in steps of 1 nm in the spectral range from 200 nm to 800 nm. Prior to the measurements, the equipment underwent an intrinsic calibration. To assess the oscillations around the 100% level of transmission and to calculate the corresponding measurement uncertainty, a second reference measurement without a sample was also performed. The difference between the highest value recorded during reference measurements and the level of 100% transmission was used to determine this uncertainty. The samples were carefully positioned ensuring that the spectrometer's complete point of light was within their glass's radiated region. The temperature, humidity, and pressure were all kept at ambient levels during all laboratory experiments.

The experimental findings are reported in [48] and summarized in Table 2.2. We recorded visible scintillation light generated by proton irradiation in the soda-lime and fused quartz samples. Additionally, the qualitative investigation of the three materials' darkening

revealed radiation-induced color centers in the soda-lime glass sample. After exposure to radiation, the optical transmission spectra of the three samples were measured. For soda-lime glass, fused quartz, and fused silica, respectively, a reduction in the optical transmission of 45%, 1%, and 0.4% was measured (with an associated error of 0.25%).

Table 2.2: Summary of the radiation-induced effects for the three tested glasses.

Glass	Scintillation	Irradiation induced colour centres	Reduction in transmission (maximum difference)	Variations in the sheet resistivity
Soda-lime	Yes — 66%	Yes (R=176, G=170, B=126)	45 %	Not observed
Fused quartz	Yes — 83%	Not observed	1%	Not observed
Fused silica	Not observed — 0.9 %	Not observed	0.4%	Not observed

The transmission loss would make it difficult for the LaGEMPix detector to faithfully replicate light signals, making the optical readout under consideration ineffective with soda-lime glass. Fused quartz appears to have a higher radiation tolerance. However, it does scintillate, adding a signal to the scintillation photons emitted in the triple-GEM. The measurements show that the fused silica substrate is the best option because it has the lowest transmission loss. Using this glass as an exit window will eventually result in a higher and more reliable signal compared to the other materials investigated. The results provided here led to a modification of the transparent anode substance for the forthcoming LaGEMPix detector for use in hadron therapy.

2.5 Readout of the Triple-GEM

The imagers of both LaGEMPix versions and its electronics were produced by Holst Centre/TNO and are presented in Figure 2.15. The readout circuits and the cables connected to the 11 x 13 x 6 cm^3 box with the FPGA module (560 grams weight), are on the right side of the baseplate.

2.5.1 Active Matrices

Focusing on the active area (green rectangle labeled as number 3 in Figure 2.15), the sensor array comprises 640 x 480 pixels at a resolution of 200 per inch (ppi), resulting in a total sensor

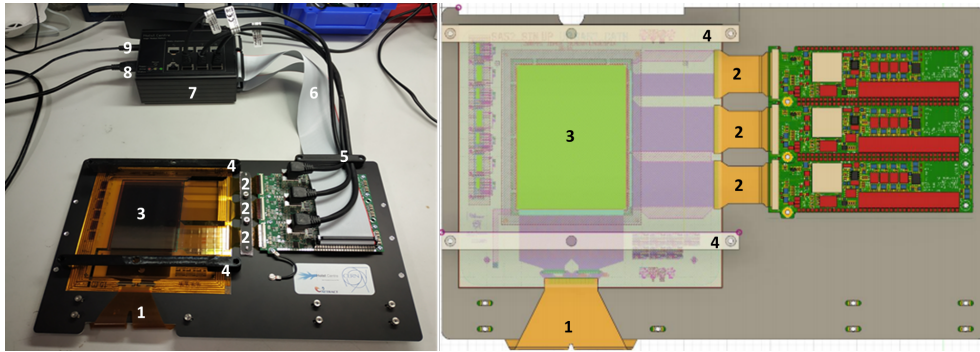
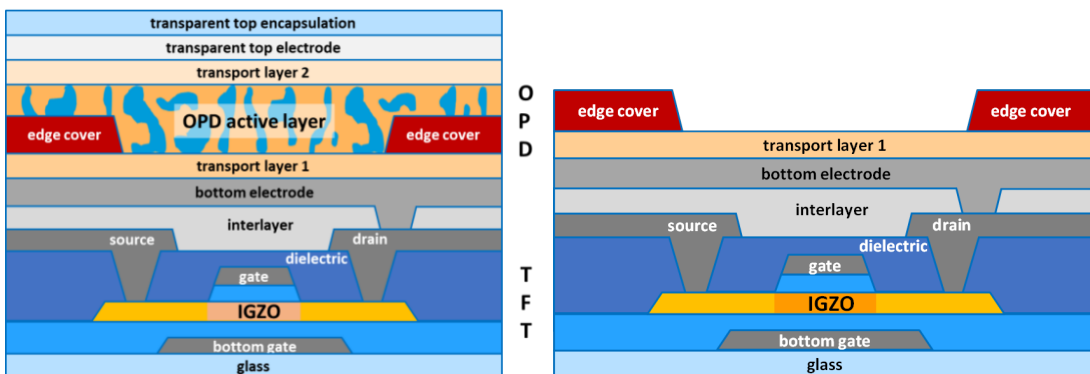


Figure 2.15: The LaGEMPix imager and its design: 1 – Flex connection to the Gate driver on glass. Gate drivers are on the backplane (chip on glass) indicated by the blue oval; 2 – Readout Integrated Circuit (ROIC); 3 – Sensitive array on glass substrate; 4 – 3D printed holders to fix the triple-GEM; 5 – three CAT 6 network cables, one from each ROIC; 6 – two flat Grey Ribbon cables, 1 x 40 pin from the 1st ROIC (top) and 1 x 26 pin, from the gate driver (bottom); 7 – box with the FPGA module; 8 - USB cable to connect to a laptop; 9 – Power connection.



(a) Optical readout (TFT and OPD).

(b) Charge readout (TFT).

Figure 2.16: Thin film image sensors produced by Holst Centre/TNO. The building blocks are scalable (developed up to $32 \times 35 \text{ cm}^2$).

area of $60 \times 80 \text{ mm}^2$. Holst Centre/TNO fabricated two types of matrices for the LaGEMPix project, TFT+OPD and TFT only, as show in Figure 2.16.

TFT and OPD

A photodiode is a semiconductor device that converts light into an electrical current. In a standard p-n junction diode, voltage is used as the energy source to generate electric current while in photodiodes, this current is generated when photons are absorbed. The performance of OPDs is nowadays reaching the point of competing with their inorganic equivalents in a number of performance criteria including linear dynamic range and color selectivity. Organic photosensors can be designed on glass, inorganic substrates and plastic substrates. Hence, lightweight, flexibility, easy integration with other electronics components, system-on-foil integration, small thickness, cost effectiveness and large area (size and shape customization) are advantages of the sensors that can be made based on OPDs, and can be easily combined with other printed electronics technologies. Therefore, OPDs can potentially be used in various applications such as pulse oximeters, digital X-ray sensors, proximity (distance) sensors, fingerprint authentication sensors, vein authentication, iris authentication, night vision [56].

Considering the Figure 2.16a it is possible to distinguish three main blocks. There is a glass substrate where the self-aligned gate oxide TFT array [57] is directly processed. Then the OPD frontplane is directly deposited on top of TFT backplane by slot-die coating. Finally, on top there is a transparent thin-film encapsulation serving as a protection against ambient conditions. The several layers are nominated in Figure 2.16a.

A photodetector such as this imaging sensor has the capability to convert the light emitted by the triple-GEM filled with $Ar : CF_4$ (90:10), the gaseous scintillator, into a current of photoelectrons. In this project, we have used an OPD based on a bulk heterojunction (BHJ) structure. It consists of a 280 nm thick blend of poly[N-9'-heptadecanyl-2,7-carbazole-alt-5,5-(4',7'-di-2-thienyl-2',1',3'-benzothiadiazole)], PCDTBT, a p-type (donor) polymer, and [6,6]-phenyl-C61-butyric acid methyl ester, PCBM, (acceptor) fullerene [58]. The sensor shows a dark current density of $10^{-7} mA/cm^2$ at -2 V and a linear behavior in a wide range of light intensities [59]. The External Quantum Efficiency (EQE) of the OPD is dictated by the absorption of the heterojunction components, potentially modified by interference effects derived from the electrodes and encapsulation. The EQE for this specific OPD layer, the sensitive component of the imager, is above 50% between 470 nm and 620 nm and about 25% at 640 nm, as can be seen in Figure 2.17.

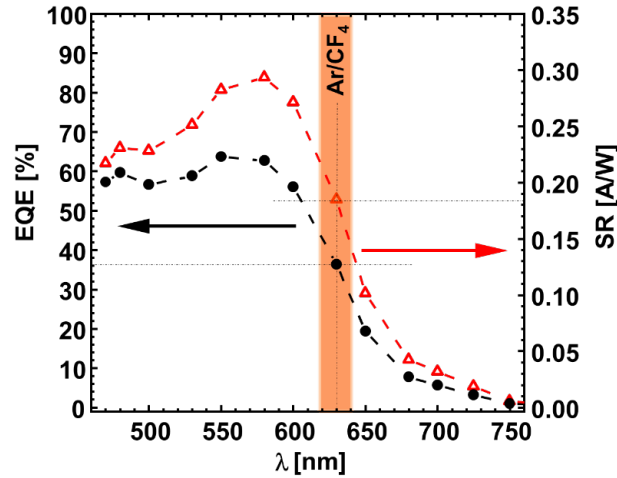


Figure 2.17: EQE (black curve and left axis) and Spectral Response (SR) (red curve and right axis) of the OPD layer deposited on the readout matrix. The broad emission band of $Ar : CF_4$ with a peak at around 630 nm is represented by the orange region.

The sensitive wavelength range of the selected photodetector, the OPD active layer, must match the wavelength range where the emitted scintillation light is more intense in order to be suitable for radiation detection by an optical readout. The readout acceptance spectrum only matches a fraction of the broad band centered at 630 nm at the emission spectrum of $Ar : CF_4$ 2.9. Therefore, only a small fraction of the VIS photons produced in the GEM will be detected with high efficiency by this imager.

Moreover, not all of the scintillation light ends up in the OPD. There could be losses also due to the presumed 4π emission of the light [60, 51], since only the photons that travel in the direction of the OPD are collected. If we take into consideration that the photons are emitted isotropically, the photons emitted in the other directions, that are not contained in solid-angles impinging the sensitive area of the OPD, are lost and do not contribute to the measured signal.

Hence, just a fraction of the visible photons produced in the triple-GEM are detected with high efficiency by this imager.

TFT

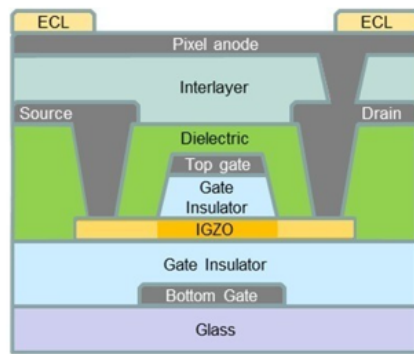
The Organic Photodiode (OPD) frontplane present in the optical option was eliminated, leaving a TFT-only electronic readout, as shown in Figure 2.16b. The TFT arrays dimensions are alike to the TFT and OPD arrays. They were similarly developed with a pixel pitch of 126 μm and 640 x 480 pixels, resulting in a total sensor area of 60 x 80 mm^2 . In this second version of the detector, the bottom pixel electrode and pixel edge cover layer on the TFT backplane define the active pixel region.

The frontplane of the triple-GEM was coupled with a high-resolution 200 ppi active matrix TFT backplane based on amorphous Indium Gallium Zinc Oxide (a-IGZO) technology. The self-aligned dual-gate TFT architecture used in the backplane, as described in [61, 62], has demonstrated superior performance in terms of higher current drive, steeper subthreshold slope, and better determined onset voltage (V_{on}) close to a gate voltage (V_g) of 0 V. The use of a-IGZO technology has also led to lower off-currents and off-current uniformity, resulting in reduced noise in the readout electronics.

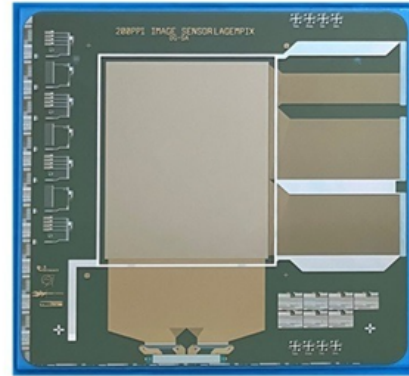
The fabrication process for the TFT backplane consists of six lithographic patterning steps, and all process steps are flat panel display compatible, making mass production facile. The TFTs ($W/L = 15/5 \mu\text{m}$) have a typical linear mobility of $29.1 \pm 0.8 \text{ cm}^2/V\text{s}$, turn-on voltage (V_{on}) of $0.8 \pm 0.3V$, ON/OFF current ratio $\approx 10^7$, and a subthreshold swing of $0.4 \pm 0.02V/\text{decade}$. Figure 2.18d provides the transfer characteristics of 70 TFTs mapped over the full 320 x 352 m^2 area of the motherglass [63].

The TFT backplane is monolithically integrated on a glass carrier, and each TFT has a metal contact pad connected to its drain electrode to enlarge the effective area on which the secondary electrons from the GEM can be collected. The metal layers, bottom/top-gate, and source/drain electrodes (100 nm Mo-alloy) are sputtered and patterned using wet etching. The bottom gate insulator (200 nm SiO_2 , 350 $^\circ\text{C}$) is PECVD-deposited, and the a-IGZO layer (16 nm, ratio 1:1:1) is sputtered at room temperature. The top gate insulator (200 nm SiO_2) and top gate metal are both formed in a single lithography mask phase, i.e., self-aligned gate stack patterning. Finally, an inter-metal dielectric (200 nm SiN) is deposited using Plasma-Enhanced Chemical Vapor Deposition (PECVP).

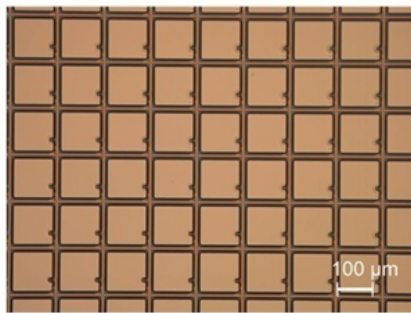
Figure 2.18a shows a cross-section of the TFT backplane, and Figures 2.18b and



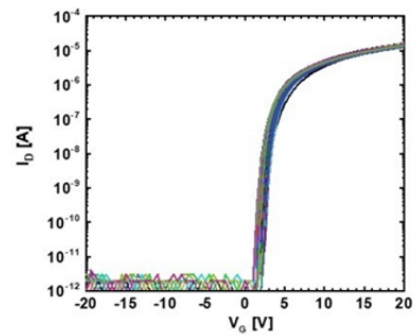
(a) Cross section of the dual gate self-aligned TFT.



(b) Photograph of the TFT backplane.



(c) Microscopy image of part of the TFT backplane array showing individual pixels.



(d) TFT characteristics of 70 dual-gate TFTs ($W/L = 15/5 \mu\text{m}$) operated in bulk accumulation mode by connecting top-gate and bottom-gate ($V = V_{G,\text{bottom}} = V_{G,\text{top}}$).

Figure 2.18: Thin Film Transistor (TFT) backplane.

2.18c show photographs of the finished backplane and a zoomed image of the individual pixels, respectively. The metal contact pad can be seen in Figure 2.18a, depicted by the pixel anode in the schematic.

2.5.2 Circuits and Readout

OPD and TFT

Each individual pixel has a photodiode size of approximately $103 \times 103 \mu\text{m}^2$ (actual active area $10522 \mu\text{m}^2$) at a pixel pitch of $126 \mu\text{m}$ and it is made of a single TFT and an OPD. The parasitic capacitance is used to store the charge of the pixel.

The schematic diagram of the active OPD and TFT matrix is shown in Figure 2.19. The V_{bias} is driven at a constant voltage of -2 V. All 640 data lines are connected to the ROICs inputs. The ROIC is composed by three ADAS1256, a 256-channel, 16-bit, digital X-Ray Analog Front End (AFE) that integrates the complete charge-to-digital conversion signal chain on a single chip. The most complete information available on the ROIC can be found in the partial datasheet [64].

All 480 gate lines that control the TFTs are driven by the gate driver (the data sheet is under Non-Disclosure Agreement and for this reason no more details can be shared). The TFT acts as a switch and therefore, there are two main states on this circuit controlled by the gate driver. When the switch is ON (Figure 2.20a), the charge from the pixel is transferred to the integrator feedback capacitor (C_{IFS}). A time of $5RC_{IFS}$ for the transfer should be respected to minimize errors. The signal gain is set by $C_{IFS} : V_{out} = Q_{pixel}/C_{IFS}$. When the switch is OFF, the circuit is reduced to the Figure 2.20b and the OPD is discharging the capacitor proportionally to the light collected.

There is only one gate line open at a time, as depicted in Figure 2.21, since they are controlled by a shift register. Hence, the readout sequence is done line by line.

The structure of the readout sequence is shown in Figure 2.22. The V_{bias} is driven at a constant voltage of -2 V. The gate driver is a big shift register that switches all TFTs one line at a time. When connected to the ROIC, the pixels are read by charging them to a

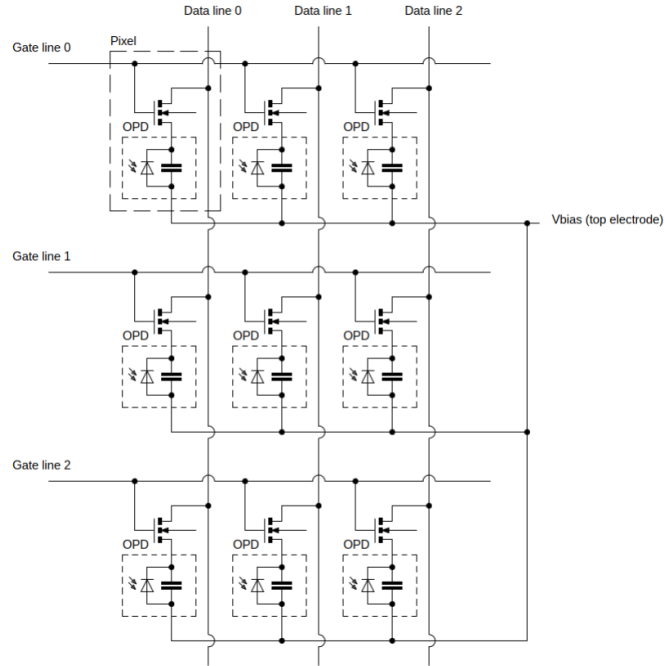


Figure 2.19: Schematic diagram of the active OPD and TFT matrix [65].

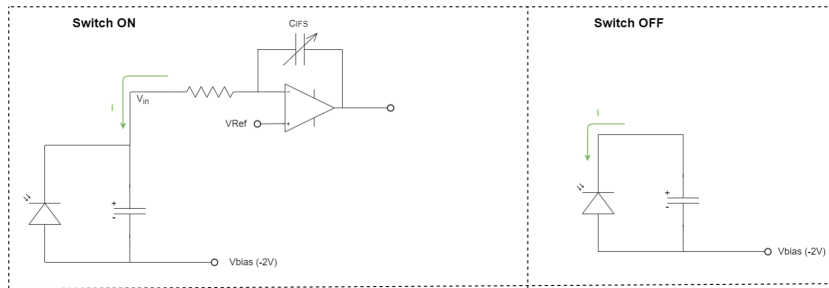


Figure 2.20: Schematic circuits: a) Switch ON b) Switch OFF.

reference voltage ($V_{ref} = REF_{TFT} = 1V$) and measuring the charge required to do so. This is all done by the ROIC that has an integrator at every input (256 inputs/ROIC). At the beginning of each line, the integrator is reset. Next the TFT is switched on to connect the OPD to the integrator input. The pixel then gets charged back to the reference voltage and the same charge that was accumulated in the parasitic capacitor accumulates in the feedback capacitor of the integrator. The TFT is switched off and the resulting output of the integrator is digitized by an Analog-to-Digital Converter (ADC). This is done simultaneously by all inputs of all 3 ROICs. During the time frame the TFTs of the line just read are all off. The charge in

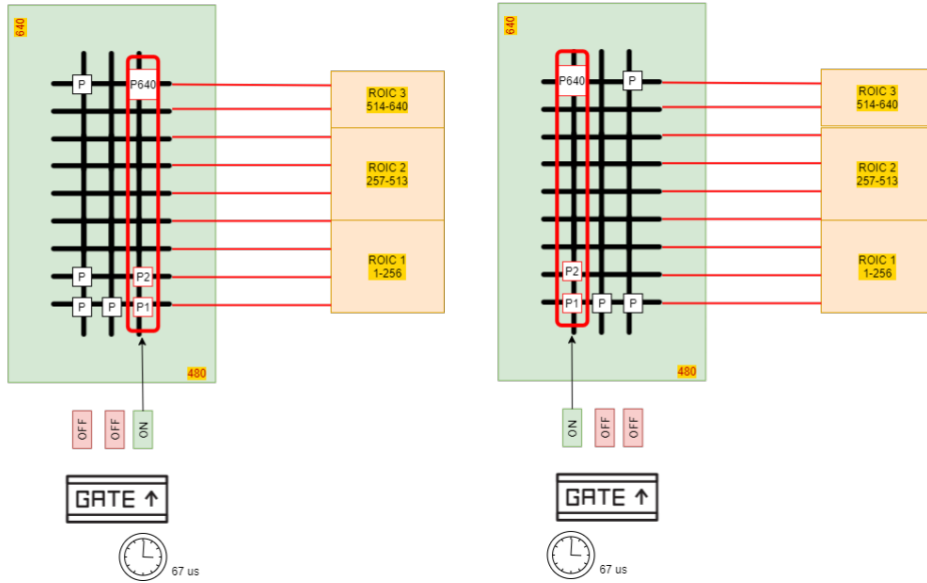


Figure 2.21: Readout line controlled by the gate driver.

the (parasitic) capacitor of the OPD in the pixel will get removed as a function of the amount of light absorbed by the pixel during the integration time (or frame time). The lighter, the more charge will be removed. Saturation of the pixel occurs when all charge is removed from the capacitor and the pixel pad voltage is equal to V_{bias} . After the time frame has passed the read cycle is repeated.

The “shifting read columns” procedure depicted in Figure 2.22 is significantly complex because the ROIC also requires several steps to reset the integrator, perform an offset correction, transfer the charge, do the AD conversion and transfer the resulting data over the serial link. The transfer of the charge is done in a few μs , however the delay time of $67 \mu\text{s}$ per line is due to the complexity of this chain of processes. The raw sensor data is transferred over the serial link as 16-bit greyscale values. The readout output format is a TIFF image (or set of images) provided by the application IRP (LabVIEW).

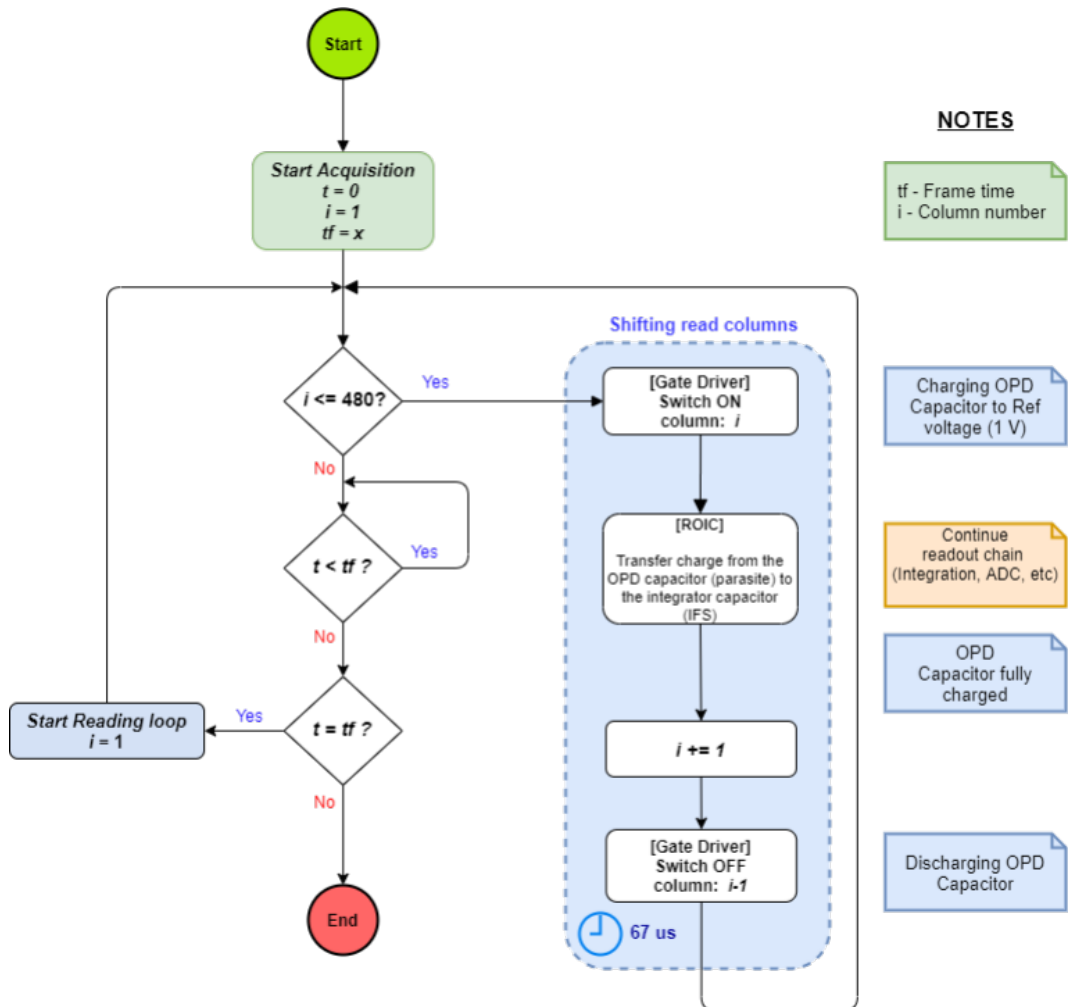


Figure 2.22: Flowchart of the readout process.

TFT

The schematic TFT array design, including the storage capacitor, is illustrated Figure 2.23. The OPD present in the optical version of LaGEMPix was eliminated, leaving a TFT-only electronic readout.

The TFT-only backplane was integrated with existing gate drivers and ROICs to perform the back-end processing. The readout sequence is similar to the one described above in Figure 2.21. The current readout hardware and mechatronics elements of the LaGEMPix

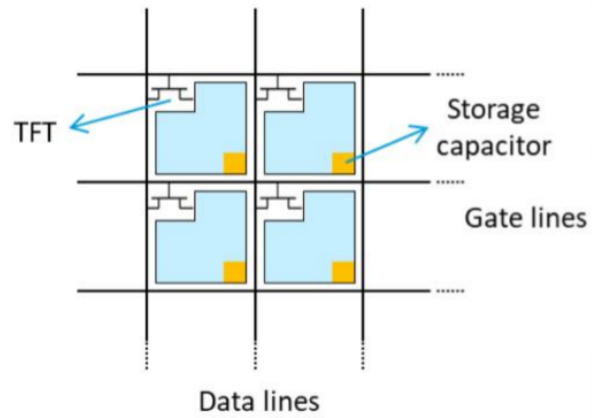


Figure 2.23: The schematic TFT array design.

with optical readout were reused for the characterization of this initial TFT-only panel.

Bibliography

- [1] A. Maia Oliveira, “LaGEMPix: a new imaging sensor,” CERN, Technical Note CERN EDMS no. 2426552, 2020.
- [2] J. Leidner, M. Ciocca, S. P. George, A. Mirandola, F. Murtas, A. Rimoldi, M. Silari, and A. Tamborini, “3D energy deposition measurements with the GEMPix detector in a water phantom for hadron therapy,” *Journal of Instrumentation*, vol. 13, no. 08, pp. P08 009–P08 009, Aug. 2018, publisher: IOP Publishing.
- [3] X. Llopart, R. Ballabriga, M. Campbell, L. Tlustos, and W. Wong, “Timepix, a 65k programmable pixel readout chip for arrival time, energy and/or photon counting measurements,” *Nuclear Instruments and Methods in Physics Research Section A: Accelerators, Spectrometers, Detectors and Associated Equipment*, vol. 581, no. 1, pp. 485–494, Oct. 2007. [Online]. Available: <https://www.sciencedirect.com/science/article/pii/S0168900207017020>
- [4] “Home | medipix.web.cern.ch.” [Online]. Available: <https://medipix.web.cern.ch/>
- [5] J. Leidner, M. Ciocca, A. Mairani, F. Murtas, and M. Silari, “A GEMPix-based integrated system for measurements of 3D dose distributions in water for carbon ion scanning beam radiotherapy,” *Medical Physics*, vol. 47, no. 6, pp. 2516–2525, Jun. 2020. [Online]. Available: <https://onlinelibrary.wiley.com/doi/abs/10.1002/mp.14119>
- [6] E. Seravalli, *A scintillating GEM detector for 2D dose imaging in hadron therapy*. Amsterdam: IOS Press, 2008, oCLC: ocn244320567.
- [7] F. M. Brunbauer, “Applications of gas scintillation properties in optically read out

- GEM-based detectors,” Ph.D. dissertation, Jul. 2018, number: CERN-THESIS-2018-106 University: Vienna, Tech. U. [Online]. Available: <https://cds.cern.ch/record/2632476>
- [8] S. Fetal, C. W. E. van Eijk, F. Fraga, J. de Haas, R. Kreuger, T. L. van Vuure, and J. M. Schippers, “Dose imaging in radiotherapy with an Ar-CF 4 filled scintillating GEM,” *Nuclear Instruments and Methods in Physics Research A*, vol. 513, pp. 42–46, Nov. 2003. [Online]. Available: <http://adsabs.harvard.edu/abs/2003NIMPA.513...42F>
- [9] B. AG, “Basler ace acA1920-40gm - Area Scan Camera.” [Online]. Available: <https://www.baslerweb.com/en/products/cameras/area-scan-cameras/ace/aca1920-40gm/>
- [10] A. Roberts, P. Svihra, A. Al-Refaie, H. Graafsma, J. Küpper, K. Majumdar, K. Mavrokoridis, A. Nomerotski, D. Pennicard, B. Philippou, S. Trippel, C. Touramanis, and J. Vann, “First demonstration of 3D optical readout of a TPC using a single photon sensitive Timepix3 based camera,” *Journal of Instrumentation*, vol. 14, no. 06, pp. P06 001–P06 001, Jun. 2019, arXiv: 1810.09955. [Online]. Available: <http://arxiv.org/abs/1810.09955>
- [11] K. I. Inc, “Model 6517A Electrometer User’s Manual,” Feb. 2021.
- [12] A. Maia Oliveira, “OptiGEM,” CERN, Technical Note CERN EDMS no. 2169268, 2019.
- [13] —, “OptiGEM ITO - Glass,” CERN, Technical Note CERN EDMS no. 2379041, 2020.
- [14] M. Brugger, P. Carbonez, F. Pozzi, M. Silari, and H. Vincke, “New radiation protection calibration facility at CERN,” *Radiation Protection Dosimetry*, vol. 161, no. 1-4, pp. 181–184, Oct. 2014. [Online]. Available: <https://doi.org/10.1093/rpd/nct318>
- [15] A. Maia Oliveira, “LaGEMPix: optimization of electric fields for operation with Ar:CF4 gas mixture,” CERN, Technical Note CERN EDMS no. 2331474, 2020.
- [16] X. Llopart, J. Alozy, R. Ballabriga, M. Campbell, R. Casanova, V. Gromov, E. H. M. Heijne, T. Poikela, E. Santin, V. Sriskaran, L. Tlustos, and A. Vitkovskiy, “Timepix4, a large area pixel detector readout chip which can be tiled on 4 sides providing sub-200 ps timestamp binning,” vol. 17, no. 1, p. C01044, publisher: IOP Publishing. [Online]. Available: <https://dx.doi.org/10.1088/1748-0221/17/01/C01044>
- [17] M. Titov and L. Ropelewski, “Micro-pattern gaseous detector technologies and rd51 collaboration,” *Modern Physics Letters A*, vol. 28, no. 13, p. 1340022,

- Apr. 2013, publisher: World Scientific Publishing Co. [Online]. Available: <https://www.worldscientific.com/doi/abs/10.1142/S0217732313400221>
- [18] F. Sauli, "GEM: A new concept for electron amplification in gas detectors," *Nuclear Instruments and Methods in Physics Research Section A: Accelerators, Spectrometers, Detectors and Associated Equipment*, vol. 386, no. 2, pp. 531–534, Feb. 1997. [Online]. Available: <http://www.sciencedirect.com/science/article/pii/S0168900296011722>
- [19] G. Bencivenni, W. Bonivento, C. Bosio, A. Cardini, G. Felici, A. Lai, F. Murtas, D. Pinci, B. Saitta, L. Satta, and P. Valente, "A fast triple-GEM detector for high-rate charged-particle triggering," *Nuclear Instruments and Methods in Physics Research Section A: Accelerators, Spectrometers, Detectors and Associated Equipment*, vol. 478, no. 1-2, pp. 245–249, Feb. 2002. [Online]. Available: <https://linkinghub.elsevier.com/retrieve/pii/S0168900201017648>
- [20] S. Bachmann, A. Bressan, M. Capeáns, M. Deutel, S. Kappler, B. Ketzer, A. Polouektov, L. Ropelewski, F. Sauli, E. Schulte, L. Shekhtman, and A. Sokolov, "Discharge studies and prevention in the gas electron multiplier (GEM)," *Nuclear Instruments and Methods in Physics Research Section A: Accelerators, Spectrometers, Detectors and Associated Equipment*, vol. 479, no. 2-3, pp. 294–308, Mar. 2002. [Online]. Available: <https://linkinghub.elsevier.com/retrieve/pii/S0168900201009317>
- [21] M. Alfonsi, G. Bencivenni, P. de Simone, F. Murtas, M. Poli Lener, W. Bonivento, A. Cardini, C. Deplano, D. Pinci, D. Raspino, and B. Saitta, "A triple-GEM detector for high-rate particle triggering," *Nuclear Instruments and Methods in Physics Research Section A: Accelerators, Spectrometers, Detectors and Associated Equipment*, vol. 525, no. 1, pp. 17–19, Jun. 2004. [Online]. Available: <http://www.sciencedirect.com/science/article/pii/S0168900204003407>
- [22] F. M. Brunbauer, F. Garcia, T. Korkalainen, A. Lugstein, M. Lupberger, E. Oliveri, D. Pfeiffer, L. Ropelewski, P. Thuiner, and M. Schinnerl, "Combined Optical and Electronic Readout for Event Reconstruction in a GEM-Based TPC," *IEEE Transactions on Nuclear Science*, vol. 65, no. 3, pp. 913–918, Mar. 2018, conference Name: IEEE Transactions on Nuclear Science.
- [23] "Indium Tin Oxide Glass." [Online]. Available: https://www.visionteksystems.co.uk/ito_glass_datasheet.htm

- [24] M. Auger, S. Braccini, T. Carzaniga, A. Ereditato, K. Nesteruk, and P. Scampoli, “A detector based on silica fibers for ion beam monitoring in a wide current range,” vol. 11, no. 3, pp. P03 027–P03 027. [Online]. Available: <https://iopscience.iop.org/article/10.1088/1748-0221/11/03/P03027>
- [25] F. A. F. Fraga, L. M. S. Margato, S. T. G. Fetal, M. M. F. R. Fraga, R. F. Marques, and A. J. P. L. Policarpo, “Luminescence and imaging with gas electron multipliers,” *Nuclear Instruments and Methods in Physics Research Section A: Accelerators, Spectrometers, Detectors and Associated Equipment*, vol. 513, no. 1, pp. 379–387, Nov. 2003. [Online]. Available: <http://www.sciencedirect.com/science/article/pii/S0168900203022915>
- [26] T. Yanagida, “Inorganic scintillating materials and scintillation detectors,” *Proceedings of the Japan Academy. Series B, Physical and Biological Sciences*, vol. 94, no. 2, pp. 75–97, 2018.
- [27] P. Lecoq, “Development of new scintillators for medical applications,” *Nuclear Instruments and Methods in Physics Research Section A: Accelerators, Spectrometers, Detectors and Associated Equipment*, vol. 809, pp. 130–139, Feb. 2016. [Online]. Available: <http://www.sciencedirect.com/science/article/pii/S0168900215009754>
- [28] W. R. Leo, *Techniques for Nuclear and Particle Physics Experiments: A How-to Approach*, 2nd ed. Berlin Heidelberg: Springer-Verlag, 1994. [Online]. Available: <https://www.springer.com/gp/book/9783540572800>
- [29] “Sauli, F., Fraga, M. and Brunbauer, F., private communication. April, 2020.”
- [30] L. Cerrito, *Radiation and Detectors: Introduction to the Physics of Radiation and Detection Devices*. Springer, May 2017, google-Books-ID: NcvbDgAAQBAJ.
- [31] A. Pansky, A. Breskin, A. Buzulutskov, R. Chechik, V. Elkind, and J. Va’vra, “The scintillation of CF₄ and its relevance to detection science,” *Nuclear Instruments and Methods in Physics Research Section A: Accelerators, Spectrometers, Detectors and Associated Equipment*, vol. 354, no. 2, pp. 262–269, Jan. 1995. [Online]. Available: <http://www.sciencedirect.com/science/article/pii/0168900294010641>
- [32] A. Morozov, L. M. S. Margato, M. M. F. R. Fraga, L. Pereira, and F. a. F. Fraga, “Secondary scintillation in CF₄: emission spectra and photon yields for MSGC and GEM,” *Journal of Instrumentation*, vol. 7, no. 02, p. P02008, Feb. 2012, publisher: IOP

- Publishing. [Online]. Available: <https://iopscience.iop.org/article/10.1088/1748-0221/7/02/P02008/meta>
- [33] M. M. Fraga, S. T. G. Fetal, F. A. F. Fraga, E. Antunes, J. Goncalves, C. C. Bueno, R. F. Marques, and A. J. P. L. Policarpo, "Study of scintillation light from microstructure based detectors," *IEEE Transactions on Nuclear Science*, vol. 47, no. 3, pp. 933–938, Jun. 2000, conference Name: IEEE Transactions on Nuclear Science.
- [34] E. Sysoeva, V. Tarasov, and O. Zelenskaya, "Comparison of the methods for determination of scintillation light yield," *Nuclear Instruments and Methods in Physics Research Section A: Accelerators, Spectrometers, Detectors and Associated Equipment*, vol. 486, no. 1, pp. 67–73, Jun. 2002. [Online]. Available: <http://www.sciencedirect.com/science/article/pii/S0168900202006769>
- [35] M. M. F. R. Fraga, F. A. F. Fraga, S. T. G. Fetal, L. M. S. Margato, R. F. Marques, and A. J. P. L. Policarpo, "The GEM scintillation in He–CF₄, Ar–CF₄, Ar–TEA and Xe–TEA mixtures," *Nuclear Instruments and Methods in Physics Research Section A: Accelerators, Spectrometers, Detectors and Associated Equipment*, vol. 504, no. 1, pp. 88–92, May 2003. [Online]. Available: <http://www.sciencedirect.com/science/article/pii/S0168900203007587>
- [36] J. H. Timmer, T. L. van Vuure, V. Bom, C. W. van Eijk, J. de Haas, and J. M. Schippers, "A scintillating GEM for 2D-dosimetry in radiation therapy," *Nuclear Instruments and Methods in Physics Research Section A: Accelerators, Spectrometers, Detectors and Associated Equipment*, vol. 478, no. 1, pp. 98–103, Feb. 2002. [Online]. Available: <http://www.sciencedirect.com/science/article/pii/S0168900201017181>
- [37] G. F. Knoll, *Radiation detection and measurement*, 2nd ed. New York: Wiley, 1989.
- [38] K. Stephan, H. Deutsch, and T. D. Märk, "Absolute partial and total electron impact ionization cross sections for CF₄ from threshold up to 180 eV," *The Journal of Chemical Physics*, vol. 83, no. 11, pp. 5712–5720, Dec. 1985, publisher: American Institute of Physics. [Online]. Available: <https://aip.scitation.org/doi/10.1063/1.449646>
- [39] U. Müller, T. Bubel, G. Schulz, A. Sevilla, J. Dike, and K. Becker, "Further studies of the continuous UV emission produced by electron impact on CF₄," *Zeitschrift für*

- Physik D Atoms, Molecules and Clusters*, vol. 24, no. 2, pp. 131–139, Jun. 1992. [Online]. Available: <https://doi.org/10.1007/BF01426697>
- [40] L. C. Lee, X. Wang, and M. Suto, “Fluorescence from extreme ultraviolet photoexcitation of CF₄,” *The Journal of Chemical Physics*, vol. 85, no. 11, pp. 6294–6300, Dec. 1986, publisher: American Institute of Physics. [Online]. Available: <https://aip.scitation.org/doi/10.1063/1.451459>
- [41] J. E. Hesser and K. Dressler, “Radiative Lifetimes of Ultraviolet Emission Systems Excited in BF₃, CF₄, and SiF₄,” *The Journal of Chemical Physics*, vol. 47, no. 9, pp. 3443–3450, Nov. 1967, publisher: American Institute of Physics. [Online]. Available: <https://aip.scitation.org/doi/10.1063/1.1712410>
- [42] K. Furuya, E. Koto, and T. Ogawa, “Fragment ion-photon coincidence investigation of carbon tetrafluoride by controlled electron impact,” *Journal of Physics B: Atomic, Molecular and Optical Physics*, vol. 34, no. 8, p. 1405, Apr. 2001, publisher: IOP Publishing. [Online]. Available: <https://iopscience.iop.org/article/10.1088/0953-4075/34/8/306/meta>
- [43] M. Tsuji, M. Furusawa, T. Mizuguchi, T. Muraoka, and Y. Nishimura, “Dissociative excitation of CF₄, CCl₄, and chlorofluoromethanes by collisions with argon and helium active species,” *The Journal of Chemical Physics*, vol. 97, no. 1, pp. 245–255, Jul. 1992, publisher: American Institute of Physics. [Online]. Available: <https://aip.scitation.org/doi/10.1063/1.463622>
- [44] J. M. Ajello, G. K. James, B. Franklin, and S. Howell, “Study of electron impact excitation of argon in the extreme ultraviolet: emission cross section of resonance lines of Ar I, Ar II,” *Journal of Physics B: Atomic, Molecular and Optical Physics*, vol. 23, no. 23, pp. 4355–4376, Dec. 1990, publisher: IOP Publishing.
- [45] E. Seravalli, M. R. d. Boer, F. Geurink, J. Huizenga, R. Kreuger, J. M. Schippers, and C. W. E. v. Eijk, “2D dosimetry in a proton beam with a scintillating GEM detector,” *Physics in Medicine and Biology*, vol. 54, no. 12, pp. 3755–3771, May 2009, publisher: IOP Publishing.
- [46] T. Fujiwara, Y. Mitsuya, T. Yanagida, T. Saito, H. Toyokawa, and H. Takahashi, “High-photon-yield scintillation detector with Ar/CF₄ and glass gas electron multiplier,”

- Japanese Journal of Applied Physics*, vol. 55, no. 10, p. 106401, Sep. 2016, publisher: IOP Publishing. [Online]. Available: <https://iopscience.iop.org/article/10.7567/JJAP.55.106401/meta>
- [47] P. Kuang, J.-M. Park, W. Leung, R. C. Mahadevapuram, K. S. Nalwa, T.-G. Kim, S. Chaudhary, K.-M. Ho, and K. Constant, “A new architecture for transparent electrodes: relieving the trade-off between electrical conductivity and optical transmittance,” *Advanced Materials (Deerfield Beach, Fla.)*, vol. 23, no. 21, pp. 2469–2473, Jun. 2011.
- [48] A. M. Oliveira, S. Braccini, P. Casolaro, N. Heracleous, J. Leidner, I. Mateu, F. Murtas, and M. Silari, “Radiation-induced effects in glass windows for optical readout GEM-based detectors,” *Journal of Instrumentation*, vol. 16, no. 07, p. T07009, Jul. 2021, publisher: IOP Publishing. [Online]. Available: <https://doi.org/10.1088/1748-0221/16/07/t07009>
- [49] S. Miranda, A. Vilanova, T. Lopes, and A. Mendes, “TiO₂-coated window for facilitated gas evolution in PEC solar water splitting,” *RSC Advances*, vol. 7, no. 47, pp. 29 665–29 671, Jun. 2017, publisher: The Royal Society of Chemistry. [Online]. Available: <https://pubs.rsc.org/en/content/articlelanding/2017/ra/c7ra01923h>
- [50] D. Nichiporov, L. Coutinho, and A. V. Klyachko, “Characterization of a GEM-based scintillation detector with he-CF₄ gas mixture in clinical proton beams,” vol. 61, no. 8, p. 2972, publisher: IOP Publishing. [Online]. Available: <https://dx.doi.org/10.1088/0031-9155/61/8/2972>
- [51] A. Klyachko, V. Moskvina, D. Nichiporov, and K. Solberg, “A GEM-based dose imaging detector with optical readout for proton radiotherapy,” *Nuclear Instruments and Methods in Physics Research Section A Accelerators Spectrometers Detectors and Associated Equipment*, vol. 694, pp. 271–279, Dec. 2012.
- [52] T. Fujiwara, Y. Koba, Y. Mitsuya, R. Nakamura, R. Tatsumoto, S. Kawahara, K. Maehata, H. Yamaguchi, W. Chang, N. Matsufuji, and H. Takahashi, “Development and characterization of optical readout well-type glass gas electron multiplier for dose imaging in clinical carbon beams,” vol. 82, pp. 72–78, publisher: Elsevier. [Online]. Available: [https://www.physicamedica.com/article/S1120-1797\(21\)00071-5/fulltext](https://www.physicamedica.com/article/S1120-1797(21)00071-5/fulltext)
- [53] A. V. Klyachko, D. L. Friesel, C. Kline, J. Liechty, D. F. Nichiporov, and K. A. Solberg, “Dose imaging detectors for radiotherapy based on gas

- electron multipliers,” vol. 628, no. 1, pp. 434–439. [Online]. Available: <https://www.sciencedirect.com/science/article/pii/S0168900210015615>
- [54] “Garchromic EBT Films - GAFchromic™.” [Online]. Available: <http://www.gafchromic.com/gafchromic-film/radiotherapy-films/EBT/index.asp>
- [55] S. Rossi, “The status of CNAO,” *The European Physical Journal Plus*, vol. 126, no. 8, p. 78, Aug. 2011. [Online]. Available: <https://doi.org/10.1140/epjp/i2011-11078-8>
- [56] R. D. Jansen-van Vuuren, A. Armin, A. K. Pandey, P. L. Burn, and P. Meredith, “Organic Photodiodes: The Future of Full Color Detection and Image Sensing,” *Advanced Materials (Deerfield Beach, Fla.)*, vol. 28, no. 24, pp. 4766–4802, Jun. 2016.
- [57] A. J. Kronemeijer, H. Akkerman, J.-L. v. d. Steen, S. Steudel, R. Pendyala, P. Panditha, T. Bel, K. v. Diesen, G. d. Haas, J. Maas, J. d. Riet, M. Rovers, R. Verbeek, M. Nag, L. Verschuere, J. Genoe, W. Dehaene, Y.-J. Lu, S.-C. Chiang, Y.-Y. Huang, M.-H. Yeh, and G. Gelinck, “P-127: Dual-Gate Self-Aligned IGZO TFTs Monolithically Integrated with High-Temperature Bottom Moisture Barrier for Flexible AMOLED,” *SID Symposium Digest of Technical Papers*, vol. 49, no. 1, pp. 1577–1580, 2018, _eprint: <https://onlinelibrary.wiley.com/doi/pdf/10.1002/sdtp.12311>. [Online]. Available: <https://onlinelibrary.wiley.com/doi/abs/10.1002/sdtp.12311>
- [58] M. Kielar, O. Dhez, G. Pecastaings, A. Curutchet, and L. Hirsch, “Long-Term Stable Organic Photodetectors with Ultra Low Dark Currents for High Detectivity Applications,” *Scientific Reports*, vol. 6, p. 39201, Dec. 2016. [Online]. Available: <https://www.ncbi.nlm.nih.gov/pmc/articles/PMC5177896/>
- [59] D. Tordera, B. Peeters, H. B. Akkerman, A. J. J. M. v. Breemen, J. Maas, S. Shanmugam, A. J. Kronemeijer, and G. H. Gelinck, “A High-Resolution Thin-Film Fingerprint Sensor Using a Printed Organic Photodetector,” *Advanced Materials Technologies*, vol. 4, no. 11, p. 1900651, 2019, _eprint: <https://onlinelibrary.wiley.com/doi/pdf/10.1002/admt.201900651>. [Online]. Available: <https://onlinelibrary.wiley.com/doi/abs/10.1002/admt.201900651>
- [60] F. a. F. Fraga, S. T. G. Fetal, M. M. F. R. Fraga, E. F. S. Balau, L. M. S. Margato, R. F. Marques, A. J. P. L. Policarpo, and F. Sauli, “The scintillation of GEMS coated with wavelength shifters,” *Nuclear Instruments and*

- Methods in Physics Research. Section A, Accelerators, Spectrometers, Detectors and Associated Equipment*, vol. 525, no. 1-2, pp. 57–61, 2004. [Online]. Available: http://inis.iaea.org/Search/search.aspx?orig_q=RN:36015092
- [61] M. Nag, R. Muller, S. Steudel, S. Smout, A. Bhoolokam, K. Myny, S. Schols, J. Genoe, B. Cobb, A. Kumar, G. Gelinck, Y. Fukui, G. Groeseneken, and P. Heremans, “Low-temperature formation of source–drain contacts in self-aligned amorphous oxide thin-film transistors,” *Journal of Information Display*, vol. 16, pp. 1–7, May 2015.
- [62] A. Sato, K. Abe, R. Hayashi, H. Kumomi, K. Nomura, T. Kamiya, M. Hirano, and H. Hosono, “Amorphous In–Ga–Zn–O coplanar homojunction thin-film transistor,” *Applied Physics Letters*, vol. 94, no. 13, p. 133502, Mar. 2009, publisher: American Institute of Physics. [Online]. Available: <https://aip.scitation.org/doi/10.1063/1.3112566>
- [63] A. J. J. M. van Breemen, R. Ollearo, S. Shanmugam, B. Peeters, L. C. J. M. Peters, R. L. van de Ketterij, I. Katsouras, H. B. Akkerman, C. H. Frijters, F. Di Giacomo, S. Veenstra, R. Andriessen, R. A. J. Janssen, E. A. Meulenkamp, and G. H. Gelinck, “A thin and flexible scanner for fingerprints and documents based on metal halide perovskites,” *Nature Electronics*, vol. 4, no. 11, pp. 818–826, Nov. 2021, number: 11 Publisher: Nature Publishing Group. [Online]. Available: <https://www.nature.com/articles/s41928-021-00662-1>
- [64] AnalogDevices. Adas1256 datasheet (pdf) - analog devices. <https://pdf1.alldatasheet.com/datasheet-pdf/view/1007828/AD/ADAS1256.html>. Last accessed 26 October 2020.
- [65] HolstCenter, “Holst centre - the future belongs to those who create it,” <https://www.holstcentre.com/home/>, last accessed 26 October 2020.

Chapter 3

Characterization with X-ray Beams

“Scientists make mistakes. Accordingly, it is the job of the scientist to recognize our weakness, to examine the widest range of opinions, to be ruthlessly self-critical. Science is a collective enterprise with the error-correction machinery often running smoothly.”

Carl Sagan

This chapter presents the characterization of the LaGEMPix prototypes using low-energy X-rays. The spatial resolution measurements for various experimental configurations are described. Firstly, I outline the importance of having a detector with high spatial resolution for radiotherapy. The following section describes the first optical version of the LaGEMPix that has proven to have limited spatial resolution, mainly attributed to the isotropic emission of the scintillation photons within the GEM holes. We conducted a comparative analysis between the prototype, GAFCHROMIC[®] films, and the GEMPix detector in charge readout mode. This research aimed to gain deeper insights into the factors influencing spatial resolution, specifically focusing on setup-related parameters, electron diffusion, and isotropic photon emission. Monte Carlo simulations using the FLUKA code were also performed to understand this effect. The results presented in this section underscore that the first prototype yielded a spatial resolution of a few millimeters. However, there is a clear mandate for further research and development to align this technology with the stringent requirements of QA in radiotherapy. To this end,

several promising avenues of investigation were explored in the pursuit of enhanced spatial resolution.

In the subsequent Section 3.4, the outcomes obtained from an advanced, upgraded optical detector prototype are shown. To improve the spatial resolution and confirm our predictions of the role of the photons, we built a new version of the detector with a reduced gap between the last GEM foil and the readout. Demonstrating that isotropic photon emission stands as the main bottleneck to superior spatial resolution, our quest for a solution has led us to consider charge readout for the latest prototype.

The Section 3.5 of this chapter showcases the promising results derived from the charge readout approach, which captures secondary electrons produced by the GEMs with a submillimeter spatial resolution. By conducting an extensive study on spatial resolution and exploring novel approaches, we designed a prototype detector with high spatial resolution and online readout, features that can potentially have applications in the field of radiotherapy and, in particular, hadron therapy.

3.1 Precision in Radiotherapy: The Crucial Role of Spatial Resolution

In QA procedures in hadron therapy, the precision of dose calculations holds paramount significance, while equally imperative is the verification of measurements through devices boosting exceptional spatial resolution. Achieving this level of accuracy demands the use of high-resolution instruments [1].

In the context of Pencil Beam Scanning (PBS) treatment plans, which often exhibit extremely steep dose gradients within the treatment field, having a high spatial resolution in the 2D dose distribution is of utmost significance. For a detailed explanation of how accuracy plays a crucial role in hadron therapy and how even slight target-depth inaccuracies with protons or carbon ions can result in significantly more critical errors than with photons see Subsection 1.4.1. These steep gradients are characterized by distal falloff values, represented as the distance between the distal positions where the dose levels drop from 80% to 20% (z80-20). In the realm of intensity-modulated proton therapy, these values can reach as low as 4 mm,

corresponding to a gradient of 15% per millimeter [2, 3]. Therefore, the accurate delivery of the prescribed dose precisely where it is intended while sparing healthy tissue is critical.

To gauge the resolution of the LaGEMPix detector, it is relevant to compare it with commercially available 2D detectors, staying in line with the definitions used by manufacturers and medical physicists. For instance, PTW employs the distance between ionization chambers to define the spatial resolution of their 2D arrays. In contrast, IBA's detectors specify spatial resolution in terms of pixel size for systems like myQA[®] SRS* and Lynx, or as pixel pitch for Giraffe [4, 5]. At hadron therapy facilities, dosimetry equipment's spatial resolution is typically provided by the manufacturer [6, 7, 8].

It is imperative to note that the pixel size or pitch imposes limitations on the system's spatial resolution and is not the sole factor influencing its effective measured value. ISO 12233:2023¹ underscores the multifaceted nature of the term "spatial resolution", emphasizing that it is often misconstrued as merely the count of addressable photoelements. Spatial resolution, as defined by ISO 12233:2023, refers to the system's ability to discriminate objects situated within a certain proximity to each other. The visual resolution is explained as the maximum spatial frequency at which the human eye can no longer distinguish individual black and white lines in a test pattern, denoting a Modulation Transfer Function (MTF) of approximately 10–20% [9].

To assess the effective spatial resolution of LaGEMPix, three methods were employed. The first method was rooted in the Edge Spread Function (ESF), depicting the system's response to a sharp edge or discontinuity. The second method involved the Line Spread Function (LSF), which assessed the system's capability to differentiate adjacent points, typically using copper masks with varying hole separations. Lastly, a lead test pattern mask was applied to evaluate the MTF of the system.

One common approach involves estimating spatial resolution via the ESF method, where a high-resolution system demonstrates a well-defined edge with minimal blurring. In this case, the projection of a 2.5 cm thick lead block's straight edge was measured, aiming for an intensity distribution resembling a step-like function. The Full Width at Half Maximum (FWHM) of the edge response was often quoted as the typical value. This value can be

¹ISO 12233:2023: "Photography - Electronic still picture imaging - Resolution and spatial frequency responses"

calculated by fitting the ESF with a logistic (Fermi) function (Equation 3.1), allowing a precise determination of FWHM [10, 11, 12].

$$ESF = a + \frac{b}{1 + \exp(-c(d - x))} \quad (3.1)$$

Where a is the offset, b is the contrast, c is the steepness and d is the centroid of the edge. The FWHM can be calculated from the fit parameters, using the relation $FWHM = 3.53/c$ [13].

The other two methods, LSF and MTF, were also applied to characterize the imaging sensors. These methods employed specialized radiation-opaque plates featuring various absorbent structures to gauge the system's ability to resolve adjacent holes or lines. For LSF, copper plates with different thicknesses and hole patterns were used [14], while for MTF, a lead mask with a bar pattern was employed while using the following equation:

$$MTF(f) = \frac{C(f)}{C(0)}; C(f) = \frac{I_{max}(f) - I_{min}(f)}{I_{max}(f) + I_{min}(f)} \quad (3.2)$$

where $I_{max}(f)$ and $I_{min}(f)$ are the maximum and minimum pixel values for a pattern with spatial frequency f respectively. $C(0)$ is the normalization factor at zero frequency, which has to be approximated in practice by using pixel intensities of a large bar and of adjacent background. Detailed results and discussions of the ESF, LSF, and MTF methods are presented in Subsections 3.2.1, 3.2.2 and 3.2.3, respectively.

3.2 Optical Readout: Gas Electron Multiplier (GEM)-Organic Photodiode (OPD) Array Detector

The evaluation of spatial resolution in the LaGEMPix system with an optical readout, GEM-OPD, was conducted using 40 kV X-rays sourced from the X-ray generator model X80-320kV by Hopewell Designs, Inc. This assessment adhered to the ISO 4037 standard [15] through the utilization of a system equipped with 10 Narrow Spectra Filters (N-series), with a specific focus on the selection of the Hopewell N-6 filter, which corresponds to the N-40 ISO 4037

standard.

The X-ray generator features a collimation system encompassing an external wheel positioned outside the protective enclosure, which serves as a holder containing various filters. This system offers a range of beam apertures, with diameters spanning from 1 cm to 7 cm. Additionally, the generator is equipped with an irradiation bench, complete with a movable platform, facilitating automated positioning and control over exposure settings. To ensure optimal alignment, the LaGEMPix was situated perpendicularly to the X-ray beam within a purpose-built vertical structure, securely placed atop the platform. The setup was further shielded from ambient light by a black covering. The assembly was positioned on the irradiation bench, with careful consideration given to Y (horizontal and perpendicular to the beam) and Z (vertical and perpendicular to the beam) positions, to ensure the center of the imager aligned precisely with the center of the X-ray beam. To achieve a nearly parallel X-ray beam, irradiations were carried out at a distance of 230 cm, using a 1 cm aperture.

In the data acquisition process, the readout was configured at the highest sensitivity level of 0.5 pC, ensuring that the Least Significant Bit (LSB) of the 16-bit readout represented an approximate charge of 50 electrons. The frame rate, which dictates the frequency at which consecutive images are recorded, was set at 1 frame per second (fps).

To mitigate the potential impact of undesirable factors like readout inhomogeneities or noise, a per-pixel threshold was applied, and any dead pixels were systematically eliminated. A background image was derived through the averaging of pixel values over 200 background frames. Subsequently, each image underwent offline processing, involving background subtraction. The final image was then obtained by averaging pixel values across 200 background-corrected images. For further analysis, a Region of Interest (ROI) was defined, as elaborated in Sections 3.2.1 and 3.2.2.

3.2.1 Edge Spread Function

To assess the spatial resolution through the edge response technique, we positioned a lead block with dimensions of $10 \times 20 \times 2.5 \text{ cm}^3$ in front of the detector, partially covering its active surface, as illustrated in Figure 3.1a. It is worth noting that this detector prototype was conceived as a proof of concept and exhibited some imperfections in its readout matrix due to

manufacturing issues in the fan-out region adjacent to the detector’s active area. Particularly, there were occurrences of disconnected lines in the backplane, making them unreadable. These anomalies manifest as non-functional horizontal and vertical black lines in the readout image shown in Figures 3.1b, 3.3b and 3.5b. To mitigate these imperfections, we defined a ROI delineated by a green rectangle, selecting an area of the readout with the least number of defects.

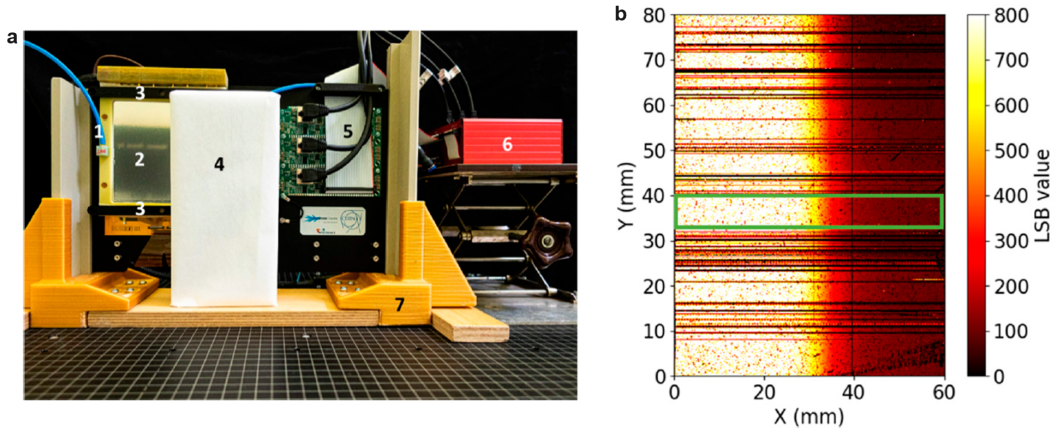


Figure 3.1: a. The LaGEMPix with a lead block, 2.5 cm in thickness, positioned in front of the detector: (1) gas outlet; (2) the $100 \times 100 \text{ mm}^2$ triple-GEM stack coupled to the optical readout with the thin Mylar window on top; (3) 3D-printed braces to hold together the triple-GEM detector and the image sensor; (4) lead block; (5) cables to connect the detector to the readout system; (6) FPGA module; (7) custom-made support. b. A heatmap representing the detector’s image following exposure to 40 kV X-rays.

Figure 3.2 shows the edge response generated by averaging the pixel values within the same column from the background-subtracted image. Additionally, this figure includes a fit performed using a logistic function in accordance with Equation 3.1. The FWHM determined through this methodology amounts to $9.70 \pm 0.09 \text{ mm}$.

3.2.2 Line Spread Function

In order to evaluate the LSF response, we employed a 3 mm thick copper plate positioned at a distance of 7 mm from the Mylar window, as depicted in Figure 3.3a. This copper plate featured a series of holes, each 5 mm in diameter, arranged in a manner such that they were

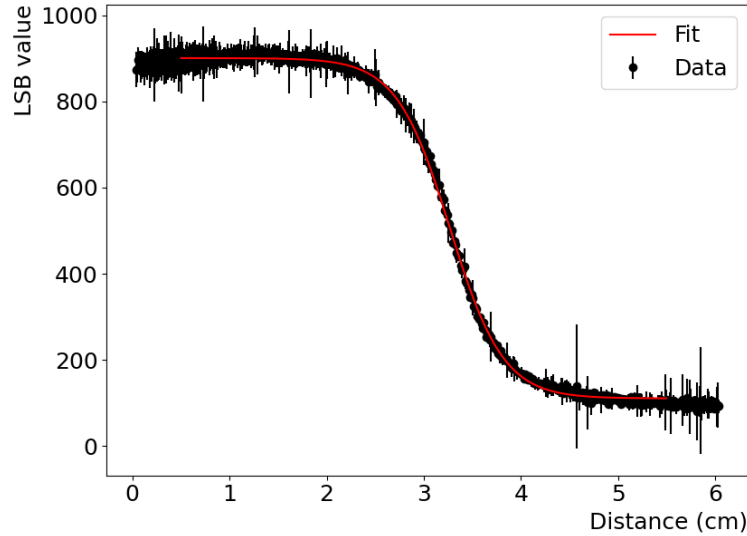


Figure 3.2: Profile depicting the response at the edge when exposed to 40 kV X-rays, using a 2.5 cm thick lead block. The data is fitted with a logistic function, as indicated by the red line.

spaced 3 to 7 mm apart, edge to edge. The individual image profiles of these 5 mm diameter holes exhibited a Gaussian distribution. Consequently, we estimated the spatial resolution by fitting this distribution with a Gaussian function. The outcome of this analysis yielded a FWHM of 6.73 ± 0.08 mm for the 5 mm diameter hole.

To further investigate the resolution, we conducted an additional measurement within a ROI marked by the green region in 3.3b, focusing on the central area of the 5 mm holes spaced 3 mm apart. In Figure 3.4, we present the response from two holes positioned closely, with their edges just 3 mm apart, demonstrating two distinct peaks and a noticeable dip in intensity. This response was obtained by averaging the pixel values within the same column from the background-subtracted image.

Applying the FWHM criterion, which dictates that the minimum resolvable distance for any detector corresponds to the FWHM of the Gaussian distribution, we observed that the center-to-center distance between the holes, measuring 8 mm, is greater than the FWHM, which measures 7.10 ± 0.30 mm. Consequently, these two adjacent holes meet the criteria for being resolved.

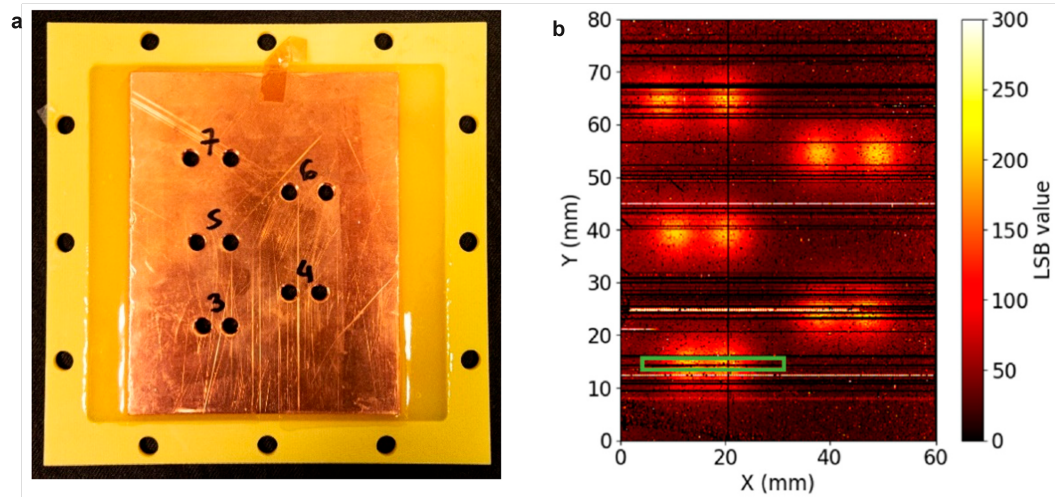


Figure 3.3: a. A 3 mm copper plate was employed to assess spatial resolution using the LSF method, with numbers indicating the millimeter spacing between holes. b. Heatmap representation of the copper mask subjected to 40 kV X-rays. A ROI marked by a green rectangle was defined for holes spaced 3 mm apart. Spatial resolution was calculated by fitting the ROI's profile with a Gaussian function.

3.2.3 Modulation Transfer Function

The MTF serves as a critical metric for gauging how accurately the spatial frequency characteristics of an object are faithfully replicated in an image, as detailed in [16]. According to the standards set forth in ISO 1233:2017, MTF analysis typically involves the presentation of results in graphical form. Nonetheless, one can also utilize summary resolution metrics, where the limiting spatial resolution stands out as a key parameter. This limiting spatial resolution is defined as the frequency at which the MTF falls below a specific percentage threshold. While various threshold values can be employed for this purpose, the 10% threshold is the most commonly used, as attested in [17, 18, 19].

When assessing the GEM -OPD MTF, we employed a Line Pair mask of type 53, which is depicted in Figure 3.5 and positioned in front of the Mylar window. This X-ray test pattern comprises a 0.05 mm thick lead material and encompasses a resolution range spanning from 0.5 to 10 line pairs per millimeter (LP/mm). To provide a clearer contrast in the output image, we conducted this specific test using 30 kV X-rays in conjunction with the

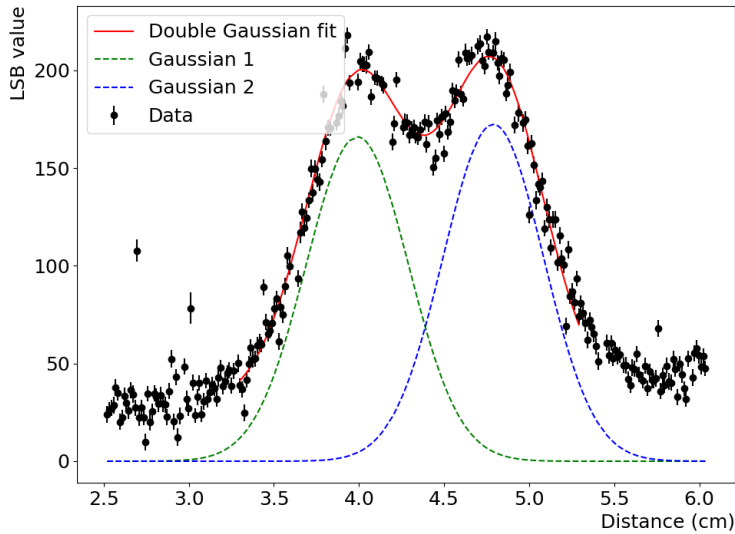


Figure 3.4: The response profile represents the average response along a line for holes with a diameter of 5 mm, positioned 3 mm apart from each other (edge to edge). The FWHM derived from the Gaussian distribution is 7.10 ± 0.30 mm for the left hole and 6.80 ± 0.20 mm for the right hole. By employing a double Gaussian function, the distance between their centers was determined to be 7.98 mm.

N-5 filter, rather than the customary 40 kV. The image displayed in Figure 3.5 illuminates that the measurement of the LaGEMPix MTF using this mask is not feasible. The present version of the LaGEMPix system cannot distinguish spatial frequencies as low as 0.5 LP/mm, corresponding to two slits separated by a 2 mm interval.

3.3 Comparison with Other Detectors and Simulation

3.3.1 GAFCHROMIC[®] Films

To investigate factors unrelated to the detector itself, we employed an 'ideal' system characterized by a well-defined spatial resolution, which is represented by high-resolution GAFCHROMIC[®] films. Film dosimetry is often regarded as the benchmark for 2D dosimetry, as acknowledged in reference [7]. In our study, we specifically utilized GAFCHROMIC[®] XR-SP2 films, suitable for X-ray energies ranging from 20 kV to 200 kV and capable of measuring

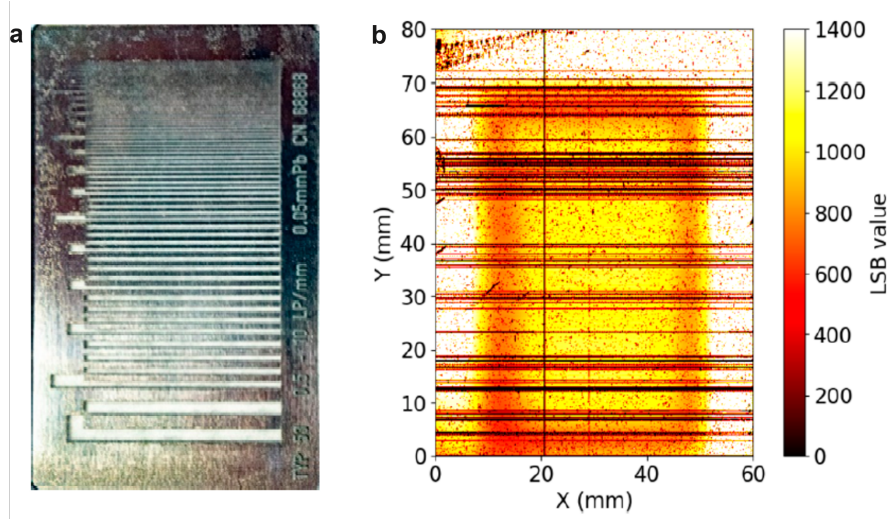


Figure 3.5: a. A lead-made imaging target in the form of a 0.05 mm lead thickness line pair mask of type 53. b. Heat map illustrating the condition of the MTF mask following exposure to 30 kV X-rays.

doses within the range of 0.5 mSv to 100 mSv. The calibration of these films was executed at the Institute of Radiation Physics (IRA) in Lausanne, Switzerland, as described in [20].

To ensure the integrity of our experimental conditions, we mirrored the parameters employed in the LaGEMPix measurements. In the edge response method, as detailed in Subsection 3.2.1, we positioned a $10 \times 20 \times 2.5 \text{ cm}^3$ lead block, covering a designated portion of the film. For the LSF response, we replicated the setup outlined in Subsection 3.2.2, where a 3 mm thick copper plate featuring 5 mm diameter holes was positioned in front of the film. The digitization of the films was carried out using an EPSON V800 scanner. The results obtained using the edge response method indicated a FWHM of $0.86 \pm 0.07 \text{ mm}$, while the FWHM for a single 5 mm diameter hole was measured at $5.09 \pm 0.03 \text{ mm}$.

A comprehensive summary and analysis of the results, along with a comparison between all the detectors and simulation, are presented and discussed in Section 3.3.4.

3.3.2 GEMPix

To assess the impact of isotropic scintillation light emission on the spatial resolution of the LaGEMPix system, we conducted a comparative study involving the GEMPix system. The GEMPix is a triple-GEM detector measuring $2.8 \times 2.8 \text{ cm}^2$ in size and employs a Timepix quad ASIC for direct charge readout, as detailed in [21, 22]. The experimental conditions for both systems were meticulously matched. These conditions encompassed the use of 40 kV X-rays in conjunction with the N-6 series filter, a minimum aperture of 1 cm, a source-detector distance of 230 cm, and maintaining identical electric field settings within the GEM structure.

Edge Spread Function (ESF)

When examining the edge response, we positioned the 2.5 cm thick lead block in precisely the same location as employed in the measurement with the LaGEMPix, as depicted in Figure 3.1. A ROI delineated by the green region was established, oriented perpendicular to the edge. In Figure 3.6, we present the edge response profile, computed by averaging 200 equalized images, as previously detailed. To gauge the spatial resolution, we applied a logistic function, as outlined in Equation 3.1, to fit the edge profile. The result for the FWHM achieved with the GEMPix system stands at $5.20 \pm 0.10 \text{ mm}$.

Line Spread Function (LSF)

We conducted an investigation into the spatial resolution using the LSF method with the GEMPix system, employing two copper plates of varying thicknesses and hole patterns. To image holes with a diameter smaller than 5 mm, we utilized a 1 mm thick plate positioned in front of the GEMPix. Notably, the results obtained with this mask in conjunction with the LaGEMPix system are not covered within this section, as they did not yield any additional insights. The mask itself featured a total of 23 holes, varying in size and spacing.

In Figure 3.7, we present the results stemming from the three 1.3 mm diameter holes, spaced just 1 mm apart (edge to edge). Employing the FWHM criterion outlined in Subsection 3.2.2, we can confidently assert that two holes, each with a diameter of 1.3 mm and separated by a mere 1 mm (edge to edge), can be effectively resolved. When we employed the 3 mm thick

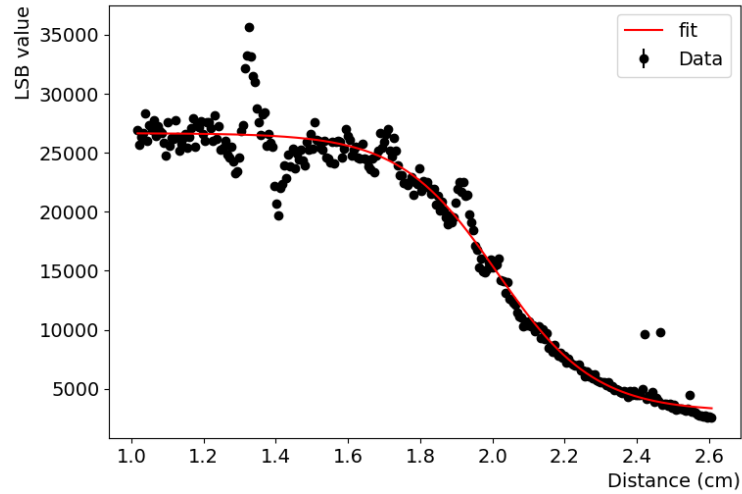


Figure 3.6: Profile showing the edge response when employing the GEMPix detector with 40 kV X-rays, facilitated by a 2.5 cm thick lead block. The data is fitted with a logistic function, illustrated by the red line. The variations observed at approximately 1.4 cm are attributed to the Timepix chip intersections.

copper plate with 5 mm diameter holes, we observed a spatial resolution of 5.23 ± 0.05 mm (FWHM). A concise summary of the outcomes obtained via the LSF method can be found in Table 3.1.

Table 3.1: FWHM values were computed for 1D profiles in three specific regions of interest within the images captured using the GEMPix and the 1 mm-thick copper plate.

\emptyset Hole	FWHM (mm)		
	Hole 1	Hole 2	Hole 3
6 mm	6.60 ± 0.10	-	-
3 mm	3.08 ± 0.06	3.04 ± 0.09	3.46 ± 0.09
1.3 mm	2.07 ± 0.05	1.49 ± 0.03	1.85 ± 0.03

Modulation Transfer Function (MTF)

As for the LaGEMPix system, a series of measurements was conducted employing the lead mask model 53, a comparison of which can be seen in Figure 3.5 and Figure 3.8. In contrast to the LaGEMPix, the GEMPix system exhibited an MTF falling below the 10% threshold at

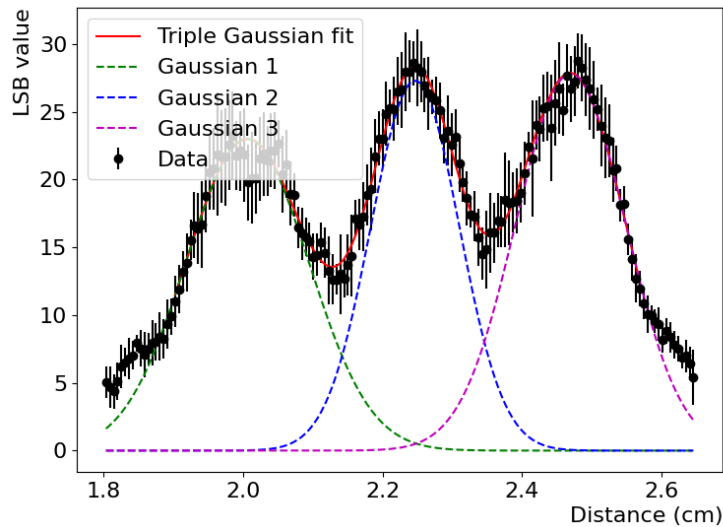


Figure 3.7: The response profile of the GEMPix detector, representing the average response along a line, pertains to holes with a diameter of 1.3 mm, positioned 1 mm apart from each other (edge to edge). To calculate the FWHM for the three holes (as specified in Table 3.1), the profile was subjected to a fitting process utilizing a triple Gaussian function.

1.4 line pairs per millimeter (LP/mm), equivalent to 0.71 mm. This achievement attests to the successful realization of submillimeter spatial resolution, aligning with our intended target. The normalized MTF, computed using Equation 3.2, is graphically represented in Figure 3.9.

3.3.3 FLUKA Simulations

A simulation of the LaGEMPix system was conducted using the FLUKA Monte Carlo code version 4-0.1, employing default settings under the PRECISIO mode [23, 24, 25]. The primary objective of this simulation was to investigate the energy deposition within the active region of the detector while also assessing its spatial resolution through the employment of the ESF and LSF methods.

To enhance the precision of energy deposition calculations, specific transport and production energy cutoffs of 1 keV were applied to electrons, positrons, and photons in all regions. Additionally, the simulation leveraged the single-scattering algorithm (via the MULSOPT card) for all charged particles. This was instrumental in mitigating the challenges associated

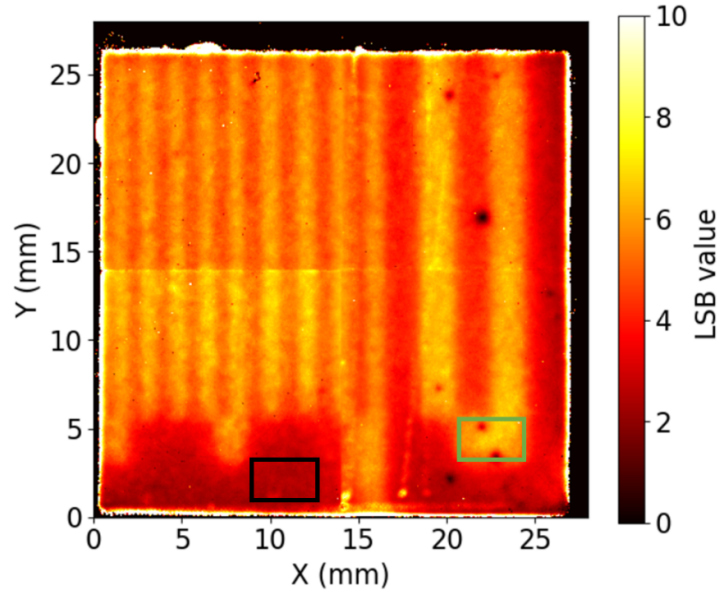


Figure 3.8: Heat map representation generated by irradiating the GEMPix with 30 kV X-rays, employing a line pair mask of type 53 as the imaging target. To calculate the normalization factor $C(0)$ in Equation 3.2, two distinct regions were identified: the upper region within a green rectangle, corresponding to maximum pixel intensities, and a lower region enclosed by a black rectangle, indicating the minimum values.

with low-energy primary photons and bolstering transport accuracy within the exceedingly thin layers of gaseous and heavy materials inherent in the LaGEMPix geometry.

The simulation reproduced the detector's intricate geometry, encompassing the triple-GEM stack, the image sensor, and the associated peripheral electronics, as detailed in Figure 3.10. To account for the spectral distribution of the X-ray beam, a user-defined source routine was incorporated due to the absence of specific information regarding the X-ray tube head. However, certain contributions resulting from scattered photons in the target or surrounding materials, which naturally occur in the X-ray beam, were not considered due to insufficient information.

It is important to clarify that the simulation was not intended to replicate experimental results precisely but rather to aid in assessing the factors impacting spatial resolution within the detector and the experimental conditions. Consequently, intricacies such as electron

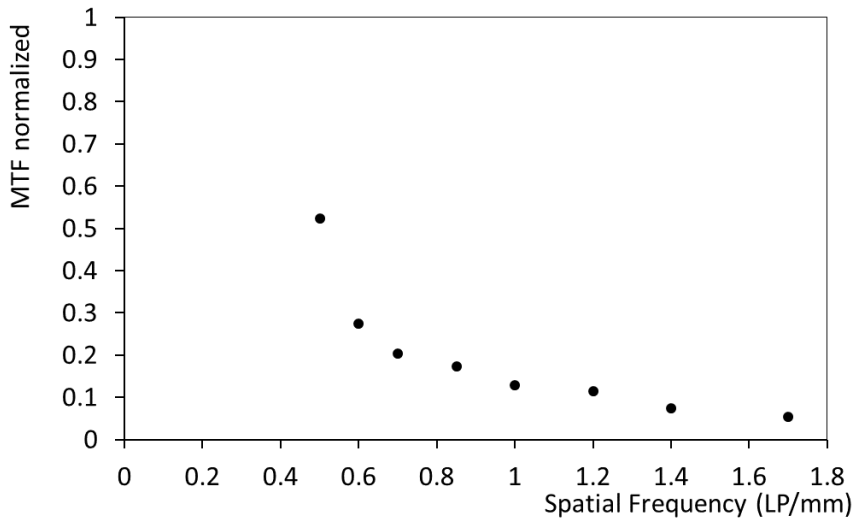


Figure 3.9: MTF as determined for the GEMPix detector utilizing equation 3.2, with the measurement conducted using mask type 53.

diffusion in the gas volume, electron recombination with positive ions, impurity absorption, electron amplification in the GEM holes, and scintillation light emission were not included in the simulation.

The number of photons detected by the LaGEMPix OPD matrix is proportional to the secondary electrons generated within the GEMs. This, in turn, is directly related to the energy deposited in the gas during the primary ionization process. Therefore, the energy deposited by the X-ray photons within the gas volume of the detector offers a rough approximation of the image produced by the scintillation photons captured by the image sensor.

To factor in the influence of primary ionizations in distinct gas regions and the effective gain for each GEM foil on the resulting image, the simulation incorporated an image generated through the average deposited energy in the drift and transfer gas layers, weighted by the corresponding effective gains. Interactions in the induction gap, which do not generate secondary scintillation photons, were excluded from contributing to the final image. To quantify the results, FLUKA USRBIN scoring was applied across the entire detector volume, and statistical uncertainties were assessed by calculating the standard deviation based on the outcomes of independent simulation runs.

We conducted three simulation sets to make a comparative analysis between the experimental data acquired through the ESF and LSF methods. These simulations encompassed various scenarios, starting with the modeling of a 2.5 cm thick lead block, as outlined in Section 3.2.1. Additionally, we simulated a 3 mm thick copper plate featuring 5 mm diameter holes and a 1 mm thick copper plate (as detailed in Section 3.2.2). The latter exhibited a more intricate structure with 23 holes of varying sizes and spacing, positioned so that the central hole aligned precisely with the image sensor's active area. To maintain consistency, the 3 mm thick plate simulation was carried out at a distance of 7 mm from the Mylar window, while the lead block and the 1 mm thick copper plate were positioned at 4 cm and 3.3 cm from the Mylar window, respectively.

Figure 3.10 illustrates two of these simulated setups, offering a visual representation of the configurations. Figure 3.10a illustrates the setup for the ESF method, while Figure 3.10b shows the setup for the LSF method. Throughout all simulations, we kept the source-detector distance constant at 230 cm, and the collimator aperture remained at a minimum of 1 cm.

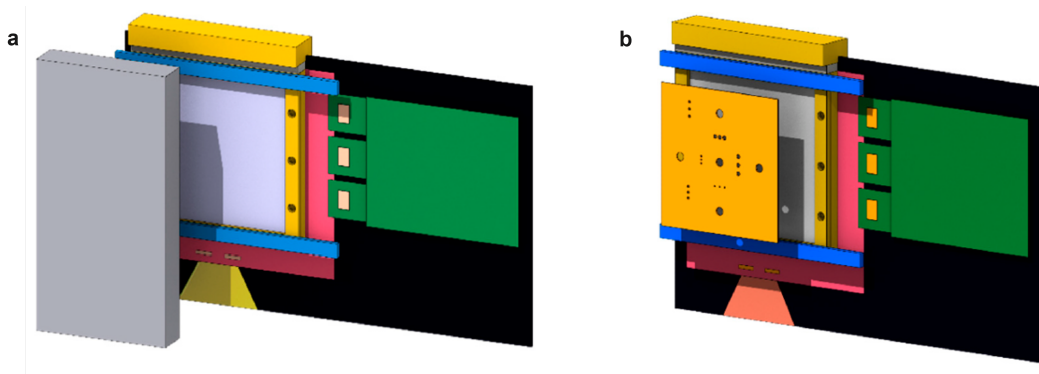


Figure 3.10: The LaGEMPix simulation, featuring a 2.5 cm thick lead block positioned 4 cm away from the Mylar window (a), and a 1 mm thick copper plate located at a distance of 3.3 cm from the Mylar window (b). These visual representations were generated using FLAIR version 3.1-8, the graphical user interface for FLUKA.

Edge Spread Function (ESF)

Figure 3.11 presents the ESF corresponding to 40 kV X-ray imaging. To obtain the ESF, we utilized the technique of projecting the edge profile in a direction perpendicular to the edge

itself. Subsequently, we determined the spatial resolution by fitting the measured ESF with the logistic function described in Equation 3.1. To ensure accuracy, we adjusted the data points, centering the distribution at the midpoint of the image sensor. The bin size used for this analysis was set at $0.25\ \mu\text{m}$, which is twice the size of a single pixel.

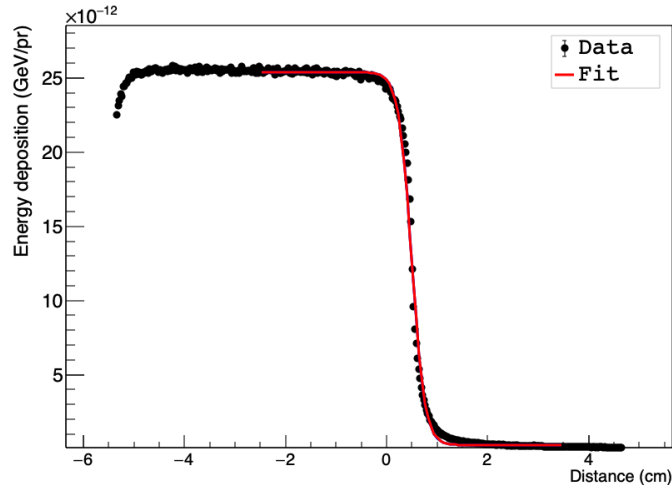


Figure 3.11: Simulated ESF obtained from edge projection and fitted with a logistic function. These results were achieved using 40 kV X-rays, a beam aperture of 1 cm, and a detector-source distance of 230 cm. The error bars are negligible in comparison to the data points.

When we constrained the fitting process to consider the entire active area of the sensor (stretching 6 cm along the x-axis), our estimation of the FWHM yielded a value of $4.53 \pm 0.01\ \text{mm}$. It is important to note that this error margin pertains solely to statistical errors in our simulation.

Line Spread Function (LSF)

The outcomes derived from the LSF method, in conjunction with the utilization of a 1 mm thick copper plate, have been concisely compiled in Table 3.2. The number of primaries was selected to ensure that statistical uncertainties remained below 5%. Our assessment of spatial resolution involved fitting the LSF data with a Gaussian function and measuring the FWHM for various scenarios. These included the central 6 mm diameter holes, the 6 mm hole located at the top of the plate, the set of three 3 mm holes spaced at a 4 mm pitch, and the 1.3 mm

holes separated by a 2.5 mm pitch, as indicated in Figure 3.12.

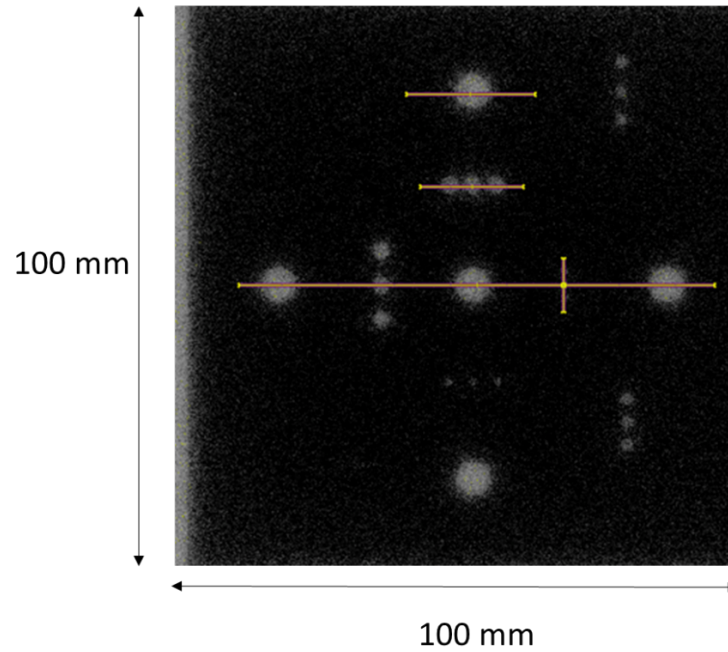


Figure 3.12: Representation of the simulated energy deposition density within the drift gap, with delineated regions for subsequent data analysis identified by solid yellow lines.

Table 3.2: FWHM values were determined from the 1D profiles for the various regions of interest (ROIs) shown in Figure 3.12. The first line of the table corresponds to the three central holes, while the second line pertains to the top hole. The third line refers to the second horizontal line from the top of the figure, while the fourth line pertains to the singular vertical ROI illustrated in Figure 3.12.

Ø Hole	FWHM (mm)		
	Hole 1	Hole 2	Hole 3
6 mm	5.70 ± 0.20	5.45 ± 0.11	5.26 ± 0.12
6 mm	5.82 ± 0.13	-	-
3 mm	2.96 ± 0.17	2.99 ± 0.24	2.82 ± 0.16
1.3 mm	1.32 ± 0.12	1.61 ± 0.16	1.48 ± 0.17

Notably, the profiles for the three 1.3 mm holes, separated by a mere 1 mm (measured from edge to edge), are graphically presented in Figure 3.13. In accordance with the FWHM criterion, these three holes were found to be perfectly resolvable. The calculated hole diameter

was either smaller than or approximately equivalent to the physical hole size, implying that the spatial resolution was superior to the size of the individual holes. These observations were corroborated by similar findings with a 3 mm thick copper plate and 5 mm diameter holes, which yielded a spatial resolution of 4.87 ± 0.03 mm (FWHM).

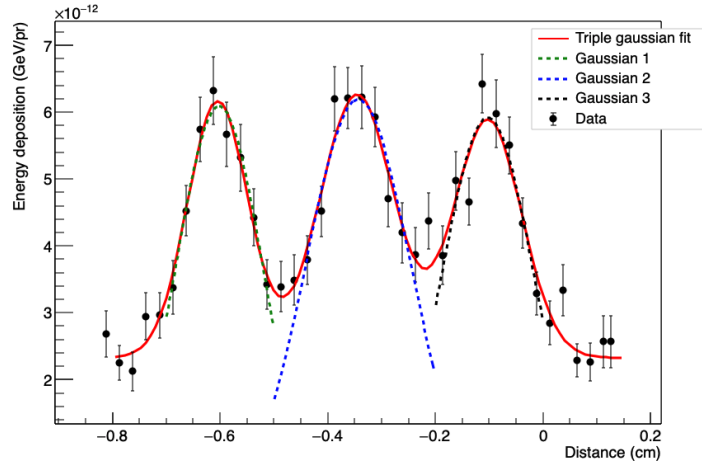


Figure 3.13: One-dimensional projection of the 1.3 mm holes spaced at 2.5 mm intervals. The LSF derived from the chosen region results in a distribution with a mean hole diameter of 1.47 mm.

3.3.4 Discussion on the Spatial Resolution

The spatial resolution of the LaGEMPix system underwent a comprehensive evaluation through a variety of methods and experimental setups, with the resulting data consolidated in Table 3.3. When using the edge response method (ESF), the measurements yielded a spatial resolution of 9.70 ± 0.09 mm for 40 kV X-rays. However, the LSF method revealed that the detector could effectively resolve two 5 mm holes spaced 3 mm apart. This discrepancy suggests that the ESF method, as presented in this study, might be underestimating the true spatial resolution of the LaGEMPix. This also elucidates the reason behind the poorer resolution of the GEMPix detector when using the ESF method, particularly when compared to the outcomes obtained through the LSF and MTF methods. The inherent spatial resolution of the LaGEMPix system is evidently superior to the 9.70 ± 0.09 mm reported by the ESF method. This discrepancy further implies that results derived from these different assessment methods may not be directly

comparable.

Table 3.3: An overview of the spatial resolution achieved with various experimental setups and different detectors, with the addition of FLUKA Monte Carlo simulation results for comparison.

Detector	Spatial Resolution (mm)		
	Edge Response	5 mm Cu Hole	Minimum Resolvable Hole Spacing
LaGEMPix	9.70 ± 0.09	6.73 ± 0.08	3 mm (edge to edge)
GEMPix	5.20 ± 0.10	5.23 ± 0.05	1 mm ¹ (edge to edge)
GAFCHROMIC [®]	0.86 ± 0.07	5.09 ± 0.03	1 mm ¹ (edge to edge)
FLUKA simulation of LaGEMPix	4.53 ± 0.01	4.87 ± 0.03	1 mm ¹ (edge to edge)

¹ minimum distance between holes in the Cu plate.

Furthermore, the MTF measurements only led to the conclusion that slits separated by a 2 mm distance could not be differentiated. These findings collectively indicate that the current LaGEMPix design falls short of achieving the criterion for sub-millimeter resolution required for hadron therapy. The precise value of the spatial resolution also appears to depend on the specific evaluation method applied.

To untangle the various sources affecting spatial resolution, including the experimental setup, electron diffusion in the gas, and isotropic photon emission within the detector, measurements were conducted with the GEMPix system and GAFCHROMIC[®] XR-SP2 films. Table 3.3 consolidates the spatial resolution values obtained for different detectors and experimental configurations. As anticipated, the GAFCHROMIC[®] films exhibited the best spatial resolution. The edge response method recorded a resolution of 0.86 mm with the film, compared to 5.20 mm with the GEMPix system. Although minor differences were noted with the LSF method, it is important to note that even with the GEMPix, holes separated by a 1 mm distance remained resolvable. The GEMPix system also displayed an MTF falling below 10% at 1.4 line pairs per millimeter (LP/mm). The ESF of the LaGEMPix and the FWHM of a 5 mm hole were higher when compared to the GEMPix. An additional reduction in spatial resolution was observed with the LaGEMPix, attributed to the isotropic emission of scintillation photons. The results indicated that, with the current LaGEMPix design, holes spaced 1 mm apart could not be resolved, and the MTF method indicated that slits separated by 2 mm were indistinguishable.

Lastly, the findings from a FLUKA Monte Carlo simulation of the LaGEMPix were juxtaposed with experimental data. Notably, the simulation delivered significantly superior resolution, primarily because it did not account for certain phenomena associated with the detector's operational principles, such as the isotropic emission of scintillation photons. However, the simulation's predictions aligned with the results obtained with the GEMPix system, suggesting that (1) the simulation effectively replicated the experimental results when only electrons played a role in the final image, (2) the isotropic emission of scintillation light introduced additional blurring in the image, and (3) other unmodeled effects, like electron diffusion and recombination, appeared to have minimal impact on spatial resolution. These findings collectively underscore that even for an ideal triple-GEM detector, where only primary energy depositions are considered, sub-millimeter spatial resolution remains elusive. Similar results were observed for 30 kV X-rays, and the edge response method, in particular, seemed to underestimate the detector's resolution, potentially due to the electron mean free path in the gas, introducing an additional blur to the image.

3.4 Optical Readout: Gas Electron Multiplier (GEM) and Organic Photodiode (OPD) Upgraded Version

The emission of photons in an isotropic manner is an inherent phenomenon, and its impact on spatial resolution depends on the distances between photon production and detection points. In our efforts to validate our hypothesis and minimize its effects, we have undertaken a redesign of the LaGEMPix system by reducing the separation between the final GEM (GEM 3) and the readout plane. This alteration is intended to mitigate the dispersion of light before it reaches the readout components.

To realize this adjustment, a novel prototype of the detector has been constructed, featuring a significantly reduced distance between GEM3 and the readout, as illustrated in Figure 3.14. The reduction from 3 mm to 1.5 mm was achieved through two key modifications: firstly, by narrowing the gap between GEM3 and the anode, commonly referred to as the induction gap, from 2 mm to 1 mm, and secondly, by substituting the existing ITO transparent electrode, coated on a 1.1 mm thick fused quartz substrate, with an ITO electrode coated on a 0.5 mm thick fused silica substrate. Importantly, measurements reported in Subsection 2.4.1

and [26] have indicated that the new transparent electrode is more radiation-resistant.

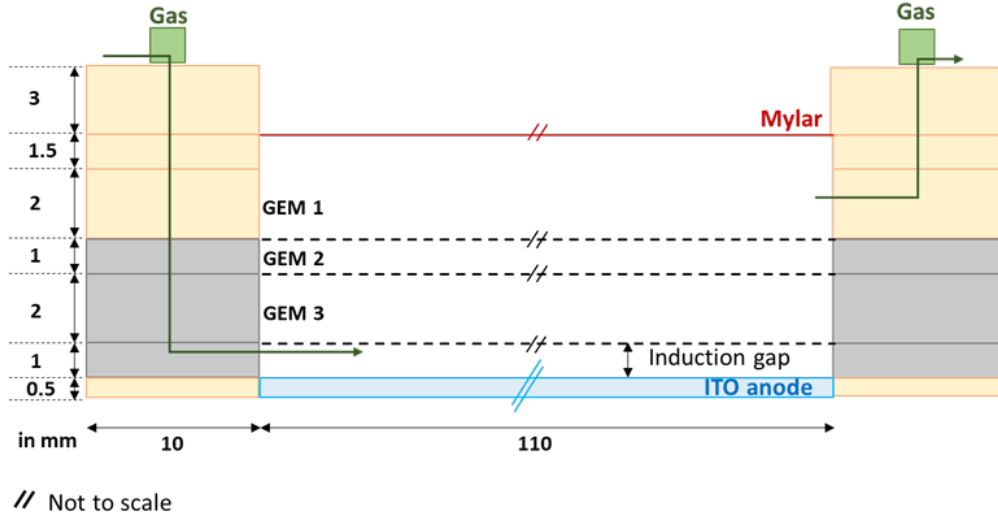


Figure 3.14: Illustration depicting the enhanced setup of the LaGEMPix detector.

It is worth noting that further reductions in these distances were constrained by mechanical considerations. Employing a glass substrate thinner than 0.5 mm would render it exceedingly fragile, leading to complications during production, coating, and assembly procedures. Moreover, the possibility of a slight bend in the last GEM surface had to be taken into account to prevent contact with the ITO anode.

The experimental conditions closely mirrored those detailed in a prior Section 3.2, encompassing the use of either 30 kV (with an N-5 series filter) or 40 kV X-rays (with an N-6 series filter). These X-ray beams featured a minimum aperture of 1 cm and were projected from a source-detector distance of 230 cm. The electric fields within the GEM structure remained consistent throughout, with specific values maintained: the transfer field 1 at 2.0 kV/cm, transfer field 2 at 1.75 kV/cm, induction field at 5.0 kV/cm, and drift field at 1 kV/cm.

It is important to note that the electric fields applied between the top and bottom copper layers within each GEM foil remained unaltered, corresponding to a constant total voltage of 940 V.

3.4.1 Modulation Transfer Function

These assessments were conducted employing 30 kV X-rays, utilizing the N-5 filter to enhance the image contrast significantly. The test involved the use of another lead mask, 0.2 mm thick, featuring a high resolution with a range of resolutions spanning from 0.177 to 3.33 Line Pairs per millimeter (LP/mm) with the widest line spacing at 2.8 mm [27]. It is a noticeable improvement achieved with the new detector. The upgraded LaGEMPix version successfully discerns 0.21 LP/mm, equivalent to two slits separated by 2.4 mm, marking its enhanced performance. A limitation becomes evident at 0.25 LP/mm (two slits separated by 2 mm). In contrast, the original LaGEMPix version proved incapable of resolving 0.177 LP/mm, corresponding to two slits separated by 2.8 mm.

3.4.2 Line Spread Function

The upgraded version of the detector delivers an improved spatial resolution, as evidenced when applying the LSF analysis. To gauge this resolution, the LSF was fitted with a Gaussian function, and the FWHM was determined for a 5 mm diameter hole. Notably, the FWHM obtained using the latest iteration of LaGEMPix stands at 5.61 ± 0.14 mm, surpassing the previously measured value of 6.73 ± 0.08 mm.

Furthermore, to assess the system's performance, a ROI was pinpointed at the center of 5 mm holes spaced 3 mm apart (as illustrated by the green area in Figure 3.15a). Figure 3.15b) offers a side-by-side comparison of the line-average response profiles for two holes separated by 3 mm, highlighting the presence of two peaks with a dip in intensity. Both the original and upgraded versions of LaGEMPix exhibited the ability to resolve two 5 mm diameter holes positioned 3 mm apart. However, the Figure 3.15b reveals a more pronounced dip in intensity for the upgraded LaGEMPix, signifying an enhancement in LSF performance.

The spatial resolution results for both detectors and experimental setups are summarized in Table 3.4. A comprehensive explanation of the results with ESF and MTF can be found in [28]. As anticipated, the upgraded LaGEMPix, with its redesigned reduced gap, exhibits better spatial resolution than the original version. For a more comprehensive analysis of the distinct methods employed here, please refer to Section 3.2.

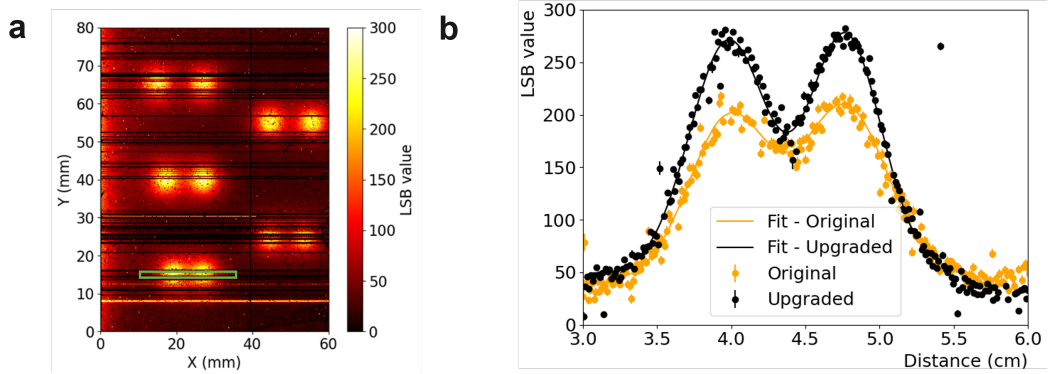


Figure 3.15: a) Heat map representation of the copper mask subjected to 40 kV X-rays, with a designated ROI marked by a green rectangle around the 3 mm spaced holes. The spatial resolution was determined by fitting the profile within the ROI using a Gaussian function. b) The line-average response profiles of 5 mm diameter holes, spaced 3 mm apart (edge to edge), are presented for both the original (depicted in orange) and upgraded (depicted in black) versions of the LaGEMPix. In the case of the upgraded version, the Full Width at Half Maximum (FWHM) measured using Gaussian distribution is 6.16 ± 0.13 mm for the left hole and 5.75 ± 0.15 mm for the right hole. Additionally, the center-to-center distance of 7.86 mm was determined by fitting the profile using a double Gaussian function.

Table 3.4: Overview of the spatial resolution achieved using various experimental setups and both editions of the LaGEMPix.

Detector	Edge Response	5 mm Cu hole	Spatial Resolution (mm)	
			Minimum resolvable hole spacing	MTF mask limit
Original LaGEMPix [11]	9.70 ± 0.09	6.73 ± 0.08	3 mm (edge to edge)	<0.177 LP/mm
Upgraded LaGEMPix	8.17 ± 0.07	5.61 ± 0.14	3 mm (edge to edge)	0.21 LP/mm

3.4.3 Discussion

We have introduced an upgraded version of the LaGEMPix, marked by a halving of the distance between the point where light is generated and the optical readout. Much like the initial prototype, in this study, the detector was subjected to characterization involving low-energy X-rays and a variety of methods designed to assess spatial resolution. The findings presented in this section underscore the significant influence of the separation between the final GEM layer and the image sensor on the measured spatial resolution. This reduction in

the GEM-readout distance has translated into an improved spatial resolution of 0.21 Line Pairs per millimeter (LP/mm), equivalent to two slits positioned 2.4 mm apart in a line pair mask. Nevertheless, it is important to emphasize that reducing the distance between the last GEM and the readout beyond certain limits is not possible due to mechanical limitations, making it extremely challenging to achieve submillimeter spatial resolution for optical readout without the use of optical lenses.

Notably, commercial vendors in the field, such as PTW and IBA, gauge the spatial resolution of their clinical detectors used in hadron therapy using pixel size or pixel pitch. For instance, IBA indicates that the spatial resolution for myQA[®] Phoenix in proton therapy is 0.2 mm [29]. In contrast, the LaGEMPix exhibits a pixel pitch of 126 μm , yielding a spatial resolution of 2.4 mm using X-rays, as elaborated earlier.

As the primary limitation to achieving the desired spatial resolution was identified as the isotropic emission of scintillation light, we implemented charge readout technology. In this scenario, secondary electrons generated within the GEMs and guided by electric fields to maintain spatial resolution would be directly detected by the readout as shown in Figure 3.16. Drawing upon insights from the GEMPix results and the FLUKA Monte Carlo simulation [30], we foresaw that this approach would facilitate achieving the targeted submillimeter resolution.

3.5 Charge Readout: Gas Electron Multiplier (GEM) and Thin Film Transistor (TFT) Array Detector

In the pursuit of developing a charge readout variant of this detector, a significant modification was made by removing the OPD layer, which was originally present in the optical version of LaGEMPix (refer to Subsection 2.5.2 for further details). This strategic alteration resulted in a TFT-only electronic readout system as shown in Figure 3.16.

In order to determine the correct voltage settings for the triple-GEM, it is essential to conduct a gain scan. The response, which is obtained by summing all the pixel values against the sum of the GEM gas amplification voltages, exhibits the expected exponential dependence. This behavior aligns with predictions, as the gain, denoting the ratio of electrons generated to primary electrons, is inherently reliant on the applied GEM voltages [12]. In addition, the

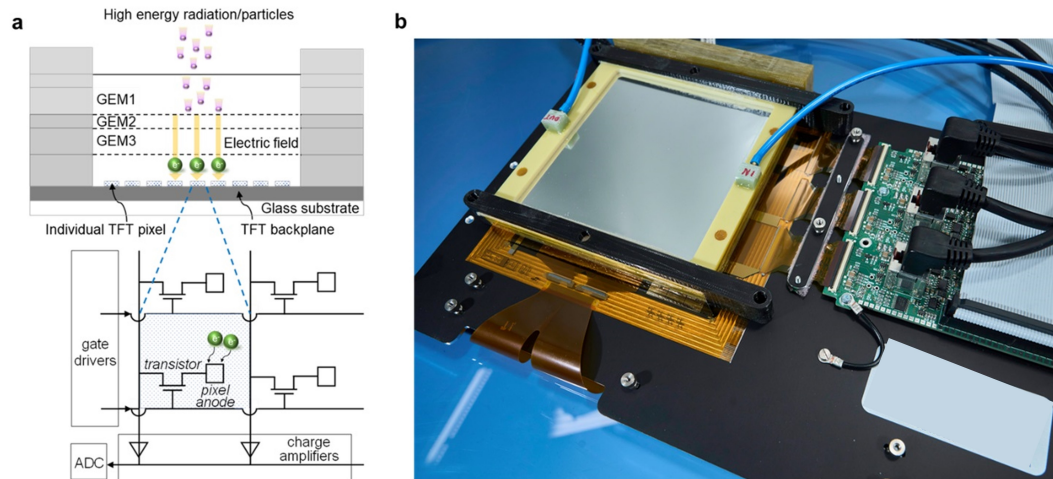


Figure 3.16: The GEM-TFT radiation detector with high-resolution. a. The detector's structure, which includes a TFT backplane array and a triple-GEM frontplane. This depiction highlights the TFT pixel arrangement and the associated drive and read-out circuit diagram. b. A photograph shows the integration of the detector with the read-out electronics.

GEM -TFT detector demonstrates a linear response to dose, which remains consistent up to the maximum current available in the X-Ray generator.

To evaluate the spatial resolution, the MTF was determined by employing a lead mask featuring a bar pattern, a common method for evaluating spatial resolution [31]. This procedure mirrors the one used with our previous optical detector described in Subsection 3.2.3. These assessments were conducted using 30 kV X-rays along with the N-5 filter, enhancing the contrast of the resulting image. The lead mask employed has a thickness of 0.2 mm and offers a resolution ranging from 0.177 to 3.33 line pairs per millimeter (LP/mm), as depicted in Figure 3.17 [32]. The detector demonstrated an MTF of less than 10% at 1.2 LP/mm, corresponding to a spatial resolution of 0.83 mm. This sub-millimeter resolution attests to the exceptional performance of our system when compared to the 2.5 mm resolution of the commercially available OCTAVIUS[®] 1000 SRS detector [33]. The spatial resolution results for both detectors, optical readout versus charge readout, are summarized in Table 3.5.

This novel detector serves as a proof of principle, marking the first instance of radiation detection coupling a gaseous detector with a TFT backplane. The primary aim was to evaluate the feasibility of generating submillimeter spatial resolution images of the radiation

Table 3.5: Comparison of spatial resolution attained with the optical readout versus charge readout.

Detector	Spatial Resolution (mm)	
	Edge response	MTF mask limit
Optical Readout: GEM-OPD	8.17 ± 0.07	0.21 LP/mm
Charge Readout: GEM-TFT	$<0.50 \pm 0.05$	1.2 LP/mm

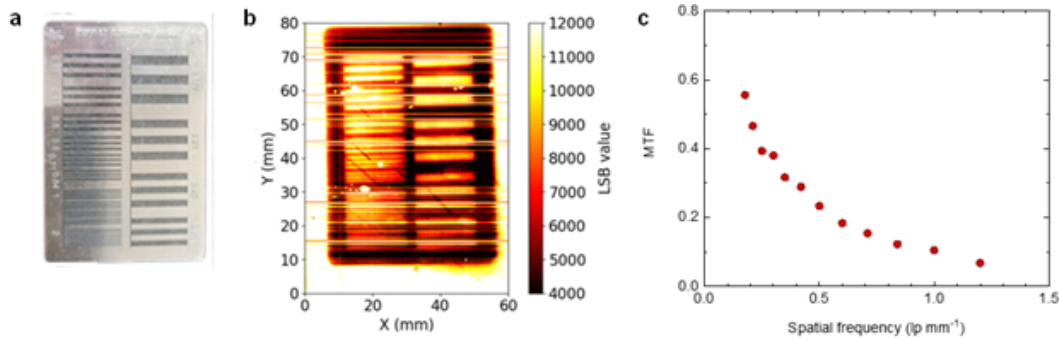


Figure 3.17: Spatial resolution assessment: a. Utilizing a line pair mask of type 17 crafted from 0.02 mm thick lead as the imaging target. b. Displaying a heatmap of the TFT readout following exposure to 30 kV X-rays. c. The MTF measurement was conducted using mask type 17 for the GEM -TFT detector.

beam. Studies using protons, offering a direct comparison with detectors in clinical use, are presented in Chapter 4.

3.6 Conclusions

The prototypes employing optical readout failed to meet the minimum required spatial resolution criteria, highlighting a notable limitation. In contrast, our charge readout system has not only met but exceeded expectations by achieving submillimetric resolution, ensuring the requisite precision and accuracy in our measurements. Furthermore, the evaluation described in this chapter has substantiated the system's robust performance, thereby satisfying the fundamental criteria imperative for progression to the subsequent developmental phase. With the confluence of all essential prerequisites that have been validated, our project was poised for

the critical milestone of clinical beam testing. This pivotal progression significantly advances us towards the realization of practical, real-world applications and the eventual integration of our technology into clinical practice.

Bibliography

- [1] M. Chea, K. Fezzani, J. Jacob, M. Cuttat, M. Croisé, J.-M. Simon, L. Feuvret, C.-A. Valery, P. Maingon, M.-A. Benadjaoud, and C. Jenny, “Dosimetric study between a single isocenter dynamic conformal arc therapy technique and Gamma Knife radiosurgery for multiple brain metastases treatment: impact of target volume geometrical characteristics,” *Radiation Oncology*, vol. 16, no. 1, p. 45, Feb. 2021. [Online]. Available: <https://doi.org/10.1186/s13014-021-01766-w>
- [2] S. Molinelli, A. Mairani, A. Mirandola, G. Vilches Freixas, T. Tessonnier, S. Giordanengo, K. Parodi, M. Ciocca, and R. Orecchia, “Dosimetric accuracy assessment of a treatment plan verification system for scanned proton beam radiotherapy: one-year experimental results and Monte Carlo analysis of the involved uncertainties,” *Physics in Medicine and Biology*, vol. 58, no. 11, pp. 3837–3847, Jun. 2013.
- [3] J. Winter, M. Ellerbrock, O. Jäkel, S. Greilich, and M. Bangert, “Analytical modeling of depth-dose degradation in heterogeneous lung tissue for intensity-modulated proton therapy planning,” *Physics and Imaging in Radiation Oncology*, vol. 14, pp. 32–38, Apr. 2020. [Online]. Available: <https://www.sciencedirect.com/science/article/pii/S2405631620300142>
- [4] “Radiation Therapy - PTW Freiburg GmbH.” [Online]. Available: <https://www.ptwdosimetry.com/en/solutions/radiation-therapy/>
- [5] I. D. GmbH, “IBA Dosimetry,” Feb. 2020. [Online]. Available: <https://www.iba-dosimetry.com/>
- [6] S. Giordanengo and H. Palmans, “Dose detectors, sensors, and their applications,” *Medical Physics*, vol. 45, no. 11, pp. e1051–e1072, 2018, _eprint:

- <https://aapm.onlinelibrary.wiley.com/doi/pdf/10.1002/mp.13089>. [Online]. Available: <https://aapm.onlinelibrary.wiley.com/doi/abs/10.1002/mp.13089>
- [7] L. Grevillot, M. Stock, H. Palmans, J. Osorio Moreno, V. Letellier, R. Dreindl, A. Elia, H. Fuchs, A. Carlino, and S. Vatnitsky, "Implementation of dosimetry equipment and phantoms at the MedAustron light ion beam therapy facility," *Medical Physics*, vol. 45, no. 1, pp. 352–369, Jan. 2018.
- [8] S. Russo, A. Mirandola, S. Molinelli, E. Mastella, A. Vai, G. Magro, A. Mairani, D. Boi, M. Donetti, and M. Ciocca, "Characterization of a commercial scintillation detector for 2-D dosimetry in scanned proton and carbon ion beams," *Physica Medica: European Journal of Medical Physics*, vol. 34, pp. 48–54, Feb. 2017, publisher: Elsevier. [Online]. Available: [https://www.physicamedica.com/article/S1120-1797\(17\)30011-X/fulltext](https://www.physicamedica.com/article/S1120-1797(17)30011-X/fulltext)
- [9] A. Gopal and S. S. Samant, "Validity of the line-pair bar-pattern method in the measurement of the modulation transfer function (MTF) in megavoltage imaging," *Medical Physics*, vol. 35, no. 1, pp. 270–279, 2008, _eprint: <https://aapm.onlinelibrary.wiley.com/doi/pdf/10.1118/1.2816108>. [Online]. Available: <https://aapm.onlinelibrary.wiley.com/doi/abs/10.1118/1.2816108>
- [10] R. Roque, L. Carramate, F. Amaro, H. Natal da Luz, J. Mir, and C. Azevedo, "Spatial resolution properties of krypton-based mixtures using a 100 m thick Gas Electron Multiplier," Jun. 2018.
- [11] J. Jakubek, T. Holy, E. Lehmann, S. Pospisil, J. Uher, J. Vacik, D. Vavrik, and S. Jr, "Properties of neutron pixel detector based on Medipix-2 device," vol. 2, Nov. 2004, p. 949 Vol. 2, journal Abbreviation: Filtration & Separation - FILTR SEP Publication Title: Filtration & Separation - FILTR SEP.
- [12] T. Fujiwara, Y. Mitsuya, T. Fushie, K. Murata, A. Kawamura, A. Koishikawa, H. Toyokawa, and H. Takahashi, "Gas scintillation glass GEM detector for high-resolution X-ray imaging and CT," *Nuclear Instruments and Methods in Physics Research Section A: Accelerators, Spectrometers, Detectors and Associated Equipment*, vol. 850, pp. 7–11, Apr. 2017. [Online]. Available: <https://www.sciencedirect.com/science/article/pii/S016890021730013X>

- [13] “Energy Resolution due to Thermal Broadening (STM),” Oct. 2016. [Online]. Available: <https://shunchi100.wordpress.com/physics-research/energy-resolution-thermal-broadening/>
- [14] M. Alvarez, A. Alves, F. B. Neto, A. L. Pavan, M. Rosa, J. R. d. A. Miranda, and D. R. d. Pina, “Comparison of Bar Pattern and Edge Method for MTF Measurement in Radiology Quality Control,” *Revista Brasileira de Física Médica*, vol. 9, no. 2, pp. 2–5, 2015, number: 2. [Online]. Available: <https://www.rbfm.org.br/rbfm/article/view/329>
- [15] 14:00-17:00, “ISO 12233:2017.” [Online]. Available: <https://www.iso.org/cms/render/live/en/sites/isoorg/contents/data/standard/07/16/71696.html>
- [16] S. N. Ahmed, *Physics and engineering of radiation detection*, 1st ed. Amsterdam ; Boston: Academic Press, 2007, oCLC: ocn122503484.
- [17] J. Seco, M. Oumano, N. Depauw, M. F. Dias, R. P. Teixeira, and M. F. Spadea, “Characterizing the modulation transfer function (MTF) of proton/carbon radiography using Monte Carlo simulations,” *Medical Physics*, vol. 40, no. 9, p. 091717, Sep. 2013.
- [18] M. U. Ghani, Z. Zhou, L. Ren, Y. Li, B. Zheng, K. Yang, and H. Liu, “Investigation of spatial resolution characteristics of an in vivo micro computed tomography system,” *Nuclear Instruments & Methods in Physics Research. Section A, Accelerators, Spectrometers, Detectors and Associated Equipment*, vol. 807, pp. 129–136, Jan. 2016.
- [19] M. Mahesh, *The Essential Physics of Medical Imaging, Third Edition*, Jul. 2013, vol. 40.
- [20] M. Jaccard, K. Petersson, T. Buchillier, C. Bailat, J. Germond, R. Moeckli, J. Bourhis, M. Vozenin, and F. Bochud, “EP-1494: Absolute dosimetry with EBT3 Gafchromic films in a pulsed electron beam at high dose-rate,” *Radiotherapy and Oncology*, vol. 119, p. S690, Apr. 2016.
- [21] J. Leidner, F. Murtas, and M. Silari, “Medical Applications of the GEMPix,” *Applied Sciences*, vol. 11, no. 1, p. 440, Jan. 2021, number: 1 Publisher: Multidisciplinary Digital Publishing Institute. [Online]. Available: <https://www.mdpi.com/2076-3417/11/1/440>
- [22] F. Murtas, “The GEMPix detector,” *Radiation Measurements*, vol. 138, p. 106421, Nov. 2020. [Online]. Available: <https://www.sciencedirect.com/science/article/pii/S1350448720302006>

- [23] “Home | The official CERN FLUKA website.” [Online]. Available: <https://fluka.cern/>
- [24] G. Battistoni, T. Boehlen, F. Cerutti, P. W. Chin, L. S. Esposito, A. Fassò, A. Ferrari, A. Lechner, A. Empl, A. Mairani, A. Mereghetti, P. G. Ortega, J. Ranft, S. Roesler, P. R. Sala, V. Vlachoudis, and G. Smirnov, “Overview of the FLUKA code,” *Annals of Nuclear Energy*, vol. 82, pp. 10–18, Aug. 2015. [Online]. Available: <https://www.sciencedirect.com/science/article/pii/S0306454914005878>
- [25] T. T. Böhlen, F. Cerutti, M. P. W. Chin, A. Fassò, A. Ferrari, P. G. Ortega, A. Mairani, P. R. Sala, G. Smirnov, and V. Vlachoudis, “The FLUKA Code: Developments and Challenges for High Energy and Medical Applications,” *Nuclear Data Sheets*, vol. 120, pp. 211–214, Jun. 2014. [Online]. Available: <https://www.sciencedirect.com/science/article/pii/S0090375214005018>
- [26] A. M. Oliveira, S. Braccini, P. Casolaro, N. Heracleous, J. Leidner, I. Mateu, F. Murtas, and M. Silari, “Radiation-induced effects in glass windows for optical readout GEM-based detectors,” *arXiv:2106.04645 [physics]*, Jun. 2021, arXiv: 2106.04645. [Online]. Available: <http://arxiv.org/abs/2106.04645>
- [27] M. Kielar, O. Dhez, G. Pecastaings, A. Curutchet, and L. Hirsch, “Long-Term Stable Organic Photodetectors with Ultra Low Dark Currents for High Detectivity Applications,” *Scientific Reports*, vol. 6, no. 1, p. 39201, Dec. 2016, bandiera_abtest: a Cc_license_type: cc_by Cg_type: Nature Research Journals Number: 1 Primary_atype: Research Publisher: Nature Publishing Group Subject_term: Electrical and electronic engineering;Optoelectronic devices and components Subject_term_id: electrical-and-electronic-engineering;optoelectronic-devices-and-components. [Online]. Available: <https://www.nature.com/articles/srep39201>
- [28] A. M. Oliveira, H. B. Akkerman, S. Braccini, A. J. van Breemen, L. G. Manzano, N. Heracleous, I. Katsouras, J. Leidner, F. Murtas, B. Peeters, and M. Silari, “A Large Area GEMPix detector for treatment plan verification in hadron therapy,” *Journal of Physics: Conference Series*, vol. 2374, no. 1, p. 012177, Nov. 2022. [Online]. Available: <https://iopscience.iop.org/article/10.1088/1742-6596/2374/1/012177>
- [29] IBA dosimetry: myQA® phoenix - digital detector array. [Online]. Available: <https://www.iba-dosimetry.com/product/myqa-phoenix/>

- [30] A. Maia Oliveira, H. B. Akkerman, S. Braccini, A. J. J. M. van Breemen, L. Gallego Manzano, N. Heracleous, I. Katsouras, J. Leidner, F. Murtas, B. Peeters, and M. Silari, "Characterization with X-rays of a Large-Area GEMPix Detector with Optical Readout for QA in Hadron Therapy," *Applied Sciences*, vol. 11, no. 14, p. 6459, Jan. 2021, number: 14 Publisher: Multidisciplinary Digital Publishing Institute. [Online]. Available: <https://www.mdpi.com/2076-3417/11/14/6459>
- [31] S. N. Friedman, G. S. K. Fung, J. H. Siewerdsen, and B. M. W. Tsui, "A simple approach to measure computed tomography (CT) modulation transfer function (MTF) and noise-power spectrum (NPS) using the American College of Radiology (ACR) accreditation phantom," *Medical Physics*, vol. 40, no. 5, p. 051907, May 2013. [Online]. Available: <https://www.ncbi.nlm.nih.gov/pmc/articles/PMC3643984/>
- [32] "Line Pair Patterns - Test Phantoms | QUART X-Ray QA QC Solutions." [Online]. Available: <https://quart.de/en/products/test-phantoms/resolution-patterns/line-pair-patterns>
- [33] "OCTAVIUS 4D QA Phantom | PTW." [Online]. Available: <https://www.ptwdosimetry.com/en/products/octavius-4d-qa-phantom/>

Chapter 4

Tests with Photon, Protons and Carbon Beams

“The truth method of knowledge is experiment.”

William Blake

In this chapter, I present the assessment of our novel detector technology based on Gas Electron Multiplier (GEM) coupled to a matrix of Thin Film Transistor (TFT) involving photon, proton and carbon clinical beams. After confirming the achievement of sub-millimetric spatial resolution through the utilization of low-energy (40 kVp) X-rays in Section 3.5, this chapter is devoted further to showcasing the capabilities of the detector’s TFT readout in measuring secondary electrons generated by the triple-GEM structure. The radiation hardness and performance of the prototype with charge readout were evaluated when exposed to various clinical radiation beams. This evaluation is carried out under exposure to high-energy radiation from diverse sources, including X-rays, protons, and carbon ion beams.

Initially, I report the radiation hardness tests conducted at the component level, employing specially prepared samples for this study. Next, the initial functional trials of the GEM-TFT detector at the Bern medical cyclotron are presented. The reasoning behind conducting tests at Bern with low-energy 18 MeV protons lies in the protons’ short range.

The occurrence of the Bragg peak, where the maximum energy deposition takes place directly within the detector, provides an opportunity to assess the full performance of the detector while analyzing its saturation response.

Continuing the evaluation of this solution, we extend our testing regime to the Linac TrueBeam Varian, where we gauge the versatility of our detector under a 6 MV Flattening Filter (FF) photon beam used for conventional photon-based radiotherapy.

The last section is devoted to the ultimate tests performed with the GEM-TFT detector at CNAO, the Italian National Centre of Oncological Hadrontherapy located in Pavia. Here, the detector was exposed to proton and carbon ions beams at clinical intensities used for cancer treatment. The studies conducted using this prototype are under revision in the paper "A high-resolution large-area detector for quality assurance in radiotherapy" of which I am the first author. These findings are reprinted in the second section of this manuscript.

4.1 Proton Radiation Hardness Testing using 18 MeV cyclotron at Bern

The radiation hardness tests were not conducted using the GEM-TFT detector itself but rather employed Process Evaluation Modules (PEM) containing discrete TFTs as shown in Figure 4.1. With only two readouts at our disposal and considering the critical importance of not jeopardizing subsequent clinical beam tests, we decided to abstain from conducting any system-level testing. The behavior of GEMs under radiation exposure has been extensively documented, and our primary focus is to closely observe and analyze the performance of the TFT under these conditions. This approach allowed us to maintain the integrity of our testing process while gaining valuable insights into the TFT's performance and durability.

To assess the radiation tolerance of Discrete Dual-Gate TFTs (with a channel width of 15 μm and a channel length of 5 μm), a series of irradiation tests were conducted utilizing three distinct doses (0.5, 29, 250 kGy). The first component-level evaluation involves irradiating three individual strips with three distinct radiation doses, and assessing their response before and after exposure.

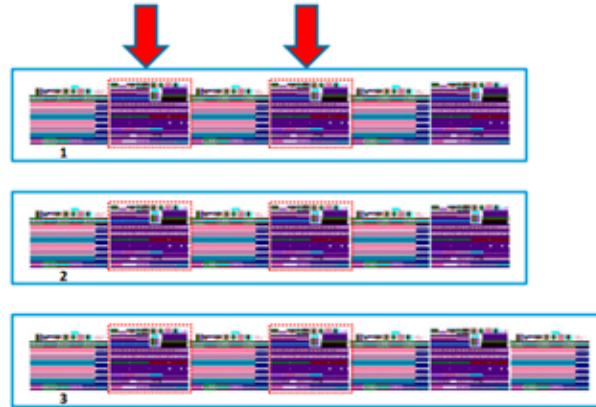


Figure 4.1: Component level radiation testing involved three strips on glass, labeled as 1, 2, and 3, encompassing TFTs within areas demarcated by dashed squares.

In order to perform these evaluations, a cluster of TFTs arranged in a strip formation was positioned perpendicular to the path of the proton beam, as illustrated in Figure 4.2b. The protons were targeted to impinge upon the TFTs, positioning their active regions to face the exit window, as illustrated in Figure 4.2c. This orientation corresponded to the same setup as the one used when coupling the TFT backplane to the triple-GEM detector (Figure 4.2a). To concurrently monitor the beam's current, an aluminum disk was placed behind the sample and connected to a Keysight B2985A electrometer. Throughout the irradiation process, all electrodes were intentionally left ungrounded or floating.

Radiation hardness plays a pivotal role in the functionality of QA devices that might encounter a weekly radiation dosage of 100 Gy in the routine operation of a particle therapy center. To gauge the radiation robustness of the prototype, we conducted a comparison between the baseline measurements without the presence of the beam and the response to a uniform 40 kVp X-ray field, both before and after uniform proton irradiation.

The electrical testing of the dual-gate TFTs took place under ambient conditions at room temperature, within a light-restricted environment. This examination was conducted using a semiconductor parameter analyzer, specifically the Agilent 4156C model. A consistent source-drain voltage of 1 V was applied uniformly in all instances.

To record the transistor's transfer characteristics, a systematic procedure was fol-

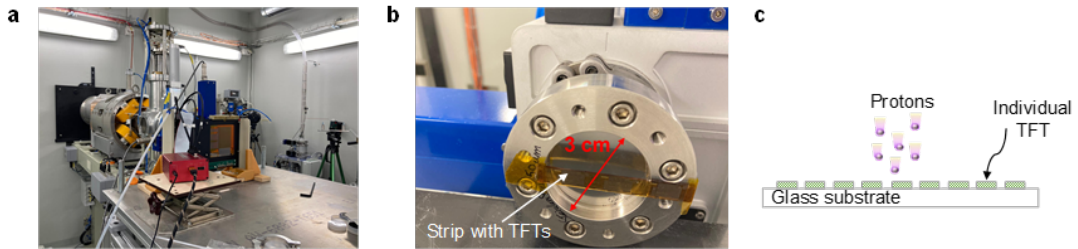


Figure 4.2: The configuration employed during the proton beam experiments conducted at the BTL of the Bern medical cyclotron: a. The UniBEaM detector and the GEM-TFT detector were installed at the end of the BTL of the IBA Cyclone 18 MeV cyclotron at the Bern University Hospital (Inselspital). An extract window is placed before the entrance Mylar window of the detector. b. Detailed image of the exit window with a diameter of 3 cm, presenting a single PEM (indicated by the arrow), which was used for the radiation hardness tests. c. A schematic illustration delineates the layout of the strip of TFTs that were subjected to direct irradiation by the proton beam.

lowed: the top gate voltage was varied while the bottom gate remained grounded. The V_{ON} , turn-on voltage (see Subsection 2.5.1), of the TFTs was precisely deduced by pinpointing the threshold point in the top-gate voltage at which the source-drain current initiated its ascent. In Figure 4.3, a comprehensive summary of the outcomes concerning radiation hardness tests is presented.

The gray curves depict the transfer characteristics of TFTs in their pristine condition prior to any irradiation. Notably, the initial V_{ON} voltage remains nearly at 0 V across all cases. However, upon exposure to 0.5, 29, and 250 kGy of 18 MeV protons, the V_{ON} voltage undergoes a shift to approximately -4 V, -13 V, and roughly -40 V, respectively (4.3 a-c, red curves). This particular negative V_{ON} shift aligns with common observations for oxide-based TFTs when subjected to high-energy radiation, such as X-rays [1, 2] and 5 MeV protons [3]. This phenomenon is attributed to an increase in electron concentration within the a-IGZO TFT's active layer. Notably, this V_{ON} shift can be effectively compensated for through our dual-gate TFT technology. Examining the green curves in Figure 4.3, it is evident that by applying a negative bias to the bottom gate, the V_{ON} voltage of the TFTs can be readily adjusted across a significant voltage range, ultimately restoring it to its original state at around 0 V.

The radiation-induced V_{ON} shift is a temporary occurrence. Over time, the device

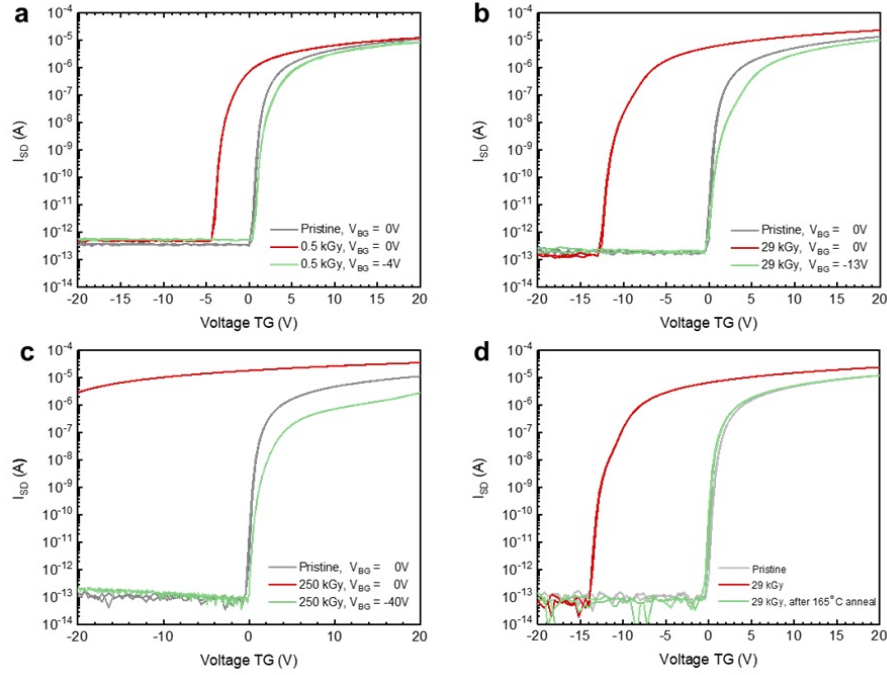


Figure 4.3: Evaluation of radiation hardness in dual gate TFTs. a-c. Transfer characteristics of $I_d - V_g$ before irradiation (Pristine - grey), after irradiation (red) with 0.5, 29, and 250 kGy 18 MeV protons, and following the mitigation of V_{ON} shift (green) by applying a bottom gate bias of -4, -13, and -40 V, respectively. d. Transfer characteristics of $I_d - V_g$ before irradiation (grey), after irradiation (red) with 29 kGy 18 MeV protons, and after recovery through a thermal annealing process for 1 hour at 165 °C (green).

characteristics naturally return to their initial configuration. To expedite this recovery process, a thermal annealing can be employed, as illustrated in Figure 4.3d, which demonstrates a complete restoration of V_{ON} to its original state after a 1-hour annealing process at 165°C.

In practice, a detector employed for treatment plan verification in operation hadron therapy center faces a weekly dose of approximately 100 Gy. This means that the dose of 29 kGy received by the second TFT sample within a short timeframe is equivalent to roughly 6 years of operation of a commercial detector. The relatively modest shift experienced at the relevant radiation doses, coupled with its temporary nature, instills confidence in our belief that the proton radiation resilience of our IGZO TFTs will be adequate for initial applications.

4.2 Proton Beam Irradiation using the 18 MeV cyclotron in Bern

We initiated the detector testing by subjecting it to proton fluxes equivalent to high clinical beam intensities, prior to its assessment at CNAO. Our primary objective was to validate our ability to capture and analyze the signals generated by protons while also gauging the potential for signal saturation. Hence, the entire GEM-TFT detector underwent irradiation with 18 MeV protons, with beam intensities reaching up to 1.3 nA. This irradiation took place at the Bern University Hospital (Inselspital) [4, 5].

To facilitate the monitoring and management of beam properties during these irradiation sessions, an UniBEaM detector was integrated into the BTL setup, as illustrated in Figure 4.2a. The UniBEaM gauges beam profiles along both the x and y transverse axes by intricately threading scintillating fibers through the path of the proton beams. The protons are extracted into the ambient air environment through a 50- μm stainless steel window positioned opposite the Mylar window.

The operational parameters of the cyclotron were configured to yield a uniform beam with a 3 cm diameter, matching precisely with the dimensions of the extraction window. This precision ensures an impeccable alignment and consistency in the beam characteristics throughout the irradiation process.

The initial trial conducted at the Bern cyclotron using protons and the GEM-TFT system is depicted in Figure 4.4b. To enable the protons to exit into the atmosphere, a circular-shaped, 50 μm stainless steel window was employed. In front of this exit window, a GAFCHROMIC[®] EBT3 film was positioned to assess the beam's configuration. The exposed film reveals a circular shape with a 3 cm diameter, as illustrated in Figure 4.4a. Concurrently, the GEM-TFT detector determined the beam's diameter to be 3.024 cm. The horizontal lines without functionality in the readout images in Figures 4.4b are, in fact, line defects within the TFT array. These measurements conclusively establish the feasibility of investigating the size and shape of the beam, indicating that this prototype holds good promise as a diagnostic tool for beams. Furthermore, an assessment was carried out involving a current scan using 18 MeV protons at beam intensities of up to 1.3 nA. In the case of a uniform beam with a 3 cm

diameter, 1.3 nA equates to roughly 10% of the maximum beam intensity utilized at CNAO [5]. We observed a linear relationship between 18 pA and 0.7 nA when the sum of the GEM voltages was set at 600 V, as depicted in Figure 4.4c. However, for current values exceeding 1 nA, there were two data points that displayed unexpected non-linear behavior. Additional investigations are needed to gain deeper insights into this phenomenon.

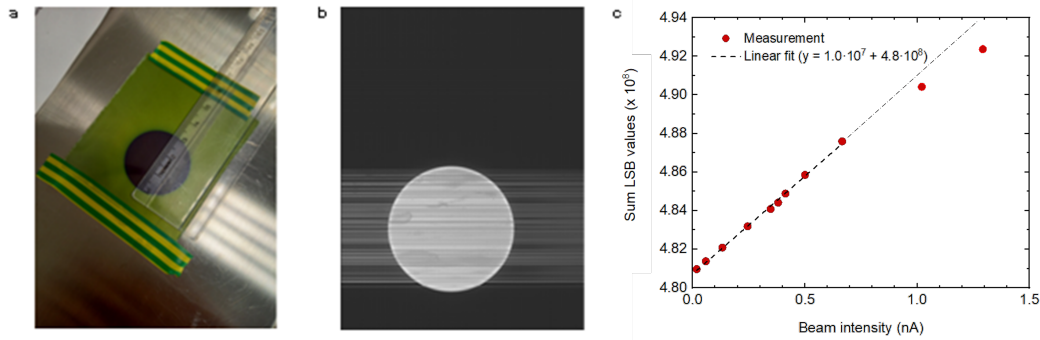


Figure 4.4: Initial operational assessment with protons at the Bern medical cyclotron. a. Captured image displaying the beam’s circular configuration using GAFCHROMIC[®] EBT3 film. b. Captured image demonstrating the beam’s circular shape using the GEM-TFT detector. c. Least Significant Bit (LSB) value in relation to beam intensity recorded by the detector during the operation of the 18 MeV cyclotron. The dashed line represents a linear regression fitted to the dataset.

We achieved the detection of protons using a GEM-based detector with charge read-out, implementing a matrix of TFT. Subsequently, we transitioned into the phase of conducting clinical beam tests.

4.3 Photon Irradiation Using a Commercial Electron Linac for Conventional Radiotherapy

The GEM-TFT detector, which was filled with an $Ar : CO_2$ mixture (70:30), was tested at a commercial Linac TrueBeam Varian, using a 6 MV FF photon beam. The depth dose curve observed for the 6 MV photon beam exhibited two distinct regions: the initial build-up region near the surface and the charge particle equilibrium region at greater depths [6]. In order to

prevent any interference from electron contamination in the build-up region, we placed solid water slabs with a combined thickness of 1.7 cm in front of the detector. The detector was visually centered within the illuminated field using laser assistance and was inserted into the vertical support, ensuring it was perpendicular to the radiation beam as shown in Figure 4.5.



Figure 4.5: Setup utilized for conducting photon beam tests with the Varian Linac TrueBeam at Zentrum für Strahlentherapie in Freiburg. The GEM-TFT detector was situated on the treatment couch, while the treatment head was oriented at 90° .

The electron linear accelerator situated at the Zentrum für Strahlentherapie in Freiburg underwent calibration to administer a precise dose of 100 Monitor Units (MU), spanning a range of dose rate variations from 100 MU/min to 600 MU/min, which approximates 0.8 Gy, all within the context of a 10×8 cm² field. The dose rate achievable with the 6 MV FF beam is capable of reaching 600 MU/min. Subsequent to a gain scan, the detector was operated with the sum of the GEM voltages set at 750 V. The readout was configured to operate at its utmost sensitivity level of 0.5 pC, and the frame rate was established at 10 frames per second. There is a 4.4% relative difference between the response of the GEM-TFT for the lowest dose rate (100 MU/min) and the highest dose rate (600 MU/min). This indicates that the GEM-TFT's response is sensitive to changes in dose rate as shown in Figure 4.6.

We then conducted a dose scan employing 6 MV photons and observed a linear behavior across the range of doses, spanning from 8 MU to 800 MU, as illustrated in Figure 4.7. This examination was carried out utilizing the highest available dose rate, which is 600

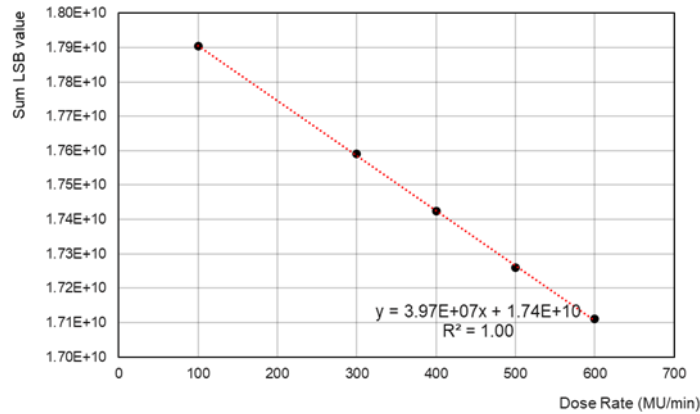


Figure 4.6: LSB value vs dose rate (MU/min) of the detector using the commercial Linac TrueBeam Varian. The dashed line represents the linear fit to the data.

MU/min, approximately equivalent to 6 Gy/min.

4.4 Test with Protons and Carbon Ions at CNAO

We tested the GEM-TFT at CNAO, the Italian National Centre of Oncological Hadrontherapy located in Pavia with the beams utilized in cancer treatment. The CNAO synchrotron offers proton beams with kinetic energies ranging from 60 to 250 MeV and carbon ion beams in the range of 120 to 400 MeV/u [7]. Proton beam intensity varies from 10^9 to 10^{10} particles/s, while for carbon ions, it ranges from 4×10^7 to 4×10^8 particles/s. Two distinct measurement approaches were employed.

Firstly, we utilized an integrated system, which included a commercial water phantom and the GEM-TFT, to conduct depth scans (Figure 4.8a). We designed and built a light-tight, waterproof box with 10mm-thick walls to immerse the GEM-TFT detector in water without damaming the electronics. This box was crafted from black polymethyl methacrylate (PMMA, type: PLEXIGLAS NOIR 811 - PERSPEX 9T30). Additionally, we designed and manufactured two supports with rails to guide and secure the baseplate inside the box.

Secondly, the detector was directly positioned on the treatment couch (Figure 4.8b). The detector was perpendicularly oriented to the beam within a custom-made vertical struc-

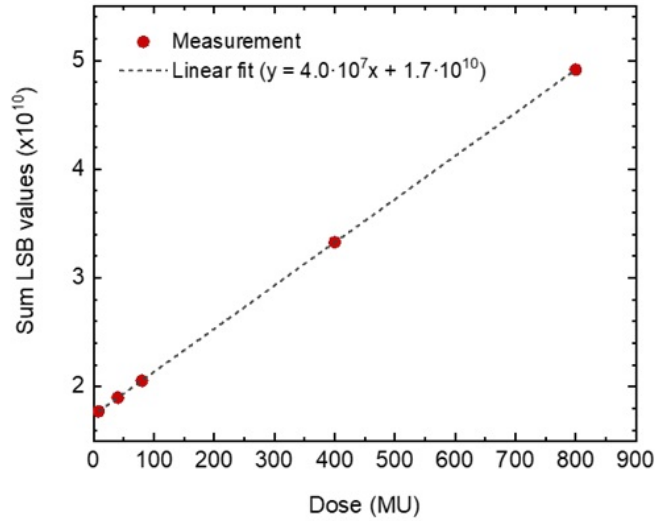


Figure 4.7: LSB value vs dose expressed in MU of the detector using the commercial Linac TrueBeam Varian. The dashed line represents the linear fit to the data.

ture, ensuring a well-aligned setup. To assess spatial resolution using the edge response method, we placed a variable thickness high-Z material in front of the detector, covering a portion of its active area to create a distinct sharp edge, as depicted in Figure 4.8b.

In the initial measurements conducted at CNAO, utilizing protons and carbon ions, the GEM-TFT was employed within a water phantom. To establish reference measurements for beam intensity, the Dose Delivery System (DDS) of CNAO was employed, encompassing a beam monitors and the control unit, serving as the core of the data acquisition setup. Notably, the CNAO DDS is a certified medical device, bearing the CE mark, and it is actively employed for clinical purposes at both CNAO and MedAustron EBG [7, 8]. Figure 4.9 illustrates a strong alignment between the responses of the GEM-TFT detector and the CNAO DDS.

The accurate measurement of the Bragg peak holds significant importance, primarily because it enables precise targeting of the tumor. Figure 4.10 shows the Bragg curves acquired with the GEM-TFT at clinical beam intensity. By ensuring that the particle beam's maximum energy is directed precisely toward the tumor, it becomes possible to spare the surrounding healthy tissue from unnecessary radiation exposure. This strategy, in turn, aids in minimizing potential side effects while augmenting the overall effectiveness of the treatment.

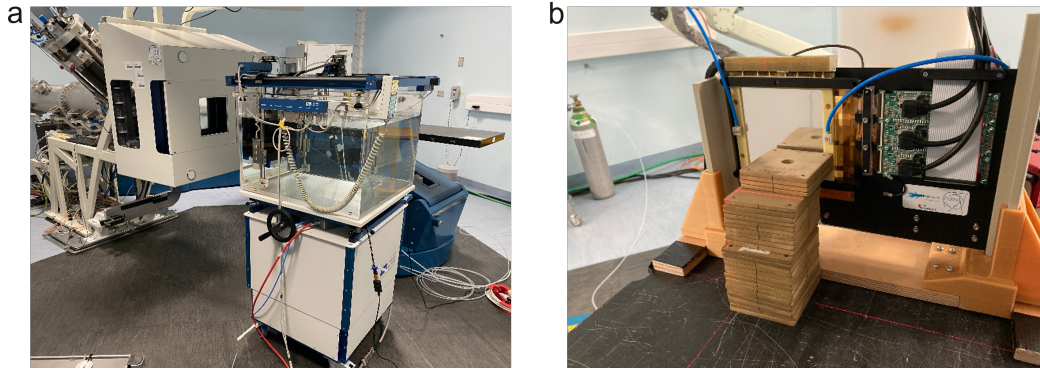


Figure 4.8: The configuration employed for conducting proton and carbon ions beam tests at CNAO. In Figure (a), the GEM+TFT detector is securely contained within a waterproof PMMA box, which is affixed to the positioning system of the water phantom. This arrangement permits the adjustment of the distance between the entrance window and the PMMA box along the beam axis. In Figure (b), the detector is positioned within a vertical support and situated on the treatment couch, with a high-Z material covering a portion of its active area for the purpose of spatial resolution analysis.

To ascertain the accuracy of the Bragg curves, we compared the results obtained with the GEM-TFT to the data collected using the Peakfinder system, which shares equivalent beam parameters. The PTW Peakfinder, developed by PTW in Freiburg, Germany, is a commercial device tailored for assessing the depth dose profile of a particle beam in water. It encompasses a height-adjustable water column and two ionization chambers. As seen in Figure 4.10, the Bragg curves acquired with the GEM-TFT at clinical beam intensity, employing 147.72 MeV protons and 207.97 MeV/n carbon ions, reveal a clear Bragg peak at a depth of approximately 150 mm, with the characteristic tail beyond the peak, distinctly visible, which is attributed to the carbon fragments. The curves are standardized to the first value in the plateau region. For protons, a correction factor of 1.1954 was applied to adjust the counts for the initial plateau point. While with the GEM-TFT detector the first value was measured at 50.9 mm, PTW PEAKFINDER measurements were available for 50.4 mm and 51.4 mm. This correction factor (1.1954) was obtained using a straightforward interpolation method between these points.

The Bragg curve results obtained from the GEM-TFT detector and the PTW Peakfinder exhibit a close resemblance when it comes to proton beams. With the exception of the tail points, the most significant deviation, measuring at 9.9%, was observed at a depth of

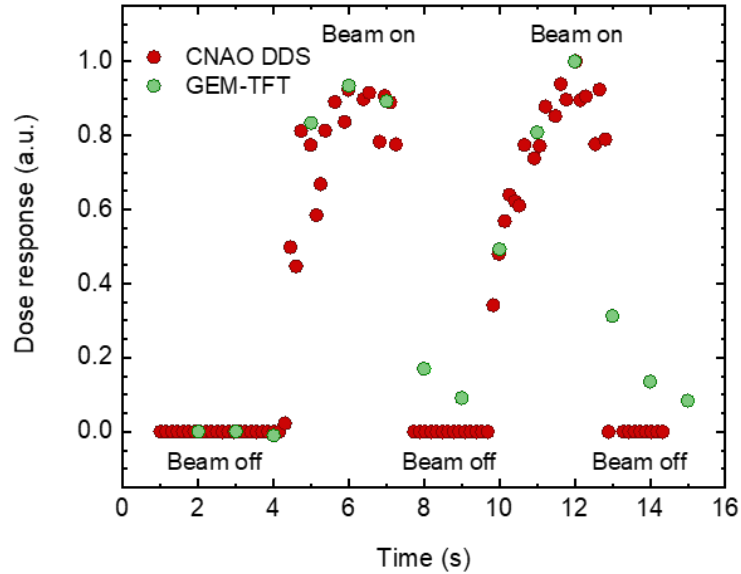


Figure 4.9: Dose response as a function of time for the GEM-TFT detector and the DDS utilized at CNAO. The data have been normalized with respect to the peak values. A selected subset of CNAO DDS data points is displayed (every third point) to improve clarity. It is important to note that the GEM-TFT data points between beam spills retain non-zero values owing to the 1-second frame rate, which captures both the beam ON and OFF states.

116.9 cm. However, when it comes to the Bragg curves for carbon ions, a more pronounced disparity between the two devices emerges. Specifically, there is a discrepancy at the peak's maximum, where the prototype's measurement falls below the expected value. In contrast, the measurements in the tail region surpass expectations.

For both protons and carbon ions, no evidence of saturation effects was observed at any depth using the chosen parameters. The reasons for the peculiar results with carbon ions remain somewhat enigmatic. One plausible explanation could be a dependency on linear energy transfer (LET). Furthermore, the disparity might be linked to the larger surface area of the GEM-TFT compared to the ionization chamber of the PTW Peakfinder, leading to increased secondary particle collection. This discrepancy may consequently result in an amplified signal beyond the Bragg peak. Additionally, variations in the detector's response due to non-uniform defect distribution could contribute to substantial fluctuations in the signal.

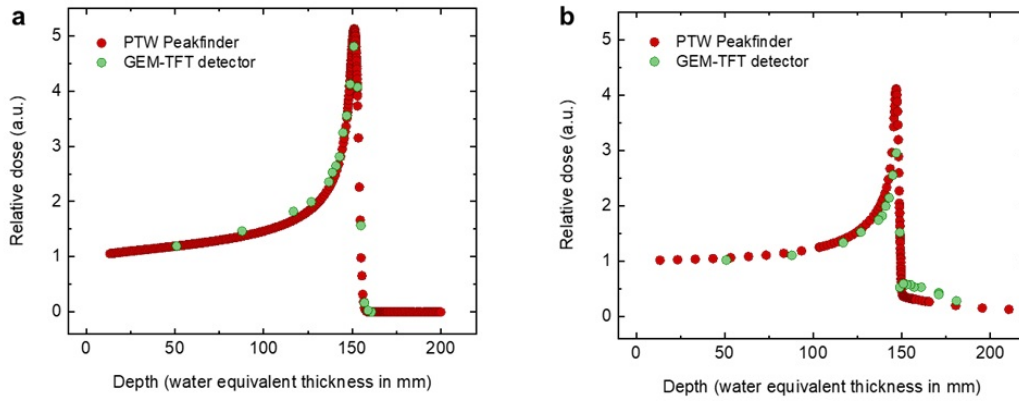


Figure 4.10: Bragg curves exhibit an increasing energy deposition as they penetrate deeper, reaching a peak at the end of their range (151 mm), which is followed by a steep decline. This phenomenon corresponds to the energy loss of ionizing radiation as it traverses through water. a) Bragg curve measurements were conducted using 147.72 MeV protons with the GEM+TFT (green) and PTW Peakfinder (red). b) Bragg curve measurements were carried out with 207.97 MeV/n carbon ions using the GEM+TFT (green) and PTW Peakfinder (red).

Conducting further experiments with an improved prototype, free from production defects, may offer insights into improving these measurements.

Tests targeting the evaluation of factors like spatial resolution were minimally impacted by the readout defects observed in the initial prototype. However, it was not feasible to perform measurements intended to assess dose uniformity due to the intrinsic nature of this early-stage prototype. Nevertheless, this preliminary prototype, created as a proof of concept, was fabricated using a new dedicated multi-layer TFT design containing 10 layers each patterned by photolithography. After fabrication, detailed characterization and inspection it became clear that a design flaw was present in the fanout electrode at the readout side for which a new repair step was performed afterwards. Unfortunately, the yield of repair is not high, leading to remaining defective non-functional lines. It is expected that a minimal number of defects are present with an updated design and in particular in production, where quality is much higher compared to a research line.

Moving forward, the spatial resolution of the GEM-TFT detector was assessed under clinically relevant hadron therapy conditions using the experimental setup depicted in Fig-

ure 4.8b. In Figure 4.11, a comparison of the detector’s performance is presented alongside GAFCHROMIC[®] EBT3 films, renowned as the gold standard for such measurements in radiation therapy. Employing in-room lasers facilitated the alignment of the collimators in relation to the detector. While assessing the potential impact of misalignment and scattered ions on the wedge face is complex due to various influential factors, including beam energy and material properties, the inclusion of films in this experiment enables a comprehensive evaluation. This approach effectively disentangles the performance characteristics of our GEM-TFT detector from external variables. The FWHM obtained through the edge response method consistently remained below 0.50 ± 0.05 mm for different lines, translating to a resolution of 1 line pair per millimeter (lp/mm). The sub-millimeter spatial resolution initially confirmed with X-rays was substantiated effectively within the context of hadron therapy.

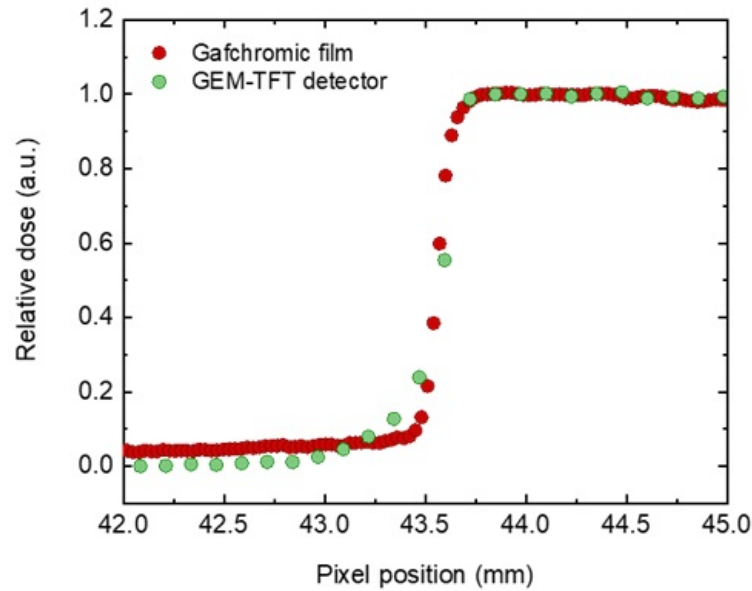


Figure 4.11: Evaluation of spatial resolution in conditions pertinent to hadron therapy. Edge response profile for 147.72 MeV protons using a high-Z material, as assessed with the GEM-TFT detector and GAFCHROMIC[®] EBT3 films.

The LET is a crucial parameter that characterizes how densely energy is deposited by a specific type of radiation. This factor significantly governs the effectiveness of radiation exposure in terms of its biological impact. In our study, we conducted experiments using three different energy levels to investigate how the GEM-TFT detector’s performance is influenced

by variations in energy. To carry out these experiments, the detector was positioned at a distance of 130 cm from the surface of a water phantom. We standardized the detector's response by comparing it to the response generated by 207.97 MeV/n carbon ions. The results are summarized in Table 4.1, which presents the LSB values measured by the TFT-based readout for each selected energy level of the carbon beam. The data revealed a variance in the GEM-TFT response, ranging between 0.5% and 1.6%.

Table 4.1: Energy response of GEM-TFT detector normalized to its response to 207.97 MeV/n

Energy (MeV/n)	GEM-TFT response
207.97	1
332.15	1.015
398.84	1.005

It is worth noting that radiochromic film, which also facilitates 2D dosimetry, has been reported to exhibit an under-response, typically falling within the range of approximately 10% to 20% [2]. While a more detailed examination of the LET dependence along the Bragg peak could permit a comprehensive comparison with other commercially available detectors in this field [3, 8], this level of analysis is beyond the scope of our current research and should be accessed in future studies.

4.5 Conclusions

This detector's versatility extends to conventional photon-based radiotherapy and hadron therapy. Comprehensive performance assessments highlight its capabilities in detecting a wide range of particles, including high-energy (6 MeV) photons, as well as clinically significant protons and carbon ions.

To summarize, this chapter presents a groundbreaking exploration into the use of flat panel TFT technology as the readout system for GEM detectors, aiming to achieve large-area beam imaging with both high spatial resolution and rapid frame rates. Our primary objective

was to investigate the feasibility of this innovative technology, which holds the promise of scalability within the semiconductor industry. This technology fusion seeks to capitalize on the strengths of gaseous detectors, such as their minimal material requirements and potential use of tissue-equivalent gases, while surmounting the limitations of ICs regarding pixel size and the number of detectors in a matrix.

While significant challenges persist and may impact feasibility and cost considerations, potential solutions appear attainable. The sub-millimeter spatial resolution achieved here is the outcome of direct charge readout, the directional behavior of charges from the GEM, and the high pixel density of the TFT array. Furthermore, the proximity of just 1 mm between the last GEM and the readout contributes to the spatial resolution.

Our experiments underscore the detector's capability to measure secondary electrons generated by the triple-GEM structure when subjected to high-intensity beams of various high-energy radiation sources, including X-rays, protons, and carbon ion beams. Notably, the detector exhibits a linear response across a broad range of proton intensities, covering the typical doses administered in hadron therapy. Additionally, it demonstrates relatively low radiation damage, which can be mitigated due to the presence of two separate gate electrodes within the TFT. This compensation strategy allows for a maximum dose difference of up to 10% compared to the reference detector.

The observed relationship between LET and detector response appears to be less pronounced when compared to conventional quenching detectors like plastic scintillators. However, we acknowledge the need for further in-depth research to investigate and confirm this observation. Based on these findings, we posit that this detector type holds significant potential for quality assurance in cancer radiation therapy.

Bibliography

- [1] G. H. Gelinck, A. Kumar, D. Moet, J.-L. P. J. van der Steen, A. J. J. M. van Breemen, S. Shanmugam, A. Langen, J. Gilot, P. Groen, R. Andriessen, M. Simon, W. Ruetten, A. U. Douglas, R. Raaijmakers, P. E. Malinowski, and K. Myny, “X-Ray Detector-on-Plastic With High Sensitivity Using Low Cost, Solution-Processed Organic Photodiodes,” *IEEE Transactions on Electron Devices*, vol. 63, no. 1, pp. 197–204, Jan. 2016, conference Name: IEEE Transactions on Electron Devices.
- [2] D.-G. Kim, J.-U. Kim, J.-S. Lee, K.-S. Park, Y.-G. Chang, M.-H. Kim, and D.-K. Choi, “Negative threshold voltage shift in an a-IGZO thin film transistor under X-ray irradiation,” *RSC Advances*, vol. 9, no. 36, pp. 20 865–20 870, Jul. 2019, publisher: The Royal Society of Chemistry. [Online]. Available: <https://pubs.rsc.org/en/content/articlelanding/2019/ra/c9ra03053k>
- [3] M.-G. Shin, S.-H. Hwang, H.-S. Cha, H.-S. Jeong, D.-H. Kim, and H.-I. Kwon, “Effects of proton beam irradiation on the physical and chemical properties of IGTO thin films with different thicknesses for thin-film transistor applications,” *Surfaces and Interfaces*, vol. 23, p. 100990, Apr. 2021. [Online]. Available: <https://www.sciencedirect.com/science/article/pii/S2468023021000675>
- [4] A. J. Cohen and G. G. Janezic, “Relationships among trapped hole and trapped electron centers in oxidized soda-silica glasses of high purity,” in *Relationships among Trapped Hole and Trapped Electron Centers in Oxidized Soda-Silica Glasses of High Purity*. De Gruyter, pp. 619–624. [Online]. Available: <https://www.degruyter.com/document/doi/10.1515/9783112494547-025/html>
- [5] S. Braccini, “The new bern PET cyclotron, its research beam line, and the

- development of an innovative beam monitor detector,” *AIP Conference Proceedings*, vol. 1525, no. 1, pp. 144–150, Apr. 2013, _eprint: https://pubs.aip.org/aip/acp/article-pdf/1525/1/144/12018990/144_1_online.pdf. [Online]. Available: <https://doi.org/10.1063/1.4802308>
- [6] A. Sigamani, A. Nambiraj, G. Yadav, A. Giribabu, K. Srinivasan, V. Gurusamy, K. Raman, K. Karunakaran, and R. Thiyagarajan, “Surface dose measurements and comparison of unflattened and flattened photon beams,” *Journal of Medical Physics*, vol. 41, no. 2, p. 85, Apr. 2016, company: Medknow Publications and Media Pvt. Ltd. Distributor: Medknow Publications and Media Pvt. Ltd. Institution: Medknow Publications and Media Pvt. Ltd. Label: Medknow Publications and Media Pvt. Ltd. Publisher: Medknow Publications. [Online]. Available: <https://www.jmp.org.in/article.asp?issn=0971-6203;year=2016;volume=41;issue=2;spage=85;epage=91;aulast=Sigamani;type=0>
- [7] M. Donetti, S. Giordanengo, C. Graeff, M. Lis, F. M. Milian, M. Pullia, T. Steinsberger, A. Vignati, and S. Rossi, “Current and Future Technologies of the CNAO Dose Delivery System,” *IEEE Instrumentation & Measurement Magazine*, vol. 24, no. 9, pp. 61–69, Dec. 2021, conference Name: IEEE Instrumentation & Measurement Magazine.
- [8] S. Giordanengo, M. A. Garella, F. Marchetto, F. Bourhaleb, M. Ciocca, A. Mirandola, V. Monaco, M. A. Hosseini, C. Peroni, R. Sacchi, R. Cirio, and M. Donetti, “The CNAO dose delivery system for modulated scanning ion beam radiotherapy,” *Medical Physics*, vol. 42, no. 1, pp. 263–275, Jan. 2015.

Conclusions and Outlook

*“Precision in medicine is a journey,
not a destination.”*

William J. Mayo

The utilization of optical readout is a versatile and promising approach for radiation detectors, providing clear and high granularity visualizations. Throughout this work, we have effectively integrated Organic Photodiode (OPD) and Thin Film Transistor (TFT) into a Triple-GEM detector using modern imaging sensors. These detectors, based on GEM technology and operating with CF_4 -containing gas mixtures, emit ultraviolet and visible light. It is worth noting that the visible scintillation band at around 630 nm aligns perfectly with the OPD’s quantum efficiency.

Throughout the thesis, we conducted extensive research and development and we have explored the potential of using optically readout GEM-based radiation detectors. We have fine-tuned customized prototypes for various scientific applications, showcasing the technology’s capabilities. However, our investigation has revealed limitations and challenges associated with flat panel OPD and TFT technology as GEM detector readout. Specifically, the detector’s performance is influenced by the distance between the last GEM and the imager, making sub-millimeter spatial resolution challenging without the use of additional lenses. Yet, introducing additional optical components like mirrors or lenses to guide and control the light from the detector to the imaging sensor poses difficulties in maintaining the compactness of the detector. This constraint has hindered our progress in achieving the crucial sub-millimetric spatial resolution needed for advanced radiotherapy techniques used in cancer therapy. A high spatial resolution of the 2D dose distribution is important because most of the conformal treat-

ment plans are characterized by very high “in-field” dose gradients. It is crucial to ensure the precise delivery of the prescribed dose to the intended location, while minimizing exposure to healthy tissues. Additionally, we have identified the isotropic emission of the scintillation light as the main limitation to the achievable spatial resolution. Based on our scientific analysis, we have concluded that the optical prototype achieves a spatial resolution of a few millimeters.

One promising path to investigate further is using a charge readout instead of an optical readout. For this reason, we coupled GEM to a matrix of TFT. This method involves collecting secondary electrons created within the GEMs and guiding by electric fields to preserve high spatial resolution. This approach successfully overcomes the limitations linked to optical methods, resulting in an improved performance of the detector. The research presented in the final section of this dissertation has provided valuable insights into using flat panel TFT technology for reading GEM detectors in large-area beam imaging with high precision and fast frame rates.

We initially concentrated on hadron therapy but have broadened our focus to include conventional therapy using linacs. We have also begun exploring the detector’s capabilities for quality control purposes with low-energy X-rays, commonly used in radiology. The findings of this research provide a strong foundation for future studies aimed at improving the performance of flat panel TFT technology as GEM detector readout. The results also highlight the technology’s potential as a quality assurance tool in cancer radiation therapy, with opportunities for further improvements through ongoing research.

In conclusion, the performance tests affirm the detector’s capability to detect a range of energies, encompassing low-energy (40 kVp X-rays) and high-energy (6 MeV) photons, as well as protons and carbon ions at clinical energy levels. The successful execution of these tests with a wide range of clinical beams was made possible through the collaborative efforts between CERN and the University of Bern. Through the course of my PhD, I successfully developed this prototype, paving the way for a future commercial detector employing this technology. Such advancements hold promise for diverse applications in medical physics, contributing significantly to the enhancement of quality assurance across various human-related beam applications.

Firstly, ensuring gas tightness is a crucial step in successfully creating a commercial product suitable for hospital settings. An option with a sealed or recirculating gas system can

eliminate the need for gas bottles in hospitals or therapy centers, simplifying the process and avoiding the complications associated with gas bottle use.

Furthermore, the detector showed relatively low radiation damage, that can be compensated by virtue of the two separate gate electrodes in the TFT. We have plans for technological improvements to make a high-quality readout system with a large active area of $200 \times 200 \text{ mm}^2$ and a minimized number of fabrication defects.

Finally, the future development of the $200 \times 200 \text{ mm}^2$ prototype with a high-quality readout and fewer production defects would allow for further testing of the technology and potential commercialization. With continued refinement and collaboration, this innovative system has the potential to make substantial contributions to scientific research and enhance quality assurance in various cancer radiation therapy modalities. Thus improving the performance of the treatments for the benefit of the patients, of the health care systems and, ultimately, of society.

List of Acronyms

ADC	Analog-to-Digital Converter
AFE	Analog Front End
ASIC	Application-Specific Integrated Circuit
BTL	Beam Transport Line
CCD	Charge-Coupled Device
CMOS	Complementary Metal–Oxide–Semiconductor
CNAO	Centro Nazionale di Adroterapia Oncologica
CT	Charge Transfer Process
CTV	Clinical Target Volume
DDS	Dose Delivery System
DNA	Deoxyribonucleic Acid
EBT	Electron Beam Therapy
EQE	External Quantum Efficiency
ESF	Edge Spread Function
FF	Flattening Filter
FPGA	Field-Programmable Gate Array
FWHM	Full Width at Half Maximum

GEM	Gas Electron Multiplier
IC	Integrated Circuit
IGZO	Indium Gallium Zinc Oxide
IMPT	Intensity Modulated Proton Therapy
IMRT	Intensity Modulated Radiation Therapy
ITO	Indium Tin Oxide
LET	Linear Energy Transfer
linacs	Linear Accelerators
LSB	Least Significant Bit
LSF	Line Spread Function
MTF	Modulation Transfer Function
NIR	Near-Infrared
OAR	Organ At Risk
OPD	Organic Photodiode
PBS	Pencil Beam Scanning
PECVP	Plasma-Enhanced Chemical Vapor Deposition
PEM	Process Evaluation Modules
PET	Photon Emission Tomography
ppi	per inch
PTV	Planning Target Volume
QA	Quality Assurance
RBE	Relative Biological Effectiveness
ROI	Region of Interest
ROIC	Readout Integrated Circuit
RT	Radiotherapy

SOBP	Spread-Out Bragg Peak
SPECT	Single Photon Emission Tomography
TFT	Thin Film Transistor
TP	Treatment Planning
TPS	Treatment Planning System
UV	Ultra-Violet
VHEE	Very High Energy Electrons
VIS	Visible

List of Figures

1.1	Estimated number of deaths in 2020, both sexes, all ages [4].	12
1.2	Dominant interaction as a function of the atomic number Z of the absorbing medium and the energy of the incident photon. The black curves show where two types of interactions have the same probability. The blue lines indicate carbon, hydrogen, oxygen, and nitrogen atoms, which are the main components of human tissue, fat and muscle. Adapted from [14].	15
1.3	Juxtaposition of photon, proton, and electron relative dose distributions with increasing tissue depth. These include (a) 6 MV Photons, (b) Bragg peak 147 MeV protons, (c) spread-out Bragg peak, (d) 10 MeV electrons, (e) collimated 200 MeV electrons, (f) collimated 2 GeV electrons, (g) 200 MeV electrons focused at 15 cm, and (h) 2 GeV electrons focused at 15 cm. To facilitate comparison, each curve is normalized to the dose at the reference depth of 15 cm, with the exception of the 10 MeV electron beam, which is normalized to its peak dose. [16].	17
1.4	Photon interactions inside the patient [18].	18
1.5	Summary of the typical stages in radiotherapy workflow.	22

1.6	The principle of therapeutic ratio. Dose–response red curves represent the tumor control probability (TCP) and the green curves the normal tissue complications probability (NTCP). Chemotherapy for example, can increase the separation between the two curves in order to achieve an optimal therapeutic window [34].	24
1.7	A slight inaccuracy in photon target depth (red vertical lines on the left) results in a tiny dose error (shaded region). A comparable slight target-depth inaccuracy with carbon-ions, on the other hand, leads in significantly more critical mistakes (shaded areas illustrate substantial areas of under- and over-dose) [37].	25
2.1	Readout options for the LaGEMPix.	41
2.2	a) Image with external light. b) Image without external light.	42
2.3	The LaGEMPix detector. The triple-GEM 10 x 10 cm^2 stack coupled to the optical readout matrix is on the left side; on top, there is the thin Mylar window. The readout board and the cables to connect the detector to the FPGA module are on the right side.	45
2.4	Gas gain for the different gas mixtures [21].	49
2.5	Two configurations of GEM-based radiation detectors.	51
2.6	Current at the last GEM vs the proton beam current of the 18 MeV cyclotron. The black dashed line represents a linear fit to the data. The bottom plot shows the residuals.	52
2.7	Number of photons produced in the gas above 400 nm per secondary electron for different CF_4 gas mixtures, as a function of the gain [35].	55
2.8	Secondary scintillation spectra of different $Ar : CF_4$ gas mixture. The broad emission bands in the UV (250 nm) and VIS (630 nm) wavelength ranges are characteristics of CF_4 scintillation. Sharp emission lines above 695 nm are due to the presence of Ar. Intensity normalized to amplitude of peak at 630 nm [7].	56

- 2.9 Scheme of the scintillation mechanisms leading to light emission in $Ar : CF_4$ in the wavelength range 400-820 nm. Emission of photons in the UV band (blue), in the VIS band (yellow) and in the Near-Infrared (NIR) range (red) is represented by undulating arrows. Image adapted from [6]. 57
- 2.10 Optical transmission of ITO glass used in the first version of the LaGEMPix detector (blue line) measured for wavelengths ranging from 200 nm to 800 nm [7]. 59
- 2.11 The 10 x 10 cm^2 Triple-GEM detector set-up in the CERN Calibration Laboratory. 60
- 2.12 The UniBEaM (1) detector and the glass sample (2) installed at the end of the BTL of the IBA Cyclone 18MeV cyclotron at the Bern University Hospital (Inselspital). An aluminium disk (3) is placed behind the glass sample to measure the beam current. 62
- 2.13 Irradiated EBT3 GafchromicTM film showing a beam spot of 3 cm in diameter. 63
- 2.14 Proton beam profiles measured with the UniBEaM. 64
- 2.15 The LaGEMPix imager and its design: 1 – Flex connection to the Gate driver on glass. Gate drivers are on the backplane (chip on glass) indicated by the blue oval; 2 – Readout Integrated Circuit (ROIC); 3 – Sensitive array on glass substrate; 4 – 3D printed holders to fix the triple-GEM; 5 – three CAT 6 network cables, one from each ROIC; 6 – two flat Grey Ribbon cables, 1 x 40 pin from the 1st ROIC (top) and 1 x 26 pin, from the gate driver (bottom); 7 – box with the FPGA module; 8 - USB cable to connect to a laptop; 9 – Power connection. 66
- 2.16 Thin film image sensors produced by Holst Centre/TNO. The building blocks are scalable (developed up to 32 x 35 cm^2). 66
- 2.17 EQE (black curve and left axis) and Spectral Response (SR) (red curve and right axis) of the OPD layer deposited on the readout matrix. The broad emission band of $Ar : CF_4$ with a peak at around 630 nm is represented by the orange region. 68
- 2.18 Thin Film Transistor (TFT) backplane. 70

2.19	Schematic diagram of the active OPD and TFT matrix [65].	72
2.20	Schematic circuits: a) Switch ON b) Switch OFF.	72
2.21	Readout line controlled by the gate driver.	73
2.22	Flowchart of the readout process.	74
2.23	The schematic TFT array design.	75
3.1	a. The LaGEMPix with a lead block, 2.5 cm in thickness, positioned in front of the detector: (1) gas outlet; (2) the 100×100 mm ² triple-GEM stack coupled to the optical readout with the thin Mylar window on top; (3) 3D-printed braces to hold together the triple-GEM detector and the image sensor; (4) lead block; (5) cables to connect the detector to the readout system; (6) FPGA module; (7) custom-made support. b. A heatmap representing the detector's image following exposure to 40 kV X-rays.	92
3.2	Profile depicting the response at the edge when exposed to 40 kV X-rays, using a 2.5 cm thick lead block. The data is fitted with a logistic function, as indicated by the red line.	93
3.3	a. A 3 mm copper plate was employed to assess spatial resolution using the LSF method, with numbers indicating the millimeter spacing between holes. b. Heatmap representation of the copper mask subjected to 40 kV X-rays. A ROI marked by a green rectangle was defined for holes spaced 3 mm apart. Spatial resolution was calculated by fitting the ROI 's profile with a Gaussian function.	94
3.4	The response profile represents the average response along a line for holes with a diameter of 5 mm, positioned 3 mm apart from each other (edge to edge). The FWHM derived from the Gaussian distribution is 7.10 ± 0.30 mm for the left hole and 6.80 ± 0.20 mm for the right hole. By employing a double Gaussian function, the distance between their centers was determined to be 7.98 mm.	95

- 3.5 a. A lead-made imaging target in the form of a 0.05 mm lead thickness line pair mask of type 53. b. Heat map illustrating the condition of the MTF mask following exposure to 30 kV X-rays. 96
- 3.6 Profile showing the edge response when employing the GEMPix detector with 40 kV X-rays, facilitated by a 2.5 cm thick lead block. The data is fitted with a logistic function, illustrated by the red line. The variations observed at approximately 1.4 cm are attributed to the Timepix chip intersections. 98
- 3.7 The response profile of the GEMPix detector, representing the average response along a line, pertains to holes with a diameter of 1.3 mm, positioned 1 mm apart from each other (edge to edge). To calculate the FWHM for the three holes (as specified in Table 3.1), the profile was subjected to a fitting process utilizing a triple Gaussian function. 99
- 3.8 Heat map representation generated by irradiating the GEMPix with 30 kV X-rays, employing a line pair mask of type 53 as the imaging target. To calculate the normalization factor $C(0)$ in Equation 3.2, two distinct regions were identified: the upper region within a green rectangle, corresponding to maximum pixel intensities, and a lower region enclosed by a black rectangle, indicating the minimum values. 100
- 3.9 MTF as determined for the GEMPix detector utilizing equation 3.2, with the measurement conducted using mask type 53. 101
- 3.10 The LaGEMPix simulation, featuring a 2.5 cm thick lead block positioned 4 cm away from the Mylar window (a), and a 1 mm thick copper plate located at a distance of 3.3 cm from the Mylar window (b). These visual representations were generated using FLAIR version 3.1-8, the graphical user interface for FLUKA. 102
- 3.11 Simulated ESF obtained from edge projection and fitted with a logistic function. These results were achieved using 40 kV X-rays, a beam aperture of 1 cm, and a detector-source distance of 230 cm. The error bars are negligible in comparison to the data points. 103

- 3.12 Representation of the simulated energy deposition density within the drift gap, with delineated regions for subsequent data analysis identified by solid yellow lines. 104
- 3.13 One-dimensional projection of the 1.3 mm holes spaced at 2.5 mm intervals. The LSF derived from the chosen region results in a distribution with a mean hole diameter of 1.47 mm. 105
- 3.14 Illustration depicting the enhanced setup of the LaGEMPix detector. 108
- 3.15 a) Heat map representation of the copper mask subjected to 40 kV X-rays, with a designated ROI marked by a green rectangle around the 3 mm spaced holes. The spatial resolution was determined by fitting the profile within the ROI using a Gaussian function. b) The line-average response profiles of 5 mm diameter holes, spaced 3 mm apart (edge to edge), are presented for both the original (depicted in orange) and upgraded (depicted in black) versions of the LaGEMPix. In the case of the upgraded version, the Full Width at Half Maximum (FWHM) measured using Gaussian distribution is 6.16 ± 0.13 mm for the left hole and 5.75 ± 0.15 mm for the right hole. Additionally, the center-to-center distance of 7.86 mm was determined by fitting the profile using a double Gaussian function. 110
- 3.16 The GEM-TFT radiation detector with high-resolution. a. The detector's structure, which includes a TFT backplane array and a triple-GEM frontplane. This depiction highlights the TFT pixel arrangement and the associated drive and read-out circuit diagram. b. A photograph shows the integration of the detector with the read-out electronics. 112
- 3.17 Spatial resolution assessment: a. Utilizing a line pair mask of type 17 crafted from 0.02 mm thick lead as the imaging target. b. Displaying a heatmap of the TFT readout following exposure to 30 kV X-rays. c. The MTF measurement was conducted using mask type 17 for the GEM -TFT detector. 113
- 4.1 Component level radiation testing involved three strips on glass, labeled as 1, 2, and 3, encompassing TFTs within areas demarcated by dashed squares. . . . 123

- 4.2 The configuration employed during the proton beam experiments conducted at the BTL of the Bern medical cyclotron: a. The UniBEaM detector and the GEM-TFT detector were installed at the end of the BTL of the IBA Cyclone 18 MeV cyclotron at the Bern University Hospital (Inselspital). An extract window is placed before the entrance Mylar window of the detector. b. Detailed image of the exit window with a diameter of 3 cm, presenting a single PEM (indicated by the arrow), which was used for the radiation hardness tests. c. A schematic illustration delineates the layout of the strip of TFTs that were subjected to direct irradiation by the proton beam. 124
- 4.3 Evaluation of radiation hardness in dual gate TFTs. a-c. Transfer characteristics of $I_d - V_g$ before irradiation (Pristine - grey), after irradiation (red) with 0.5, 29, and 250 kGy 18 MeV protons, and following the mitigation of V_{ON} shift (green) by applying a bottom gate bias of -4, -13, and -40 V, respectively. d. Transfer characteristics of $I_d - V_g$ before irradiation (grey), after irradiation (red) with 29 kGy 18 MeV protons, and after recovery through a thermal annealing process for 1 hour at 165 °C (green). 125
- 4.4 Initial operational assessment with protons at the Bern medical cyclotron. a. Captured image displaying the beam's circular configuration using GAFCHROMIC[®] EBT3 film. b. Captured image demonstrating the beam's circular shape using the GEM-TFT detector. c. Least Significant Bit (LSB) value in relation to beam intensity recorded by the detector during the operation of the 18 MeV cyclotron. The dashed line represents a linear regression fitted to the dataset. 127
- 4.5 Setup utilized for conducting photon beam tests with the Varian Linac True-Beam at Zentrum für Strahlentherapie in Freiburg. The GEM-TFT detector was situated on the treatment couch, while the treatment head was oriented at 90°. 128
- 4.6 LSB value vs dose rate (MU/min) of the detector using the commercial Linac TrueBeam Varian. The dashed line represents the linear fit to the data. 129

- 4.7 LSB value vs dose expressed in MU of the detector using the commercial Linac TrueBeam Varian. The dashed line represents the linear fit to the data. 130
- 4.8 The configuration employed for conducting proton and carbon ions beam tests at CNAO. In Figure (a), the GEM+TFT detector is securely contained within a waterproof PMMA box, which is affixed to the positioning system of the water phantom. This arrangement permits the adjustment of the distance between the entrance window and the PMMA box along the beam axis. In Figure (b), the detector is positioned within a vertical support and situated on the treatment couch, with a high-Z material covering a portion of its active area for the purpose of spatial resolution analysis. 131
- 4.9 Dose response as a function of time for the GEM-TFT detector and the DDS utilized at CNAO. The data have been normalized with respect to the peak values. A selected subset of CNAO DDS data points is displayed (every third point) to improve clarity. It is important to note that the GEM-TFT data points between beam spills retain non-zero values owing to the 1-second frame rate, which captures both the beam ON and OFF states. 132
- 4.10 Bragg curves exhibit an increasing energy deposition as they penetrate deeper, reaching a peak at the end of their range (151 mm), which is followed by a steep decline. This phenomenon corresponds to the energy loss of ionizing radiation as it traverses through water. a) Bragg curve measurements were conducted using 147.72 MeV protons with the GEM+TFT (green) and PTW Peakfinder (red). b) Bragg curve measurements were carried out with 207.97 MeV/n carbon ions using the GEM+TFT (green) and PTW Peakfinder (red). 133
- 4.11 Evaluation of spatial resolution in conditions pertinent to hadron therapy. Edge response profile for 147.72 MeV protons using a high-Z material, as assessed with the GEM-TFT detector and GAFCHROMIC[®] EBT3 films. 134

List of Tables

2.1	List of ITO-bases glass materials.	61
2.2	Summary of the radiation-induced effects for the three tested glasses.	65
3.1	FWHM values were computed for 1D profiles in three specific regions of interest within the images captured using the GEMPix and the 1 mm-thick copper plate.	98
3.2	FWHM values were determined from the 1D profiles for the various regions of interest (ROIs) shown in Figure 3.12. The first line of the table corresponds to the three central holes, while the second line pertains to the top hole. The third line refers to the second horizontal line from the top of the figure, while the fourth line pertains to the singular vertical ROI illustrated in Figure 3.12.	104
3.3	An overview of the spatial resolution achieved with various experimental setups and different detectors, with the addition of FLUKA Monte Carlo simulation results for comparison.	106
3.4	Overview of the spatial resolution achieved using various experimental setups and both editions of the LaGEMPix.	110
3.5	Comparison of spatial resolution attained with the optical readout versus charge readout.	113
4.1	Energy response of GEM-TFT detector normalized to its response to 207.97 MeV/n	135

Part II

Part II

Reprinted Publications

A.C. Maia Oliveira, H.B. Akkerman, S. Braccini, A.J.J.M. van Breemen, Gerwin H. Gelinck, N. Heracleous, J. Leidner, F. Murtas, B. Peeters, M. Silari, “A high-resolution large-area detector for quality assurance in radiotherapy” (submitted to Scientific Reports - Nature).

A. Maia Oliveira, HB. Akkerman, S. Braccini, A. J. J. M. van Breemen, L. Manzano, N. Heracleous, I. Katsouras, J. Leidner, F. Murtas, B. Peeters, M. Silari, “Characterization with X-rays of a Large-Area GEMPix Detector with Optical Readout for QA in Hadron Therapy,” Applied Sciences, vol. 11, no. 14, Art. no. 14, Jan. 2021, doi: 10.3390/app11146459.

A. Maia Oliveira, S. Braccini, P. Casolaro, N. Heracleous, J. Leidner, I. Mateu; F. Murtas, M. Silari, “Radiation-induced effects in glass windows for optical readout GEM-based detectors,” J. Inst., vol. 16, no. 07, p. T07009, Jul. 2021, doi: 10.1088/1748-0221/16/07/T07009.

A. Maia Oliveira et al., “A Large Area GEMPix detector for treatment plan verification in hadron therapy” submitted to TIP2021 Proceedings.

“A large area GEMPix detector with optical readout for hadron therapy (LaGEM-Pix),” ATTRACT Project. <https://phase1.attract-eu.com/selected-projects/lagempix-a-large-area-gempix-detector-with-optical-readout-for-hadron-therapy/> (accessed Feb. 25, 2021).



OPEN

A high-resolution large-area detector for quality assurance in radiotherapy

Andreia Maia Oliveira^{1,2,6}✉, Hylke B. Akkerman³, Saverio Braccini², Albert J. J. M. van Breemen³, Gerwin H. Gelinck³, Natalie Heracleous^{1,4}, Johannes Leidner^{1,7}, Fabrizio Murtas^{1,5,8}, Bart Peeters³ & Marco Silari¹

Hadron therapy is an advanced radiation modality for treating cancer, which currently uses protons and carbon ions. Hadrons allow for a highly conformal dose distribution to the tumour, minimising the detrimental side-effects due to radiation received by healthy tissues. Treatment with hadrons requires sub-millimetre spatial resolution and high dosimetric accuracy. This paper discusses the design, fabrication and performance tests of a detector based on Gas Electron Multipliers (GEM) coupled to a matrix of thin-film transistors (TFT), with an active area of $60 \times 80 \text{ mm}^2$ and 200 ppi resolution. The experimental results show that this novel detector is able to detect low-energy (40 kVp X-rays), high-energy (6 MeV) photons used in conventional radiation therapy and protons and carbon ions of clinical energies used in hadron therapy. The GEM-TFT is a compact, fully scalable, radiation-hard detector that measures secondary electrons produced by the GEMs with sub-millimetre spatial resolution and a linear response for proton currents from 18 pA to 0.7 nA. Correcting known detector defects may aid in future studies on dose uniformity, LET dependence, and different gas mixture evaluation, improving the accuracy of QA in radiotherapy.

Radiotherapy is a modality of cancer treatment that uses ionising radiation to kill cancer cells. It is often used to shrink or eliminate tumours, by damaging the DNA of cancer cells, which prevents them from dividing and growing. One of the main goals of radiotherapy is to deliver a high dose of radiation to the tumour while minimising the dose received by surrounding healthy tissue, in order to minimize side effects and maximize the therapeutic effect. Patient specific quality assurance (PSQA) is a crucial process in radiation therapy to verify the accuracy of treatment plans and ensure the delivery of the correct radiation dose to the intended target volume. PSQA can be conducted through either measurements or independent dose calculation systems, involving a series of tests and checks to compare the calculated dose from the treatment planning system (TPS) with the dose delivered by the treatment machine. The PSQA process typically includes comparisons of measured/evaluated and planned radiation dose distributions, aiming to identify any discrepancies between the two and address them appropriately.

The development of techniques like Intensity Modulated Radiation Therapy (IMRT) and Volumetric Modulated Arc Therapy (VMAT) allows for a better conformity of the dose to the tumour and in numerous cases offers significant improvements with respect to conventional radiotherapy^{1,2}. The resulting treatment plans are often complex, involving multiple beams. The PSQA of these plans, therefore requires accurate evaluation with good spatial resolution³. F. S. Matar et al.³ emphasize the use of detectors with submillimetric precision, even employing solid-state detectors, which results in an outstandingly high spatial resolution of 0.784 mm and 0.2 mm.

Treatment with hadrons (currently protons and ¹²C ions) is a radiotherapy technique that for several types of tumours offers considerable advantages over conventional photon and electron treatments. Since its initial application in 1954, it is gaining popularity as a cancer treatment modality, with a growing number of patients benefiting from its unique properties. By the end of 2022, more than 360,000 patients have undergone particle therapy globally⁴. However, it is worth noting that despite its remarkable potential, the utilization of this

¹CERN - Occupational Health & Safety and Environmental Protection Unit, Radiation Protection Group, 1211 Geneva 23, Switzerland. ²Laboratory for High Energy Physics (LHEP), Albert Einstein Center for Fundamental Physics (AEC), University of Bern, Sidlerstrasse 5, 3012 Bern, Switzerland. ³Holst Centre/TNO, High Tech, Campus 31, 5656 AE Eindhoven, The Netherlands. ⁴Institute of Radiation Physics, Lausanne University Hospital and Lausanne University, Lausanne, Switzerland. ⁵INFN-LNF, 00044 Frascati, Italy. ⁶Present address: EBG MedAustron GmbH, Marie Curie-Straße 5, 2700 Wiener Neustadt, Austria. ⁷Present address: Medidee Services SA, Chemin de Rovéréaz 5, 1012 Lausanne, Switzerland. ⁸Fabrizio Murtas is deceased. ✉email: andreia.cristina.maia.oliveira@cern.ch

cutting-edge approach remains relatively limited when compared to the conventional use of photons and electrons in radiotherapy, which annually treats around 7 million patients⁵. Hadrons are used to irradiate tumours since, unlike photons, they have the unique property of increasing energy deposition with penetration depth, with a peak at the end of the range followed by a sharp drop (Bragg curve). This characteristic provides a more conformal dose distribution to tumours, reducing the negative side-effects due to radiation delivered to healthy tissue⁶. Carbon ions have a higher relative biological effectiveness (RBE) than protons or photons i.e., the same absorbed dose leads to higher cell damage. There is considerably less dependence on biological variations between and within tumours for the response to ¹²C ion irradiation that makes this advanced modality suitable for the treatment of tumours with known resistance factors (such as hypoxia, undifferentiation and heterogeneity of the tumour) against photons and protons⁷.

To provide an effective dose delivery, radiation therapy requires instruments with high spatial resolution but also extremely accurate dose calculation. The International Commission on Radiation Units and Measurements (ICRU) states that at the level of one standard deviation, a relative accuracy of 3% is desirable, although 5% is often accepted, while a reproducibility of 2% is required⁸. The evaluation of dose and dose distribution administered to patients is a fundamental quality control process during the radiation treatment and it is even more crucial for the evaluation of the dose delivered through advanced techniques such as stereotactic radiosurgery that combines high conformity and high dose gradient. This technique has demonstrated remarkable effectiveness in treating a wide range of cancers, including brain metastases, primary non-small cell lung cancer, metastatic lung tumours, and hepatocellular carcinoma^{9,10}. This form of radiation therapy delivers high doses of radiation within a few fractions and dose fall-off values can reach up to 30%/mm¹¹. Additionally, a Quality Assurance (QA) procedure in hadron therapy requires not only an accurate dose calculation, but also a high spatial resolution. A high spatial resolution of the 2D dose distribution is important because most of the treatment plans in Pencil Beam Scanning (PBS) are characterized by very high “in-field” dose gradients. Distal falloff values defined as the distance between the distal position of the 80% and 20% dose levels, z80-20, at intensity-modulated proton therapy can reach 4 mm, which corresponds to a gradient of 15%/mm¹². The positioning systems employed at particle therapy centres strive to achieve submillimetric precision. QA techniques and equipment are put in place to guarantee that these requirements are met. Detectors for monitoring important beam parameters, such as beam position and delivered dose, are essential to carry out an efficient QA procedure¹³. In routine QA checks, diverse types of dosimeters are used to measure the 2D dose distribution. An all-in-one system that offers accurate and real-time measurements with sub-millimetre spatial resolution and uniform response to the beam energy is highly desirable, but not available today.

To enhance QA capabilities and optimize treatments with hadron beams, we recently presented a first proof-of-concept based on a Gas Electron Multiplier (GEM) detector coupled to a Timepix readout for applications in radiation therapy¹⁴. However, the detector area was rather small ($2.8 \times 2.8 \text{ cm}^2$) and could not be scaled up cost-effectively to cover the typical maximum field size of $20 \times 20 \text{ cm}^2$ in radiation therapy. In order to achieve larger areas, another prototype based on a GEM detector coupled to an optical readout was developed¹². This detector combines a triple-GEM¹⁵ and a pixelated readout based on a matrix of organic photodiodes (OPDs). A more comprehensive explanation as well as the results of its characterization using X-Rays can be found in Ref.¹². However, the obtained spatial resolution of only a few millimetres, limited by the isotropic emission of the photons, is insufficient for QA in hadron therapy (Supplementary Fig. 1). As a first attempt to improve the spatial resolution, the gap between the last GEM and the readout was reduced to minimize the impact of this effect. Even though the results with the reduced gap¹⁶ demonstrated an important improvement, the desired sub-millimetre spatial resolution was not achievable for a compact system with optical readout, i.e., without the introduction of collimators or lenses in the set-up¹⁷⁻²⁰.

Based on the knowledge gained from studying the characteristics of the original detector, we developed a new prototype with the goal of enhancing the spatial resolution. This novel detector utilizes a charge readout based on a matrix of thin-film transistors (TFT) where the OPD frontplane which was present in the previous version is eliminated, leaving a TFT-only electronic readout. In this case, secondary electrons produced in the triple-GEM are guided by electric fields and are directly measured by the readout, thus avoiding the worsening of the spatial resolution by the isotropic light emission (Supplementary Fig. 1). This allows a compact, and more easily scalable device with an expected submillimetre spatial resolution fulfilling the criteria outlined in Ref.¹².

In this article, we report on a prototype consisting of a triple-GEM detector and a 200 ppi resolution TFT-based charge readout with $60 \times 80 \text{ mm}^2$ active area. The novel detector can be employed in both conventional radiation therapy with X-ray photons as well as in hadron therapy using protons and carbon ions. It measures secondary electrons produced by the GEMs with sub-millimetre spatial resolution, allows reconstruction of the Bragg curve and shows linear response for proton currents from 18 pA to 0.7 nA.

Detector design

The new GEM-based prototype consists of a triple-GEM coupled to a pixelated readout using a TFT array. Figure 1 shows the schematic of the detector. The triple-GEM includes a 3.5 mm drift gap between the top GEM electrode (GEM1) and the cathode, which is a 15 μm thick Mylar window. The drift gap is large enough to minimize inefficiencies in charged particle detection²¹ but not too large to affect the time performance. The transfer gaps between GEM1 and GEM2 and between GEM2 and GEM3 have a thickness of 1 mm and 2 mm, respectively. The last gas region between GEM3 and the readout, identified as the induction gap, is 1 mm thick. The triple-GEM was supplied with a high voltage system (not shown in Fig. 1) designed specifically for the high voltage power supply of this kind of detector²². The triple-GEM detector is operated in a continuous flow of Ar/CF₄ (90/10) or Ar/CO₂ (70/30) gas mixture supplied at a rate of 5 l/h. These types of gas mixtures for GEMs feature attractive

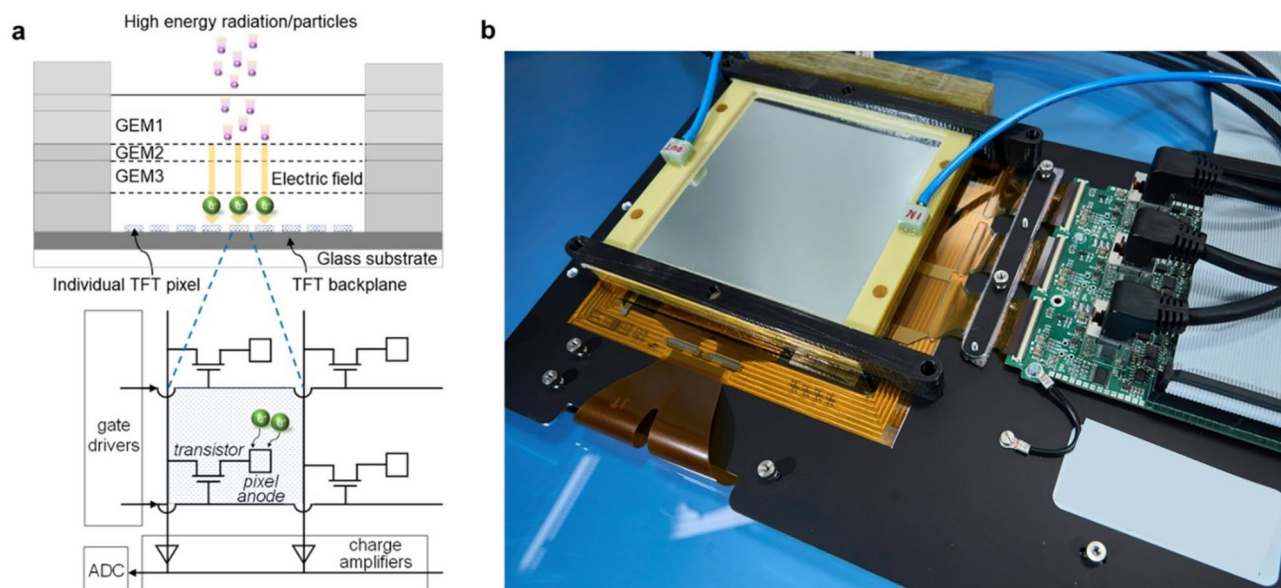


Figure 1. High resolution GEM-TFT radiation detector. **(a)** Schematic of the detector, consisting of a TFT backplane array and a triple-GEM frontplane. The magnification shows the TFT pixel layout, together with the drive and read-out circuit diagram. **(b)** Photograph of the detector integrated with the read-out electronics.

properties, such as high electron drift velocity and low electron diffusion²³. Moreover, these gases are inherently safe, as they are non-flammable, which is particularly important for use in a hospital environment.

GEMs offer several advantages, including a low material budget and high amplification factors enabling single-particle detection. Furthermore, they have a well-established track record in particle detection, and their radiation hardness and aging characteristics have been documented, particularly in radiation-harsh environments like the Large Hadron Collider experiments at CERN²⁴. The robust radiation resilience of GEMs, alongside the convenience of accessing standardized items, eliminates the need for custom fabrication to meet the specific requirements of this innovative detector prototype. However, drawbacks such as potential saturation at higher gains and the risk of discharges, particularly under mishandling or excessive gain conditions, should be taken into account.

GEM based detectors show a well-known exponential dependence of the effective gain on the GEM voltages. The electric fields between the top and bottom copper layers in each GEM foil can be adapted to the intensity of the beam and the type of primary particles impinging on the detector. We performed a gain scan for the different incident beams to find a stable operation condition for the detector.

The triple-GEM frontplane was coupled to a 200 ppi a-Indium Gallium Zinc oxide (IGZO) based active matrix TFT backplane. The backplane has a self-aligned dual-gate (SA-DG) TFT architecture^{25,26}, which was demonstrated previously to yield a superior performance in higher current drive, steeper subthreshold slope and better determined onset voltage (V_{on}) close to a gate voltage (V_g) of 0 V. The use of a-IGZO leads to lower off-currents and off-current uniformity compared to other TFT technologies, positively impacting the noise of the readout electronics.

Figure 2a shows a cross-section of the TFT backplane, monolithically integrated on a glass carrier. Connected to the TFT drain electrode is a metal contact pad (in Fig. 2a depicted by *pixel anode* in the schematic) fabricated on top of an interlayer to enlarge the effective area on which the secondary electrons from the GEM can be collected. Figure 2b and c show a photograph of the finished backplane and a zoomed image to show the individual pixels, respectively. The fabrication process of the TFT backplane consists of 6 lithographic patterning steps and is described in the Methods section. All process steps are flat panel display compatible, illustrating a facile route to mass-production. The dual-gate TFT performance is provided in Fig. 2d, where the transfer characteristics of 70 TFTs ($W/L = 15/5 \mu\text{m}$) mapped over the full $320 \times 352 \text{ mm}^2$ area of the motherglass are shown. The TFTs have a typical linear mobility of $29.1 \pm 0.8 \text{ cm}^2/\text{Vs}$, turn-on voltage (V_{on}) of $0.8 \pm 0.3 \text{ V}$, ON/OFF current ratio $\sim 10^7$, and a subthreshold swing of $0.4 \pm 0.02 \text{ V/decade}$.

It is important to note that the detector—being a first prototype—exhibits several pixel defects, including non-functioning lines and other imperfections resulting from a limited yield of a repair step performed for the TFT backplane, where a design flaw was observed after completion. We would like to acknowledge that these issues are inherent to this particular backplane design and further design optimization will remove all defective lines. Tests targeting the evaluation of factors like spatial resolution were minimally impacted by the readout defects observed in the initial prototype. However, it was not feasible to perform measurements intended to assess dose uniformity due to the intrinsic nature of this early-stage prototype.

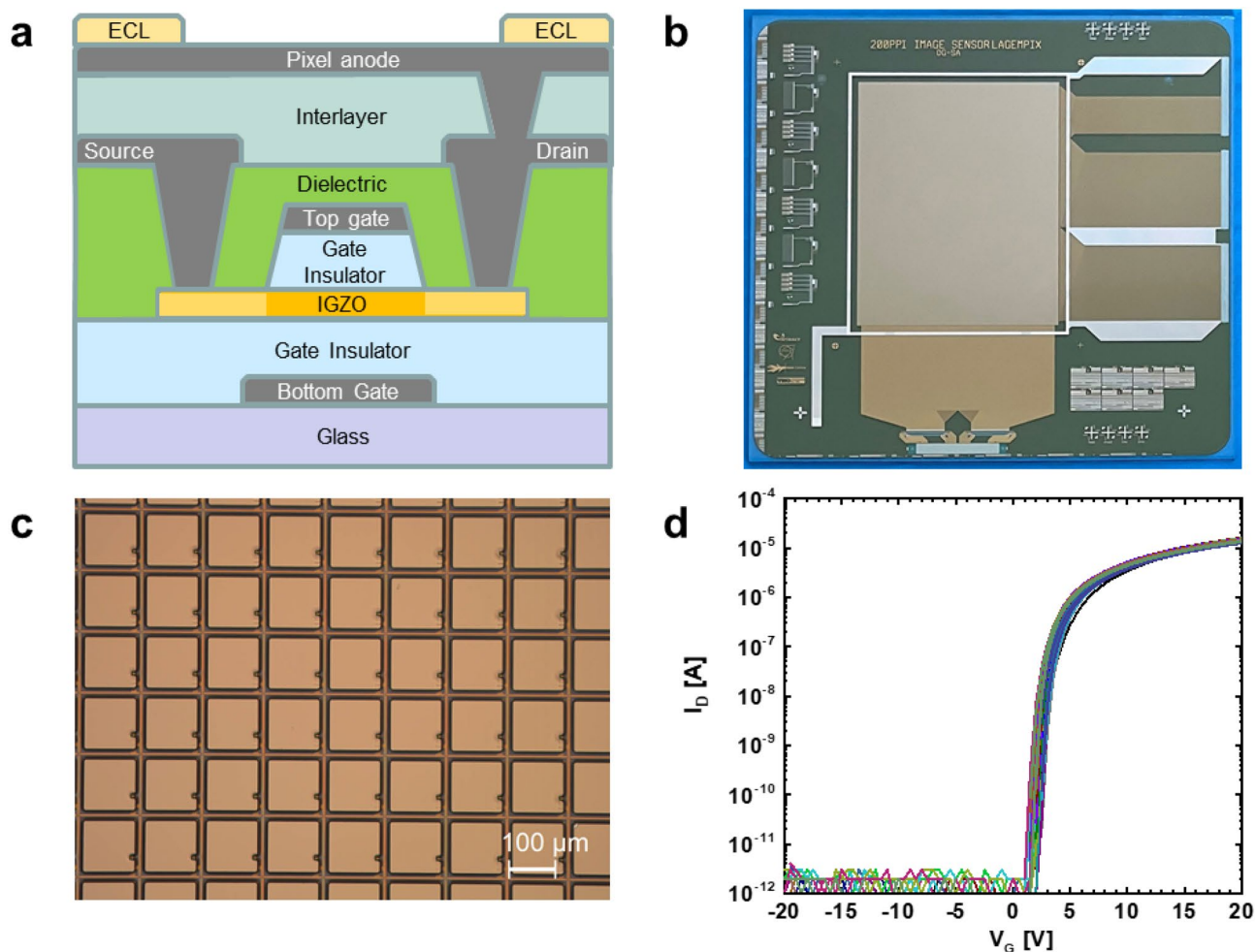


Figure 2. TFT backplane. (a) Cross section of the dual gate self-aligned TFT. (b) Photograph of the TFT backplane. (c) Microscopy image of part of the TFT backplane array showing individual pixels. (d) TFT characteristics of 70 dual-gate TFTs ($W/L = 15/5 \mu\text{m}$) operated in bulk accumulation mode by connecting top-gate and bottom-gate ($V = V_{G,\text{bottom}} = V_{G,\text{top}}$).

Methods

TFT backplane fabrication

The full stack cross-section is shown in Fig. 2a. Details of the TFT fabrication are described in Ref.²⁷. As a final process step, a $1.8 \mu\text{m}$ thick SU8 edge cover / pixel definition layer is deposited and photolithographically structured to define the active pixel area.

TFT characterization

The electrical characterization of the dual gate TFTs was performed at room temperature in a dark ambient using a semiconductor parameter analyser (4156C, Agilent). A source-drain voltage of 1 V was used in all cases. Transistor transfer characteristics were recorded by sweeping the top-gate and grounding the bottom-gate. The V_{on} of the TFTs was determined from the onset of the top-gate voltage at which the source-drain current starts to increase.

Drivers and read-out

The gate drivers (Sitronix ST5041) and readout integrated circuits (Analog Devices AD71124) are bonded to the fan-out electrodes. The detector response was measured using a custom-made electronic system and readout software (LabVIEW based). The detector is biased using a custom-made board and connected to an FPGA digital interface that reads the data and connects to the computer.

The readout was set to the sensitivity level of 0.5 pC, so that the least significant bit (LSB) of the 16-bit readout corresponds to a charge of approximately 47 electrons. The maximum frame rate is 95 fps ($22 \mu\text{s}$ line time \times 480 lines). The standard frame rate used for the majority of the experiments was 1 fps. However, during the clinical evaluation with photons utilizing the commercial Linac TrueBeam Varian, a frame rate of 10 fps was employed. The sum of all pixels for the selected ROI for 200 recorded images was averaged. The LSB value measured by

the TFT-based readout vs high voltage gain follows an exponential trend as expected with low-energy (40 kVp X-rays) and high-energy (6 MeV) photons, protons and carbon ions of clinical energies.

GEM-TFT detector characterization

The GEM-TFT detector was characterized using low energy X-rays (30–40 kV) at the Calibration Laboratory of CERN Radiation Protection Group²⁸. To evaluate the spatial resolution, we placed an X-ray test pattern in front of the Mylar window to calculate the modulation transfer function (MTF). The MTF measurements were performed according to a method previously described¹².

Next, the detector was irradiated with 17.5 MeV protons at beam intensities of up to 1.3 nA using the research Beam Transfer Line (BTL) of the IBA Cyclone 18 MeV cyclotron in operation at the Bern University Hospital (Inselspital), which is used as an irradiation facility for multi-disciplinary research^{29,30}. In order to measure and control the beam characteristics during the irradiations, a UniBEaM detector³¹ was installed in the BTL, as shown in Supplementary Fig. 2a. The UniBEaM measures the beam profiles in the x and y transverse directions by passing scintillating fibres through the beam. The protons are extracted into air through a 50 μm stainless steel window facing the Mylar window. The parameters of the cyclotron operation were selected aiming for a uniform dose to the 3 cm diameter target, which is the diameter of the beam exit window.

Discrete dual-gate TFTs (channel width 15 μm , channel length 5 μm), were irradiated with three different doses (0.5, 28, 250 kGy) to evaluate their radiation hardness. A strip with multiple TFTs was placed perpendicular to the proton beam, as shown in Supplementary Fig. 2b. Protons directly hit the TFT with the active area facing the exit window (Supplementary Fig. 2c), which is the same orientation in which the TFT backplane was coupled to the triple-GEM detector (Fig. 1a and Supplementary Fig. 2a). An aluminium disk was placed behind the sample, connected to a Keysight B2985A electrometer to measure the beam current simultaneously. All electrodes were kept floating during the irradiation.

Clinical evaluation with photon and proton/carbon ion beams

We tested the GEM-TFT detector flushed with ArCO_2 (70:30) using a commercial Linac TrueBeam Varian using a 6 MV flattening filter (FF) photon beam at Zentrum für Strahlentherapie in Freiburg (Supplementary Fig. 3). The depth dose curve measured for the 6 MV photon beam has two distinct regions: the characteristic build-up region close to the surface and the charge particle equilibrium region at deeper depths³². To avoid perturbations in the measurements as a result of the contamination of electrons in the build-up region, solid water slabs with a total thickness of 1.7 cm were positioned in front of the detector. The detector was centred visually in the luminous field with the help of the lasers. The detector was inserted in the vertical support and perpendicular to the radiation beam (Supplementary Fig. 3).

The GEM-TFT was finally tested at CNAO (*Centro Nazionale di Adroterapia Oncologica*, the Italian National Centre of Oncological Hadrontherapy sited in Pavia) with the beams used in cancer treatment. The CNAO synchrotron provides proton beams with kinetic energies from 60 to 250 MeV and carbon ion beams in the range 120–400 MeV/u³³. The beam intensity for protons varies from 10^9 to 10^{10} particles/s, while for carbon ions it ranges from 4×10^7 to 4×10^8 particles/s. We performed two types of measurements with two different set-ups.

Firstly, an integrated system consisting of a commercial water phantom and the GEM-TFT was used to perform depth scans (Supplementary Fig. 4a). A light-tight and waterproof box with a wall thickness of 10 mm was designed and manufactured to house the GEM-TFT detector in water. The box is made of black polymethyl methacrylate (PMMA, type: PLEXIGLAS NOIR 811—PERSPEX 9T30). Additionally, two supports with rails to guide and fix the baseplate inside the box were designed and manufactured.

Secondly, the detector was placed directly on the treatment couch (Supplementary Fig. 4b). The detector was positioned perpendicular to the beam in a vertical custom-made structure providing a well-aligned set-up. To evaluate the spatial resolution using the edge response method, we placed a high-Z material of variable thickness in front of the detector covering a portion of its active area to create a sharp edge as shown in Supplementary Fig. 4b.

Results and discussion

Characterization of the GEM-TFT detector

To find the correct working point (voltages) that should be applied to the triple-GEM, it is necessary to perform a gain scan. The response obtained by summing all pixel values versus the sum of the GEM gas amplification voltages shows the expected exponential dependence. This was the expected behaviour since the gain, i.e., the ratio of the number of electrons produced over the number of primary electrons, depends exponentially on the applied GEM voltages¹⁵. Besides that, a current scan using photons at beam intensities ranging from 5 mA up to the maximum current of 25 mA available in the X-Ray generator was performed. The GEM-TFT detector demonstrates a linear dose response across the entire range ($R^2 = 0.9965$).

The modulation transfer function (MTF) was acquired using a lead mask with a bar pattern, a common method to determine the spatial resolution³⁴ and identical to the procedure used for our previous optical detector¹². These tests were performed using 30 kV X-rays with the N-5 filter to increase the contrast of the output image. The lead mask is 0.2 mm thick with a resolution of 0.177 to 3.33 LP/mm, as shown in Fig. 3³⁵. The detector yielded an MTF below 10% at 1.2 LP/mm, which corresponds to 0.83 mm spatial resolution. This sub-millimetre resolution confirms the state-of-the-art performance when benchmarked against the 2.5 mm resolution of the commercial OCTAVIUS[®] 1000 SRS detector³⁶.

The first experimental test at the Bern cyclotron using protons with the GEM-TFT system is shown in Fig. 4b. The protons are extracted into air by means of a 50 μm stainless steel window with a circular shape. A GAF-CHROMIC[®] EBT3 film was placed in front of the exit window to inspect the shape of the beam. The irradiated

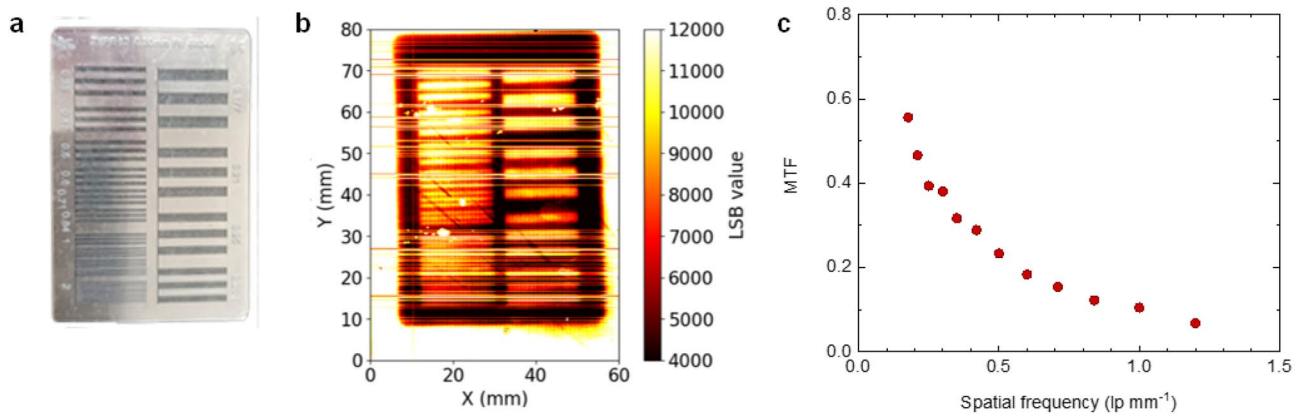


Figure 3. Spatial resolution. (a) Line pair mask type 17 made of 0.02 mm thick lead used as an imaging target. (b) Heat map of the TFT readout after irradiation with 30 kV X-rays. (c) Measured MTF with mask type 17 for the GEM-TFT detector.

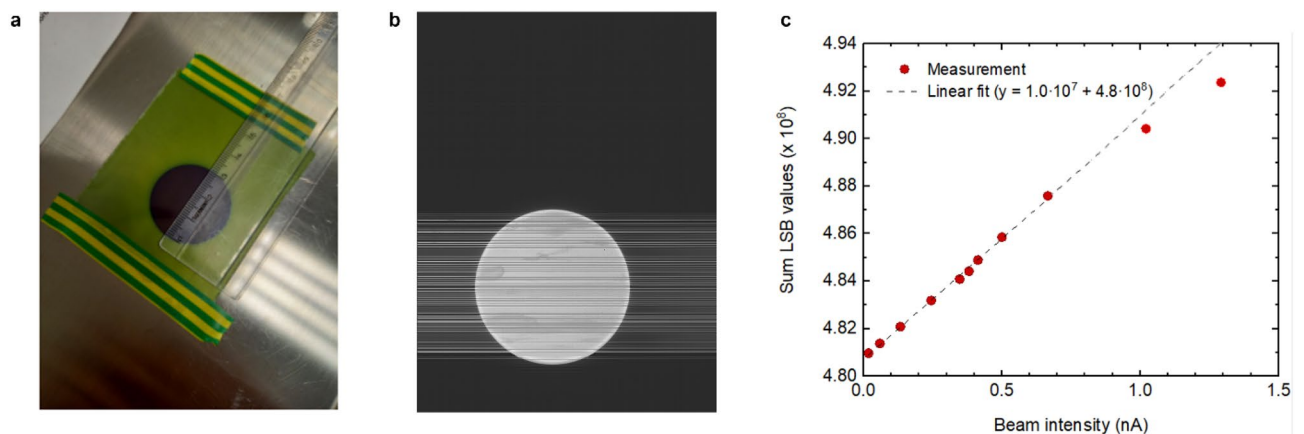


Figure 4. First functional test using protons at the Bern medical cyclotron. (a) Acquired image showing the circular shape of the beam using a GAFCHROMIC® EBT3 film. (b) Acquired image showing the circular shape of the beam using the GEM-TFT detector. (c) LSB value vs beam intensity of the detector using the 18 MeV cyclotron. The dashed line represents the linear fit to the data up to 0.7 nA (●).

film indicates a 3 cm diameter circle as shown in Fig. 4a. The measured result with the GEM-TFT detector showed that the full width at half maximum (FWHM) for the beam was 3.024 ± 0.005 cm. The horizontal non-functional lines in the readout images in Figs. 3b and 4b are line defects in the TFT array. These measurements confirm that it is possible to study the beam size and shape indicating that the prototype is a promising tool for beam diagnosis. Additionally, a current scan with 18 MeV protons at beam intensities up to 1.3 nA was performed. For a uniform beam of 3 cm diameter, 1.3 nA corresponds to a beam intensity of approximately 10% of the maximum beam intensity for protons used at CNAO³³. We measured a linear behaviour between 18 pA and 0.7 nA with the sum of the GEM voltages equal to 600 V as shown in Fig. 4c. Nevertheless, the two data points acquired for currents exceeding 1 nA exhibit unexplained non-linearity. To gain a better understanding, further investigations are planned.

Radiation hardness plays an important role in devices, which may be subjected to 100 Gy weekly radiation dose in a routinely operated particle therapy centre. To evaluate the radiation hardness of the prototype, we compared the background in the absence of the beam and the response to a uniform 40 kVp X-Ray field before and after a uniform irradiation with protons.

Figure 5 shows a comprehensive overview of the radiation hardness results. The grey curves correspond to the transfer characteristics of TFTs in their pristine state, before irradiation. V_{on} is close to 0 V in all cases. After exposure to 0.5, 28, 250 kGy of 18 MeV protons, V_{on} shifts to -4 V, -13 V and ~ -40 V respectively (Fig. 5a–c, red curves). Such a negative V_{on} shift is typically observed for oxide based TFTs when exposed to high energy radiation (X-rays^{37,38} and 5 MeV protons³⁹) and attributed to an increase in electron concentration of the a-IGZO TFT active layer. The shift in V_{on} can however be compensated for in our dual-gate TFT technology. From the green curves in Fig. 5 it can be observed that by negatively biasing the bottom gate, the V_{on} of the TFTs can be clearly tuned over a large voltage range and shifted back to its initial state at about 0 V. The radiation induced V_{on} shift has a temporal character. With time, the device characteristics return to their original position. The

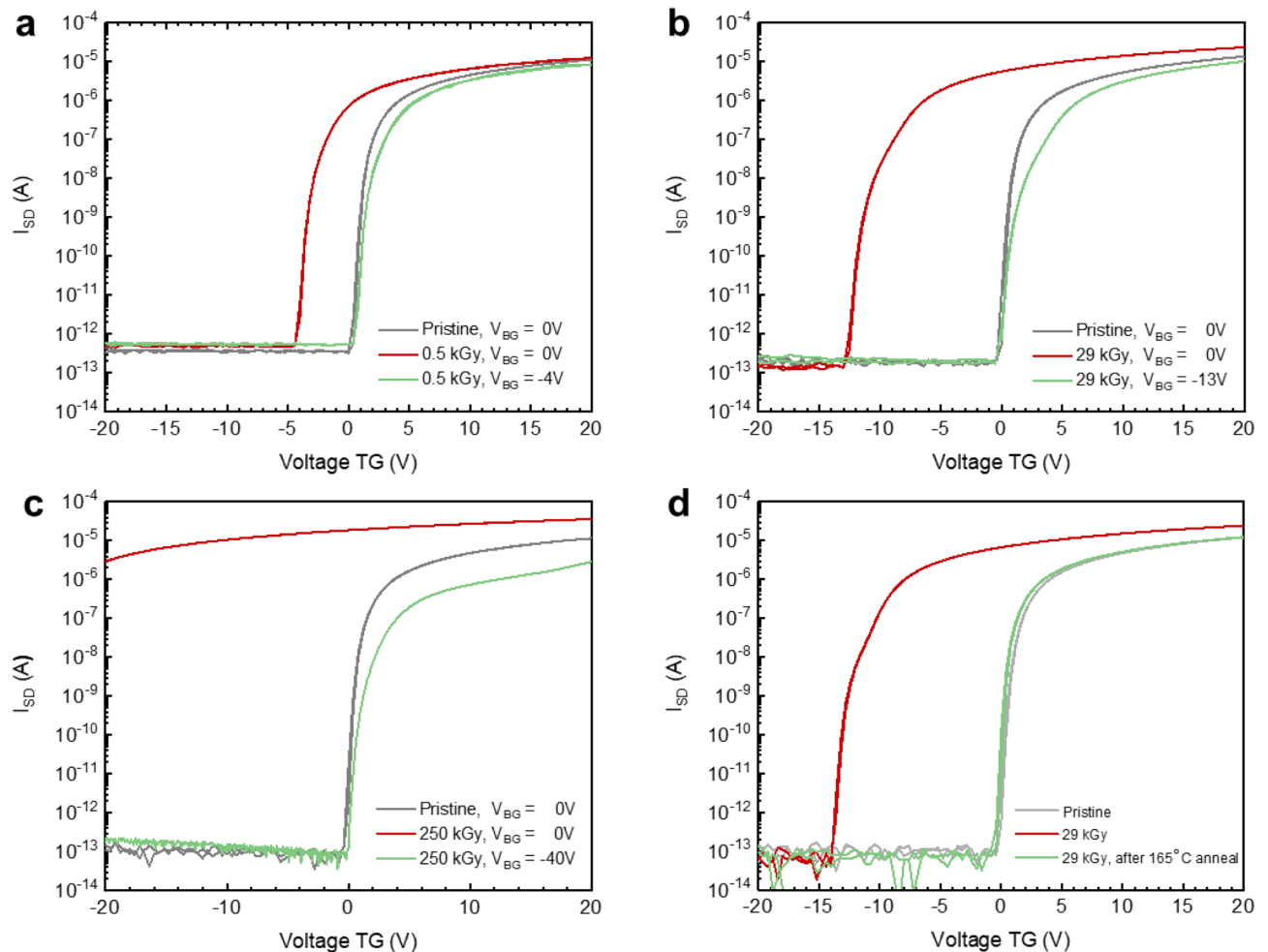


Figure 5. Radiation hardness of dual gate TFTs. (a–c) I_d – V_g transfer characteristics before (grey), after irradiation (red) with 0.5, 29 and 250 kGy 18 MeV protons respectively, and after compensation of the V_{on} shift (green) by applying a bottom gate bias of –4, –13 and –40 V respectively. (d) I_d – V_g transfer characteristics before (grey), after irradiation (red) with 29 kGy 18 MeV protons, and after recovery by a thermal annealing process for 1 h at 165 °C (green).

recovery process of the TFT can be accelerated by thermal annealing. Figure 5d shows the fully recovered V_{on} to its initial state after an annealing process for 1 h at 165 °C.

A detector used for treatment plan verifications in a busy hadron therapy centre is exposed to a dose of approximately 100 Gy per week. This means that the dose of 29 kGy received by the second TFT sample over a short period of time would be equivalent to approximately 6 years of operation of a commercial detector. The relatively small shift at relevant radiation doses combined with its temporal character led us to believe that the proton radiation hardness of our IGZO TFTs will be sufficient for first applications.

Clinical evaluation with photon and proton/carbon ion beams

The electron linear accelerator was calibrated to administer a dose of 100 Monitor Units (MU) for a dose rate dependence from 100 MU/min to 600 MU/min, approximately 0.8 Gy, for a 10×8 cm² field. The dose rate at 6 MV FF beam can reach 600 MU/min. After a gain scan, the detector was operated with the sum of the GEM voltages equal to 750 V. The readout was set to the highest sensitivity level of 0.5 pC and the frame rate was 10 fps. A relative difference of 4.4% between the response to the lowest (100 MU/min) and the highest dose rate (600 MU/min) was observed. We performed a dose scan with 6 MV photons and we measured a linear behaviour between 8 and 800 MU as shown in Fig. 6. The highest dose rate available of 600 MU/min, approximately 6 Gy/min, was selected.

Electronic portal imaging devices (EPID) dosimetry, also referred to as Portal dosimetry, presents notable advantages for patient-specific quality assurance (PSQA) in IMRT and VMAT^{40,41}. EPID systems offer exceptional spatial resolution and sensitivity, which is crucial for precise dosimetry measurements and PSQA tasks. Study⁴⁰ reports a-Si 1000 flat panel imager from Varian Medical Systems featuring a phosphor screen, 1.0 mm Cu build-up layer, and a hydrogenated a-Si:H photodiode array with a 30×40 cm² detection area with 768×1024 pixels,

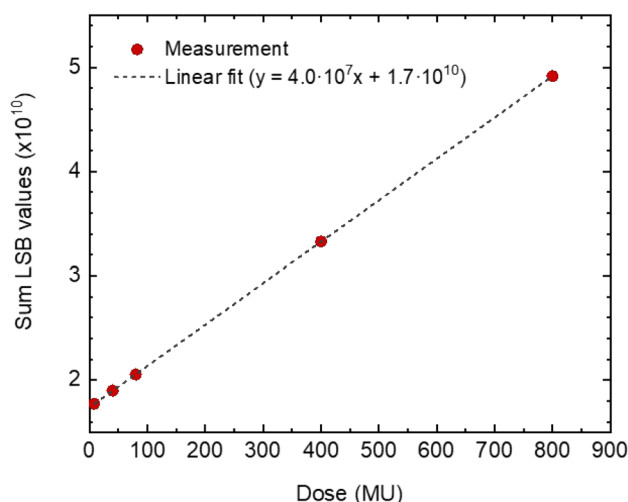


Figure 6. LSB value vs dose expressed in MU of the detector using the commercial Linac TrueBeam Varian. The dashed line represents the linear fit to the data.

achieving a spatial resolution of 65 pixels per inch (PPI). The spatial resolution obtained in this study with the GEM-TFT detector (pixel size of 0.126 mm) is 200 PPI, hence a factor of three higher as compared to the EPID.

The process of converting pixel values to dose in Gray at the reconstruction plane and its calibration procedure are complex^{42,43}. For Elekta Synergy machines a physics model was established based on manufacturer recommendations to translate EPID panel pixel data into dose through a four-step approach⁴¹. Absolute dosimetry with the GEM-TFT requires a comparable calibration procedure as well. Nevertheless, they stand out as sensitive and accurate dosimetry tools, requiring relatively short setup times and boasting user-friendly operation. This characteristic makes the EPID panel a more practical choice for dosimetry compared to other detectors like the full characterized GEM-TFT detector that demand a longer setup procedure.

During the first measurements with the GEM-TFT in a water phantom at CNAO using protons and carbon ions, reference measurements of the beam intensity were performed with the Dose Delivery System (DDS) of CNAO. The CNAO DDS includes the beam monitors and the control unit that constitutes the data acquisition system. It is a CE-marked medical device in clinical use at both CNAO and MedAustron EBG^{33,44}. The GEM-TFT detector response shows a good agreement with the CNAO DDS (Supplementary Fig. 5).

An accurate measurement of the Bragg peak is important because it allows for precise targeting of the tumour. The Bragg curves measured with the GEM-TFT were compared to the Peakfinder data acquired with equal beam parameters. The PTW Peakfinder (PTW, Freiburg, Germany) is a commercial device for measuring the depth dose profile of a particle beam in water, containing a height adjustable water column and two large-area ionisation chambers.

Figure 7a shows the Bragg curve measured with the GEM-TFT with 147.72 MeV with an approximate 13 mm spot size, the clinical beam intensity was set at 2×10^9 particles/s. Additionally, Fig. 7b shows the Bragg curve with 207.97 MeV/n carbon ions with a 6.5 mm spot size, the clinical beam intensity was adjusted to 10^7 particles/s. The Bragg peak is evident at a depth of around 150 mm and the tail beyond the Bragg peak produced by the carbon fragments is well visible.

The GEM-TFT detector and the PTW Peakfinder present similar results for the Bragg curve of protons. Excluding the tail points, the maximum difference of 9.9% was measured at 116.9 mm. The comparison for the Bragg curves of carbon ions yields a larger difference between devices. There is a discrepancy in the maximum of the peak where the value measured with the prototype is 16.7% lower than expected. In contrast, in the tail the measured values were higher.

No saturation effect was observed with protons or carbon ions for any depth with the selected settings. The reason for the observed results with carbon ions remains unclear. One possible explanation could be a dependence on linear energy transfer (LET).

Additionally, the discrepancy could be attributed to the larger surface area of the GEM-TFT compared to the ionizing chamber of the PTW Peakfinder. This difference potentially results in a greater collection of secondary particles, subsequently augmenting the signal beyond the Bragg peak. The area can exert a significant influence. The Peakfinder has a diameter of 57.6 mm and an area of 26 cm². In contrast, the GEMs used in this prototype measure 10 × 10 cm² (ratio 3.8), while our readout—the relevant parameter in this context, as it is smaller than the sensitive area—encompasses 6 × 8 = 48 cm² (ratio 1.8). The entrance window of the measuring chamber of the PTW Peakfinder is 0.0702 ± 0.0084 cm. In the absence of the measured value, we employed a simple SRIM-2008 simulation⁴⁵ to estimate the water-equivalent thickness of our prototype. Specifically, our assessment pertained to a 116 MeV/n carbon ion beam in water in comparison to the GEM-TFT detector inside the water phantom. The discernible variance in range when employing the detector was 0.0442 cm. No relevant impact on the beam fragmentation is expected. Nevertheless, it is worth noting that the distinct materials involved in the GEM chamber and in the readout can influence the characteristics of the Bragg curve. To illustrate this phenomenon,

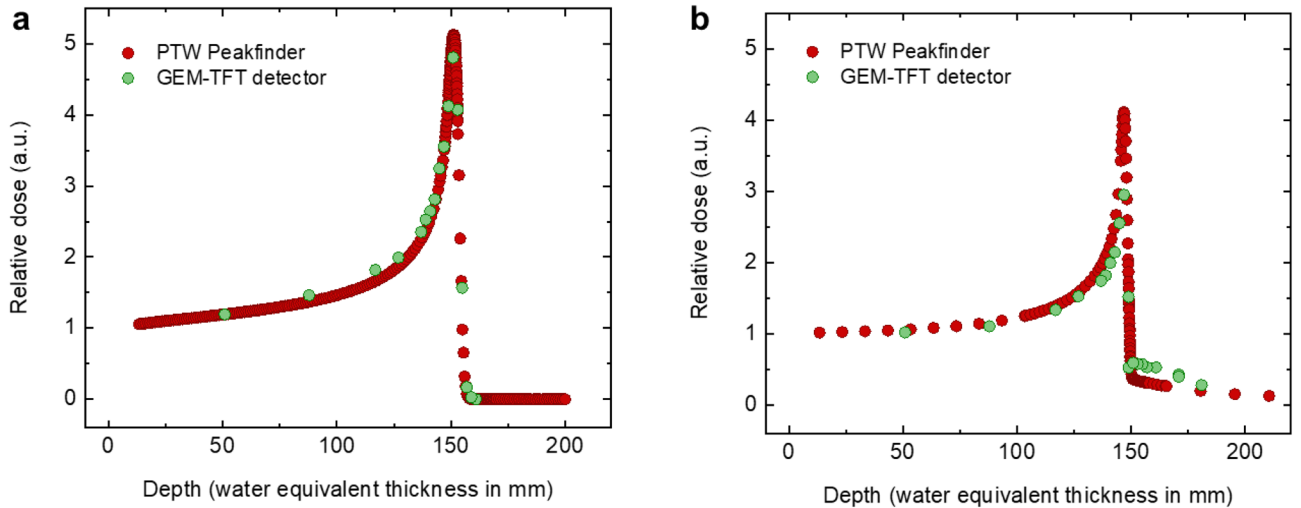


Figure 7. Bragg curves. Increasing energy deposition with penetration depth, with a maximum at the end of the range (151 mm) followed by a sharp decrease. The curves are normalized to unity in the plateau region (50 mm depth in water). (a) Bragg curve measured with the GEM + TFT (●) and PTW Peakfinder (●) with 147.72 MeV protons. (b) Bragg curve measured with the GEM + TFT (●) and PTW Peakfinder (●) with 207.97 MeV/n carbon ions.

we have selected two pertinent studies that effectively highlight the impact of different materials. A study⁴⁶ was conducted to investigate the water-to-detector stopping power ratio for the plateau region. Additionally, the influence of the quartz window on the Peakfinder was investigated through comprehensive studies conducted at Heidelberg⁴⁷. Moreover, alterations in the detector's response due to uneven distribution of defects might lead to significant signal variations. Further tests with an improved version of this prototype with no production defects could help to improve these measurements.

Finally, the spatial resolution of the GEM-TFT detector was determined under clinically relevant hadron therapy settings using the experimental set-up shown in Supplementary Fig. 4b. Figure 8 shows a comparison of the detector response with GAFCHROMIC[®] EBT3 films⁴⁸, the gold standard for this type of measurements in radiation therapy. Employing in-room lasers, we achieved millimetric precision in the alignment of the collimators in relation to the detector. While quantifying the potential impact of misalignment and scattered ions on the wedge face proves complex due to multiple influencing factors, such as beam energy and material properties, the inclusion of films in this experiment facilitates a thorough evaluation. This approach effectively discerns our GEM-TFT detector's performance attributes from external variables. The FWHM obtained by the edge response method for different lines was consistently below 0.50 ± 0.05 mm, corresponding to a resolution of 1 lp/mm. The sub-millimetre spatial resolution obtained using X-rays was nicely confirmed in the hadron therapy setting. A

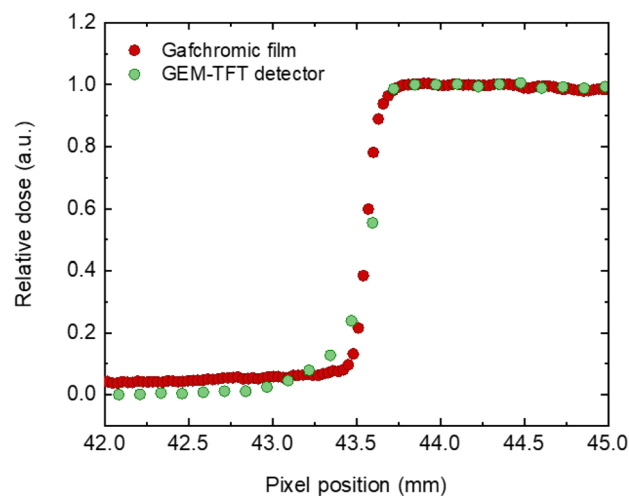


Figure 8. Spatial resolution test under clinically relevant hadron therapy settings. Edge response profile for 147.72 MeV protons using high Z material measured with the GEM-TFT detector (●) and GAFCHROMIC[®] EBT3 films (●).

slight difference in the response of the detector compared to that of the Gafchromic film can be seen within the range of 43.0 to 43.5 mm.

Conclusions

In this paper we presented for the first time the applicability of flat panel TFT technology as GEM detector readout to obtain large area beam imaging with high spatial resolution at high frame rates. The goal was to explore the feasibility of this promising technology which offers benefits from larger scale production in semiconductor industry. We can see potential improvements such as combining advantages of a gaseous detector (low material budget, potentially tissue-equivalent gases) with high-resolution readouts, where ICs have limitations in terms of pixel size/number of detectors for a matrix. The sub-millimetre spatial resolution is achieved by the direct readout of the charge, the directionality of the charges from the GEM and the high pixel density of the TFT array. Moreover, the effective resolution is bolstered by the short 1 mm distance between the last GEM and the readout. We demonstrated that the detector can measure secondary electrons produced by the triple-GEM structure under high intensity beams of various types and sources of high-energy radiation, i.e., X-rays, protons, and carbon ion beams. Dose measurements conducted with 6 MV photons displayed linear behaviour within the range of 8 MU to 800 MU. Similarly, dose-rate measurements using protons, with an intensity range spanning two orders of magnitude demonstrated a linear response. Moreover, the detector showed relatively low radiation damage, that can be compensated by virtue of the two separate gate electrodes in the TFT and maximum dose difference to the reference detector of up to 10%. The observed LET dependence seems to have reduced prominence compared to well-known quenching detectors like plastic scintillators; however, further comprehensive investigation is necessary to study this phenomenon and confirm this observation. We therefore believe that this type of detector has potential for quality assurance in cancer radiation therapy.

Engineering challenges remain and have a potentially large impact on feasibility and costs, but solutions seem at least possible. The presence of line defects in the GEM-TFT detector limited our ability to assess dose uniformity using the current detector. We understand the importance of dose uniformity measurements and plan to investigate this further in future studies, utilizing advancements in both design and fabrication of TFT readout technology. The future development of a 200 × 200 mm² prototype with a high-quality readout and reduced defect level, would allow for further testing of the technology in view of its potential commercialization. Since IGZO based TFT technology is nowadays used in liquid-crystal display (LCDs), organic light-emitting diode (OLED) displays and X-ray detectors at different panel sizes and resolution, we foresee a clear roadmap for the commercial use of this readout technology in GEM based large-area detectors for quality assurance in radiotherapy. Ensuring gas tightness is a crucial step in successfully creating a commercial product suitable for hospital settings. An option with a sealed or recirculating gas system can eliminate the need for gas bottles in a clinical environment, simplifying the detector operation.

Data availability

The datasets generated and analysed during the current study are available from the corresponding author on request.

Received: 7 February 2023; Accepted: 30 April 2024

Published online: 09 May 2024

References

1. Cho, B. Intensity-modulated radiation therapy: A review with a physics perspective. *Radiat. Oncol. J.* **36**, 1–10 (2018).
2. Teoh, M., Clark, C. H., Wood, K., Whitaker, S. & Nisbet, A. Volumetric modulated arc therapy: A review of current literature and clinical use in practice. *Br. J. Radiol.* **84**, 967–996 (2011).
3. Matar, F. S. *et al.* Quality assurance of VMAT on flattened and flattening filter-free accelerators using a high spatial resolution detector. *J. Appl. Clin. Med. Phys.* **21**, 44–52 (2020).
4. PTCOG - Patient Statistics <https://www.ptcog.site/index.php/patient-statistics-2> (Accessed 09 February 2024).
5. Majeed, H. & Gupta, V. Adverse effects of radiation therapy. In *StatPearls* (eds Majeed, H. & Gupta, V.) (StatPearls Publishing, 2023).
6. Ishikawa, H., Nakai, K., Nonaka, T. & Sakurai, H. Particle therapy in cancer treatment-current and future perspective. *Gan To Kagaku Ryoho* **46**, 1219–1225 (2019).
7. Glowa, C., Peschke, P., Brons, S., Debus, J. & Karger, C. P. Intrinsic and extrinsic tumor characteristics are of minor relevance for the efficacy of split-dose carbon ion irradiation in three experimental prostate tumors. *Radiother. Oncol.* **133**, 120–124 (2019).
8. ICRU Report 78, Prescribing, Recording, and Reporting Proton-Beam Therapy – ICRU. <https://www.icru.org/report/prescribing-recording-and-reporting-proton-beam-therapy-icru-report-78/> (2023).
9. Abreu, C. E. C. V. *et al.* Stereotactic body radiotherapy in lung cancer: An update *. *J. Bras. Pneumol.* **41**, 376–387 (2015).
10. Matsuo, Y. Stereotactic body radiotherapy for hepatocellular carcinoma: A brief overview. *Curr. Oncol.* **30**, 2493–2500 (2023).
11. Chea, M. *et al.* Dosimetric study between a single isocenter dynamic conformal arc therapy technique and Gamma Knife radiosurgery for multiple brain metastases treatment: Impact of target volume geometrical characteristics. *Radiat. Oncol.* **16**, 45 (2021).
12. Maia Oliveira, A. *et al.* Characterization with X-rays of a large-area GEMPix detector with optical readout for QA in hadron therapy. *Appl. Sci.* **11**, 6459 (2021).
13. Amaldi, U. *et al.* Advanced quality assurance for CNAO. *Nuclear Instrum. Methods Phys. Res. Sect. A* **617**, 248–249 (2010).
14. Leidner, J., Ciocca, M., Mairani, A., Murtas, F. & Silari, M. A GEMPix-based integrated system for measurements of 3D dose distributions in water for carbon ion scanning beam radiotherapy. *Med. Phys.* **47**, 2516–2525 (2020).
15. Sauli, F. A new concept for electron amplification in gas detectors. *Nuclear Instrum. Methods Phys. Res. Sect. A* **386**, 532–534 (1997).
16. Oliveira, A. M. *et al.* A large area GEMPix detector for treatment plan verification in hadron therapy. *J. Phys. Conf. Ser.* **2374**, 012177 (2022).
17. Safai, S., Lin, S. & Pedroni, E. Development of an inorganic scintillating mixture for proton beam verification dosimetry. *Phys. Med. Biol.* **49**, 4637–4655 (2004).
18. Seravalli, E. *et al.* 2D dosimetry in a proton beam with a scintillating GEM detector. *Phys. Med. Biol.* **54**, 3755–3771 (2009).

19. Brunbauer, F. M. *Applications of Gas Scintillation Properties in Optically Read Out GEM-Based Detectors* (Technical University of Vienna, 2018).
20. Klyachko, A. V., Moskvina, V., Nichiporov, D. F. & Solberg, K. A. A GEM-based dose imaging detector with optical readout for proton radiotherapy. *Nuclear Instrum. Methods Phys. Res. Sect. A* **694**, 271–279 (2012).
21. Bencivenni, G. *et al.* A triple GEM detector with pad readout for high rate charged particle triggering. *Nuclear Instrum. Methods Phys. Res. Sect. A* **488**, 493–502 (2002).
22. Corradi, G., Murtas, F. & Tagnani, D. A novel High-Voltage System for a triple GEM detector. *Nuclear Instrum. Methods Phys. Res. Sect. A* **572**, 96–97 (2007).
23. Pansky, A. *et al.* The scintillation of CF₄ and its relevance to detection science. *Nuclear Instrum. Methods Phys. Res. Sect. A* **354**, 262–269 (1995).
24. Fallavollita, F., Fiorina, D. & Merlin, J. A. Advanced aging study on triple-GEM detectors. *J. Phys. Conf. Ser.* **1498**, 012038 (2020).
25. Sato, A. *et al.* Amorphous In–Ga–Zn–O coplanar homojunction thin-film transistor. *Appl. Phys. Lett.* **94**, 133502 (2009).
26. Manoj, N. *et al.* Low-temperature formation of source–drain contacts in self-aligned amorphous oxide thin-film transistors. *J. Inf. Display* **16**(2), 111–117 (2015).
27. van Breemen, A. J. J. M. *et al.* A thin and flexible scanner for fingerprints and documents based on metal halide perovskites. *Nat. Electron.* **4**, 818–826 (2021).
28. Brugger, M., Carbonez, P., Pozzi, F., Silari, M. & Vincke, H. New radiation protection calibration facility at CERN. *Radiat. Protect. Dosimetry* **161**, 181–184 (2014).
29. Anders, J. *et al.* A facility for radiation hardness studies based on a medical cyclotron. *J. Inst.* **17**, P04021 (2022).
30. Braccini, S. The new Bern PET cyclotron, its research beam line, and the development of an innovative beam monitor detector. *AIP Conf. Proc.* **1525**, 144–150 (2013).
31. Potkins, D. E. *et al.* A low-cost beam profiler based on cerium-doped silica fibers. *Phys. Procedia* **90**, 215–222 (2017).
32. Sigamani, A. *et al.* Surface dose measurements and comparison of unflattened and flattened photon beams. *J. Med. Phys.* **41**, 85 (2016).
33. Donetti, M. *et al.* Current and future technologies of the CNAO dose delivery system. *IEEE Instrum. Meas. Magaz.* **24**, 61–69 (2021).
34. Friedman, S. N., Fung, G. S. K., Siewerdsen, J. H. & Tsui, B. M. W. A simple approach to measure computed tomography (CT) modulation transfer function (MTF) and noise-power spectrum (NPS) using the American College of Radiology (ACR) accreditation phantom. *Med. Phys.* **40**, 051907 (2013).
35. Line Pair Patterns - Test Phantoms, QUART X-Ray QA QC Solutions. <https://quart.de/en/products/test-phantoms/resolution-patterns/line-pair-patterns> (2023).
36. OCTAVIUS 4D QA Phantom, PTW. <https://www.ptwdosimetry.com/en/products/octavius-4d-qa-phantom/> (2024).
37. Gelinck, G. H. *et al.* X-ray detector-on-plastic with high sensitivity using low cost, solution-processed organic photodiodes. *IEEE Trans. Electron Dev.* **63**, 197–204 (2016).
38. Kim, D.-G. *et al.* Negative threshold voltage shift in an a-IGZO thin film transistor under X-ray irradiation. *RSC Adv.* **9**, 20865–20870 (2019).
39. Shin, M.-G. *et al.* Effects of proton beam irradiation on the physical and chemical properties of IGTO thin films with different thicknesses for thin-film transistor applications. *Surf. Interfaces* **23**, 100990 (2021).
40. More, M., Jain, V. & Gurjar, O. P. Clinical experience of intensity modulated radiotherapy pre-treatment quality assurance for carcinoma head and neck patients with EPID and IMatriXX in rural center. *J. Biomed. Phys. Eng.* **10**, 691–698 (2020).
41. Mousli, M. & Cummins, D. EPID dosimetry for IMRT and VMAT PSQA. *Physica Medica* **52**, 173 (2018).
42. Wendling, M. *et al.* Accurate two-dimensional IMRT verification using a back-projection EPID dosimetry method. *Med. Phys.* **33**, 259–273 (2006).
43. Steciw, S., Warkentin, B., Rathee, S. & Fallone, B. G. Three-dimensional IMRT verification with a flat-panel EPID. *Med. Phys.* **32**, 600–612 (2005).
44. Giordanengo, S. *et al.* The CNAO dose delivery system for modulated scanning ion beam radiotherapy. *Med. Phys.* **42**, 263–275 (2015).
45. SRIM-2008, Stopping Power and Range of Ions in Matter. <https://www.oecd-nea.org/tools/abstract/detail/nea-0919> (2024).
46. Bolsa-Ferruz, M., Palmans, H., Boersma, D., Stock, M. & Grevillot, L. Monte Carlo computation of 3D distributions of stopping power ratios in light ion beam therapy using GATE-RTion. *Med. Phys.* **48**, 2580–2591 (2021).
47. Kurz, C., Mairani, A. & Parodi, K. First experimental-based characterization of oxygen ion beam depth dose distributions at the Heidelberg Ion-Beam Therapy Center. *Phys. Med. Biol.* **57**, 5017 (2012).
48. Anderson, S. E., Grams, M. P., Tseung, H. W. C., Furutani, K. M. & Beltran, C. J. A linear relationship for the LET-dependence of Gafchromic EBT3 film in spot-scanning proton therapy. *Phys. Med. Biol.* **64**, 055015 (2019).

Acknowledgements

The authors wish to thank: Rui de Oliveira for the special design of the GEM foils; Pierre Carbonez and Alix Chantelauze for granting us access to the Calibration Laboratory of CERN Radiation Protection Group; Florian Brunbauer for the useful discussions; the colleagues from Holst Centre's Gen1 R&D TFT pilot line and Santhosh Shanmugam for their contributions in thin-film imager fabrication; Pierluigi Casolaro and Isidre Mateu for the support with the measurements on IBA Cyclone 18 MeV cyclotron of the Bern University Hospital; Jan Würfel for allowing the measurements in Freiburg; Mario Ciocca and colleagues of the medical physics team for the beam tests at CNAO. This project has been partly financed by the ATTRACT project funded by the EC under Grant Agreement 777222. The project has also been supported by CERN's Budget for Knowledge Transfer to Medical Applications. Andreia Maia Oliveira was co-supported by a grant from FCT with reference SFRH/BEST/142965/2018. In Memoriam of Fabrizio Murtas.

Author contributions

All the authors conceptualized the system, A.J.J.M.v.B.; H.B.A.; I.K.; B.P. and F.M. contributed to the design and construction of the prototype with the help of A.M.O. and J.L. for the merging. A.M.O., N.H. and J.L. developed the methodology; A.M.O., N.H. and B.P. developed the software, A.M.O. collected the data and was responsible for the data curation, A.M.O. contributed to the formal data analysis, A.M.O. validated the data; A.M.O., J.L. and N.H. conducted the investigation process, specifically performing the experiments. A.M.O. prepared the original draft; S.B. coordinated the beam tests at the Bern medical cyclotron laboratory; M.S. and S.B. supervised the research activities. M.S. and N.H. acquired the financial support for the project leading to this publication. All the authors revised and edited the paper. All authors read and approved the final manuscript.

Competing interests

The authors declare no competing interests.

Additional information

Supplementary Information The online version contains supplementary material available at <https://doi.org/10.1038/s41598-024-61095-2>.

Correspondence and requests for materials should be addressed to A.M.O.

Reprints and permissions information is available at www.nature.com/reprints.

Publisher's note Springer Nature remains neutral with regard to jurisdictional claims in published maps and institutional affiliations.






Open Access This article is licensed under a Creative Commons Attribution 4.0 International License, which permits use, sharing, adaptation, distribution and reproduction in any medium or format, as long as you give appropriate credit to the original author(s) and the source, provide a link to the Creative Commons licence, and indicate if changes were made. The images or other third party material in this article are included in the article's Creative Commons licence, unless indicated otherwise in a credit line to the material. If material is not included in the article's Creative Commons licence and your intended use is not permitted by statutory regulation or exceeds the permitted use, you will need to obtain permission directly from the copyright holder. To view a copy of this licence, visit <http://creativecommons.org/licenses/by/4.0/>.

© The Author(s) 2024

Article

Characterization with X-rays of a Large-Area GEMPix Detector with Optical Readout for QA in Hadron Therapy

Andreia Maia Oliveira ^{1,2,*} , Hylke B. Akkerman ³, Saverio Braccini ² , Albert J. J. M. van Breemen ³, Lucia Gallego Manzano ^{1,4}, Natalie Heracleous ^{1,4}, Ilias Katsouras ^{3,5}, Johannes Leidner ¹, Fabrizio Murtas ^{1,6}, Bart Peeters ³ and Marco Silari ¹ 

- ¹ CERN, 1211 Geneva, Switzerland; Lucia.Gallego-Manzano@chuv.ch (L.G.M.); natalie.heracleous@cern.ch (N.H.); johannes.leidner@cern.ch (J.L.); fabrizio.murtas@cern.ch (F.M.); marco.silari@cern.ch (M.S.)
- ² Albert Einstein Center for Fundamental Physics (AEC), Laboratory for High Energy Physics (LHEP), University of Bern, Sidlerstrasse 5, 3012 Bern, Switzerland; saverio.braccini@lhep.unibe.ch
- ³ Holst Centre/TNO, High Tech Campus 31, 5656 AE Eindhoven, The Netherlands; hylke.akkerman@tno.nl (H.B.A.); albert.vanbreemen@tno.nl (A.J.J.M.v.B.); ilias.katsouras@asml.com (I.K.); bart.peeters@tno.nl (B.P.)
- ⁴ Institute of Radiation Physics, Lausanne University Hospital and Lausanne University, 1007 Lausanne, Switzerland
- ⁵ ASML Netherlands B.V., 5504 DR Veldhoven, The Netherlands
- ⁶ INFN-LNF, 00044 Frascati, Italy
- * Correspondence: andreia.cristina.maia.oliveira@cern.ch



Citation: Maia Oliveira, A.;

Akkerman, H.B.; Braccini, S.; van Breemen, A.J.J.M.; Gallego Manzano, L.; Heracleous, N.; Katsouras, I.; Leidner, J.; Murtas, F.; Peeters, B.; et al. Characterization with X-rays of a Large-Area GEMPix Detector with Optical Readout for QA in Hadron Therapy. *Appl. Sci.* **2021**, *11*, 6459. <https://doi.org/10.3390/app11146459>

Academic Editors: Cinzia Talamonti, Marco Petasecca and Simona Giordanengo

Received: 10 June 2021
Accepted: 9 July 2021
Published: 13 July 2021

Publisher's Note: MDPI stays neutral with regard to jurisdictional claims in published maps and institutional affiliations.



Copyright: © 2021 by the authors. Licensee MDPI, Basel, Switzerland. This article is an open access article distributed under the terms and conditions of the Creative Commons Attribution (CC BY) license (<https://creativecommons.org/licenses/by/4.0/>).

Featured Application: An optical readout GEM-based detector based on a matrix of organic photodiodes with an active area of $60 \times 80 \text{ mm}^2$, called the LaGEMPix, was assembled and characterized, using low energy X-rays as a preliminary step toward the development of a $200 \times 200 \text{ mm}^2$ detector for use in Quality Assurance in hadron therapy.

Abstract: Quality Assurance (QA) in hadron therapy is crucial to ensure safe and accurate dose delivery to patients. This can be achieved with fast, reliable and high-resolution detectors. In this paper, we present a novel solution that combines a triple Gas Electron Multiplier (GEM) and a highly pixelated readout based on a matrix of organic photodiodes fabricated on top of an oxide-based thin-film transistor backplane. The first LaGEMPix prototype with an active area of $60 \times 80 \text{ mm}^2$ was developed and characterized using low energy X-rays. The detector comprises a drift gap of 3.5 mm, a triple-GEM stack for electron amplification, and a readout featuring 480×640 pixels at a $126 \mu\text{m}$ pitch. Here, we describe the measurements and results in terms of spatial resolution for various experimental configurations. A comparison with GAFCHROMIC[®] films and the GEMPix detector used in the charge readout mode was performed to better understand the contribution to the spatial resolution from both the electron diffusion and the isotropic emission of photons. The measurements were compared to Monte Carlo simulations, using the FLUKA code. The simulation predictions are in good agreement with the GEMPix results. Future plans with respect to applications in hadron therapy are discussed.

Keywords: hadron therapy; particle detectors; dosimetry; quality assurance; GEM; optical readout

1. Introduction

Hadron therapy is an advanced radiation therapy modality for treating cancer, which currently uses protons and carbon ions. As of January 2021, 103 particle therapy facilities are in operation worldwide and more than 30 centers are under construction [1]. Hadrons have the unique feature of increasing energy deposition with penetration depth, with a maximum at the end of their range followed by a sharp decrease (Bragg peak). Thus, hadron therapy offers considerable improvements to conventional radiation therapy treatments by

allowing better conformity of the dose to the tumor [2], but also requires very accurate dose planning. A precise verification of the dose delivered to the patient is, therefore, mandatory and has to be guaranteed by appropriate quality assurance (QA) procedures with high spatial resolution.

A proper set of detectors for measuring the beam parameters, in particular, the beam position and the delivered dose, is fundamental to achieve an efficient QA protocol [3]. Nowadays, there is still room for improvement toward a robust and complete solution providing accurate and real-time measurements with high spatial resolution and a uniform response to the beam energy.

The LaGEMPix detector, which is the subject of this paper, is a promising tool for more efficient QA procedures with high spatial resolution. It consists of a triple-GEM (Gas Electron Multiplier) [4] coupled to a highly pixelated readout based on a matrix of organic photodiodes (OPDs). The potential of a triple-GEM detector combined with high pixel granularity for QA in hadron therapy was initially demonstrated with the GEMPix [5,6]. The GEMPix has shown very promising results but its application is limited by the relatively small active area of $28 \times 28 \text{ mm}^2$. In hadron therapy, typical sensitive areas of $200 \times 200 \text{ mm}^2$ are required to cover the maximum clinical field size [7,8]. The new readout, based on the detection of the scintillation photons generated in the GEM holes, allows for the development of a compact detector to perform imaging at larger areas, further scalable with an expected high spatial resolution.

In this paper, we report on the development of the first LaGEMPix prototype with an active area of $60 \times 80 \text{ mm}^2$, which is six times larger than that of the GEMPix. The detector and the experimental set-up are described in Section 2. The results obtained using an X-ray irradiator are reported in Section 3 and discussed in Section 4. Finally, Section 5 draws the conclusions and outlines the next steps of the project.

2. Materials and Methods

2.1. Detector Design

The current prototype of the LaGEMPix combines a triple-GEM detector with an area of $100 \times 100 \text{ mm}^2$, and an optical readout by means of a thin-film imager composed of a thin-film transistor (TFT) backplane, an OPD frontplane, and a transparent thin-film encapsulation [9], the latter serving as protection against ambient conditions. The imager consists of a matrix of 480×640 pixels at a resolution of 200 ppi. A schematic diagram of the LaGEMPix is depicted in Figure 1.

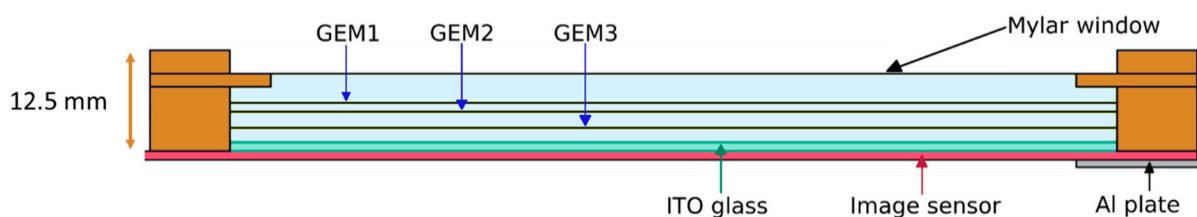


Figure 1. Schematic drawing of the LaGEMPix (to scale). Electrons produced in the drift gap between the Mylar window and the top GEM (GEM1) are multiplied in the triple-GEM stack and collected on the transparent indium tin oxide (ITO) glass anode. Scintillation photons of certain wavelengths pass through the ITO glass and are detected by the image sensor.

The triple-GEM detector includes a 3.5 mm drift gap between the top GEM electrode (GEM1) and the cathode, which is a $15 \mu\text{m}$ thick Mylar window. The drift gap is large enough to minimize inefficiencies in charged particle detection [10] but not large enough to affect the time performance. The transfer gaps between GEM1 and the second GEM foil (GEM2) and between GEM2 and the last GEM foil (GEM3) have a thickness of 1 and 2 mm, respectively. This asymmetrical configuration does not compromise the temporal performance of the detector thanks to a first transfer gap of 1 mm, while reducing the probability of discharge by increasing the second transfer gap by 1 mm [10]. Each GEM

foil consists of a 50 μm Kapton layer electroplated with a 5 μm thick copper layer on both sides and pierced with holes of 70 μm diameter and 140 μm pitch. An ITO transparent electrode, coated on a 1.1 mm-thick fused quartz substrate with a resistivity of 100 Ω/sq , is used both as an anode and as an optical window [11,12]. The last gas region between GEM3 and the anode, known as the induction gap, is 1.9 mm thick.

The triple-GEM detector is operated in a continuous flow of Ar/CF₄ (90/10) gas mixture supplied at a rate of 5 l/h. We chose Ar/CF₄ because it has the highest light yield among the typically used gas mixtures (He/CF₄, Ne/CF₄, Ar/CO₂, Ar-TEA (trimethylamine), Xe-TEA). The reported light yield varies between 0.1 and 0.5 photons per secondary electron [11,13,14]. The addition of CF₄ gas acting as quencher allows a stable detector operation. Furthermore, it features other attractive properties, such as high electron drift velocity, low electron diffusion and fast scintillation time (of the order of a few ns) [15]. Additionally, Ar/CF₄ has a strong visible emission band of around 630 nm, which is well suited for standard optical readout systems [16,17].

GEM-based detectors coupled to CCD/CMOS cameras were previously studied for particle therapy [11,18,19]. However, the degradation of the camera due to radiation requires placing it outside the beam, leading to a more complex system with, for example, mirrors or lenses. In contrast to CCD/CMOS-based detectors, in the LaGEMPix, the highly pixelated readout is adjacent to the GEM anode. This allows for a more compact, relatively easy-to-build and low material budget set-up. A first LaGEMPix prototype (Figure 2) was successfully assembled as a preliminary step toward the development of a 200 \times 200 mm² detector.

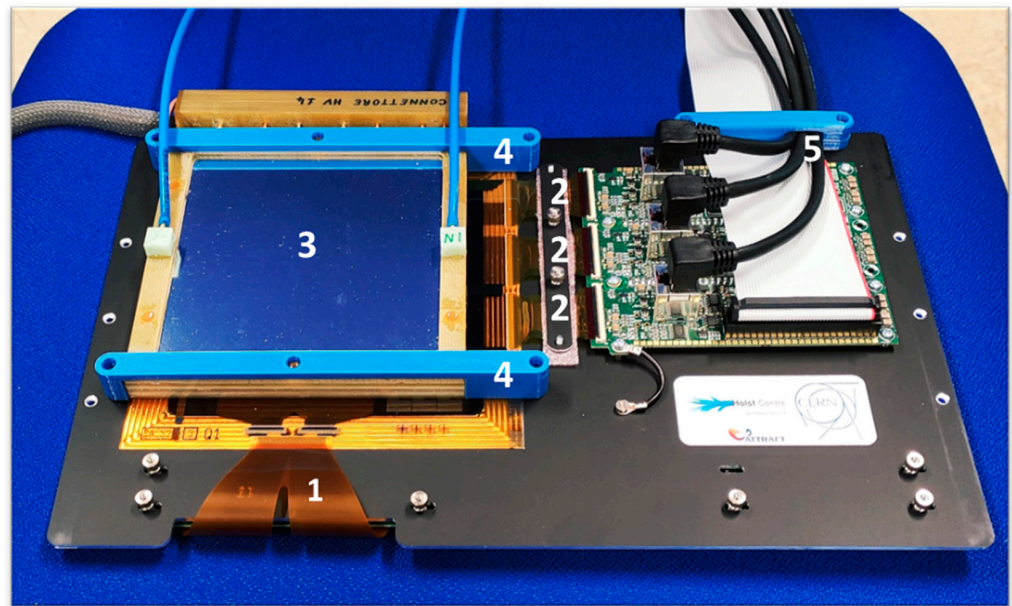


Figure 2. The first LaGEMPix prototype: (1) flex gate driver integrated circuit; (2) flex Read-out Integrated Circuits (ROICs); (3) the triple-GEM 100 \times 100 mm² stack coupled to the optical readout with the thin Mylar window on top; (4) 3D-printed braces to hold together the triple-GEM detector and the image sensor; and (5) cables to connect the detector to the readout system.

The sensor array of the LaGEMPix has a resolution of 200 pixels per inch (ppi). It comprises 480 \times 640 pixels resulting in a total sensor area of 60 \times 80 mm². Each individual pixel has a photodiode with a size of 103 \times 103 μm^2 (actual active area of 10522 μm^2) at a pixel pitch of 126 μm . The OPD frontplane is directly fabricated on top of the TFT backplane, and the organic light-absorbing layer of the OPD is deposited by slot-die coating. The TFT backplane has a self-aligned dual-gate architecture and is based on indium gallium zinc oxide (IGZO) [20]. The sensor shows a dark current density of 10⁻⁷ mA/cm² at -2 V and a linear response in a wide range of light intensities [21].

The OPDs have a maximum external quantum efficiency (EQE) of ca. 60% at 550 nm, as shown in Figure 3. The EQE is approximately constant down to 450 nm and decreases toward longer wavelengths, reaching about 25% at 640 nm. Ar/CF₄ shows a broad emission band between 500 and 800 nm with a peak at around 630 nm, which is well suited for this application [11]. In this work, we used an OPD based on a bulk heterojunction (BHJ) structure. It consists of a 280 nm thick blend of poly[N-9'-heptadecanyl-2,7-carbazole-alt-5,5-(4',7'-di-2-thienyl-2',1',3'-benzothiadiazole)], PCDTBT, a p-type (donor) polymer, and [6,6]-phenyl-C61-butyric acid methyl ester, PCBM, (acceptor) fullerene [22]. The EQE of the OPD is dictated by the absorption of the heterojunction components, potentially modified by interference effects derived from the electrodes and encapsulation. The spectral response (SR) curve has a similar response to the EQE with a maximum of ca. 65% at 0.3 A/W as shown by the red curve in Figure 3. Due to the decrease in the LaGEMPix readout efficiency at larger wavelengths, the LaGEMPix readout only partially matches the visible band of the emission spectrum of Ar/CF₄. Nevertheless, a sufficient signal was obtained during the measurements.

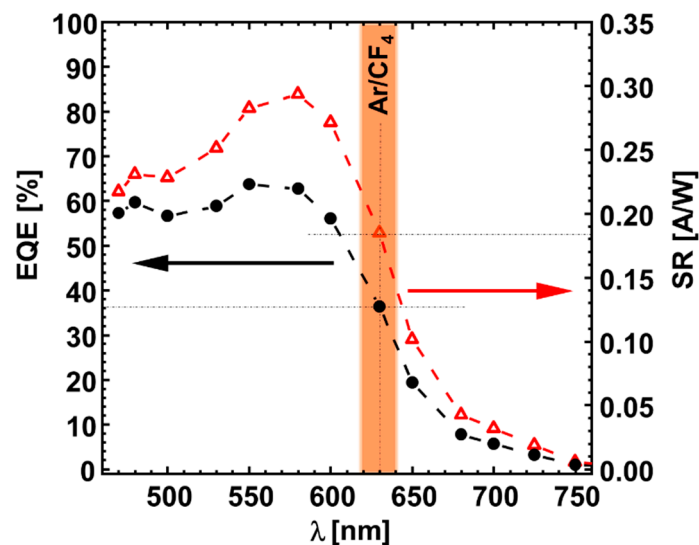


Figure 3. External Quantum Efficiency (EQE) (black curve and left axis) and Spectral Response (SR) (red curve and right axis) of the OPD layer deposited on the readout matrix. The broad emission band of Ar/CF₄ with a peak at around 630 nm is represented by the orange region.

2.2. Optimization of Electric Fields

As a first step, we tested the triple-GEM detector with a 3 TBq Cs-137 source to optimize the electric fields before coupling it to the optical matrix. The optimal selection of the electric fields is important to maximize the total charge gain (defined as the ratio of the detected charges in the anode plane per incident primary charge), and consequently achieve a high signal-to-noise ratio [23]. The ratio of the number of emitted scintillation photons to the number of secondary electrons produced during the avalanche is called the light yield. As mentioned above, the Ar/CF₄ (90/10) gas mixture offers a high secondary scintillation light yield of up to 0.5 photons per secondary electron. Hence, it is expected that the number of photons that reaches the photodiode layer is proportional to the induced current in the anode [24]. Based on this consideration, the electric field selection performed by maximizing the anode current is also optimal to maximize the number of detected photons.

The measurements were performed at the Calibration Laboratory of CERN Radiation Protection group [25]. The detector was placed on a support table at 0.82 cm from the source. A 6157 Keithley electrometer [26] was connected to the ITO anode to measure the induced current. The transfer, drift and induction fields were optimized to maximize the absolute value of the current at the anode. On the other hand, based on the well-

known exponential dependence of the effective gain on the GEM voltages, the electric fields between the top and bottom copper layers in each GEM foil were kept constant for a total voltage of 960 V [27]. The fields were optimized one after the other by keeping all but the field under investigation constant.

2.3. Spatial Resolution

A QA procedure in hadron therapy requires not only an accurate dose calculation, but also a high spatial resolution. A high spatial resolution of the 2D dose distribution is important because most of the treatment plans in Pencil Beam Scanning (PBS) are characterized by very high “in-field” dose gradients. Distal falloff values defined as the distance between the distal position of the 80% and 20% dose levels, z_{80-20} , at intensity-modulated proton therapy can reach 4 mm, which corresponds to a gradient of 15%/mm [28,29]. Therefore, it is critical to validate that the required dose is delivered exactly where needed to spare the healthy tissue.

The resolution of the LaGEMPix can be compared with that of commercially available 2D detectors, using the appropriate definitions applied by manufacturers and medical physicists. For example, the company PTW (PTW-Freiburg, Lörracher Strasse 7, 79115 Freiburg, Germany, Web: <https://www.ptwdosimetry.com/>, accessed on 21 February 2021) uses the distance between the ionization chambers to define the spatial resolution of their two-dimensional arrays [30]. On the other hand, the spatial resolution of IBA (IBA Dosimetry, Bahnhofstraße 5, 90592 Schwarzenbruck, Germany, Web: <https://www.ibadosimetry.com/>, accessed on 21 February 2021) detectors is stated as the pixel size for the myQA[®] SRS* and Lynx, or as the pixel pitch for the Giraffe [31]. The spatial resolution of dosimetry equipment used at hadron therapy facilities is often given as the value provided by the manufacturer [32–34].

The pixel size or pixel pitch limit the system’s spatial resolution. Moreover, they are not the only factors that contribute to its true or effective measured value. ISO 12233:2017 raises awareness to the various connotations of the term “spatial resolution”, stating that “the term resolution is often incorrectly interpreted as the number of addressable photoelements” [35]. The spatial resolution can be defined, on the other hand, as the ability to differentiate objects that are found within a certain distance from each other. ISO 12233:2017 states that the visual resolution is the maximum value of the spatial frequency at which the individual black and white lines of a test pattern can no longer be distinguished by the human eye. This observation is also called vanishing resolution and corresponds to a modulation transfer function (MTF) of roughly 10–20% [36].

To estimate the effective spatial resolution of the LaGEMPix, we used three methods. The first method is based on the evaluation of the Edge Spread Function (ESF), which describes the response of the system to a sharp edge (discontinuity). The second method determines the Line Spread Function (LSF) of the system in one dimension. The goal is to evaluate the capability of the LaGEMPix to resolve the adjacent points. For that, two copper masks with holes separated by different distances were imaged. Finally, a lead test pattern mask was used to evaluate the MTF of the system.

A typical method consists of estimating the spatial resolution using the ESF [37]. According to the ESF method, a high-resolution system will exhibit a well-defined edge with minimum blurring. We applied this approach by measuring the projection of the straight edge of a 2.5 cm thick lead block, as explained in more detail in Section 3.2.1. Ideally, the intensity distribution should be a step-like function, where the maximum intensity corresponds to the illuminated area and zero intensity to the non-irradiated region blocked by the lead.

The typical value quoted for the edge response is the full width at half maximum (FWHM) [38–40]. A region of interest (ROI) perpendicular to the edge is selected. The FWHM can be obtained analytically by fitting the ESF by a logistic (Fermi) function [41] given by the following:

$$\text{ESF} = a + \frac{b}{1 + e^{-c(d-x)}} \quad (1)$$

where a is the offset, b is the contrast, c is the steepness and d is the centroid of the edge. The FWHM can be calculated from the fit parameters, using the relation $\text{FWHM} = 3.53/c$ [42].

The other two methods (LSF and MTF) were also applied for the characterization of imaging sensors. In this case, we used dedicated radiation-opaque plates with several absorbent structures to assess the capacity of the system under study to resolve adjacent holes or lines. In particular, the MTF measurement was acquired from a lead mask with a bar pattern [43] with groups of slits with variable separation (in line pairs (LP) per mm) using the following equation:

$$\text{MTF}(f) = \frac{C(f)}{C(0)}; C(f) = \frac{I_{\max}(f) - I_{\min}(f)}{I_{\max}(f) + I_{\min}(f)} \quad (2)$$

where $I_{\max}(f)$ and $I_{\min}(f)$ are the maximum and minimum pixel value for a pattern with spatial frequency f respectively. $C(0)$ is the normalization factor at zero frequency, which has to be approximated in practice by using pixel intensities of a large bar and of adjacent background. For the LSF, we used two types of copper plates of various thicknesses and hole patterns, as explained in Sections 3.2.2 and 3.3.2. The results are discussed in Sections 3.2.1–3.2.3 for the ESF, LSF and MTF methods, respectively.

2.4. Experimental Set-Up to Determine the Spatial Resolution

The spatial resolution of the LaGEMPix was evaluated with 40 kV X-rays from an X-ray generator, type X80-320kV from Hopewell Designs, Inc. A system equipped with 10 Narrow Spectra Filters (N-series) was used in order to provide X-rays conforming to the ISO 4037 standard [44]. In particular, the Hopewell N-6 filter, corresponding to the N-40 ISO 4037, was selected.

The X-ray generator has a collimation system that consists of a wheel mounted outside the shielding enclosure to provide beam apertures with diameters of 1 cm to 7 cm. It is also equipped with an irradiation bench provided with a movable platform, which allows automated positioning and exposure control. The LaGEMPix was placed perpendicular to the X-ray beam in a vertical custom-made structure, providing a well-aligned set-up on top of the platform (see Section 3.2), and covered by a black tissue to shield it from ambient light. The assembly was positioned on the irradiation bench and Y (horizontal and perpendicular to the beam) and Z (vertical and perpendicular to the beam) positions were chosen in such a way that the center of the imager was aligned with the center of the beam. In order to obtain a nearly parallel X-ray beam, the irradiations were performed at a distance of 230 cm, using a 1 cm aperture.

The readout was set to the highest sensitivity level of 0.5 pC so that the least significant bit (LSB) of the 16-bit readout corresponded to a charge of approximately 50 electrons. The frame rate, which is the frequency at which consecutive images are recorded, was 1 frame per second (fps).

To ensure that undesirable effects, such as readout inhomogeneities or noise, did not affect the results, a threshold per pixel was applied and dead pixels were removed. A background image was obtained by averaging each pixel value over 200 background frames. Next, each image was processed offline, and the background was subtracted. The final image was obtained by averaging each pixel over 200 background-corrected images. A ROI was defined for further analysis as presented in the Results section (Section 3).

2.5. FLUKA Simulations

A simulation of the LaGEMPix was carried out using the FLUKA Monte Carlo code version 4-0.1 [45–47] with the default settings PRECISIO. The goal of the simulation was to study the energy deposition in the active area of the detector, and to evaluate its spatial resolution using the ESF and LSF methods. Transport and production energy cuts for electrons, positrons and photons were set to 1 keV in all regions. To overcome most of the limitations arising from low energy primary photons and enhance the transport precision for the energy deposition in the very thin layers of both gaseous and heavy

materials present in the LaGEMPix geometry, the single-scattering algorithm was activated everywhere for all charged particles by adding the MULSOPT card.

The simulation comprises a realistic implementation of the detector geometry, which includes the triple-GEM stack, the image sensor and peripheral electronics, as shown in Section 3.5. Due to the lack of information on the X-ray tube head, we implemented a user-defined source routine, using the reference radiation fields for the ISO N-40 for the simulation of the spectral distribution of the X-ray beam. Other contributions due to scattered photons in the target or in any surrounding material that are inherently present in the beam were not simulated, due to the lack of information.

It should be noted that the simulation did not intend to reproduce the experimental results, but rather help in evaluating the contributions to the spatial resolution associated with the detector and the experimental conditions. Therefore, neither the electron diffusion in the gas volume nor the electron recombination with positive ions, impurity absorption, electron amplification in the GEM holes and scintillation light emission were taken into consideration. Nonetheless, as explained in Section 2.1, the number of photons detected by the LaGEMPix matrix of OPDs is proportional to the number of secondary electrons produced in the GEMs, which is in turn proportional to the energy deposited in the gas during the primary ionization process. Therefore, we can assume that the energy deposited by the X-ray photons in the gas volume of the detector is a rough approximation of the image produced by the scintillation photons detected by the image sensor. To account for the contribution of primary ionizations in the different gas regions and the effective gain per GEM foil to the image, we used the image obtained as the average deposited energy in the drift and transfer gas layers weighted by the corresponding effective gains. Interactions in the induction gap will not generate secondary scintillation photons and therefore, will not contribute to the final image. A FLUKA USRBIN scoring was superimposed in the entire detector volume. The statistical uncertainties were estimated by calculating the standard deviation of the results from independent runs.

3. Results

3.1. Optimization of the Electric Fields of the LaGEMPix

The transfer, drift and induction fields were optimized to maximize the absolute value of the anode current. Initially, only the value of the drift field was modified, keeping the other fields fixed. The current was measured to be almost stable for drift field strengths in the range 0.5–1.25 kV/cm (Figure 4). The measurements were repeated, in turn varying one of the electric fields while keeping the others constant. A drift field of 1 kV/cm was selected. The optimization procedure showed a dependence of the anode current on the applied voltages. The optimal values are as follows: a transfer field between GEM1 and GEM2 of 2.0 kV/cm and a transfer field between GEM2 and GEM3 of 1.75 kV/cm. It was established that the absolute value of the current increases as a function of the induction field. In order to achieve an efficient and safe operation of the detector, the initial value of the induction field was not changed, keeping it at 5 kV/cm.

We repeated the drift field intensity scan with the final configuration. Figure 4 shows a comparison of the anode current before and after the optimization of the fields. For a drift field of 1 kV/cm, the maximum value of the current is 273 nA (absolute value), 180 nA higher than the absolute value measured with the initial settings of the fields.

The observed behavior of the drift and transfer field scans is in agreement with the results published by Marafini et al. [48]. The difference in the values of the two transfer fields can be explained by the asymmetry of the transfer gaps (1 mm and 2 mm). By applying the optimized configuration to the drift and transfer fields, we measured a 180 nA higher signal compared to the approach with non-optimized fields, representing an increase of the detectable signal by around 150%.

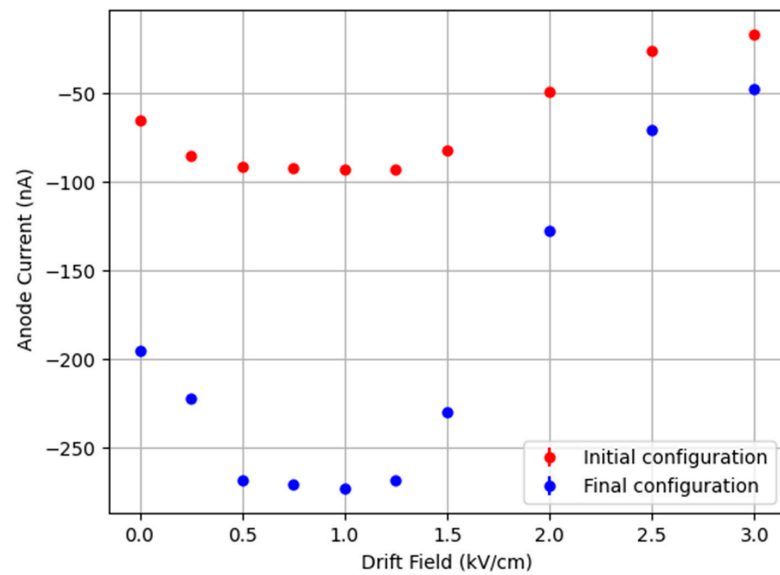


Figure 4. Current at the anode as a function of the drift field strength. Initial configuration (red): transfer field 1 = 3.0 kV/cm; transfer field 2 = 3.0 kV/cm; induction field = 5.0 kV/cm. Final configuration (blue): transfer field 1 = 2.0 kV/cm; transfer field 2 = 1.75 kV/cm; induction field = 5.0 kV/cm. A drift field of 1 kV/cm was selected as it yielded the maximum signal. The uncertainties are smaller than the data points.

3.2. Spatial Resolution with the LaGEMPix

3.2.1. Edge Spread Function (ESF)

To evaluate the spatial resolution using the edge response method, we placed a lead block of $10 \times 20 \times 2.5 \text{ cm}^3$ size in front of the detector covering a portion of its active area, as shown in Figure 5a. This detector prototype was developed as a proof of concept; the readout matrix has some defects, resulting from a yield issue in the fan-out area toward the active area of the detector. In particular, some lines in the backplane are disconnected and can therefore not be read out. These appear as horizontal and vertical non-functional black lines in the readout image in Figure 5b.

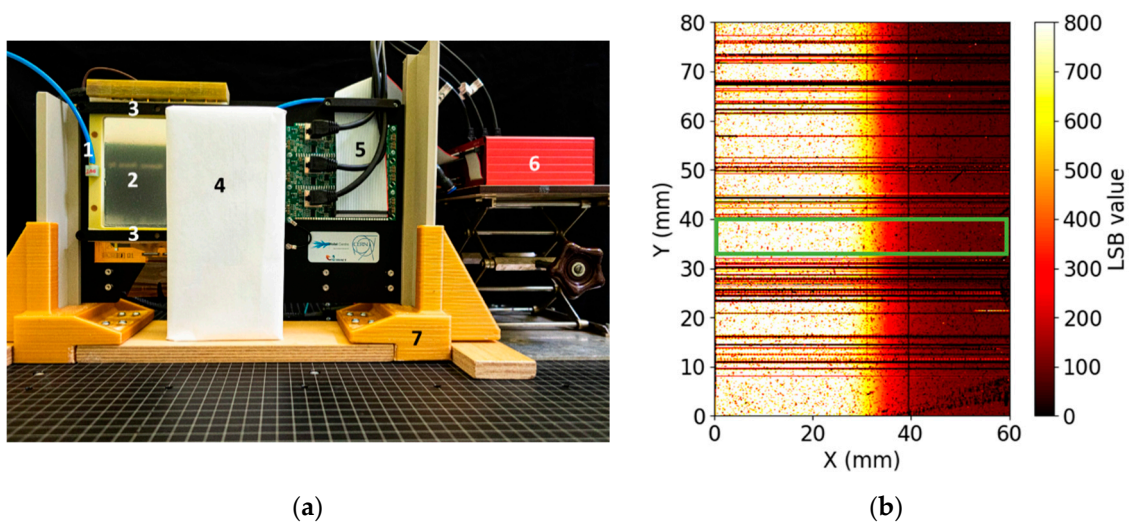


Figure 5. (a) The LaGEMPix with a 2.5 cm thick lead block placed in front of the detector: (1) gas outlet; (2) the $100 \times 100 \text{ mm}^2$ triple-GEM stack coupled to the optical readout with the thin Mylar window on top; (3) 3D-printed braces to hold together the triple-GEM detector and the image sensor; (4) lead block; (5) cables to connect the detector to the readout system; (6) FPGA module; (7) custom-made support. (b) Heat map of the imager after irradiation with 40 kV X-rays.

A ROI indicated by a green rectangle was defined around an area of the readout with a minimum number of defects. Figure 6 shows the edge response obtained by averaging all pixel values in the same column from the averaged background-subtracted image. This figure also shows a fit with a logistic function according to Equation (1). The FWHM obtained by this method is 9.70 ± 0.09 mm.

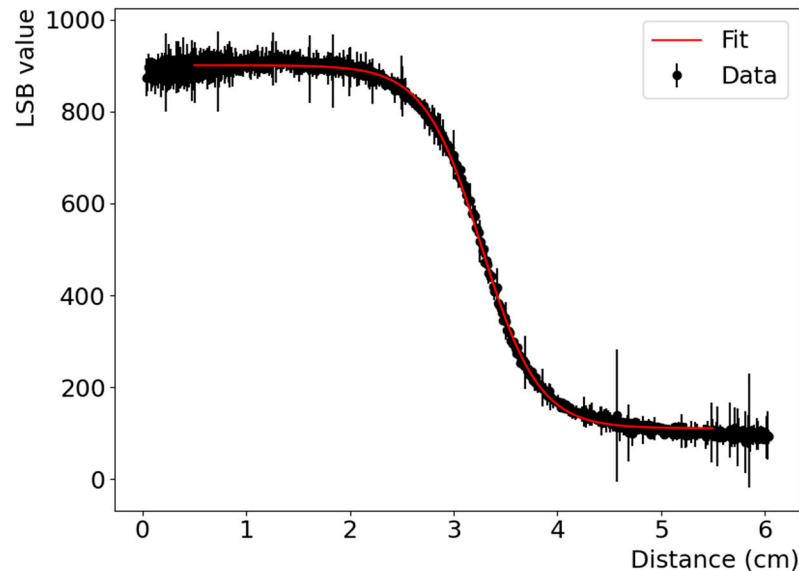


Figure 6. Edge response profile for 40 kV X-rays using a 2.5 cm thick lead block. The red line represents a logistic function fit to the data.

3.2.2. Line Spread Function (LSF)

For the LSF response, we used a 3 mm thick copper plate placed at 7 mm from the Mylar window (see Figure 7a). Various holes of 5 mm diameter spaced by 3 to 20 mm, edge to edge were drilled in the plate. The average image profile on a single hole is Gaussian. The spatial resolution was, therefore, estimated by fitting the distribution by a Gaussian function. The obtained FWHM for a 5 mm diameter hole is 6.73 ± 0.08 mm.

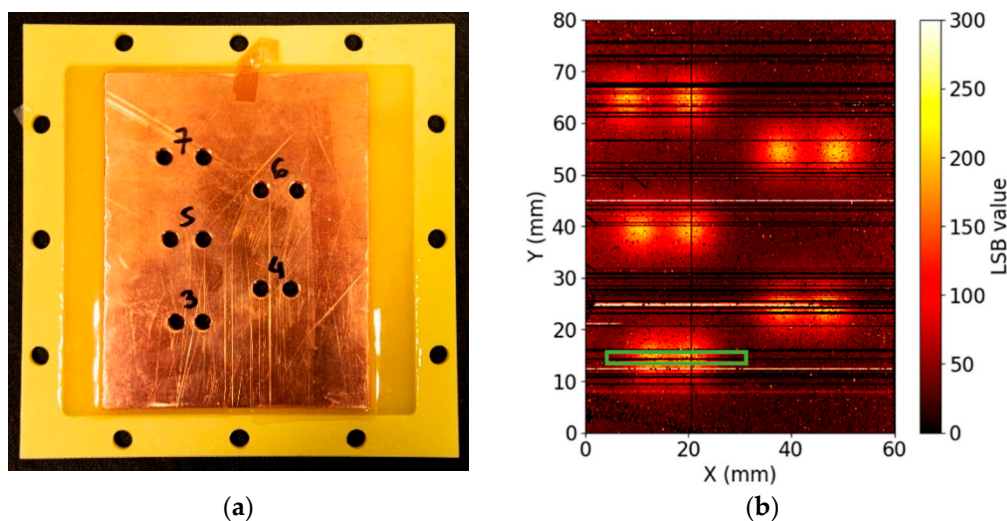


Figure 7. (a) The 3 mm-thick copper plate used for the evaluation of the spatial resolution using the LSF method. The numbers written on the plate represent the space between the holes in millimeters. (b) Heat map of the copper mask for 40 kV X-rays. A ROI (green rectangle) was set on the holes separated by 3 mm. The spatial resolution was estimated by fitting the profile in the ROI by a Gaussian function.

An additional measurement was made by selecting a ROI (green region in Figure 7b) at the center of the 5 mm holes spaced by 3 mm. Figure 8 shows the response of two holes spaced by 3 mm (edge to edge), featuring two peaks with a dip in the intensity. The response was again obtained by averaging all pixel values in the same column from the averaged background-subtracted image. The so-called FWHM criterion states that the minimum distance that any detector is able to resolve is equal to the FWHM value of the Gaussian distribution. The relevant values in this case are the center-to-center distance between the holes, 8 mm, and the FWHM, 7.10 ± 0.30 mm. Following this criterion, the two holes can be resolved.

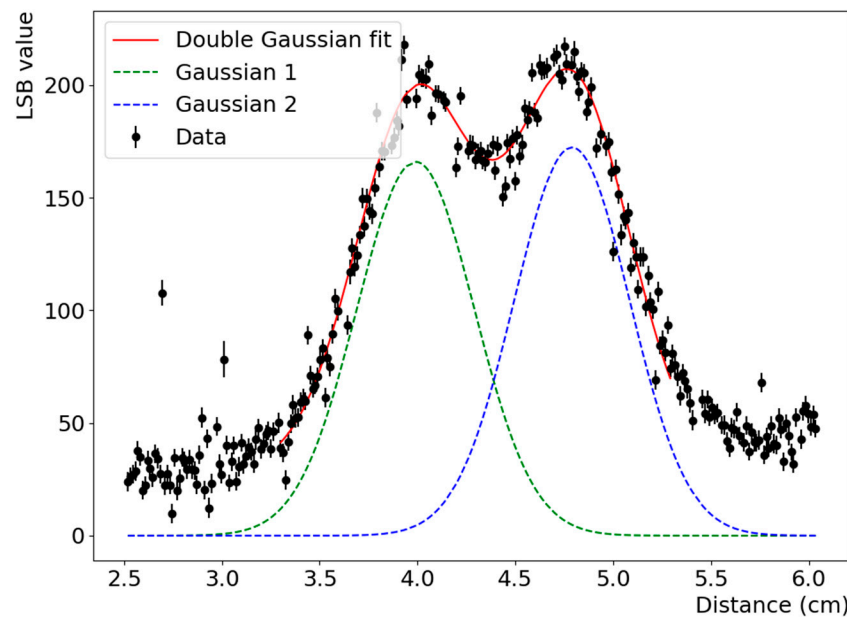


Figure 8. The line-average response profile of the 5 mm diameter holes spaced by 3 mm (edge to edge). The FWHM obtained by the Gaussian distribution is 7.10 ± 0.30 mm for the left hole and 6.80 ± 0.20 mm for the right hole. The distance (center-to-center fit) = 7.98 ± 0.23 mm was obtained by fitting the profile by a double Gaussian function.

3.2.3. Modulation Transfer Function (MTF)

The MTF characterizes how faithfully the spatial frequency content of the object is transferred to the image [49]. According to ISO 1233:2017, the results of the MTF analysis is reported using a graph plot. Nevertheless, the summary resolution metrics may also be used; the limiting spatial resolution is defined as the frequency at which the MTF drops below a certain percent value. Several values can be used; however, the 10% level is the most common one [50–52].

A line pair mask type 53 [53] was placed in front of the Mylar window to evaluate the MTF of the LaGEMPix as shown in Figure 9. This X-ray test pattern is made of 0.05 mm thick lead and the resolution range is from 0.5 up to 10 LP/mm. For this particular mask, 0.5 LP/mm means that one black and one white line within 4 mm are projected on the image sensor.

This test was carried out using 30 kV X-rays (instead of 40 kV) with the N-5 filter, in order to increase the contrast of the output image. The image in Figure 9 shows that it is not possible to measure the MTF of the LaGEMPix with this mask. We can conclude that the current version of the LaGEMPix is not able to distinguish 0.5 LP/mm, which corresponds to two slits separated by 2 mm.

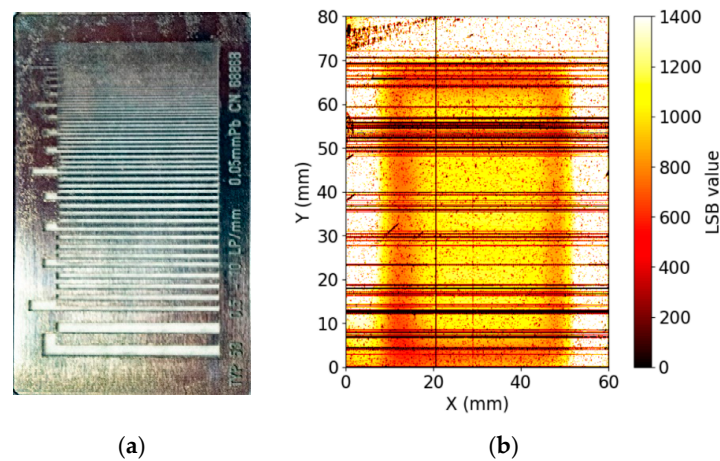


Figure 9. (a) Line pair mask type 53 made of 0.05 mm thick lead used as an imaging target. (b) Heat map of the MTF mask after irradiation with 30 kV X-rays.

3.3. Spatial Resolution with the GEMPix

In order to evaluate the contribution of the isotropic emission of the scintillation light to the spatial resolution in the LaGEMPix, we carried out comparative measurements with the GEMPix, a $2.8 \times 2.8 \text{ cm}^2$ triple-GEM detector that uses a Timepix quad ASIC to readout charges directly [6,54]. The experimental conditions were identical: 40 kV X-rays (N-6 series filter), minimum aperture 1 cm, 230 cm source-detector distance and same electric fields in the GEM structure.

3.3.1. Edge Spread Function

For the edge response, the 2.5 cm thick lead block was placed in the same position as for the measurement with the LaGEMPix (see Figure 5). A ROI (green region) was set perpendicularly to the edge. Figure 10 shows the edge response profile calculated from the average of 200 equalized images as explained earlier. The spatial resolution was estimated by fitting the edge profile by the logistic function of Equation (1). The FWHM obtained with the GEMPix is $5.20 \pm 0.10 \text{ mm}$.

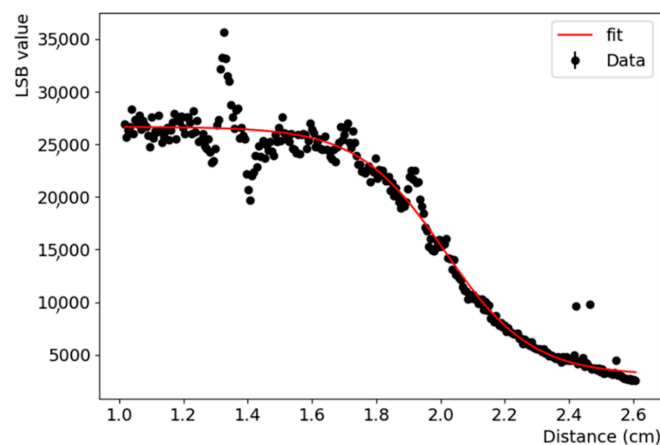


Figure 10. Edge response profile with the GEMPix for 40 kV X-rays obtained using a 2.5 cm-thick lead block. The red line represents a logistic function fit to the data. The signal fluctuations at around 1.4 cm are caused by the physical gap between the Timepix chips, which may lead to distortions of the electric field close to the edge. Other features, such as those around 1.7 and 1.9 cm, are due to imperfections in the detector that the equalization procedure cannot compensate for. These artefacts are most likely the result of radiation effects, as the detector was already used in several experiments with ionizing radiation.

3.3.2. Line Spread Function

The study of the spatial resolution using the LSF method and the GEMPix was carried out using two copper plates of different thicknesses and hole patterns. Holes with a diameter smaller than 5 mm were imaged using a 1 mm thick plate placed in front of the GEMPix. Results with this mask and the LaGEMPix are not reported in this paper, as they do not provide additional information. This mask had 23 holes of several sizes and spacing. The results for three 1.3 mm holes spaced by 1 mm (edge to edge) are depicted in Figure 11. Following the FWHM criterion introduced in Section 3.2.2, we can conclude that two holes of 1.3 mm diameter at a distance of 1 mm (edge to edge) can be resolved. Measurements with the 3 mm thick copper plate and 5 mm diameter holes showed a spatial resolution of 5.23 ± 0.05 mm (FWHM). The results from the LSF method are summarized in Table 1.

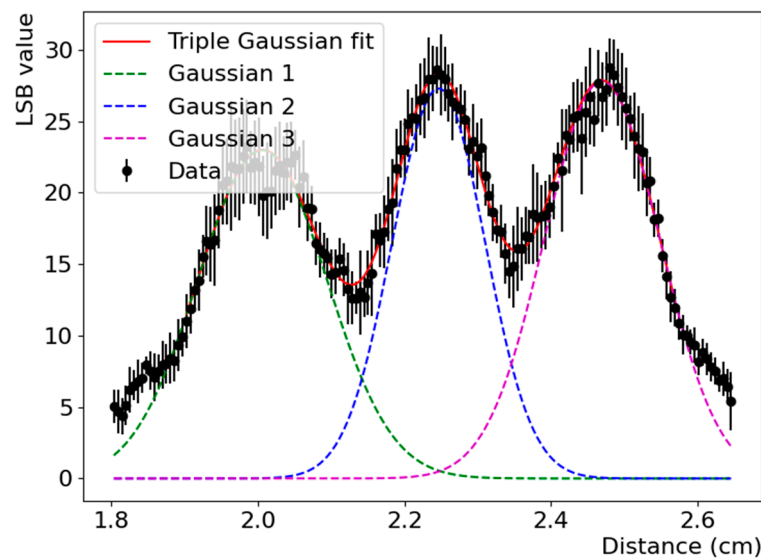


Figure 11. The line-average response profile of 1.3 mm diameter holes spaced by 1 mm (edge to edge). The FWHM of the Gaussian distribution of the three holes (Table 1) were obtained by fitting the profile by a triple Gaussian function.

Table 1. Calculated FWHM of the 1D profiles for three regions of interest of the images obtained by the GEMPix and the 1 mm-thick copper plate.

Ø Hole	FWHM (mm)		
	Hole 1	Hole 2	Hole 3
6 mm	6.60 ± 0.10	-	-
3 mm	3.08 ± 0.06	3.04 ± 0.09	3.46 ± 0.09
1.3 mm	2.07 ± 0.05	1.49 ± 0.03	1.85 ± 0.03

3.3.3. Modulation Transfer Function

As for the LaGEMPix, we carried out a set of measurements using the lead mask model 53 (see Figures 9 and 12). Contrary to the LaGEMPix, the GEMPix yielded an MTF below 10% at 1.4 LP/mm which corresponds to 0.71 mm, achieving the targeted submillimeter spatial resolution. The normalized MTF obtained by using Equation (2) is shown in Figure 13.

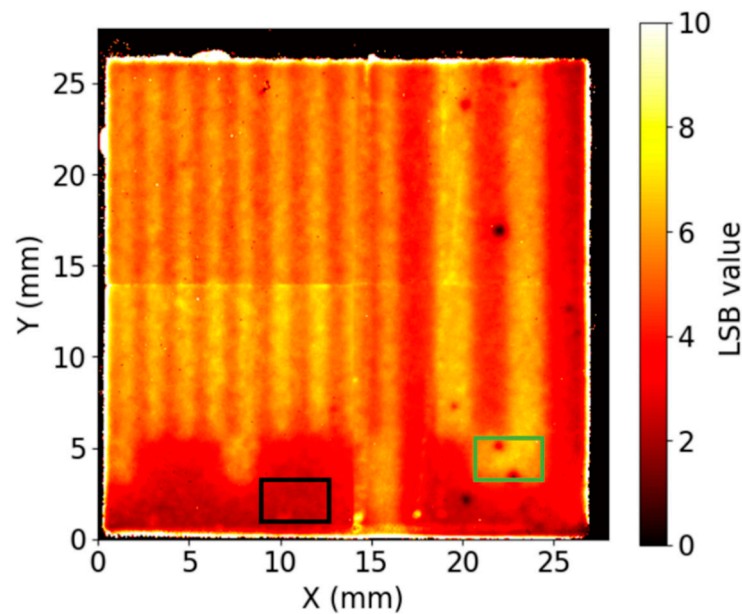


Figure 12. Heat map for 30 kV X-rays using a line pair mask type 53 as an imaging target in front of the GEMPix. For the normalization factor C_0 in Equation (2), two regions were selected: the green rectangle on top of the first bar for the maximum pixel intensities and a black rectangle on the bottom part of the mask for the minimum.

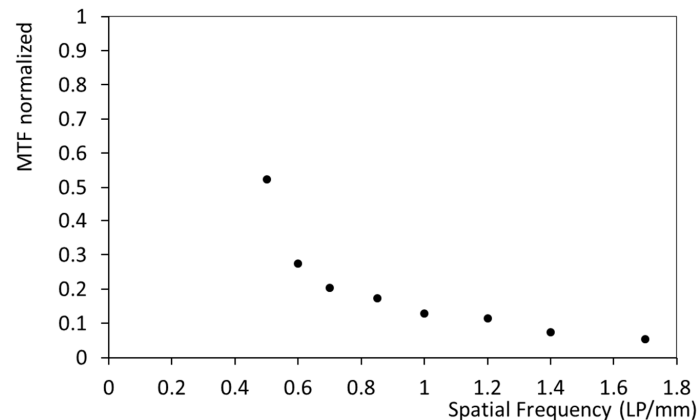


Figure 13. Measured MTF with mask type 53 by using Equation (2) for the GEMPix detector.

3.4. Spatial Resolution with GAFCHROMIC® Films

Effects not related to the detector itself can be studied with an “ideal” system of known spatial resolution, such as high resolution GAFCHROMIC® films. Film dosimetry is frequently classified as the gold standard for 2D dosimetry [33]. We selected GAFCHROMIC® XR-SP2 films that are appropriate for X-ray energies from 20 kV to 200 kV, and dose range from 0.5 mSv to 100 mSv. The film calibration was performed at the Institute of Radiation Physics (IRA) in Lausanne, Switzerland [55].

The experimental conditions were identical to those of the LaGEMPix measurements. For the edge response method (Section 3.2.1), we placed the lead block of $10 \times 20 \times 2.5 \text{ cm}^3$ size covering a portion of the film. For the LSF response, the 3 mm thick copper plate with 5 mm diameter holes was also placed in front of the film (see Section 3.2.2 for details). The films were digitalized with an EPSON V800 scanner. The FWHM obtained by the edge response method is $0.86 \pm 0.07 \text{ mm}$ and the FWHM of a single 5 mm diameter hole is $5.09 \pm 0.03 \text{ mm}$. The results and the comparison between the films and the GEM-based detectors are summarized and discussed in Section 4.

3.5. Spatial Resolution with the FLUKA Simulation

We performed three sets of simulations to compare the experimental values for both the ESF and LSF methods. The study includes the simulation of the 2.5 cm thick lead block described in Section 3.2.1, the 3 mm thick copper plate with 5 mm diameter holes (Section 3.2.2), and the 1 mm thick copper plate (Section 3.3.2). The latter had 23 holes of several sizes and spacing, simulated in such a way that the central hole was aligned to the center of the active area of the image sensor. The 3 mm thick plate was simulated at 7 mm from the Mylar window. The lead block and the 1 mm thick copper plate were simulated at 4 cm and 3.3 cm from the Mylar window, respectively. Figure 14 shows two of the simulated set-ups. In all cases, the source-detector distance was fixed at 230 cm with the minimum collimator aperture of 1 cm.

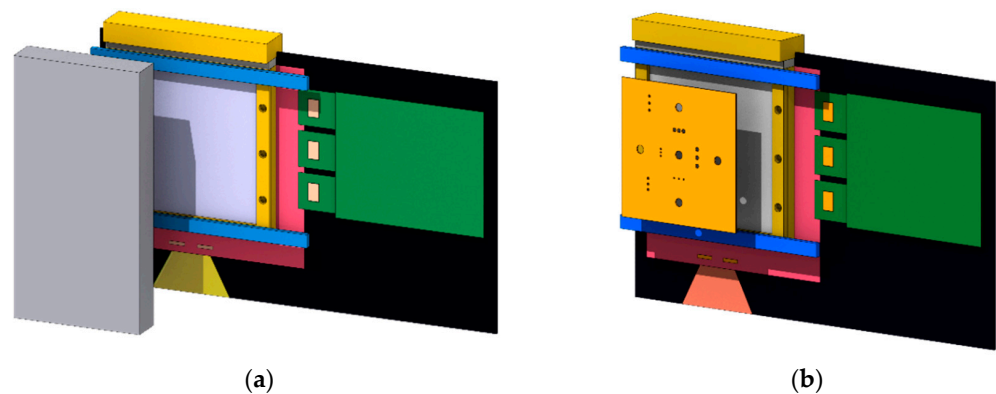


Figure 14. The simulated LaGEMPix with the 2.5 cm thick lead block in front, at 4 cm distance from the Mylar window (a) and a 1 mm-thick copper plate placed at 3.3 cm from the Mylar window (b). The figures were produced using FLAIR [56] version 3.1-8, the FLUKA graphical user-interface.

3.5.1. Edge Spread Function

Figure 15 shows the ESF for 40 kV X-rays. The ESF was determined by projecting the edge profile in the direction perpendicular to the edge. The spatial resolution was then estimated by fitting the measured ESF by the logistic function of Equation (1). The data points were shifted to center the distribution at the center of the image sensor; the bin size is $0.25 \mu\text{m}$ (twice the pixel size). When limiting the fit to the full active area of the sensor (6 cm along the x-axis), the estimated value of the FWHM is $4.53 \pm 0.01 \text{ mm}$ (statistical errors only).

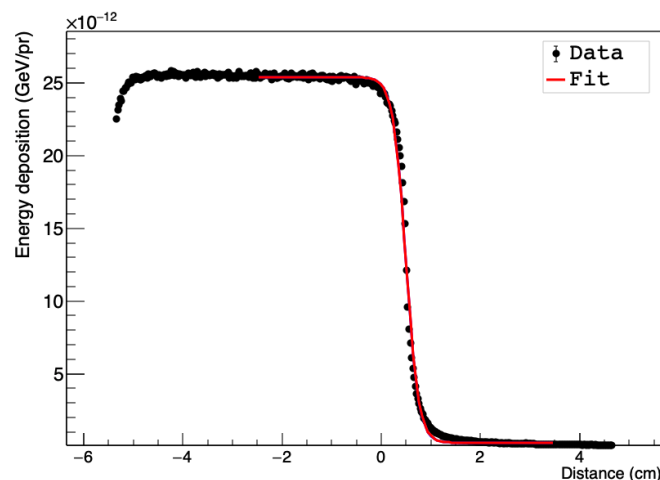


Figure 15. Simulated ESF for the edge projection fitted by a logistic function. The results were obtained for a detector-source distance of 230 cm, a beam aperture of 1 cm and 40 kV X-rays. The error bars are smaller than the data points.

3.5.2. Line Spread Function

The results from the LSF method and the 1 mm thick copper plate are summarized in Table 2. The number of primaries was chosen such that the statistical uncertainties were smaller than 5%. The spatial resolution was estimated by fitting the LSF by a Gaussian function and measuring the FWHM of the central 6 mm diameter holes, the 6 mm hole at the top of the plate, the three 3 mm holes separated by 4 mm pitch and the 1.3 mm holes separated by 2.5 mm pitch (see Figure 16).

Table 2. Calculated FWHM of the 1D profiles for the different regions of interest depicted in Figure 16.

Ø Hole	FWHM (mm)		
	Hole 1	Hole 2	Hole 3
6 mm	5.70 ± 0.20	5.45 ± 0.11	5.26 ± 0.12
6 mm	5.82 ± 0.13	-	-
3 mm	2.96 ± 0.17	2.99 ± 0.24	2.82 ± 0.16
1.3 mm	1.32 ± 0.12	1.61 ± 0.16	1.48 ± 0.17

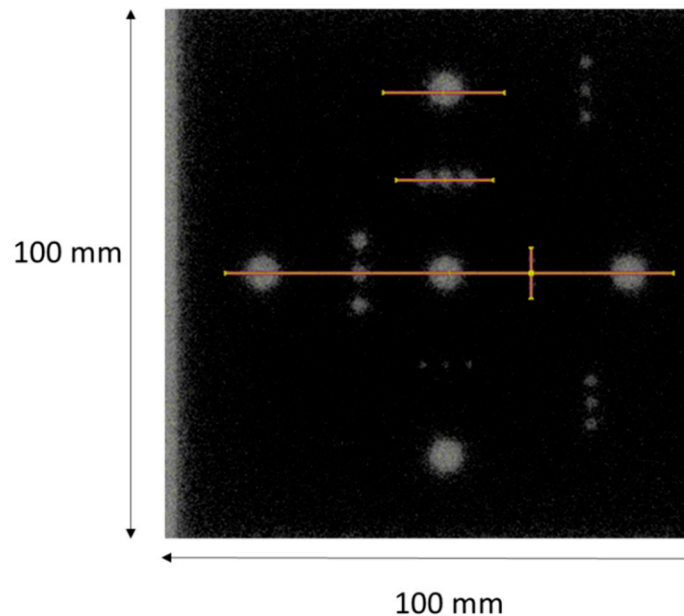


Figure 16. Image of the simulated energy deposition density in the drift gap. The solid yellow lines represent the selected regions for data analysis.

The profiles obtained for the three 1.3 mm holes separated by 1 mm (distance calculated from edge to edge) are shown in Figure 17. The three holes are perfectly resolvable following the FWHM criterion; the calculated hole diameter is smaller than or of the order of the hole. This implies that the spatial resolution is better than the hole size. Similar results were obtained with 3 mm thick copper plate and 5 mm diameter holes, which showed a spatial resolution of 4.87 ± 0.03 mm (FWHM).

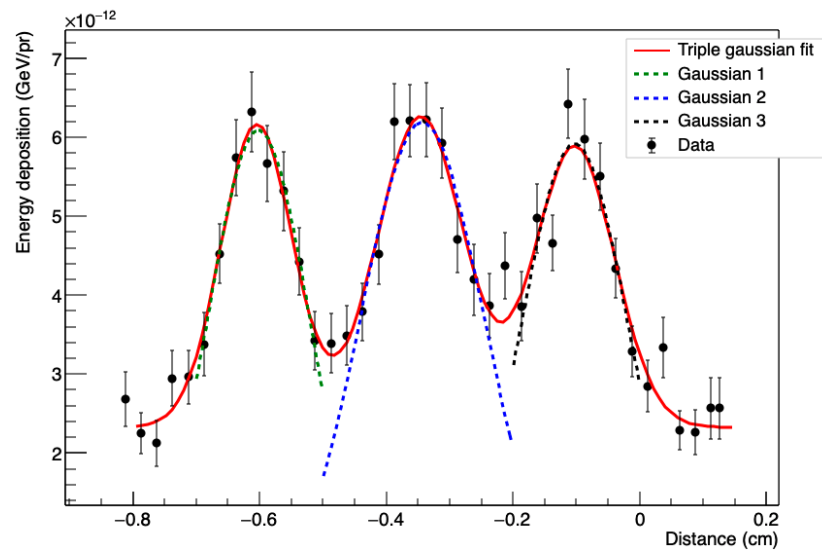


Figure 17. One-dimensional projection of the 1.3 mm holes with 2.5 mm pitch. The LSF of the selected area gives a distribution with an average hole diameter of 1.47 mm.

4. Discussion on the Spatial Resolution

The spatial resolution of the LaGEMPix was evaluated, using different methods and experimental configurations. The results are summarized in Table 3. The measurements with the lead block (ESF) yielded a spatial resolution of 9.70 ± 0.09 mm for 40 kV X-rays. On the other hand, the LSF method showed that the detector can resolve two 5 mm holes separated by 3 mm. This suggests that the ESF method reported here underestimates the spatial resolution of the LaGEMPix, whose intrinsic spatial resolution is better than 9.70 ± 0.09 mm. It also means that the results obtained from the different methods cannot be directly compared. Additionally, the MTF measurements only allow to conclude that slits at 2 mm distance cannot be distinguished. These results show that the spatial resolution of the current LaGEMPix does not fulfil the criterion of sub-millimeter resolution for hadron therapy and that the exact value depends on the method applied to evaluate the spatial resolution.

Table 3. Summary of the spatial resolution obtained for different experimental configurations and by different detectors. Results from the FLUKA Monte Carlo simulation are also included for comparison.

Detector	Spatial Resolution (mm)		
	Edge Response	5 mm Cu Hole	Minimum Resolvable Hole Spacing
LaGEMPix	9.70 ± 0.09	6.73 ± 0.08	3 mm (edge to edge)
GEMPix	5.20 ± 0.10	5.23 ± 0.05	1 mm ¹ (edge to edge)
GAFCHROMIC [®]	0.86 ± 0.07	5.09 ± 0.03	1 mm ¹ (edge to edge)
FLUKA simulation of LaGEMPix	4.53 ± 0.01	4.87 ± 0.03	1 mm ¹ (edge to edge)

¹ minimum distance between holes in the Cu plate.

In order to disentangle the effects on the spatial resolution from different sources, such as the experimental setup, electron diffusion in the gas, and isotropic emission of photons in the detector, measurements were performed with the GEMPix and GAFCHROMIC[®] XR-SP2 films. Table 3 summarizes the values of spatial resolution obtained for the various detectors and experimental configurations. As expected, the GAFCHROMIC[®] films show the best spatial resolution. The edge response worsens from 0.86 mm with the film to 5.20 mm with the GEMPix, while slight differences are observed with the LSF method.

In both cases, holes separated by a distance of 1 mm can still be resolved. The GEMPix yielded an MTF below 10% at 1.4 LP/mm. The ESF of the LaGEMPix and the FWHM of a 5 mm hole are higher than with the GEMPix. A further decrease in the spatial resolution is observed with the LaGEMPix, associated to the isotropic emission of scintillation photons. The results show that with the current design of the LaGEMPix, holes at a distance of 1 mm can no longer be resolved; the MTF method also shows that slits spaced by 2 mm cannot be resolved.

Finally, the results of a FLUKA Monte Carlo simulation of the LaGEMPix were compared with the experimental results. Unsurprisingly, the resolution obtained from the simulation is much better than the experimental one. This can be explained by the fact that the simulation does not take into account some phenomena associated with the detector working principle, such as the isotropic emission of the scintillation photons. On the other hand, the simulation predictions agree with the GEMPix results. This implies that (1) the simulation is able to reproduce the experimental results where only electrons are involved in the final image, (2) the isotropic emission of the scintillation light introduces an additional blurring in the image, and (3) other effects not included in the simulation, such as electron diffusion and recombination, seem to have a little effect on the spatial resolution. It can also be concluded that even for an ideal triple-GEM detector, where only primary energy depositions are taken into consideration, a sub-millimeter spatial resolution is not reachable. Similar results were obtained for 30 kV X-rays. The edge response method underestimates the resolution of the detector as compared to the other methods. This effect can be caused by the electron mean free path in the gas that introduces an additional blur to the image.

5. Conclusions

In this paper, we present for the first time the characterization of a GEM-based detector with optical readout based on a matrix of OPDs fabricated on top of a TFT backplane using low energy X-rays. The results presented in this paper show that the current LaGEMPix prototype achieves a spatial resolution of a few millimeters. The value obtained from the ESF using a 2.5 cm lead block underestimates the intrinsic spatial resolution when comparing it to the ability of the detector to resolve features such as two holes spaced by 3 mm. Similar conclusions can be extracted from the GEMPix measurements and the FLUKA simulation.

Several avenues of investigation are being explored to improve the spatial resolution and reach the desired target for QA in hadron therapy. Considering the better spatial resolution obtained with the GEMPix, the major limitation to the spatial resolution stems from the isotropic emission of the photons, and its effect on the spatial resolution depends on the distance between the places of production and detection of the photons. Therefore, a new detector prototype is under design in which the distance between GEM3 and the readout is reduced from 3 to 1.5 mm. To further improve on spatial resolution, an optical collimator film could be placed between the ITO on quartz and the thin-film imager, such that emitted photons under larger off-normal angles to the imaging plane are prevented to reach the optical imager frontplane.

Another general improvement is to employ a different type of OPD to increase the signal strength by providing a better match between the emission spectrum in the gas and the acceptance spectrum of the OPD. The ITO transparent anode with the fused quartz substrate will be replaced by the ITO coated fused silica glass following results of recent measurements [57]. Measurements with clinical hadron beams are also planned in the future.

An alternative solution currently being assessed is to eliminate the OPD frontplane, leaving a TFT-only electronic readout. With this approach, secondary electrons produced in the avalanche would be directly measured by the readout, yielding an even more compact and possibly more efficient device with a higher signal-to-noise ratio. In this case, a

sub-millimeter resolution can be expected based on the MTF results obtained with the GEMPix.

Author Contributions: All the authors conceptualized the system, A.J.J.M.v.B.; H.B.A.; I.K.; B.P. and F.M. contributed to the design and construction of the prototype with the help of A.M.O., L.G.M. and J.L. for the merging. A.M.O., N.H., L.G.M. and J.L. developed the methodology; A.M.O., N.H. and B.P. developed the software, A.M.O. collected the data and was responsible for the data curation, A.M.O. and N.H. contributed to the formal data analysis, A.M.O., N.H. and L.G.M. validated the data; L.G.M. performed the FLUKA Monte Carlo simulations; A.M.O., J.L., L.G.M. and N.H. conducted the investigation process, specifically performing the experiments. A.M.O. prepared the original draft and L.G.M. wrote Sections 2.5 and 3.5.; M.S. and S.B. supervised the research activities. M.S. and N.H. acquired the financial support for the project leading to this publication. All the authors revised the paper. All authors have read and agreed to the published version of the manuscript.

Funding: This project has received funding from the ATTRACT project funded by the EC under Grant Agreement 777222. The project has also been supported by CERN's Budget for Knowledge Transfer to Medical Applications. Andreia Maia Oliveira was co-supported by a grant from FCT with reference SFRH/BEST/142965/2018.

Acknowledgments: The authors wish to thank: Rui de Oliveira for the special design of the GEM foils; Pierre Carbonez and Alix Chantelauze for granting us access to the Calibration Laboratory of CERN Radiation Protection Group; Pierre Carbonez, Thierry Buchillier, Claude Bailat and Jerome Damet for the calibration measurements with GAFCHROMIC® films performed at the Institute of Radiation Physics (IRA) in Lausanne, Switzerland; Florian Brunbauer for providing the MTF mask and for the useful discussions; the people from Holst Centre's Gen1 R&D TFT pilot line and Santhosh Shanmugam for their contributions in thin-film imager fabrication.

Conflicts of Interest: The authors declare no conflict of interest. The funders had no role in the design of the study; in the collection, analyses, or interpretation of data; in the writing of the manuscript, or in the decision to publish the results.

References

1. Particle Therapy Facilities in Clinical Operation. Available online: <https://www.ptcog.ch/index.php/facilities-in-operation> (accessed on 17 January 2021).
2. Ishikawa, H.; Nakai, K.; Nonaka, T.; Sakurai, H. Particle Therapy in Cancer Treatment—Current and Future Perspective. *Gan to kagaku ryoho. Cancer Chemother.* **2019**, *46*, 1219–1225.
3. Rana, S.; Bennouna, J.; Samuel, E.J.J.; Gutierrez, A.N. Development and Long-Term Stability of a Comprehensive Daily QA Program for a Modern Pencil Beam Scanning (PBS) Proton Therapy Delivery System. *J. Appl. Clin. Med. Phys.* **2019**, *20*, 29–44. [[CrossRef](#)]
4. Sauli, F. The Gas Electron Multiplier (GEM): Operating Principles and Applications. *Nucl. Instrum. Methods Phys. Res. Sect. A Accel. Spectrometers Detect. Assoc. Equip.* **2016**, *805*, 2–24. [[CrossRef](#)]
5. Leidner, J.; Ciocca, M.; Mairani, A.; Murtas, F.; Silari, M. A GEMPix-Based Integrated System for Measurements of 3D Dose Distributions in Water for Carbon Ion Scanning Beam Radiotherapy. *Med. Phys.* **2020**, *47*, 2516–2525. [[CrossRef](#)] [[PubMed](#)]
6. Leidner, J.; Murtas, F.; Silari, M. Medical Applications of the GEMPix. *Appl. Sci.* **2021**, *11*, 440. [[CrossRef](#)]
7. Mirandola, A.; Molinelli, S.; Vilches Freixas, G.; Mairani, A.; Gallio, E.; Panizza, D.; Russo, S.; Ciocca, M.; Donetti, M.; Magro, G.; et al. Dosimetric Commissioning and Quality Assurance of Scanned Ion Beams at the Italian National Center for Oncological Hadrontherapy. *Med. Phys.* **2015**, *42*, 5287–5300. [[CrossRef](#)] [[PubMed](#)]
8. Grevillot, L.; Osorio Moreno, J.; Letellier, V.; Dreindl, R.; Elia, A.; Fuchs, H.; Carlino, A.; Kragl, G.; Palmans, H.; Vatnitsky, S.; et al. Clinical Implementation and Commissioning of the MedAustron Particle Therapy Accelerator for Non-Isocentric Scanned Proton Beam Treatments. *Med. Phys.* **2020**, *47*, 380–392. [[CrossRef](#)] [[PubMed](#)]
9. Van de Weijer, P.; Akkerman, H.B. Spotless Hybrid Thin-Film Encapsulation Stack for Organic Light-Emitting Diodes on Organic Foils. *Org. Electron.* **2019**, *66*, 43–46. [[CrossRef](#)]
10. Bencivenni, G.; Felici, G.; Murtas, F.; Valente, P.; Bonivento, W.; Cardini, A.; Lai, A.; Pinci, D.; Saitta, B.; Bosio, C. A Triple GEM Detector with Pad Readout for High Rate Charged Particle Triggering. *Nucl. Instrum. Methods Phys. Res. Sect. A Accel. Spectrometers Detect. Assoc. Equip.* **2002**, *488*, 493–502. [[CrossRef](#)]
11. Brunbauer, F.M. *Applications of Gas Scintillation Properties in Optically Read out GEM-Based Detectors*; Technical University of Vienna: Vienna, Austria, 2018.
12. Indium Tin Oxide Glass. Available online: http://www.visionteksystems.co.uk/ito_glass_datasheet.htm (accessed on 21 February 2021).

13. Fraga, M.; Fraga, F.; Fetal, S.T.G.; Margato, L.; Marques, R.; Policarpo, A. The GEM Scintillation in He-CF₄, Ar-CF₄, Ar-TEA and Xe-TEA Mixtures. *Nucl. Instrum. Methods Phys. Res. A* **2003**, *504*, 88–92. [[CrossRef](#)]
14. Timmer, J.; Van Vuure, T.; Bom, V.; Eijk, C.W.E.; de Haas, J.; Schippers, J. A Scintillating GEM for 2D-Dosimetry in Radiation Therapy. *Nucl. Instrum. Methods Phys. Res. A* **2002**, *478*, 98–103. [[CrossRef](#)]
15. Pansky, A.; Breskin, A.; Buzulutskov, A.; Chechik, R.; Elkind, V.; Va'vra, J. The Scintillation of CF₄ and Its Relevance to Detection Science. *Nucl. Instrum. Methods Phys. Res. A* **1995**, *354*, 262–269. [[CrossRef](#)]
16. Hamamatsu. Image Sensors. Available online: https://www.hamamatsu.com/resources/pdf/ssd/image_sensor_kmpd0002e.pdf (accessed on 4 July 2021).
17. Hamamatsu. Handbook Image Sensors—Chapter 5. Available online: https://www.hamamatsu.com/resources/pdf/ssd/e05_handbook_image_sensors.pdf (accessed on 3 July 2021).
18. Seravalli, E.; de Boer, M.R.; Geurink, F.; Huizenga, J.; Kreuger, R.; Schippers, J.M.; van Eijk, C.W.E. 2D Dosimetry in a Proton Beam with a Scintillating GEM Detector. *Phys. Med. Biol.* **2009**, *54*, 3755–3771. [[CrossRef](#)]
19. Klyachko, A.V.; Moskvina, V.; Nichiporov, D.F.; Solberg, K.A. A GEM-Based Dose Imaging Detector with Optical Readout for Proton Radiotherapy. *Nucl. Instrum. Methods Phys. Res. A* **2012**, *694*, 271–279. [[CrossRef](#)]
20. Kronemeijer, A.J.; Akkerman, H.; van der Steen, J.-L.; Steudel, S.; Pendyala, R.; Panditha, P.; Bel, T.; van Diesen, K.; de Haas, G.; Maas, J.; et al. P-127: Dual-Gate Self-Aligned IGZO TFTs Monolithically Integrated with High-Temperature Bottom Moisture Barrier for Flexible AMOLED. In *SID Symposium Digest of Technical Papers*; SID: Los Angeles, CA, USA, 2018; pp. 1577–1580. Volume 49. [[CrossRef](#)]
21. Tordera, D.; Peeters, B.; Akkerman, H.B.; van Breemen, A.J.J.M.; Maas, J.; Shanmugam, S.; Kronemeijer, A.J.; Gelinck, G.H. A High-Resolution Thin-Film Fingerprint Sensor Using a Printed Organic Photodetector. *Adv. Mater. Technol.* **2019**, *4*, 1900651. [[CrossRef](#)]
22. Kielar, M.; Dhez, O.; Pecastaings, G.; Curutchet, A.; Hirsch, L. Long-Term Stable Organic Photodetectors with Ultra Low Dark Currents for High Detectivity Applications. *Sci. Rep.* **2016**, *6*, 39201. [[CrossRef](#)]
23. Sauli, F. GEM: A New Concept for Electron Amplification in Gas Detectors. *Nucl. Instrum. Methods Phys. Res. A* **1997**, *386*, 531–534. [[CrossRef](#)]
24. Brunbauer, F.M.; Garcia, F.; Korkalainen, T.; Lugstein, A.; Lupberger, M.; Oliveri, E.; Pfeiffer, D.; Ropelewski, L.; Thuiner, P.; Schinnerl, M. Combined Optical and Electronic Readout for Event Reconstruction in a GEM-Based TPC. *IEEE Trans. Nucl. Sci.* **2018**, *65*, 913–918. [[CrossRef](#)]
25. Brugger, M.; Carbonez, P.; Pozzi, F.; Silari, M.; Vincke, H. New Radiation Protection Calibration Facility at CERN. *Radiat. Prot. Dosim.* **2014**, *161*, 181–184. [[CrossRef](#)]
26. Tektronix. Model 6517A Electrometer User's Manual Rev. C. Available online: <https://www.tek.com/manual/model-6517a-electrometer-users-manual-rev-d-manual> (accessed on 23 February 2021).
27. Curioni, A.; Dinar, N.; La Torre, F.P.; Leidner, J.; Murtas, F.; Puddu, S.; Silari, M. Measurements of ⁵⁵Fe Activity in Activated Steel Samples with GEMPix. *Nucl. Instrum. Methods Phys. Res.* **2017**, *849*, 60–71. [[CrossRef](#)]
28. Molinelli, S.; Mairani, A.; Mirandola, A.; Vilches Freixas, G.; Tessonnier, T.; Giordanengo, S.; Parodi, K.; Ciocca, M.; Orecchia, R. Dosimetric Accuracy Assessment of a Treatment Plan Verification System for Scanned Proton Beam Radiotherapy: One-Year Experimental Results and Monte Carlo Analysis of the Involved Uncertainties. *Phys. Med. Biol.* **2013**, *58*, 3837–3847. [[CrossRef](#)] [[PubMed](#)]
29. Winter, J.; Ellerbrock, M.; Jäkel, O.; Grelich, S.; Bangert, M. Analytical Modeling of Depth-Dose Degradation in Heterogeneous Lung Tissue for Intensity-Modulated Proton Therapy Planning. *Phys. Imaging Radiat. Oncol.* **2020**, *14*, 32–38. [[CrossRef](#)] [[PubMed](#)]
30. PTW Freiburg GmbH. Radiation Therapy. Available online: <https://www.ptwdosimetry.com/en/solutions/radiation-therapy/> (accessed on 21 February 2021).
31. GmbH. IBA Dosimetry. Available online: <https://www.iba-dosimetry.com/> (accessed on 21 February 2021).
32. Giordanengo, S.; Palmans, H. Dose Detectors, Sensors, and Their Applications. *Med Phys.* **2018**, *45*, e1051–e1072. [[CrossRef](#)] [[PubMed](#)]
33. Grevillot, L.; Stock, M.; Palmans, H.; Osorio Moreno, J.; Letellier, V.; Dreindl, R.; Elia, A.; Fuchs, H.; Carlino, A.; Vatnitsky, S. Implementation of Dosimetry Equipment and Phantoms at the MedAustron Light Ion Beam Therapy Facility. *Med. Phys.* **2018**, *45*, 352–369. [[CrossRef](#)]
34. Russo, S.; Mirandola, A.; Molinelli, S.; Mastella, E.; Vai, A.; Magro, G.; Mairani, A.; Boi, D.; Donetti, M.; Ciocca, M. Characterization of a Commercial Scintillation Detector for 2-D Dosimetry in Scanned Proton and Carbon Ion Beams. *Phys. Med.* **2017**, *34*, 48–54. [[CrossRef](#)]
35. ISO. *ISO 12233:2017, Photography—Electronic Still Picture Imaging—Resolution and Spatial Frequency Responses*; ISO: Geneva, Switzerland, 2017.
36. Gopal, A.; Samant, S.S. Validity of the Line-Pair Bar-Pattern Method in the Measurement of the Modulation Transfer Function (MTF) in Megavoltage Imaging. *Med Phys.* **2008**, *35*, 270–279. [[CrossRef](#)]
37. Smith, S.W. *The Scientist and Engineer's Guide to Digital Signal Processing*; California Technical Pub.: San Diego, CA, USA, 1999; pp. 423–432. ISBN 9780966017649.
38. Roque, R.; Carramate, L.; Amaro, F.; Natal da Luz, H.; Mir, J.A.; Azevedo, C.D.R. Spatial Resolution Properties of Krypton-Based Mixtures Using a 100 Mm Thick Gas Electron Multiplier. In *Proceedings of the XRS 2018, Ljubljana, Slovenia, 26–29 June 2018*.

39. Jakubek, J.; Holy, T.; Lehmann, E.; Pospisil, S.; Uher, J.; Vacik, J.; Vavrik, D.; Andrikos, I.O. Properties of Neutron Pixel Detector Based on Medipix-2 Device. In Proceedings of the IEEE Symposium Conference Record Nuclear Science 2004, Rome, Italy, 16–22 October 2004; Volume 2, p. 949.
40. Fujiwara, T.; Mitsuya, Y.; Fushie, T.; Murata, K.; Kawamura, A.; Koishikawa, A.; Toyokawa, H.; Takahashi, H. Gas Scintillation Glass GEM Detector for High-Resolution X-Ray Imaging and CT. *Nucl. Instrum. Methods Phys. Res. A* **2017**, *850*, 7–11. [[CrossRef](#)]
41. Li, T.; Feng, H.; Xu, Z.; Li, X.; Cen, Z.; Li, Q. Comparison of Different Analytical Edge Spread Function Models for MTF Calculation Using Curve-Fitting. *Proc. SPIE* **2009**, *7498*. [[CrossRef](#)]
42. Energy Resolution Due to Thermal Broadening (STM). Available online: <https://shunchi100.wordpress.com/physics-research/energy-resolution-thermal-broadening/> (accessed on 23 February 2021).
43. Alvarez, M.; Alves, A.; Neto, F.B.; Pavan, A.L.; Rosa, M.; Miranda, J.R.D.A.; de Pina, D.R. Comparison of Bar Pattern and Edge Method for MTF Measurement in Radiology Quality Control. *Rev. Bras. Fis. Med.* **2015**, *9*, 2–5. [[CrossRef](#)]
44. ISO. ISO 4037-2:2019. *Radiological Protection—X and Gamma Reference Radiation for Calibrating Dosimeters and Doserate Meters and for Determining Their Response as a Function of Photon Energy—Part 2: Dosimetry for Radiation Protection over the Energy Ranges from 8 keV to 1,3 MeV and 4 MeV to 9 MeV*; ISO: Geneva, Switzerland, 2019.
45. The Official CERN FLUKA Website. Available online: <https://fluka.cern/> (accessed on 23 February 2021).
46. Battistoni, G.; Boehlen, T.; Cerutti, F.; Chin, P.W.; Esposito, L.S.; Fassò, A.; Ferrari, A.; Lechner, A.; Empl, A.; Mairani, A.; et al. Overview of the FLUKA Code. *Ann. Nucl. Energy* **2015**, *82*, 10–18. [[CrossRef](#)]
47. Bohlen, T.T.; Cerutti, F.; Chin, M.P.W.; Fassò, A.; Ferrari, A.; Ortega, P.G.; Mairani, A.; Sala, P.R.; Smirnov, G.; Vlachoudis, V. The FLUKA Code: Developments and Challenges for High Energy and Medical Applications. *Nucl. Data Sheets* **2014**, *120*, 211–214.
48. Marafini, M.; Patera, V.; Pinci, D.; Sarti, A.; Sciubba, A.; Spiriti, E. Optical Readout of a Triple-GEM Detector by Means of a CMOS Sensor. *Nucl. Instrum. Methods Phys. Res. A* **2016**, *824*, 562–564. [[CrossRef](#)]
49. Ahmed, S.N. Position-sensitive detection and imaging. In *Physics and Engineering of Radiation Detection*, 1st ed.; Academic Press: Amsterdam, The Netherlands, 2007; pp. 423–463. ISBN 9780120455812.
50. Seco, J.; Oumano, M.; Depauw, N.; Dias, M.F.; Teixeira, R.P.; Spadea, M.F. Characterizing the Modulation Transfer Function (MTF) of Proton/Carbon Radiography Using Monte Carlo Simulations. *Med. Phys.* **2013**, *40*, 091717. [[CrossRef](#)]
51. Ghani, M.U.; Zhou, Z.; Ren, L.; Li, Y.; Zheng, B.; Yang, K.; Liu, H. Investigation of Spatial Resolution Characteristics of an in Vivo Micro Computed Tomography System. *Nucl. Instrum. Methods Phys. Res. A* **2016**, *807*, 129–136. [[CrossRef](#)] [[PubMed](#)]
52. Mahesh, M. Image Quality. In *The Essential Physics of Medical Imaging*, 3rd ed.; LWW: Philadelphia, PA, USA, 2013; pp. 60–101. Volume 40.
53. QUART X-ray QA QC Solutions. Line Pair Patterns—Test Phantoms. Available online: <https://quart.de/en/products/test-phantoms/resolution-patterns/line-pair-patterns> (accessed on 6 June 2021).
54. Murtas, F. The GEMPix Detector. *Radiat. Meas.* **2020**, *138*, 106421. [[CrossRef](#)]
55. Jaccard, M.; Petersson, K.; Buchillier, T.; Bailat, C.; Germond, J.F.; Moeckli, R.; Bourhis, J.; Vozenin, M.C.; Bochud, F. EP-1494: Absolute Dosimetry with EBT3 Gafchromic Films in a Pulsed Electron Beam at High Dose-Rate. *Radiother. Oncol.* **2016**, *119*, S690. [[CrossRef](#)]
56. Vlachoudis, V. Flair: A Powerful but User Friendly Graphical Interface for FLUKA. In Proceedings of the Conference on Mathematics, Computational Methods & Reactor Physics (M&C 2009), Saratoga Springs, NY, USA, 3–7 May 2009.
57. Maia Oliveira, A.; Braccini, S.; Casolaro, P.; Heracleous, N.; Leidner, J.; Mateu, I.; Murtas, F.; Silari, M. Radiation-Induced Effects in Glass Windows for Optical Readout GEM-Based Detectors. *arXiv* **2021**, arXiv:2106.04645. Available online: <https://arxiv.org/abs/2106.04645> (accessed on 9 June 2021).

PAPER • OPEN ACCESS

Radiation-induced effects in glass windows for optical readout GEM-based detectors

To cite this article: A. Maia Oliveira *et al* 2021 *JINST* **16** T07009

View the [article online](#) for updates and enhancements.



IOP | ebooks™

Bringing together innovative digital publishing with leading authors from the global scientific community.

Start exploring the collection—download the first chapter of every title for free.

TECHNICAL REPORT

Radiation-induced effects in glass windows for optical readout GEM-based detectors

A. Maia Oliveira,^{a,b,*} S. Braccini,^b P. Casolaro,^b N. Heracleous,^a J. Leidner,^a I. Mateu,^b F. Murtas^{a,c} and M. Silari^a

^aCERN,

1211 Geneva 23, Switzerland

^bLaboratory for High Energy Physics (LHEP),

Albert Einstein Center for Fundamental Physics (AEC),

University of Bern, Sidlerstrasse 5, 3012, Bern, Switzerland

^cINFN-LNF,

00044 Frascati, Italy

E-mail: andrea.cristina.maia.oliveira@cern.ch

ABSTRACT: In this paper we present irradiation measurements performed to select a transparent anode substrate that best meets the requirements of an optical readout for a novel detector, the LaGEMPix. The modification of the optical properties of the material due to proton irradiation were studied in soda-lime, fused quartz and fused silica glasses coated with an Indium Tin Oxide layer. The irradiations were performed using the research Beam Transfer Line (BTL) of the IBA Cyclone 18 MeV cyclotron of the Bern University Hospital (Inselspital). We recorded visible scintillation light generated by proton irradiation in the soda-lime and fused quartz samples. We also investigated the darkening of these three glasses and observed radiation-induced colour centres in the soda-lime glass sample. The optical transmission spectra of the samples were measured before and after irradiation. Reductions of 45%, 1% and 0.4% were observed for soda-lime glass, fused quartz and fused silica, respectively (with an associated error of 0.25%). We conclude that the best option for our specific application is the fused silica substrate, which will be the transparent anode for the next generation of the LaGEMPix detector.

KEYWORDS: Detector design and construction technologies and materials; Materials for gaseous detectors; Instrumentation for hadron therapy; Instrumentation for particle-beam therapy

*Corresponding author.

Contents

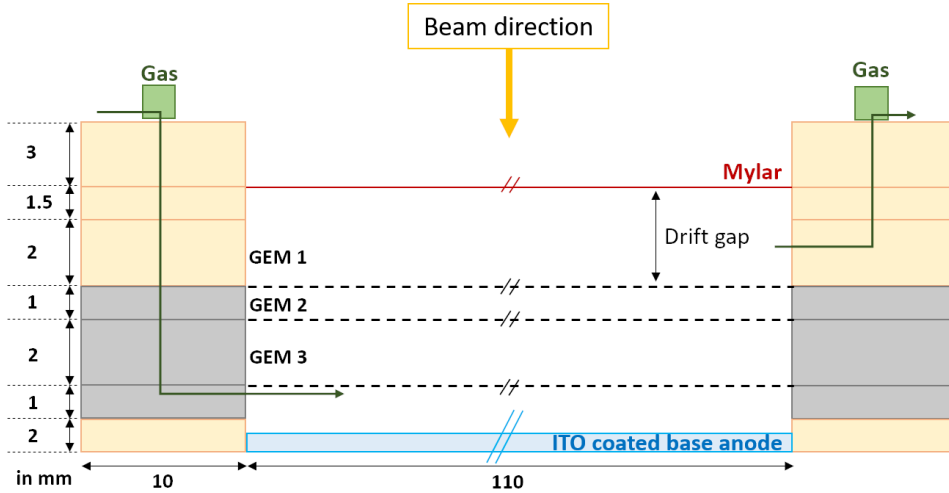
1	Introduction	1
2	ITO-based glass materials	2
2.1	Soda-lime	3
2.2	Fused quartz	3
2.3	Synthetic fused silica	4
3	Proton beam irradiation	4
4	Results and discussions	6
4.1	Scintillation	6
4.2	Transmission	6
4.3	Sheet resistivity	9
4.4	Colour centres	9
4.5	Summary of results	10
4.6	Conclusions	11

1 Introduction

The LaGEMPix is a novel imaging detector with an active area of $60 \times 80 \text{ mm}^2$ currently under development [1]. It combines a triple Gas Electron Multiplier (GEM) with an area of $10 \times 10 \text{ cm}^2$ continuously flushed with Ar/CF₄ gas (90/10 ratio) with a matrix of organic photodiodes (OPDs) coated on an oxide thin film transistor (TFT) backplane produced by Holst Centre/TNO.¹ The detector is designed to be used for quality assurance in hadron therapy, which at present uses protons and carbon ions.

Three GEMs are placed on top of each other to build the triple-GEM as shown in figure 1. This detector includes a 15 μm thick Mylar window used as the cathode at 3.5 mm from the first GEM, yielding the drift gap between the Mylar cathode and the first GEM. In order to evaluate the feasibility of an optical readout, it is essential to place a transparent electromagnetic shielding below the last GEM and above the readout matrix [2], the ITO (Indium Tin Oxide) coated glass anode shown in figure 1. This transparent anode collects the drifting electrons while allowing the scintillation photons to pass through, ensuring that photons rather than electrons are responsible for inducing a current in the photodiodes of the image sensor. The probability of a photon reaching the image sensor depends on several factors, including the number of photons that are transmitted by the glass exit window. A higher transmission of the window will translate into a higher induced signal in the readout system. Radiation effects can reduce the window transmission efficiency

¹Holst Centre, PO BOX 8550, 5605 KN Eindhoven, The Netherlands.



// Not to scale

Figure 1. Transversal schematics of $10 \times 10 \text{ cm}^2$ triple-GEM assembled to the ITO glass. The optical readout with an active area of $60 \times 80 \text{ mm}^2$ is then placed below the ITO coated based transparent anode.

and radiation damage on specific irradiated areas may induce a non-uniform response. Hence, the selection of the material of the transparent anode is crucial for this application because it affects the response uniformity and the signal stability of the LaGEMPix detector.

Optical readout GEM-based detectors coupled to CCD/CMOS cameras used for particle therapy have been studied by several groups [2–6]. The setups included transparent exit windows, which were in some cases [2, 6, 7] coated with ITO. ITO is used to produce optically transparent anodes due to the combination of electrical conductivity and high light transmission in the visible range. With the exception of Seravalli et al. — who used Duran 50 glass — no decrease in the transmission of the exit window was reported. Scintillation in the exit window was mentioned as a possible source of light production contributing to the noise by Seravalli et al. and Klyachko et al., where it was either regarded as negligible [5] or easy to subtract [4].

We were interested in studying the optical transmission at the visible wavelengths since the Ar/CF_4 has a strong visible emission band around 630 nm, which is also well suited for standard optical readouts. Ar/CF_4 also presents a broad emission band in the ultra-violet (250 nm) and sharp emission lines above 695 nm [8]. The goal was to determine the best ITO-coated transparent anode material that could be coupled to the triple-GEM. It is important to maximize the transmission of Ar/CF_4 scintillation photons to maximize their collection and, consequently, the signal in the readout system.

2 ITO-based glass materials

Three different ITO-based anodes were manufactured with the same rounded square shape of $11 \times 11 \text{ cm}^2$ with rounded corners and a thickness of 1.1 mm. Each sample has one surface coated with ITO with a resistivity of $100 \text{ } \Omega/\text{sq}$. The selected materials are listed in table 1.

Table 1. List of ITO-bases glass materials.

Material	Provider
Soda-lime glass	VisionTek Systems Ltd ⁽¹⁾
Heraeus ⁽²⁾ TSC-3 Quartz	Newcastle Optical Engineering Ltd ⁽³⁾
Heraeus Spectrosil [®] 2000	Newcastle Optical Engineering Ltd

⁽¹⁾: VisionTek Systems Ltd., 1 The Acorns, Upton Chester, Cheshire CH2 1JL, U.K.; www.visionteksystems.co.uk/

⁽²⁾: Heraeus Holding GmbH Heraeusstraße, 12-14 D-63450, Hanau Germany; <https://www.heraeus.com/>

⁽³⁾: Newcastle Optical Engineering Ltd., Unit 1B, Buddle Industrial Estate, Benton Way, Wallsend, Tyne & Wear NE28 6DL, U.K.; www.newcastleoptical.co.uk

The level of purity is vital for high transmission and low radiation damage. Defects like inclusions or impurities present in the glass can originate absorption bands that will reduce the efficiency of the transmission. The manufacturing process affects the quality of the glass and consequently the number of defects. The soda-lime glass is the least pure option and the fused silica the most pure option and therefore the most expensive one.

Duran 50 glass was used as glass exit window in optically read out GEM-based detectors by other groups. The transmission of the exit window decreased in the range 400–600 nm, after 3600 Gy of proton irradiation [9]. This option was therefore excluded in this study.

2.1 Soda-lime

The first sample is an ITOGLASS 100P [10] consisting of a polished soda-lime glass with a thickness of 1.1 mm. The glass was coated with a first layer of Silicon Oxide (SiO₂) of 25 nm thickness and a second layer of 80 nm of ITO, with a resistivity of 100 Ω/sq.

The exposure to radiation is known to alter the colour of a glass. Depending on the type of glass, the colour induced by radiation can be brown, purple or red [11]. The radiation induced colour centres for the soda-lime were reported by several studies after irradiations with protons, electrons and photons [12–14]. The non-bridging oxygen hole centres (NBOHCs), which are associated with absorption bands at 623 nm and 412 nm, are the defects responsible for the brown colour after irradiation. The band of 297 nm is recognised as absorption of trapped electrons (TEs) [15].

2.2 Fused quartz

According to Heraeus, the manufacturing process regularly used for their TSC samples, in particular for Heraeus TSC-3 Quartz, is the flame fusion process. This process ensures a high purity material with the lowest possible amount of bubbles and inclusions that are normally present in fused quartz materials [16]. The level of purity is vital for high transmission and radiation insensitivity and therefore the flame fusion process is critical for the quality of the final material.

Mitchell and Paige measured the optical absorption of neutron irradiated fused quartz and reported two absorption bands associated with atomic displacements (oxygen ion vacancies and interstitial oxygen ions) at 163 nm and at 218 nm [17]. The latter could affect the detection of the broad emission band in the ultra-violet of Ar/CF₄ gas.

The ATLAS experiment at the CERN LHC [18] tested fused quartz GE214 in long-term operations during proton-proton or heavy ion runs in the Zero Degree Calorimeter and concluded that the specific type of fused quartz is not suitable for extreme radiation environments [19]. However, their measurements were performed for doses of the order of 10^4 Gy in 10 seconds while we expect doses of the order of 2 Gy per 60 seconds in a clinical hadron therapy beam. Therefore, we included quartz glass in this study.

2.3 Synthetic fused silica

Heraeus Spectrosil[®] 2000 [20] is a synthetic fused silica glass, which does not contain chlorine, bubbles or inclusions. According to Heraeus, it is an ultra-high purity glass with excellent optical transmission in the deep ultraviolet and visible ranges.

The ATLAS experiment also tested Spectrosil[®] materials and at 630 nm (broad emission range of Ar/CF₄, the selected gas), they measured about 25% relative absorption (irradiated/control). There is an absorption centre at 629 nm due to a NBOHC [21]. The ATLAS and CMS experiments selected fused silica based on its remarkable radiation hardness when compared to other glasses [19, 22].

Other groups have also identified defects in high-purity silica glasses such as oxygen-vacancies and oxygen-interstitial pairs [23, 24]. Cohen and Janezic observed the development of colour centre absorption bands with peaks centred at 629 nm, 463 nm, 310 nm, and 240 nm after X-ray exposure [25].

3 Proton beam irradiation

The glasses were irradiated with 17.5 MeV protons at beam intensities of up to 11 nA using the research Beam Transfer Line (BTL) of the IBA Cyclone 18 MeV cyclotron in operation at the Bern University Hospital (Inselspital) [26]. The dose rate (to silicon) on the surface of glass samples was 53.8 Gy/s. A UniBEaM detector [27] was installed in the BTL, as shown in figure 2. It was used to measure and control the beam characteristics on-line during the irradiations. The UniBEaM measures the beam profiles in both transverse directions by passing scintillating fibres through the beam. The protons are extracted into air by means of a 50 μ m stainless steel window, which faces the glass sample. An aluminium disk is placed behind the sample, connected to a Keysight B2985A electrometer to measure the beam current [28]. Each transparent anode was placed perpendicular to the proton beam and with the coated side facing the exit window, which is the same orientation in which they would be placed coupled to the triple-GEM detector.

Before irradiating the samples, an EBT3 Gafchromic[™] film [29] was positioned in front of the aluminium disk to evaluate the shape and the diameter of the beam. The goal was to have a proton flux similar to a hadron therapy beam. At the National Centre for Oncological Hadron therapy (CNAO) in Italy [30], the proton flux is of the order of magnitude of 10^8 protons/s/mm². For a uniform beam of 3 cm diameter from the Bern cyclotron (see figure 3), it is necessary to set a beam current of 11 nA to reach the same flux.

The horizontal and vertical beam profiles measured by the UniBEaM just before the extraction window are shown in figure 4. On the basis of the measured beam profile, the average proton flux in the region of interest was evaluated to be 1.5×10^8 protons/s/mm².

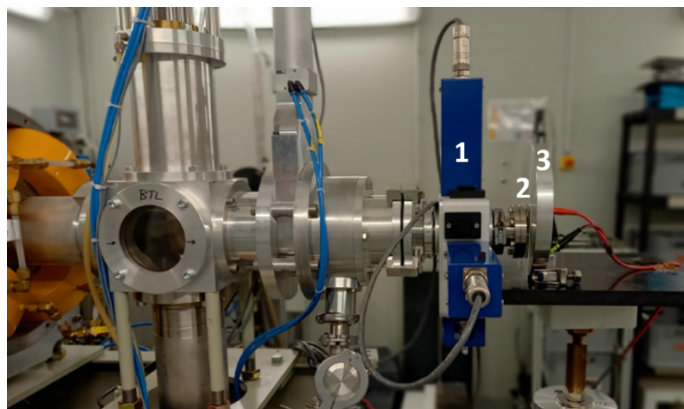


Figure 2. The UniBEaM (1) detector and the glass sample (2) installed at the end of the BTL of the IBA Cyclone 18 MeV cyclotron at the Bern University Hospital (Inselspital). An aluminium disk (3) is placed behind the glass sample.

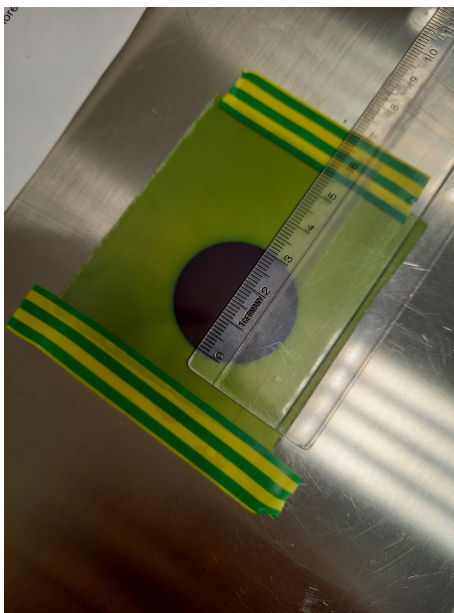


Figure 3. Irradiated EBT3 Gafchromic™ film showing a beam spot of 3 cm in diameter.

All samples were irradiated two times: a short irradiation with a duration of about 20 seconds to evaluate the scintillation light with a Bosh VTC-206 Mini Bullet Camera, and a 15-minute irradiation to study the optical effects. We removed the aluminium disk shown in figure 2 during the short irradiation to detect the light with the camera. We placed a camera pointing to the transparent anode in order to record images and to detect the scintillation light emitted by each sample.

An inspection by eye was performed after each irradiation to evaluate the presence of colour centres on each sample.

The radiation-induced effects were evaluated by measuring the transmission of each sample before the irradiation and one week after. The measurements were performed with a Perkin Elmer Lambda 650 UV/VIS Spectrometer (Standard detector Module) in the spectral range from 200 nm

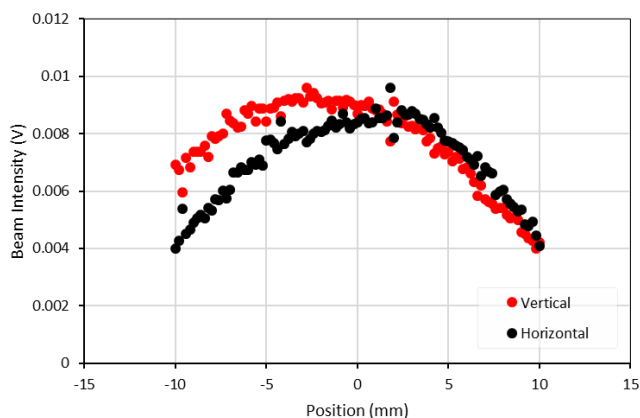


Figure 4. Proton beam profiles measured with the UniBEam.

to 800 nm, in steps of 1 nm. An intrinsic calibration of the equipment was performed before the measurements. An additional reference measurement with no sample was also carried out to evaluate the fluctuations around 100% level of transmission and to estimate the associated uncertainty of the measurements taken on that day. This uncertainty was estimated by the difference between the maximum value registered at the reference measurements and the 100% transmission level. The samples were placed carefully such that the entire point of light emitted by the spectrometer is within the irradiated area of the glass.

All laboratory experiments were conducted in ambient conditions of temperature, humidity and pressure.

4 Results and discussions

4.1 Scintillation

The camera detected scintillation generated by proton irradiation in the soda-lime and fused quartz glasses, is clearly visible as bright spots. Figure 5 shows the scintillation light from the fused quartz glass. The mean intensity of the bright spot was analyzed using the ImageJ software [31] by comparing the brightness in images taken during irradiation to those taken without irradiation for a defined rectangular ROI (region of interest). This ROI, which is shown in figure 5 b), was selected in the centre of the glass sample and it includes the complete bright spot. A relative increase of 66% was measured for soda-lime, 83% for fused quartz and 0.9% for fused silica, which is consistent with the visual observations. The camera did not detect any visible light from the fused silica glass.

4.2 Transmission

Figure 6 shows the measured transmission spectra of the soda-lime glass sample before and after irradiation. A general degradation in the transmission is observed in all wavelengths in the visible region, as well as an intense reduction centred at the three expected absorption bands. The induced defects of NBOHCs associated with bands at 623 nm and 412 nm are responsible for the brown colour (see section 4.4). A maximum decrease of 45% in the transmission was measured with an uncertainty of 0.25%.



Figure 5. Image of the fused quartz sample when the beam is OFF (a) and when the beam is ON (b). The yellow square determines the ROI selected of the recorded visible light with the ImageJ software.

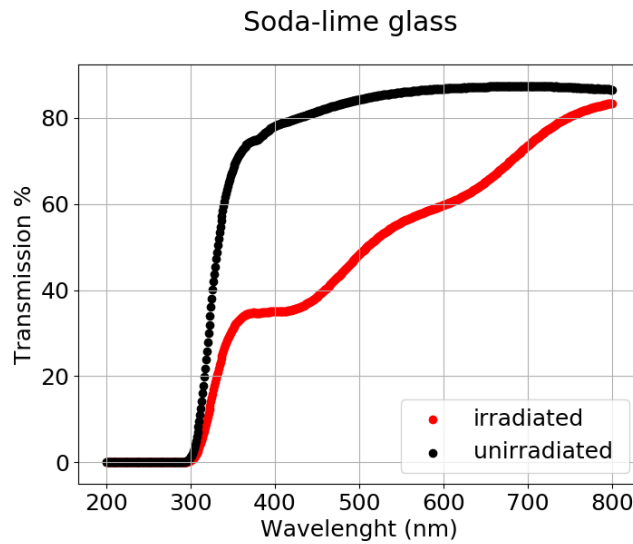


Figure 6. Optical transmission spectra of soda-lime glass sample before and after proton beam irradiation. The experimental uncertainties are smaller than the data points.

As all light that is not transmitted must be absorbed, neglecting reflection, the difference $100\% - \text{Transmission}\%$ is equal to the Absorption %. Figure 7 shows the absorption as a function of the energy in order to compare directly the centres of the three emission bands with the results reported by A. Serrano et al. [11]. The centres of the peaks' absorption bands, which corresponds to the mean values of each Gaussian, were obtained by fitting the profile by a triple Gaussian function. Table 2 shows that the present results are in agreement with literature data within maximum 2.2%.

Figure 8 shows the measured transmission spectra of the fused quartz glass sample before and after irradiation. A maximum decrease of 1% was measured with an uncertainty of 0.25%.

Figure 9 shows the measured transmission spectra of the fused silica glass sample before and after irradiation. A maximum decrease of 0.4% was measured with an uncertainty of 0.25%.

The fused silica substrate presents the smallest transmission loss. Consequently, a more consistent number of photons will reach the readout over time for the fused silica glass when compared with other samples.

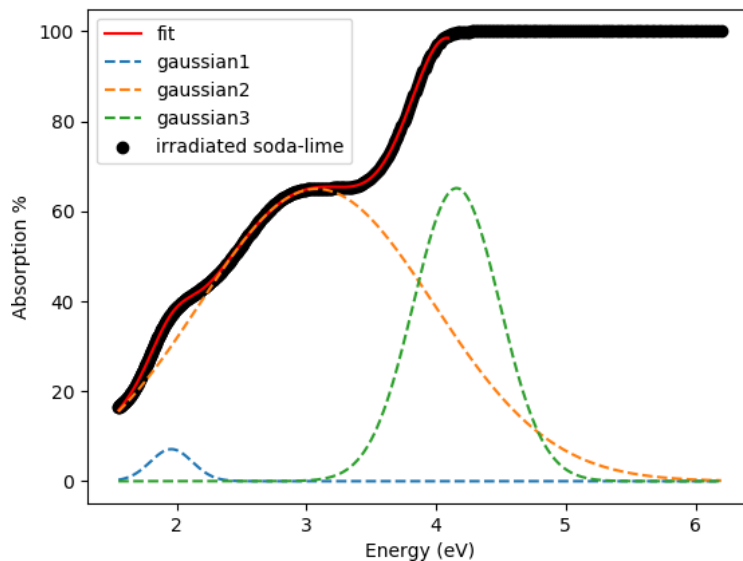


Figure 7. Optical absorption spectrum of proton irradiated soda-lime glass.

Table 2. Centres of the peaks of the three Gaussian fits to the optical absorption spectrum. The present results are compared with those from ref. [15].

Energy (eV) [11]	Energy (eV) [this work]	% difference
1.990 ± 0.001	1.958 ± 0.001	1.6
3.012 ± 0.002	3.078 ± 0.002	2.2
4.171 ± 0.001	4.157 ± 0.003	0.3

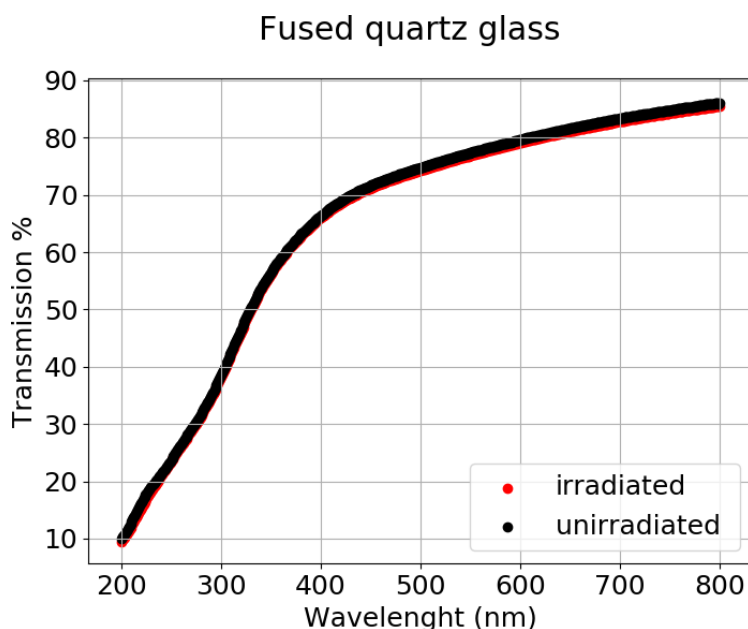


Figure 8. Optical transmission spectra of fused quartz glass before and after proton beam irradiation. The experimental uncertainties are smaller than the data points.

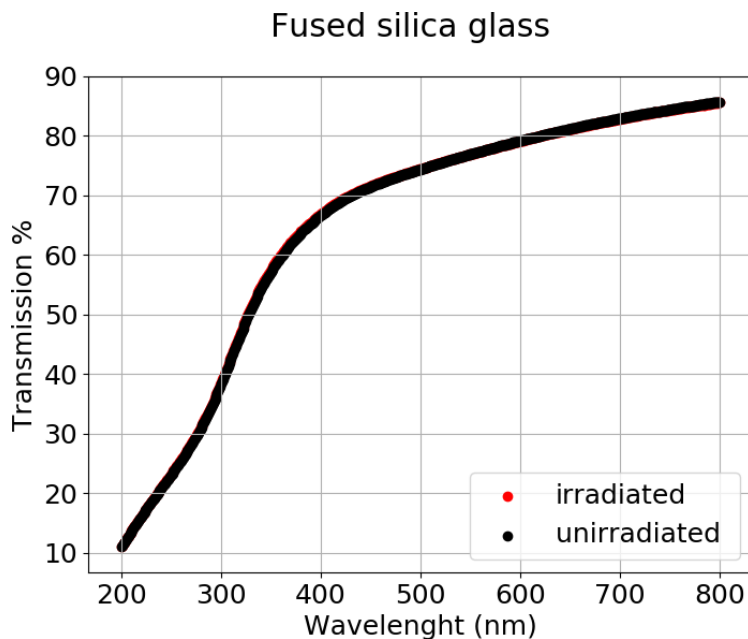


Figure 9. Optical transmission spectra of fused silica glass sample before and after proton beam irradiation. The experimental uncertainties are smaller than the data points.

4.3 Sheet resistivity

To estimate the resistivity of each type of glass, we produced a 19-pin probe to obtain a more accurate Ω/sq value rather than using a standard 2-pin multi-meter [32], which only gives a point-to-point measurement. Each sample was divided into small square regions and the resistivity was measured before and after the irradiations. For the soda-lime glass, values from 80 to 93 Ω/sq were measured, for the fused quartz values from 160 to 480 Ω/sq and fluctuations between 120 and 240 Ω/sq were observed for fused silica. The differences between the resistivity of soda-lime sample and the other two samples may be due to the fact that the samples are produced by different manufacturers. No alteration in the sheet resistivity of the samples was registered due to irradiation. Wei et al. [33] reported an alteration in the optical properties of ITO films deposited on quartz substrate after irradiation with 100 keV protons. They measured an increase of the sheet resistivity using the four-point probe method when the fluence exceeded $2 \times 10^{16} \text{ cm}^{-2}$.

4.4 Colour centres

To evaluate the quick formation of colour centres, it is necessary to compare the pictures of the ITO soda-lime glass sample for different irradiation periods. After the first irradiation lasting 20 seconds, a brownish circle was observed, while after the second irradiation of 15 minutes the circle became darker, as depicted in figure 10.

The opacity caused by the radiation in ITO soda-lime glass is clearly visible by eye. The colour of the darkened circle after 15 minutes and 20 seconds irradiations was measured using a colorimeter Pantone CapsureTM Model RM200 [34]. This colorimeter allows the identification of colours according to Pantone colour libraries. The colour Pantone[®] 452C has been identified in the darkened circle that corresponds to Red = 176, Green = 170, Blue = 126 in the RGB system, one of

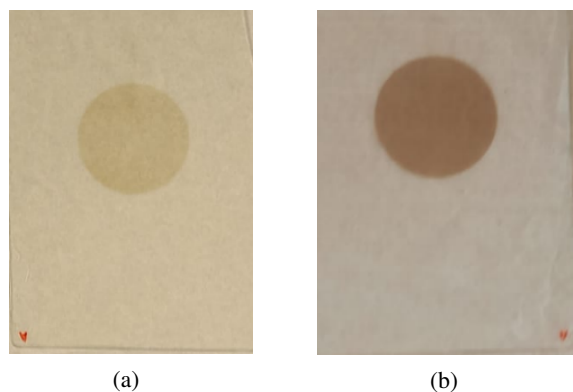


Figure 10. Visible radiation damages of ITO soda-lime glass after (a) short — 20 seconds — and (b) long — 15 minutes — irradiations.

Table 3. Summary of the radiation-induced effects for the three tested glasses.

Glass	Scintillation	Irradiation induced colour centres	Reduction in transmission (maximum difference)	Variations in the sheet resistivity
Soda-lime	Yes — 66%	Yes (R=176, G=170, B=126)	45 %	Not observed
Fused quartz	Yes — 83%	Not observed	1%	Not observed
Fused silica	Not observed — 0.9 %	Not observed	0.4%	Not observed

most common ways to encode colours. The device was incapable of identifying the precise colour in transparent regions, i.e. the non-irradiated area in the soda-lime glass and the whole area of the other two samples (fused quartz and fused silica). Similar effects on this type of substrate under proton irradiation have been reported in the literature [7]. There are radiation-induced absorption sites in the glass, and the number of these sites increases with the number of impurities present in the glass.

After radiation exposure, the soda-lime glass shows a drastic reduction in the transmission. One common method to recover transparency is to heat the glass. However, after the transparent anode has been assembled in the LaGEMPix detector, it is not possible to submit the full detector to an annealing above 100 °C to allow the recovery of these absorption bands. Therefore, soda-lime is not a viable option for the substrate of the anode and a more radiation-tolerant material must be selected. On the other hand, no creation of colour centres was observed on fused quartz and fused silica samples after both irradiations.

4.5 Summary of results

Table 3 summarizes the experimental results. Visible scintillation light generated by proton irradiation was observed in the soda-lime and fused quartz samples. The darkening of the three materials was also qualitatively investigated; radiation-induced colour centres in the soda-lime glass sample were observed. The optical transmission spectra of the three samples were measured after irradiation. A decrease in the optical transmission of 45%, 1% and 0.4% was measured for soda-lime glass, fused quartz and fused silica respectively (with an associated error of 0.25%).

4.6 Conclusions

The soda-lime glass is not a suitable option for the optical readout under study, since the loss in transmission would affect the light signal reproducibility of the LaGEMPix detector. Fused quartz appears to be more tolerant to radiation. However, it scintillates, which will add a signal to the scintillation photons emitted in the triple-GEM. Based on the measurements, the best option is the fused silica substrate, since it presents the lowest transmission loss. The incorporation of this glass as exit window will produce a higher and more reliable signal over time when compared with the other materials investigated. The results here reported motivated a replacement of the transparent anode material for the next generation of the LaGEMPix detector for applications in hadron therapy.

Acknowledgments

The authors wish to thank Rui de Oliveira for the materials, and Thomas Schneider for the technical help and the measurements performed at the Optical Quality Control Lab — Thin Film & Glass service of CERN, and Lucia Gallego for providing the image that was adapted to figure 1, and Imprimerie Villière — Villir (Beaumont, France) for providing the colorimeter Pantone Capsure™ Model RM200. This Project has been co-funded by the CERN Budget for Knowledge Transfer to Medical Applications. This project has also received funding from the ATTRACT project funded by the EC under Grant Agreement 777222. Andreia Maia Oliveira was co-supported by a grant from FCT (Portugal) with reference SFRH/BEST/142965/2018. This research was partially funded by the Swiss National Science Foundation (SNSF) grant CRSII5_180352.

References

- [1] ATTRACT project, *A large area GEMPix detector with optical readout for hadron therapy (LaGEMPix)*, <https://attract-eu.com/selected-projects/lagempix-a-large-area-gempix-detector-with-optical-readout-for-hadron-therapy> (2021).
- [2] F.M. Brunbauer et al., *Combined optical and electronic readout for event reconstruction in a GEM-based TPC*, *IEEE Trans. Nucl. Sci.* **65** (2018) 913.
- [3] D. Nichiporov, L. Coutinho and A.V. Klyachko, *Characterization of a GEM-based scintillation detector with He-CF₄ gas mixture in clinical proton beams*, *Phys. Med. Biol.* **61** (2016) 2972.
- [4] E. Seravalli et al., *A scintillating gas detector for 2D dose measurements in clinical carbon beams*, *Phys. Med. Biol.* **53** (2008) 4651.
- [5] A. V. Klyachko et al., *Dose imaging detectors for radiotherapy based on gas electron multipliers*, *Nucl. Instrum. Meth. A* **628** (2011) 434.
- [6] T. Fujiwara et al., *Development and characterization of optical readout well-type glass gas electron multiplier for dose imaging in clinical carbon beams*, *Phys. Med. Eur. J. Med. Phys.* **82** (2021) 72.
- [7] T. Fujiwara et al., *High-photon-yield scintillation detector with Ar/CF₄ and glass gas electron multiplier*, *Jpn. J. Appl. Phys.* **55** (2016) 106401.
- [8] F.M. Brunbauer, *Applications of gas scintillation properties in optically read out GEM-based detectors*, PhD Thesis, Technischen Universität Wien, Vienna, Austria (2018).

- [9] E. Seravalli et al., *2D dosimetry in a proton beam with a scintillating GEM detector*, *Phys. Med. Biol.* **54** (2009) 3755.
- [10] *OLED ITO glass polished indium tin oxide*, https://www.visionteksystems.co.uk/oled_ito_glass.htm (2021).
- [11] A. Sakka, *Radiation-induced color centers in glasses*, *Bull. Inst. Chem. Res. Kyoto Univ.* **48** (1970) 53.
- [12] G. Onay and R. Şahin, *Optical properties of the electron and gamma-ray irradiated soda-lime glass samples*, *Sakarya Univ. J. Sci.* **22** (2018) 1518.
- [13] J. Cermak et al., *Proton irradiation induced changes in glass and polyethylene terephthalate substrates for photovoltaic solar cells*, *Sol. Energy Mater. Sol. Cells* **186** (2018) 284.
- [14] K.R. Kim, S.J. Ra, M.H. Jung and T.K. Yang, *Activation of 45 MeV proton irradiation and proton-induced neutron irradiation in polymer*, *J. Korean Phy. Soc.* **56** (2010) 2093.
- [15] A. Serrano, F. Gálvez, O. Rodríguez de la Fuente and M. A. García, *X-ray irradiation of soda-lime glasses studied in situ with surface plasmon resonance spectroscopy*, *J. Appl. Phys.* **113** (2013) 113104.
- [16] Heraeus TSC Series Fused Quartz Data Sheet, https://www.heraeus.com/media/media/hca/doc_hca/products_and_solutions_8/solids/TSC_Series_EN.pdf (2021).
- [17] E.W.J. Mitchell and E.G.S. Paige, *CXI. The optical effects of radiation induced atomic damage in quartz*, *Phil. Mag.* **1** (1956) 1085.
- [18] O. Brüning, *LHC design report. Volume 1* (2004).
- [19] M.W. Phipps, *A new ATLAS ZDC for the high radiation environment at the LHC* in the proceedings of the 18th *International Conference on Calorimetry in Particle Physics*, May 21–25, Eugene U.S.A. (2018).
- [20] Data and properties optics fused silica, https://www.heraeus.com/media/media/hca/doc_hca/products_and_solutions_8/optics/Data_and_Properties_Optics_fused_silica_EN.pdf (2021).
- [21] S. Munekuni et al., *Various types of nonbridging oxygen hole centre in high-purity silica glass*, *J. Appl. Phys.* **68** (1990) 1212.
- [22] CMS collaboration, *The CMS-HF quartz fiber calorimeters*, *J. Phys. Conf. Ser.* **160** (2009) 012014.
- [23] E.J. Friebele, D.L. Griscom, M. Stapelbroek and R.A. Weeks, *Fundamental defect centers in glass: the peroxy radical in irradiated, high-purity, fused silica*, *Phys. Rev. Lett.* **42** (1979) 1346.
- [24] T.E. Tsai and D.L. Griscom, *Experimental evidence for excitonic mechanism of defect generation in high-purity silica*, *Phys. Rev. Lett.* **67** (1991) 2517.
- [25] A.J. Cohen and G.G. Janezic, *Relationships among trapped hole and trapped electron centers in oxidized soda-silica glasses of high purity*, *Phys. Stat. Sol. A* **77** (1983) 619.
- [26] S. Braccini, *The new Bern PET cyclotron, its research beam line, and the development of an innovative beam monitor detector*, *AIP Conf. Proc.* **1525** (2013) 144.
- [27] D. Potkins et al., *A low-cost beam profiler based on cerium-doped silica fibers*, *Phys. Proc.* **90** (2017) 215.
- [28] B2980A Series Femto/Picoammeter and Electrometer/High Resistance Meter, www.keysight.com.
- [29] Gafchromic EBT Films — GAFchromic™, <http://www.gafchromic.com/gafchromic-film/radiotherapy-films/EBT/index.asp> (2021).

- [30] S. Rossi, *The status of CNAO*, *Eur. Phys. J. Plus* **126** (2011) 78.
- [31] C.A. Schneider, W.S. Rasband and K.W. Eliceiri, *NIH Image to ImageJ: 25 years of image analysis*, *Nature Meth.* **9** (2012) 671.
- [32] Fluke 179 True-RMS digital multimeter, <https://www.fluke.com/en-us/product/electrical-testing/digital-multimeters/fluke-179> (2021).
- [33] Q. Wei, S.Y. He, J.C. Liu and D.Z. Yang, *Optical and electrical properties of transparent conductive ITO thin films under proton radiation with 100 KeV*, *Mater. Sci. Forum* **475–479** (2005) 3697.
- [34] Planetecouleur, *Pantone CAPSURETM*, <https://www.planetecouleur.com/products/pantone-capsure> (2021).

A Large Area GEMPix detector for treatment plan verification in hadron therapy

Andreia Maia Oliveira^{1,2*}, Hylke B. Akkerman³, Saverio Braccini², Albert J.J.M. van Breemen³, Lucia Gallego Manzano^{1,4}, Natalie Heracleous^{1,4}, Ilias Katsouras^{3,5}, Johannes Leidner¹, Fabrizio Murtas^{1,6}, Bart Peeters³, Marco Silari¹

1 CERN, 1211 Geneva 23, Switzerland

2 Laboratory for High Energy Physics (LHEP), Albert Einstein Center for Fundamental Physics (AEC), University of Bern, Sidlerstrasse 5, 3012, Bern, Switzerland

3 Holst Centre/TNO, High Tech Campus 31, 5656 AE Eindhoven, The Netherlands

4 Institute of Radiation Physics, Lausanne University Hospital, Lausanne University, Lausanne, Switzerland

5 Now at ASML, Veldhoven, The Netherlands

6 INFN-LNF, 00044 Frascati, Italy.

*Correspondence: andrea.cristina.maia.oliveira@cern.ch

Abstract. Quality Assurance in hadron therapy is crucial to ensure a safe and accurate dose delivery to the patients. This requires fast and reliable detectors with high spatial resolution. A first LaGEMPix prototype that combines a triple Gas Electron Multiplier and a highly pixelated readout based on a matrix of organic photodiodes coated on an oxide thin film transistor backplane has been built. The first version of the LaGEMPix has proven to have a limited spatial resolution, mainly attributed to the isotropic emission of the scintillation photons within the GEM holes. To improve the spatial resolution and confirm our predictions of the role of the photons, we built a new version of the detector with a reduced gap between the last GEM foil and the readout. Experimental results acquired using different methods and experimental set-ups show that the spatial resolution significantly improved with the new design.

1. Introduction

Hadron therapy is an advanced radiotherapy technique that offers significant benefits over traditional photon and electron treatments, and is rapidly gaining popularity as one of the radiation modalities for cancer treatment [1]. The physical properties of hadrons, predominantly protons and carbon ions, produce better dose distributions and improve treatment of some tumors [2], with better sparing of the healthy tissue.

Treatment with hadrons requires not just high spatial resolution, but also exceptionally accurate dose calculation in order to accomplish optimal dose delivery. A high spatial resolution of the 2D dose distribution is essential since most of the treatment plans in Pencil Beam Scanning (PBS) are delivered through a large number of small beams with varying intensity to treat small well-defined lesions [3]. The treatment can involve very high “in-field” dose gradients, up to 15%/mm in intensity modulated proton therapy (IMRT), with the purpose of accomplishing high conformity to the planning target volume (PTV) [4, 5]. It is therefore crucial that the required dose is delivered exactly where prescribed (in the PTV) to spare the healthy tissue and/or organs at risk. This is ensured by appropriate quality assurance (QA) techniques and tools. To accomplish an efficient QA procedure, detectors for measuring

the relevant beam characteristics, in particular beam position and delivered dose, is needed [6]. Nowadays, improvements are still possible towards an all-in-one solution providing accurate and real-time measurements with submillimeter spatial resolution, and a uniform response to the beam energy. QA programs based on different types of detectors can be very complex and time consuming. A single solution that includes all the information will minimize the equipment costs, the setup time and therefore the necessary resources in the treatment facility, improving the overall performance of the QA programs [7, 8, 9].

1.1. LaGEMPix: original version

A promising tool for more efficient QA procedures with high spatial resolution is the LaGEMPix detector (figure 1). It consists of a triple-GEM (Gas Electron Multiplier) [10] coupled to a highly pixelated readout based on a matrix of organic photodiodes (OPDs). Scintillation photons generated in the GEM holes after electron avalanche multiplication are detected by the matrix of OPDs, placed at 3 mm from the production point. A more detailed description of the LaGEMPix and the results summarized in the following can be found in reference [11].

The detector was characterized using low energy X-rays (30-40 kV) at the Calibration Laboratory of CERN Radiation Protection Group [12]. Extensive measurements to determine the spatial resolution for various experimental configurations were performed. The detector's spatial resolution was evaluated using three different methods: (1) calculating the Edge Spread Function (ESF) along the sharp edge of a 2.5 cm thick lead block, (2) measuring the Line Spread Function (LSF) and distance between adjacent holes using two copper masks with holes of different sizes and spacing, and (3) determining the Modulation Transfer Function (MTF) of a commercial lead plate. Results showed that the ESF underestimated the spatial resolution, yielding a resolution of 9.70 ± 0.09 mm for 40 kV X-rays. The LSF method revealed that the LaGEMPix was able to resolve two 5 mm holes separated by 3 mm. However, a limitation was observed with the MTF, which showed that slits separated by 2 mm were not distinguishable. From these measurements we concluded that the spatial resolution achieved with the first version of the LaGEMPix was not as high as needed for QA in hadron therapy and therefore, some modifications were planned based on the following considerations.

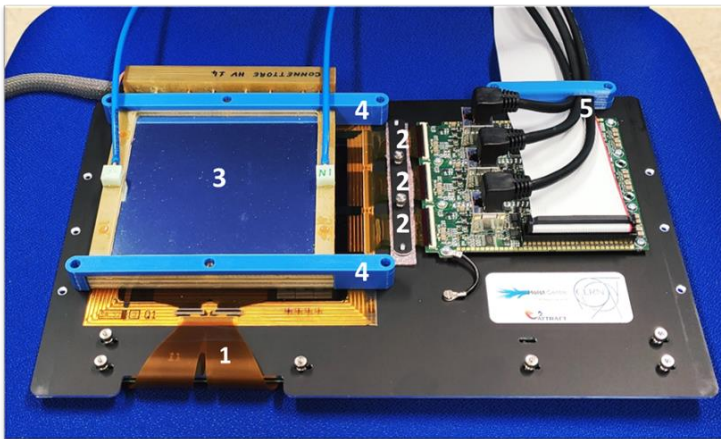


Figure 1. The LaGEMPix prototype [11]: (1) flex gate driver integrated circuit; (2) flex Read-out Integrated Circuits (ROICs); (3) the triple-GEM 10 x 10 cm² stack coupled to the optical readout with the thin Mylar window on top; (4) 3D-printed braces to hold together the triple-GEM detector and the image sensor; (5) cables to connect the detector to the readout system.

A comparison with GAFCHROMIC® films [13], the GEMPix detector [14] – a triple-GEM stack coupled to a pixelated charge readout –, and Monte Carlo simulations using FLUKA [15] showed that the main contribution to the spatial resolution is most likely the isotropic emission of the scintillation photons. It should be emphasized that even if, to date, there is no precise information in the literature regarding the directionality of light emission in GEM-based detectors, there is a consensus that photons are emitted isotropically [16, 17, 18]. Based on this assumption and on the obtained results, we concluded that the isotropic emission of the scintillation light introduces an additional blurring in the image, worsening the spatial resolution measured with the lead block from 5.20 ± 0.10 mm (GEMPix) to 9.70 ± 0.09 mm (LaGEMPix). The isotropic emission of photons is unavoidable. Its impact on the spatial resolution is determined by the distance between the points where photons are produced and

detected. To prove our hypothesis and to reduce its effect, we modified the design of the LaGEMPix by decreasing the distance between the last GEM (GEM3) and the readout plane. This modification will reduce the dispersion of the light before reaching the readout.

2. Materials and methods

2.1. Detector design

A new detector prototype featuring a reduced distance between GEM3 and the readout was built. Figure 2 shows the schematic details of the new design. The reduction of the distance from 3 to 1.5 mm was achieved by (1) changing the gap between the GEM3 and the anode, known as induction gap, from 2 mm to 1 mm and (2) by replacing the indium tin oxide (ITO) transparent electrode, coated on a 1.1 mm thick fused quartz substrate, with an ITO electrode coated on a 0.5 mm thick fused silica substrate. The new transparent electrode is also more radiation resistant according to recent measurements [19]. Due to mechanical reasons it was not possible to further reduce these distances. A glass substrate thinner than 0.5 mm would be extremely fragile causing problems during the production, coating and assembly procedures. In addition, the last GEM surface might exhibit a slight bend which had to be taken into consideration in order to avoid contact with the ITO anode.

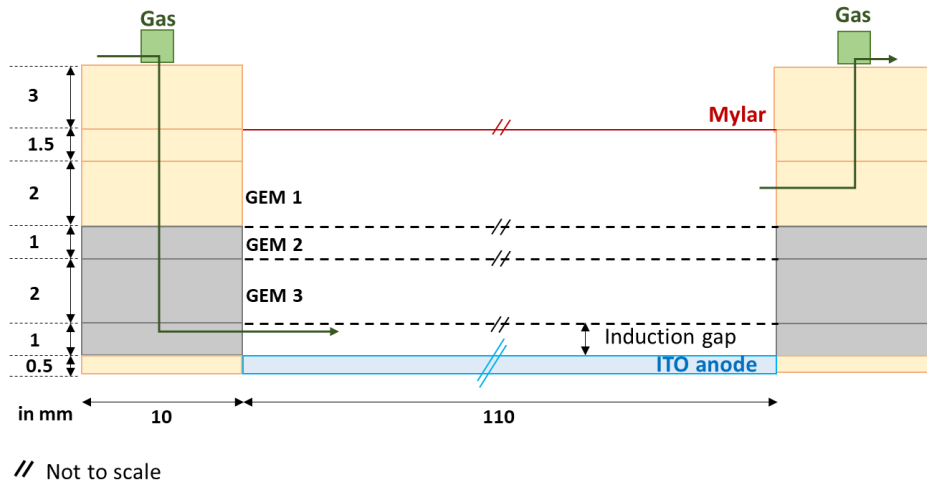


Figure 2. Schematic diagram of the improved design of the LaGEMPix detector.

2.2. Experimental set-up

The spatial resolution of the LaGEMPix has been evaluated with 30 kV and 40 kV X-rays from an X-ray generator, Model X80-320kV from Hopewell Designs, Inc. This system, equipped with 10 Narrow Spectra Filters (N-series), was used to provide X-rays in compliance to the ISO 4037 standard [20]. More specifically, the Hopewell N-5 and N-6 filters, matching to the N-30 and N-40 ISO 4037 standard, respectively, were chosen.

Measurements similar to those reported in [11] were carried out with the new detector. For the ESF, we placed a lead block of 10 x 20 x 2.5 cm³ dimensions in front of the detector, covering part of its active area. A region of interest (ROI) was set perpendicularly to the edge, and the edge response profile was calculated from the average of 200 background corrected images. The spatial resolution was estimated by fitting the edge profile by a logistic function [11, 21].

The LSF was measured using a 3 mm thick copper plate placed at 7 mm from the Mylar window. The mask has several holes of 5 mm diameter spaced by 3 to 7 mm, edge to edge. This method allowed to evaluate the capability of the LaGEMPix to resolve adjacent holes. Finally, we placed various X-ray test patterns in front of the Mylar window to calculate the MTF.

3. Results

The experimental conditions were identical as in [11]: 30 kV (N-5 series filter) or 40 kV X-rays (N-6 series filter), minimum aperture of 1 cm, 230 cm source-detector distance and same electric fields in the GEM structure: transfer field 1 = 2.0 kV/cm; transfer field 2 = 1.75 kV/cm; induction field = 5.0 kV/cm; drift field = 1 kV/cm. The electric fields between the top and bottom copper layers in each GEM foil were kept constant corresponding to a total voltage of 940 V.

3.1. Edge spread function (ESF)

The new detector shows a slight improvement on the spatial resolution when using the ESF. Results show an FWHM of 8.17 ± 0.07 mm compared to 9.70 ± 0.09 mm obtained with the first version of the detector.

3.2. Line spread function (LSF)

The upgraded detector presents an enhanced spatial resolution when using the LSF. Since the average image profile on a single hole is Gaussian, the spatial resolution was assessed by fitting the LSF by a Gaussian function and determining the FWHM of a 5 mm diameter hole. The obtained FWHM using the new version of the LaGEMPix was 5.61 ± 0.14 mm compared to 6.73 ± 0.08 mm previously measured.

Additionally, a ROI was selected at the centre of the 5 mm holes spaced by 3 mm (edge to edge) as depicted by the green region in figure 3a). Figure 3b) compares the line-average response profile of two holes spaced by 3 mm for the original and upgraded versions, featuring two peaks with a dip in the intensity. Two holes of 5 mm diameter at a distance of 3 mm can be resolved by both detectors, however figure 3b) shows a more pronounced dip in the intensity with the upgraded version of the LaGEMPix and consequently an improvement of the LSF.

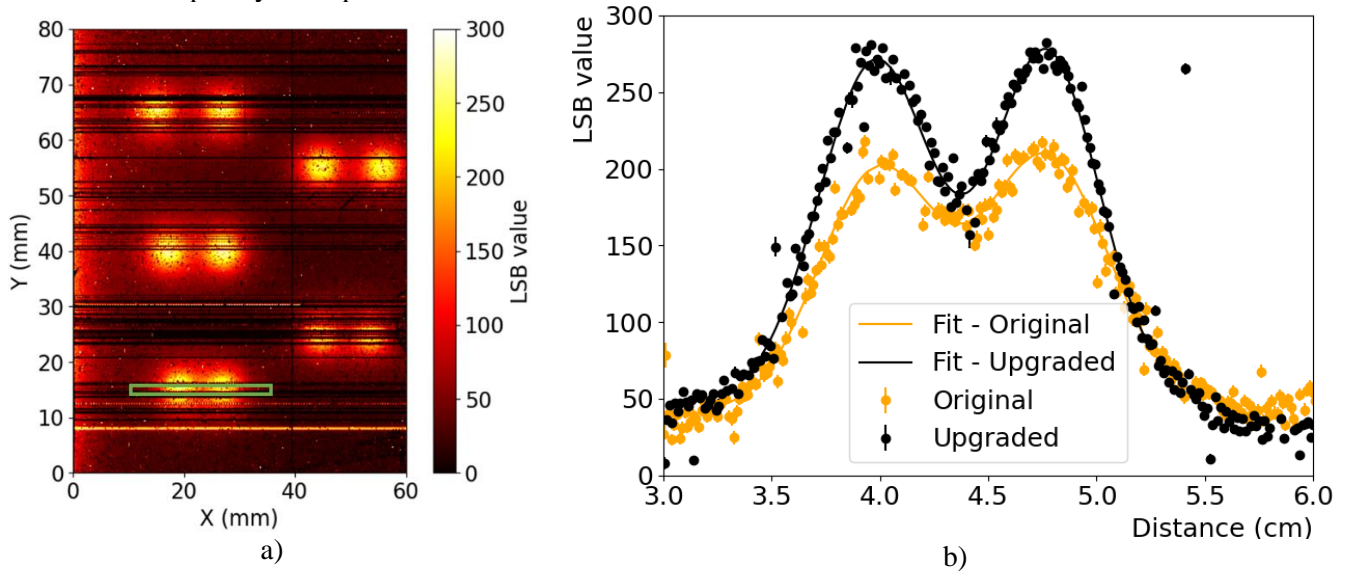


Figure 3. a) Heat map of the copper mask for 40 kV X-rays. A ROI (green rectangle) was set on the holes separated by 3 mm. The spatial resolution was estimated by fitting the profile in the ROI by a Gaussian function. b) The line-average response profile of 5 mm diameter holes spaced by 3 mm (edge to edge) for the original (orange) and upgraded (black) versions of the LaGEMPix. The FWHM obtained by the Gaussian distribution for the upgraded version is 6.16 ± 0.13 mm for the left hole and 5.75 ± 0.15 mm for the right hole. The distance (centre-to-centre fit) of 7.86 mm was obtained by fitting the profile by a double Gaussian function.

3.3. Modulation Transfer Function (MTF)

These tests were carried out using 30 kV X-rays with the N-5 filter in order to increase the contrast of the output image. The mask is made of lead with 0.2 mm thickness and resolution ranging from 0.177 to 3.33 LP/mm, as shown in figure 4, with the larger line spacing being 2.8 mm [22].



Figure 4. Line pair mask type 17 made of 0.02 mm thick lead used as an imaging target. For this particular mask, 0.5 LP/mm means that one black and one white line within 2 mm will be projected on the image sensor.

As can be clearly seen in figure 5, an improvement was obtained with the new detector. The upgraded version of the LaGEMPix is able to distinguish 0.21 LP/mm, which corresponds to two slits separated by 2.4 mm. A limit is observed at 0.25 LP/mm (two slits separated by 2 mm). The first version of the LaGEMPix was, on the other hand, unable to resolve 0.177 LP/mm, corresponding to two slits separated by 2.8 mm.

Table 1 summarizes the values of spatial resolution obtained for the various detectors and experimental configurations. As expected, the upgraded LaGEMPix with reduced gap exhibits the best spatial resolution. A more detailed discussion of the different methods presented here can be found in [11].

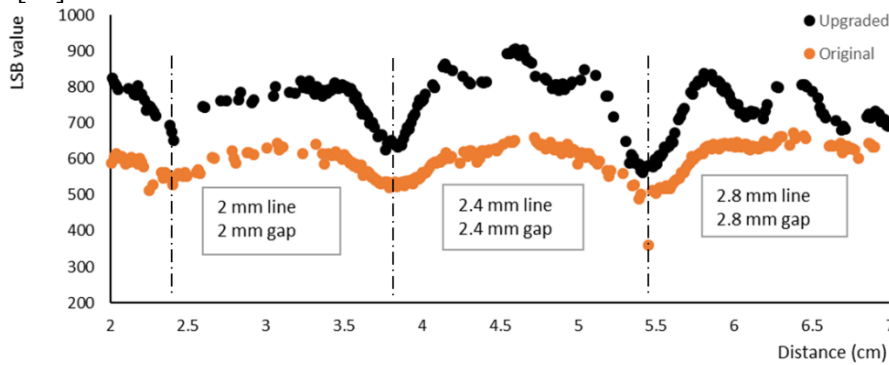


Figure 5. The line-average response profile of line pair mask type 17 with original version of LaGEMPix (orange) versus upgraded LaGEMPix (black).

Table 1. Summary of the spatial resolution obtained for different experimental configurations and by both versions of the LaGEMPix.

Detector	Edge Response	5 mm Cu hole	Spatial Resolution (mm)	
			Minimum resolvable hole spacing	MTF mask limit
Original LaGEMPix [11]	9.70 ± 0.09	6.73 ± 0.08	3 mm (edge to edge)	<0.177 LP/mm
Upgraded LaGEMPix	8.17 ± 0.07	5.61 ± 0.14	3 mm (edge to edge)	0.21 LP/mm

4. Conclusion

An upgraded version of the LaGEMPix has been developed, featuring a reduction of the distance between the light production and optical readout by a factor of two compared to the first version of the detector. Similar to the original prototype, the new detector has been characterized using low energy X-rays and different methods to determine the spatial resolution. The results shown in this paper demonstrate that the distance between the last GEM and the imager has an impact on the measured spatial resolution. A decrease in GEM-readout distance resulted in a spatial resolution of 0.21 LP/mm, corresponding to two slits separated by 2.4 mm in a line pair mask. Since the distance between the last GEM and the readout cannot be further reduced due to mechanical reasons, a submillimetre spatial resolution is hardly reachable for an optical readout without the introduction of lenses.

Commercial vendors, such as PTW¹ and IBA², define the spatial resolution of their clinical detectors used in hadron therapy by the pixel size or pixel pitch. For example, IBA states that the spatial resolution of myQA® Phoenix for proton therapy is 0.2 mm [23]. The pixel pitch of the LaGEMPix is 126 µm. However, this results in a spatial resolution of 2.4 mm using X-Rays, as stated above. Studies using protons in order to directly compare with the detectors in clinical use are foreseen.

As the isotropic emission of the scintillation light was identified as the main limitation to the achievable spatial resolution, a charge readout is currently being considered. In this case, secondary electrons produced in the GEMs and guided by electric fields to preserve the spatial resolution would be directly detected by the readout. Based on the GEMPix results and the FLUKA Monte Carlo simulation [11], the targeted sub-millimetre resolution is expected.

References

- [1] Particle Therapy Co-Operative Group - Particle therapy facilities in clinical operation (last update: June 2021) . Available online: <https://www.ptcog.ch/index.php/facilities-in-operation> (accessed June. 5, 2021)
- [2] Ishikawa H, Nakai K, Nonaka T and Sakurai H 2019 Particle Therapy in Cancer Treatment-Current and Future Perspective *Gan To Kagaku Ryoho* **46** 1219–25
- [3] Journal of the ICRU Report 78 *Oxford University Press* 7 2
- [4] Molinelli S, Mairani A, Mirandola A, Vilches Freixas G, Tessonnier T, Giordanengo S, Parodi K, Ciocca M and Orecchia R 2013 Dosimetric accuracy assessment of a treatment plan verification system for scanned proton beam radiotherapy: one-year experimental results and Monte Carlo analysis of the involved uncertainties *Phys Med Biol* **58** 3837–47
- [5] Winter J, Ellerbrock M, Jäkel O, Greilich S and Bangert M 2020 Analytical modeling of depth-dose degradation in heterogeneous lung tissue for intensity-modulated proton therapy planning *Physics and Imaging in Radiation Oncology* **14** 32–8
- [6] Mirandola A, Molinelli S, Vilches Freixas G, Mairani A, Gallio E, Panizza D, Russo S, Ciocca M, Donetti M, Magro G, Giordanengo S and Orecchia R 2015 Dosimetric commissioning and quality assurance of scanned ion beams at the Italian National Center for Oncological Hadrontherapy *Med Phys* **42** 5287–300
- [7] Zhu X Ronald, Li Y, Mackin D, Li H, Poenisch F, Lee A K, Mahajan A, Frank S J, Gillin M T, Sahoo N and Zhang X 2015 Towards Effective and Efficient Patient-Specific Quality Assurance for Spot Scanning Proton Therapy *Cancers (Basel)* **7** 631–47
- [8] Lambert J, Bäumer C, Koska B and Ding X 2014 Daily QA in proton therapy using a single commercially available detector *Journal of applied clinical medical physics / American College of Medical Physics* **15** 5005
- [9] Hernandez Morales D, Shan J, Liu W, Augustine K E, Bues M, Davis M J, Fatyga M, Johnson J E, Mundy D W, Shen J, Younkin J E and Stoker J B 2019 Automation of routine elements for spot-scanning proton patient-specific quality assurance *Med Phys* **46** 5–14
- [10] Sauli F 2016 The gas electron multiplier (GEM): Operating principles and applications *Nucl. Instr. Meth. A* **805** 2–24
- [11] Maia Oliveira A, B Akkerman H, Braccini S, van Breemen J J M, Gallego Manzano L, Heracleous N, Katsouras I, Leidner J, Murtas F, Peeters B and Silari M 2021 Characterization with X-rays of a Large-area GEMPix detector with optical readout submitted to Special Issue Detectors for Medical Physics of Applied Sciences.
- [12] Brugger M, Carbonez P, Pozzi F, Silari M and Vincke H 2014 New radiation protection calibration facility at CERN *Radiat Prot Dosimetry* **161** 181–4
- [13] Gafchromic™ XR film State-of-the-art processor-less products for radiology applications

¹ PTW-Freiburg, Lörracher Strasse 7, 79115 Freiburg, Germany, Web: <https://www.ptwdosimetry.com/>

² IBA Dosimetry, Bahnhofstraße 5, 90592 Schwarzenbruck, Germany, Web: <https://www.iba-dosimetry.com/>

Available online: http://www.gafchromic.com/documents/PC-11805_Gafchromic_XR.pdf (accessed June. 19, 2021)

[14] Leidner J, Ciocca M, Mairani A, Murtas F and Silari M 2020 A GEMPix-based integrated system for measurements of 3D dose distributions in water for carbon ion scanning beam radiotherapy *Medical Physics* **47** 2516–25

[15] Home | The Official CERN FLUKA Website Available online: <https://fluka.cern/> (accessed on 21 June 2021).

[16] Oliveira C A B, Correia P M M, Schindler H, Ferreira A L, Monteiro C M B, Santos J M F dos, Biagi S, Veenhof R and Veloso J F C A 2012 Simulation of VUV electroluminescence in micropattern gaseous detectors: the case of GEM and MHSP *J. Inst.* **7** P09006–P09006

[17] Fraga F A F, Fetal S T G, Fraga M M F R, Balau E F S, Margato L M S, Marques R F, Policarpo A J P L and Sauli F 2004 The scintillation of GEMS coated with wavelength shifters *Nuclear Instruments and Methods in Physics Research Section A: Accelerators, Spectrometers, Detectors and Associated Equipment* **525** 57–61

[18] Klyachko A V, Moskvina V, Nichiporov D F and Solberg K A 2012 A GEM-based dose imaging detector with optical readout for proton radiotherapy *Nuclear Instruments and Methods in Physics Research Section A: Accelerators, Spectrometers, Detectors and Associated Equipment* **694** 271–9

[19] Maia Oliveira A, Braccini S, Casolaro P, Heracleous N, Leidner J, Mateu I, Murtas F and Silari M 2021 Radiation-induced effects in glass windows for optical readout GEM-based detectors *arXiv:2106.04645 [physics]* (accepted for publication in JINST).

[20] ISO 4037-2:2019, Radiological protection — X and gamma reference radiation for calibrating dosimeters and doserate meters and for determining their response as a function of photon energy — Part 2: Dosimetry for radiation protection over the en-ergy ranges from 8 keV to 1,3 MeV and 4 MeV to 9 MeV

[21] Energy Resolution Due to Thermal Broadening (STM) Available online: <https://shunchi100.wordpress.com/physics-research/energy-resolution-thermal-broadening/> (accessed on 22 June 2021)

[22] Line Pair Patterns - Test Phantoms | QUART X-Ray QA QC Solutions Available online: <https://quart.de/en/products/test-phantoms/resolution-patterns/line-pair-patterns> (accessed on 21 June 2021)

[23] GmbH, I.D. Product myQA® Phoenix High-resolution digital detector array Available online: <https://www.iba-dosimetry.com/product/myqa-phoenix/> (accessed on 22 October 2021)

LaGEMPix: a large area GEMPix detector with optical readout for hadron therapy

Hylke B. Akkerman¹, Albert J.J.M. van Breemen¹, Lucia Gallego Manzano^{2,3}, Natalie Heracleous², Ilias Katsouras¹, Johannes Leidner², Andreia Maia Oliveira^{2,4*}, Fabrizio Murtas^{2,5}, Bart Peeters¹, Marco Silari²

¹ Holst Centre/TNO, High Tech Campus 31, 5656 AE Eindhoven, The Netherlands; ² CERN, 1211 Geneva 23, Switzerland; ³ Institute of Radiation Physics, Lausanne University Hospital, Lausanne, Switzerland; ⁴ Albert Einstein Center for Fundamental Physics (AEC), Laboratory for High Energy Physics (LHEP), University of Bern, Hochschulstrasse 6, 3012 Bern, Switzerland; ⁵ INFN-LNF, 00044 Frascati, Italy.

*Corresponding author: andrea.cristina.maia.oliveira@cern.ch

ABSTRACT

Quality Assurance in hadron therapy is crucial to ensure a safe and accurate dose delivery to the patient. This requires fast and reliable detectors with high spatial resolution. Here we present a cutting-edge solution that combines a triple Gas Electron Multiplier and a highly pixelated readout based on a matrix of organic photodiodes coated on an oxide thin film transistor backplane. A first LaGEMPix prototype with an active area of 60 x 80 mm² has been successfully built and tested demonstrating promising results for quality assurance and treatment plan verification.

Keywords: Hadron therapy, dosimetry, quality assurance, GEM, optical readout.

1. INTRODUCTION

Hadron therapy is an advanced radiation modality for treating cancer, which at present uses protons and carbon ions. As of July 2020, there exist 97 particle therapy facilities worldwide and more than 30 centres are under construction [1]. Hadrons have the unique feature of increasing energy deposition with penetration depth, with a maximum at the end of their range followed by a sharp decrease (Bragg peak). Thus, hadron therapy offers considerable improvements to conventional radiation treatments by allowing better conformity of the dose to the tumour [2], but also requires a very accurate dose planning. A precise verification of the dose delivered to the patient with high spatial resolution is guaranteed by appropriate quality assurance (QA) procedures.

A proper set of detectors for measuring the important beam parameters, in particular the beam position and the delivered dose, is fundamental to achieve an efficient QA protocol [3]. Nowadays, there is still room for improvement towards a robust and complete solution providing accurate and real-time measurements with submillimetre spatial resolution and a uniform response to the beam energy.

A promising tool is the LaGEMPix detector. It consists of a triple-GEM (Gas Electron Multiplier) [4] coupled to a highly pixelated readout based on a matrix of organic photodiodes (OPDs). The potential of a triple-GEM

detector combined with a high pixel granularity for QA in hadron therapy has already been demonstrated by its predecessor, the GEMPix [5]. Although promising, a wider sensitive area is required to cover the typical 20 x 20 cm² radiation field size. The new readout, based on the detection of the scintillation photons generated in the GEM holes, allows the development of a compact detector for larger-area imaging, further scalable with an expected good spatial resolution.

In this paper we report on the development of the first LaGEMPix prototype with a six times larger active area compared to the GEMPix (6 x 8 cm²). The detector is described in Section 3. The first results obtained using an X-Ray irradiator are reported in Section 4. Finally, Section 5 discusses the next steps of the project.

2. STATE OF THE ART

One of the advantages of hadron therapy is the possibility of driving the beam to accurately conform the dose to the tumour. To achieve this, it is critical to monitor the beam characteristics and the delivered dose. In routine QA checks, different kinds of dosimeters are employed to measure the 2D dose distribution [6].

International dosimetry guidelines propose the use of an array of ionization chambers for the weekly QA checks in a water phantom, due to their well-known performance and their accuracy and stability (small variation in

response with energy, dose and dose rate) [7]. However, ionization chamber-based systems have a poor spatial resolution limited by the size of the currently available detectors. The OCTAVIUS® Detector 1600 SRS, for example, consists of a matrix of 1521 vented plane-parallel ion chambers, with a spacing in the central area of 2.5 mm and 5 mm [8].

Films such as radiochromic EBT3 are generally used due to their very good spatial resolution down to 25 μm [9], but they provide an off-line response, which is also highly dependent on the particle energy [10].

Optical readout-based detectors are ideally suited for online monitoring of the beam. Scintillating screens coupled to CCD cameras with high spatial resolution for 2D dosimetry have been developed [11]. Other examples, such as the Lynx® commercial detector, which consists of a gadolinium-based plastic material, is only appropriate for relative 2D dosimetry measurements due to the strong energy dependence [12].

3. BREAKTHROUGH CHARACTER OF THE PROJECT

GEM detectors have been used in the past in particle therapy. In particular, the feasibility of optical-readout GEM-based detectors was previously investigated with CCD/CMOS cameras [13-15]. However, the degradation of the camera due to radiation requires placing it outside the beam, needing a more complex system with e.g. mirrors or lenses. In contrast to CCD/CMOS-based detectors, the highly pixelated readout of the LaGEMPix is adjacent to the GEM anode. This allows a more compact, easily scalable and low material budget set-up.

The LaGEMPix combines a triple-GEM detector with an area of 10 x 10 cm^2 and an optical readout based on three main building blocks: a Thin Film Transistor (TFT) backplane, a light sensitive OPD frontplane and a transparent thin-film encapsulation, serving as a protection against ambient conditions [16].

The triple-GEM detector includes a 20 μm thick Mylar window used as the cathode at 3.5 mm from the first GEM. The distance between the first and the second GEM is 1 mm and between the second and the third GEM is 2 mm. Each GEM foil consists of a 50 μm Kapton layer electroplated with a 5 μm thick Cu layer on both sides and pierced with holes of 70 μm diameter and 140 μm pitch. On the bottom of the third GEM, an ITO (Indium Tin Oxide) coated glass anode, with a thickness of 1.1 mm and resistivity of 100 Ω/sq , is placed at 1.9 mm distance to collect the electrons produced during the amplification process while allowing the optical photons to pass through [14, 17].

The sensor array has a resolution of 200 pixels per inch (ppi). It comprises 640 x 480 pixels, resulting in a total sensor area of 60 x 80 mm^2 . The OPD frontplane is

directly deposited on the TFT backplane by slot-die coating. The backplane is a self-aligned dual-gate oxide thin-film transistor array [18]. The sensor shows a dark current density of 10^{-7} mA/cm^2 at -2 V and a linear behaviour in a wide range of light intensities [19]. The OPD has a maximum external quantum efficiency (EQE) of ca. 50% at 550 nm, and about 25% at 640 nm (peak of the visible band emitted by the GEMs using an Ar:CF₄ (90/10) gas mixture).

4. PROJECT RESULTS

A first LaGEMPix prototype (Fig. 1) has been successfully built and tested as a preliminary step towards the development of a 20 x 20 cm^2 detector.

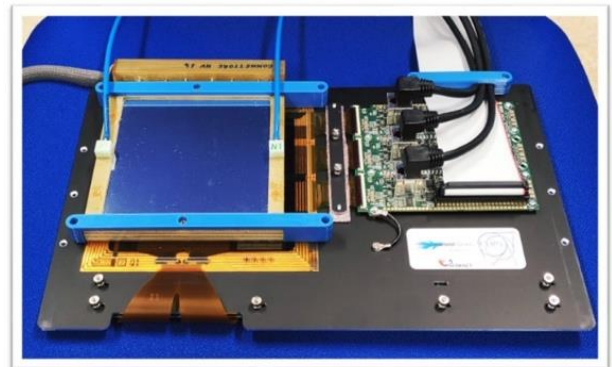


Fig. 1. The first LaGEMPix prototype.

We initially tested the triple-GEM detector at proton fluxes corresponding to high clinical beam intensities before coupling it to the optical matrix. We performed a current scan with 18 MeV protons at beam intensities up to 1.5 nA at the cyclotron at Inselspital in Bern [20]. We measured a linear behaviour between 2 pA and 1.5 nA with the sum of the GEM voltages equal to 500 V as shown in Fig. 2.

Later, the LaGEMPix was placed inside a custom made black PMMA box to shield the ambient light and provide a well aligned set-up. The readout was set to the highest sensitivity level of 0.5 pC, so that the least significant bit (LSB) of the 16-bit readout corresponds to a charge of approximately 70 electrons. The frame rate was 1 fps.

4.1. Dose response to Cs-137 photons

We performed a gain scan at the CERN Radiation Calibration Facility [21] with a 3 TBq Cs-137 source at 93.9 cm from the detector. The sum of the GEM voltages varied from 0 to 1030 V. The results are shown in Fig. 3. Each point is the average of the sum of all pixels for 10 recorded images. The light intensity vs high voltage gain follows an exponential trend. This was expected since the gain, i.e. the ratio of the number of electrons produced over the number of primary electrons, depends

exponentially on the applied GEM voltages. The number of scintillation photons increases proportionally with the number of secondary electrons, hence increasing exponentially with the gain [13].

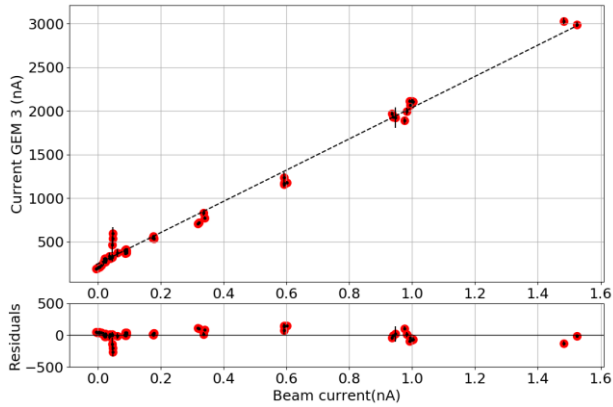


Fig. 2. Current at the last GEM vs the proton beam current of the 18 MeV cyclotron. The black dashed line represents a linear fit to the data. The bottom plot shows the residuals.

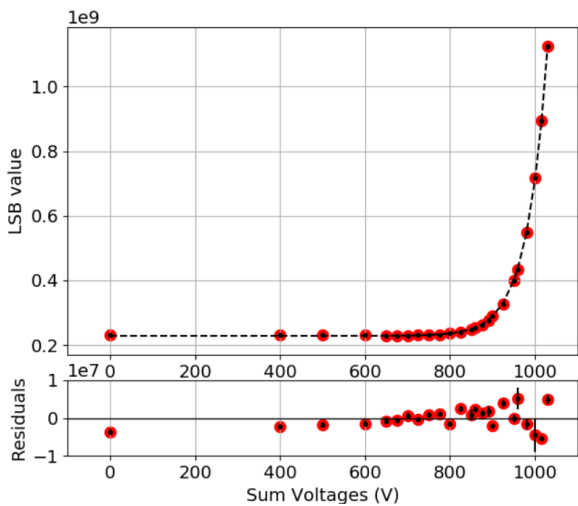


Fig. 3. Light intensity vs high voltage gain of the LaGEMPix using a 3 TBq Cs-137 source. The black dashed line represents an exponential fit to the data. The bottom plot shows the residuals.

4.2. Spatial Resolution

The spatial resolution of the LaGEMPix has been evaluated with 40 kV x-rays from an X-Ray irradiator, Model X80-320kV from Hopewell Designs, Inc. To ensure that undesirable effects such as readout inhomogeneities or noise are not affecting the results, a threshold per pixel was applied and dead pixels were removed. A background image was obtained by averaging each LSB pixel value over 200 background images. Then, each image was processed offline and the background subtracted. The final image was obtained by averaging each pixel over 200 background corrected images and the ROI (region of interest) selected.

To estimate the spatial resolution, we used two methods: the “edge response” and the “hole” response [22]. For the former method, we placed a lead block of $10 \times 20 \times 2.5 \text{ cm}^3$ size in front of the PMMA box covering half of the active area of the detector, while for the latter we used a 1 mm thick copper plate placed on the inner wall of the box at 3.3 cm from the Mylar window. Various holes of different sizes from 1.3 to 6 mm spaced by 2.5 to 17 mm were drilled in the plate. Results for both methods are shown in Figs. 4 and 5. The spatial resolution obtained by the first method is $8.40 \pm 1.93 \text{ mm}$ (FWHM). The spatial resolution measured by the second method varied between $6.67 \pm 0.47 \text{ mm}$ for the 6 mm hole and $5.35 \pm 0.70 \text{ mm}$ for the 3 mm holes (FWHM).

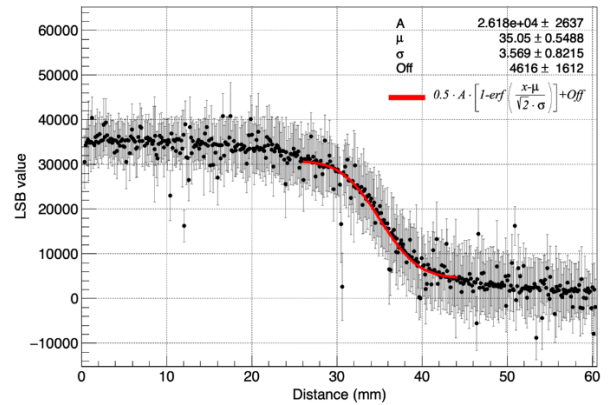


Fig. 4. Edge response profile for 40 kV x-rays using a lead block. The red line represents an error function fit to the data.

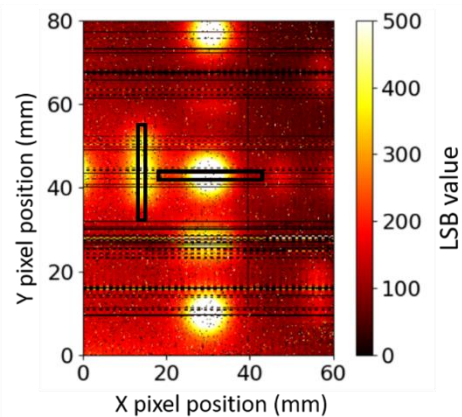


Fig. 5. Heat map of the Cu mask for 40 kV x-rays. Two ROIs (black lines) were set on the 6 mm and 3 mm holes. The spatial resolution is estimated by fitting the integrated profile in the ROIs by a Gaussian function.

5. FUTURE PROJECT VISION

During the ATTRACT phase 2, we would focus on the development of a compact and sealed $20 \times 20 \text{ cm}^2$

LaGEMPix. Our intention is, independently of ATTRACT Phase 2 funding, to start its development on a shorter time scale, seeking for alternative funding sources and including additional partners. For the detector part, CERN has some funds already secured from the Medical Application section of the KT (Knowledge Transfer) group.

5.1. Technology Scaling

The ATTRACT project allowed us to develop the first LaGEMPix prototype (TRL 3 to 4) as a preliminary step for the development of a 20 x 20 cm² detector. The results show that the required sub-millimeter spatial resolution is not yet achievable. Two possible modifications on the detector are here briefly discussed. Decreasing the distance between the last GEM and the readout plane could reduce the dispersion of the light before reaching the readout. To increase the light detection efficiency, the OPD active layer could be replaced by another one with a better match between the emitted light and the OPD's quantum efficiency. An alternative solution to this readout system would be to eliminate the OPD layer leaving a TFT-only electronic readout. With this approach, secondary electrons produced in the electron avalanche would be directly measured by the readout, yielding an even more compact and possibly more efficient device with a higher signal-to-noise ratio. Additional options are currently being assessed.

In order to reach TRL 5, we would need to perform tests in clinical proton and carbon ion beams, to define the exact specifications for machine and patient QA. CERN RP group has an open collaboration with CNAO (the Italian Centre for Oncological Hadron Therapy). However, due to the COVID-19 pandemic, travelling to CNAO was not possible during the timeframe of this project.

To demonstrate the application of the LaGEMPix in QA for hadron therapy, we need to scale up the present prototype. Based on the experience with coupling the current OPD-TFT readout with the GEMs, we do not expect major issues to increase the detector size. The major efforts will be devoted to achieve the required spatial resolution of about 0.5 mm, and to prove the radiation hardness of the detector in clinical ion beams. A further planned step is to develop a sealed version of the LaGEMPix, which would avoid the installation of a gas system inside the treatment room thus simplifying the detector setup.

5.2. Project Synergies and Outreach

We are currently exploring the possibility of extending the CERN-TNO consortium mostly to secure funding for the development of the new TFT-only readout. Preliminary contacts have been established with the University of Groningen and the University of Delft in The Netherlands and CNAO in Italy.

We also plan to merge the results of this project with those of the ATTRACT GEMTEQ project, which has developed a version of the GEMPix for microdosimetry. Very interesting results have been achieved [23] paving the way to structural track microdosimetry. We also had an informal discussion with the ATTRACT project H2I2, (Hybrid high-precision in vivo imaging in particle therapy), which we plan to deepen in the future.

5.3. Technology application and demonstration cases

Merging a 20 x 20 cm² LaGEMPix imaging detector with the microdosimetric capability of the GEMPix demonstrated by the ATTRACT GEMTEQ project, and integrating such innovative device in a motorised water phantom (already built and tested outside the ATTRACT framework [5]), would yield an exceptional quality assurance tool for treatment planning and dose delivery in particle therapy, driven by a detailed knowledge of the radiobiological effectiveness (RBE) of the radiation. This approach, which has never been implemented until now, would bring a contribution to "personalised medicine" in cancer therapy.

5.4. Technology commercialization

For the commercialisation of a final product, we will need a dosimetry company or a medical instrumentation company with the required competences for industrialising the prototype. Some interest has been shown by a vendor of medical equipment, Philips, with whom we have established a preliminary contact.

5.5. Envisioned risks

The project started on a very solid basis, as the GEMPix was thoroughly studied by CERN RP group, specifically for medical applications, and TNO has a solid knowledge of TFT backplanes. Large area TFT backplanes are extensively used, generally as active electronic switching elements.

A preliminary risk analysis has been carried out leading to the identification of different types of risk, technological and organizational. The key risks concerning the technology development are: 1) radiation damage to the electronics; 2) delay in the development of the new TFT-only readout; 3) insufficient performance of the new readout; 4) insufficient performance of the new detector such as an insufficient spatial resolution. The lack of successful collaboration among partners or the withdrawal of one of the partners has been identified as a low-likelihood risk.

5.6. Liaison with Student Teams and Socio-Economic Study

The project has involved one Portuguese trainee (AMO), initially funded by the CERN-Portugal trainee program,

who subsequently enrolled as doctoral student at the University of Bern. She will use the work performed during ATTRACT for her PhD thesis, that will be completed in the coming 18 months within CERN doctoral student program.

An ATTRACT Phase 2 project will involve a larger consortium; a mixture of research institution and companies. It will offer very interesting opportunities for master and doctoral theses, to train experts in advanced dosimetric instrumentation who will later be able to work either in research institutions, in the private sector or in hospitals. With an estimated 3-year duration of a Phase 2 project, we envisage to organise annual scientific workshops in order that all partners can regularly meet. These workshops will also provide the occasion to organise training courses for the students involved in the project. A typical format of such workshops may include: 1) scientific meetings to discuss work progress; 2) a training course on one of the research areas of the project, during which experts will deliver seminars on recent progress in the field. The courses will be open to external researchers and local PhD students; 3) one full “Outreach day” dedicated to e.g. an Hackathon or an outreach event with students from local high schools, organised by the hosting organisation, where EU’s role in supporting young scientists and in promoting research will also be explained; 4) an open discussion with the general public.

6. ACKNOWLEDGEMENTS

We wish to thank S. Braccini and colleagues at the University of Bern for the test at the Inselspital.

This project has received funding from the ATTRACT project funded by the EC under Grant Agreement 777222. The project has also been supported by CERN’s Budget for Knowledge Transfer to Medical Applications.

7. REFERENCES

- [1] Particle therapy facilities in clinical operation (last update: July 2020), <https://www.ptcog.ch/index.php/facilities-in-operation>, accessed on 18 July 2020.
- [2] Ishikawa et al., H., 2019. Particle Therapy in Cancer Treatment - Current and Future Perspective, *Gan to Kagaku Ryoho, Cancer & Chemotherapy*, 46(8): pp. 1219-1225.
- [3] Rana, S. et al., 2019. Development and long-term stability of a comprehensive daily QA program for a modern pencil beam scanning (PBS) proton therapy delivery system, *Journal of Applied Clinical Medical Phys.*, 20(4):pp. 29-44.
- [4] Sauli, F. 2016. The gas electron multiplier (GEM): Operating principles and applications, *Nuclear Instruments and Methods in Physics Research Section A: Accelerators, Spectrometers, Detectors and Associated Equipment*, 805: pp. 2-24.
- [5] Leidner, J. et al., 2020. A GEMPix-based integrated system for measurements of 3D dose distributions in water for carbon ion scanning beam radiotherapy, *Medical Physics*, 47(6): pp. 2516-2525.
- [6] Grevillot, L. et al., 2018. Implementation of dosimetry equipment and phantoms at the MedAustron light ion beam therapy facility, *Medical Physics*, 45 (1): pp.352-369
- [7] Journal of the ICRU Vol 7 No 2 (2007) Report 78, Oxford University Press.
- [8] OCTAVIUS® Detector 1600 SRS, Detector array for patient plan verification and quality control of SRS applications, <https://www.ptwdosimetry.com/en/products/octavius-detector-1600-srs/>, accessed on 4 August 2020.
- [9] GAFChromic™ EBT3 film specifications, www.gafchromic.com, access on 18 July 2020.
- [10] Spielberger, B. et al., 2001. Experimental investigations of the response of films to heavy-ion irradiation, *Physics in Medicine and Biology*, 46 (11): pp. 2889-2897.
- [11] Safai, S. et al., 2004. Development of an inorganic scintillating mixture for proton beam verification dosimetry, *Physics in Medicine and Biology*, 49(19): pp. 4637-4655
- [12] Russo, S. et al., M., 2017. Characterization of a commercial scintillation detector for 2-D dosimetry in scanned proton and carbon ion beams, *Physica Medica*, 34 (2017): pp. 48-54.
- [13] Seravalli, E., 2009. 2D dosimetry in a proton beam with a scintillating GEM detector, *Physics in Medicine and Biology*, 54: pp. 3755–3771
- [14] Brunbauer, F., 2018. Applications of gas scintillation properties in optically read out GEM-based detectors. CERN-THESIS-2018-106.
- [15] Klyachko, A., 2012. A GEM-based dose imaging detector with optical readout for proton radiotherapy, *Nuclear Instruments and Methods in Physics Research Section A: Accelerators, Spectrometers, Detectors and Associated Equipment*, 694: pp. 271-279
- [16] Weijer, P. van de et al., 2019. Spotless hybrid thin-film encapsulation stack for organic light-emitting diodes on organic foils, *Organic Electronics*, 66: pp. 43-46
- [17] ITO Glass - Conductive Coated Glass Slides & Sheet. http://www.visionteksystems.co.uk/ito_glass_datasheet.htm on 25 February 2020.
- [18] Kronemeijer, A. J. et al., 2018. Dual-gate self-aligned IGZO TFTs monolithically integrated with high-temperature bottom moisture barrier for flexible AMOLED, *SID International Symposium: Digest of Technical Papers*, 49(1): pp. 1577-1580.
- [19] Tordera, D. et al., 2019. A High-Resolution Thin-Film Fingerprint Sensor Using a Printed Organic Photodetector, *Advanced Materials Technologies*, 4(11): 1900651.
- [20] Auger, M., et al., 2015. Low current performance of the Bern medical cyclotron down to the pA range, *Measurement Science and Technology*, 26(9): pp. 094006.
- [21] Brugger, M. et al., 2014. New radiation protection calibration facility at CERN. *Radiation Protection Dosimetry*, 161(1-4): pp. 181-184.
- [22] Smith, S. W., 1997, *Special Imaging Techniques*. In *The Scientist and Engineer's Guide to Digital Signal Processing*. California Technical Publishing, San Diego, California, USA, pp. 423-432.
- [23] GEMTEQ: GEMPix detector for microdosimetry with tissue-equivalent gas, ATTRACT final report, 2020.

Contributors and Funding Sources

This Project has been co-funded by the CERN Budget for Knowledge Transfer to Medical Applications.

This project has received funding from the ATTRACT project funded by the EC under Grant Agreement 777222.

Andreia Maia Oliveira was co-supported by a grant from FCT with reference SFRH/BEST/142965/2018.

Declaration of consent

on the basis of Article 18 of the PromR Phil.-nat. 19

Name/First Name: Maia Oliveira/ Andreia Cristina

Registration Number: 18-131-995

Study program: AEC Graduate Student Programme

Bachelor Master Dissertation

Title of the thesis: A high-resolution large-area detector for quality assurance in cancer radiation therapy

Supervisor: Prof. Dr. Saverio Braccini

I declare herewith that this thesis is my own work and that I have not used any sources other than those stated. I have indicated the adoption of quotations as well as thoughts taken from other authors as such in the thesis. I am aware that the Senate pursuant to Article 36 paragraph 1 litera r of the University Act of September 5th, 1996 and Article 69 of the University Statute of June 7th, 2011 is authorized to revoke the doctoral degree awarded on the basis of this thesis.

For the purposes of evaluation and verification of compliance with the declaration of originality and the regulations governing plagiarism, I hereby grant the University of Bern the right to process my personal data and to perform the acts of use this requires, in particular, to reproduce the written thesis and to store it permanently in a database, and to use said database, or to make said database available, to enable comparison with theses submitted by others.

Wien/ 05.02.2014

Place/Date



Signature